Microgel Technology to Advance Modular Tissue Engineering

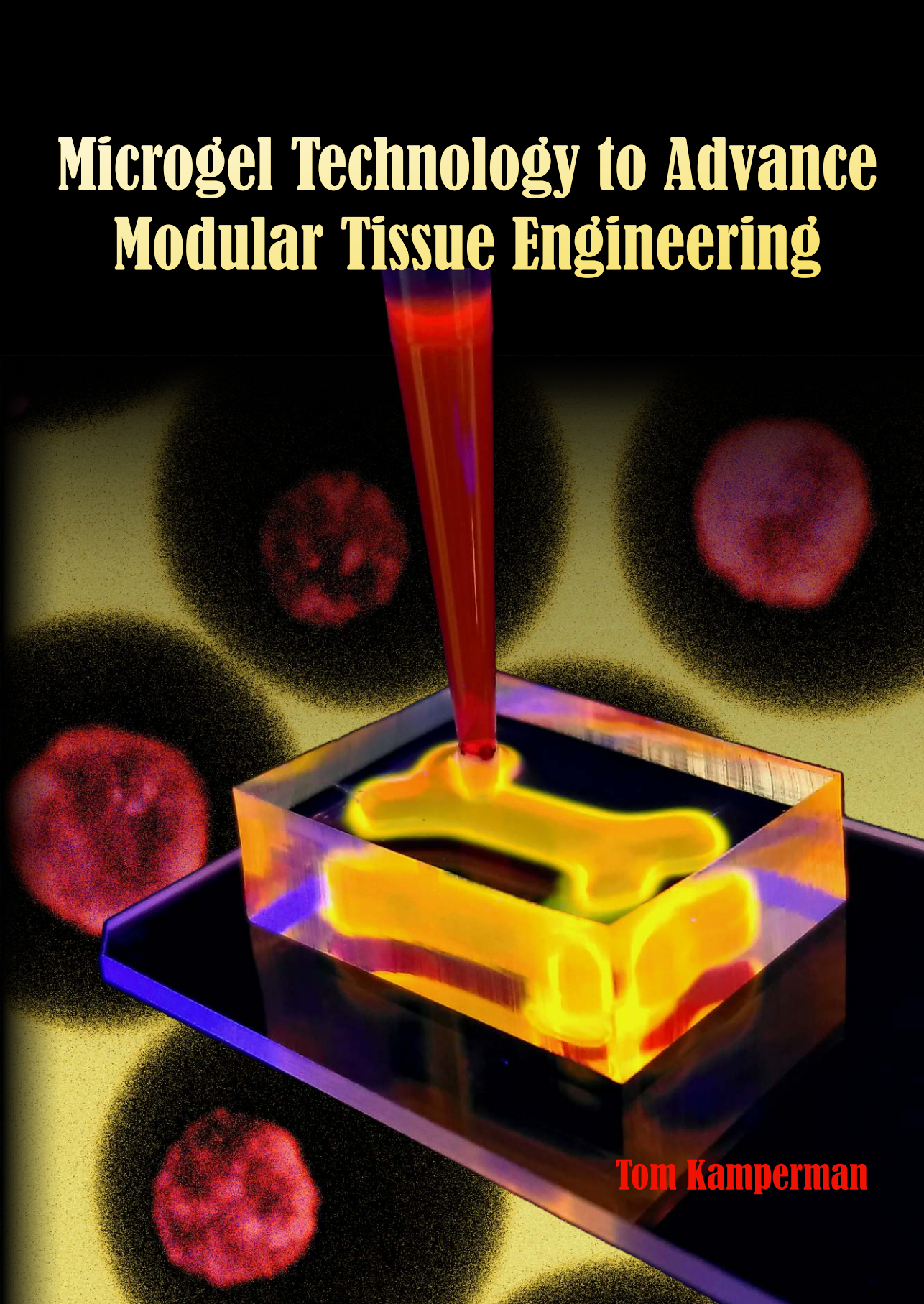

Tom Kamperman

MICROGEL TECHNOLOGY TO ADVANCE MODULAR TISSUE ENGINEERING

Tom Kamperman

2018

Graduation Committee

prof. dr. ir. J.W.M. Hilgenkamp (chairman)	University of Twente
prof. dr. H.B.J. Karperien (supervisor)	University of Twente
dr. J.C.H. Leijten (co-supervisor)	University of Twente
prof. dr. ir. A. van den Berg	University of Twente
prof. dr. D. Lohse	University of Twente
prof. dr. L.W.M.M. Terstappen	University of Twente
prof. dr. W.T.S. Huck	Radboud University
prof. dr. ir. J. Malda	University of Utrecht
prof. dr. ir. J.M.J. den Toonder	Eindhoven University of Technology

Microgel Technology to Advance Modular Tissue Engineering

Tom Kamperman, 2018

The work in this PhD thesis was performed in the department of Developmental BioEngineering within the MIRA Institute for Biomedical Technology and Technical Medicine, and the Faculty of Science and Technology of the University of Twente, Enschede, The Netherlands

The research was funded by the Dutch Arthritis Foundation and the printing of this thesis was supported by the Netherlands society for Biomaterials and Tissue Engineering (NBTE).

Cover design: Fluorescent photographs of injection molded modular bio-ink (foreground) that contains single-cell-laden microgels embedded in distinct polymer matrix (background).

Printed by Gildeprint, Enschede, The Netherlands

ISBN: 978-90-365-4461-0

DOI: 10.3990/1.9789036544610

MICROGEL TECHNOLOGY TO ADVANCE MODULAR TISSUE ENGINEERING

DISSERTATION

to obtain
the degree of doctor at the University of Twente,
on the authority of the rector magnificus,
prof. dr. T.T.M. Palstra
on account of the decision of the graduation committee,
to be publicly defended
on Friday, January 26th 2018, at 16.45

by

Tom Kamperman

Born on February 13th, 1988
in Winterswijk, The Netherlands

This dissertation has been approved by:

prof. dr. H.B.J. Karperien (supervisor)
dr. J.C.H. Leijten (co-supervisor)

Summary

The field of tissue engineering aims to restore the function of damaged or missing tissues by combining cells and/or a supportive biomaterial scaffold into an engineered tissue construct. The construct's design requirements are typically set by native tissues – the gold standard for tissue engineers. Closely observing native tissues from an engineering perspective reveals a complex multiscale modular design. This natural architecture is essential for proper tissue functioning, but not trivial to manufacture. Recapitulating the complexity of native tissues requires high-resolution manufacturing technologies such as microfluidics. However, increasing resolution is typically at the cost of production throughput and *vice versa*, which hampers the clinical translation of complex tissue engineering strategies. New advanced concepts that integrate both high-resolution and rapid additive manufacturing techniques are thus prerequisite to upgrade the field of modular tissue engineering.

This thesis describes: i) the development of various innovative biomaterials and microfluidic platforms for the production of (cell-laden) hydrogel microparticles (i.e. microgels) that act as tissue engineering building blocks; ii) the modification of microgels with *in situ* tunable biomechanical and biochemical properties to enable specific tailoring of the cellular microenvironment; iii) their incorporation into modular bio-inks, which is a novel concept to enable the facile engineering of complex tissues using standard biofabrication methods; and iv) the invention of a platform technology called 'in-air microfluidics' (IAMF), which uniquely enables the chip-free micromanufacturing of droplets, particles, and 3D modular biomaterials at rates that are readily compatible with clinical applications.

Together, this thesis introduces a number of innovative biomaterial modifications and microfluidics-based manufacturing concepts that facilitate the development and clinical translation of modular tissue engineering applications.

Samenvatting

Het vakgebied weefselengineering heeft tot doel de functie van beschadigde of ontbrekende weefsels te herstellen door cellen en/of een ondersteunend biomateriaal te combineren tot een weefselconstruct. De ontwerpcriteria van het weefselconstruct worden doorgaans bepaald door natuurlijke weefsels – de gouden standaard voor weefselingenieurs. Nauwkeurige observatie van natuurlijke weefsels vanuit een engineering perspectief onthult een complexe hiërarchische modulaire architectuur. Deze natuurlijke architectuur is essentieel voor een goede weefselfunctie, maar niet triviaal om te vervaardigen. Het kopiëren van de complexiteit van natuurlijke weefsels vereist hoge resolutie productietechnologieën, zoals microfluïdica. Echter, toenemende resolutie gaat typisch ten koste van de productie capaciteit en *vice versa*, wat de klinische translatie van complexe weefseltechnologie belemmert. Nieuwe geavanceerde concepten die zowel hoge resolutie als snelle fabricatietechnieken integreren, zijn dus essentieel om modulaire weefselengineering te verbeteren.

Dit proefschrift beschrijft: i) de ontwikkeling van diverse innovatieve biomaterialen en microfluïdische platformen voor de productie van (cel bevattende) hydrogel micropartikels (microgels) die fungeren als weefselbouwstenen; ii) de verrijking van microgels met *in situ* modificeerbare biomechanische en biochemische eigenschappen om specifieke adaptatie van de micro-omgeving van de cel mogelijk te maken; iii) het combineren van microgels in modulaire bio-inkt, wat een nieuw concept is om complexe weefsels te produceren met behulp van standaard biofabricatiemethoden; en iv) de uitvinding van een platformtechnologie genaamd 'in-air microfluidics' (IAMF), die uniek de chipvrij microfabricatie van druppels, deeltjes en 3D modulaire biomaterialen mogelijk maakt op snelheden die klinisch transleerbaar zijn.

Samengevat presenteert dit proefschrift een aantal innovatieve biomateriaal modificaties en microfluïdica-gebaseerde productieconcepten die de ontwikkeling en de klinische vertaling van modulaire weefselengineering concepten stimuleert.

Contents

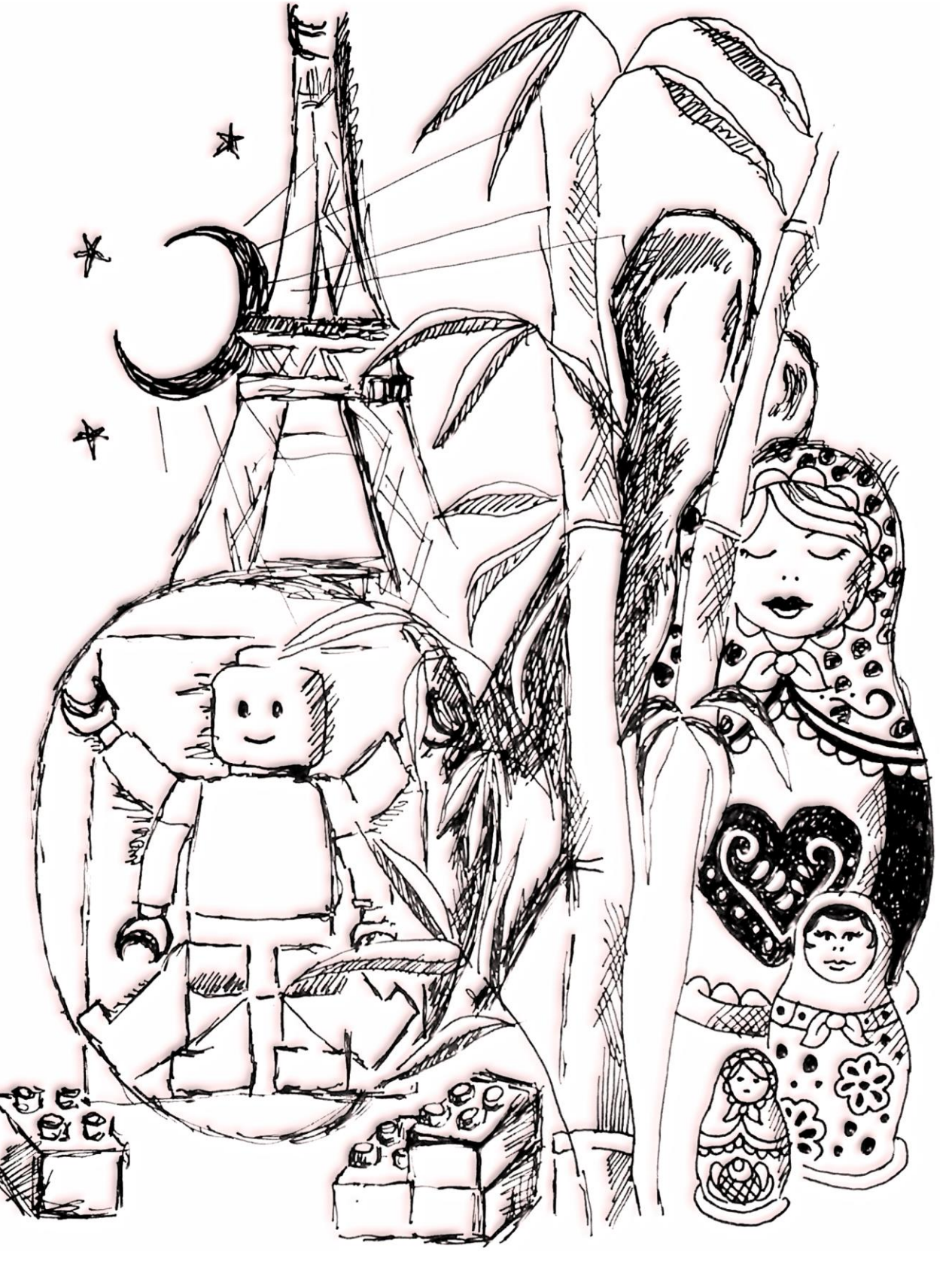

1

Introduction and Motivation

1.1 Introduction

1.1.1 Tissue Engineering

The idea to create man-made tissues to repair or replace natural tissues has existed since ancient times. Early Greek literature, passages in the Old Testament, and descriptive paintings of the Roman Empire are among the oldest records of this subject.[1-3] The discoveries of an Egyptian wooden toe prosthesis (1065–740 BC) and a first-century Roman metallic tooth implant provide direct evidence of ancient tissue engineers who pioneered in restoring body functions using man-made tissue substitutes.[4, 5] Based on developments in clinical medicine (e.g. prosthetics, anesthetics, transplantation) and biology (e.g. microbiology, biochemistry, genetics), tissue engineering has emerged into a mature interdisciplinary field within the area of life sciences.[6] To date, tissue engineers have attempted to develop substitutes for virtually every mammalian tissue.[7]

1.1.2 Natural Tissue Architecture

The original modern tissue engineering paradigm is based on homogeneously combining cells and tissue-inducing substances with an isotropic supportive scaffold to form a substitute graft.[8-10] Although such top-down engineering results in grafts with clinically relevant sizes, their simplistic design often does not recapitulate the complex architecture of native tissue. In fact, native tissues are characterized by repetitive functional units that span several length scales and are arranged into a multiscale modular design (**Figure 1.1**).[11] This multiscale modularity is essential to combine multiple otherwise paradoxical material properties into one construct. For example, the structural hierarchy in natural wood and bone provides both strength and toughness, which enables large and strong, but light-weight porous constructs that support nutrition through liquid transport.[12]

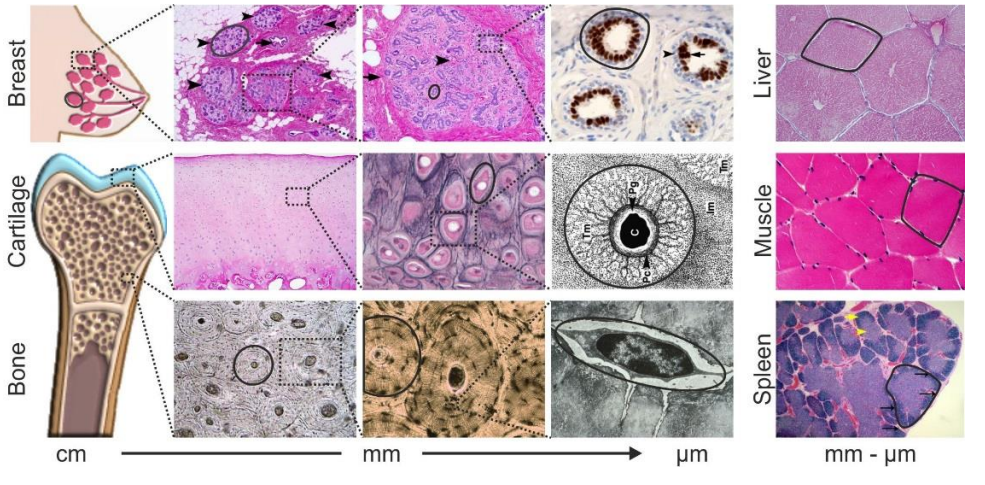

Figure 1.1. Multiscale modularity in native tissues. Zooming in on various native tissues reveals well-structured functional modules across several length scales. The modules are encircled by solid black lines. Adapted from references.[13-21]

1.1.3 Modular Tissue Engineering

A new paradigm based on modular, or bottom-up, tissue engineering has been proposed to enable facile incorporation of complex multiscale modularity into man-made tissue constructs.[22-26] This approach relies on the fabrication and assembly of particles and cells that act as building blocks to engineer larger tissues (**Figure 1.2**). The (cell-laden) building blocks are typically made of hydrogel, as these water containing polymer networks structurally mimic the extracellular matrix of native tissues.[27-29] Several micromanufacturing technologies based on molding, emulsification, or spraying have been developed to produce such hydrogel microparticles, also called microgels).[30-32]

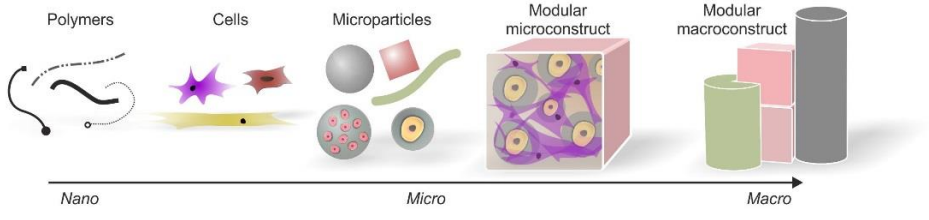

Figure 1.2. The concept of modular tissue engineering. Modular tissue engineering is a bottom-up approach where typically polymers, cells, and (cell-laden) microparticles are assembled into larger modular constructs.

Droplet microfluidics offers the resolution and control to continuously produce monodisperse microgels with defined size, shape, and composition, which could act as 3D (cell-laden) building blocks (**Figure 1.3**).[33-35] Mixing and matching various building blocks readily enables the engineering of myriad tissue constructs with intricate microstructural features as present in native tissues.[14, 36] However, several technical hurdles have still to be taken before man-made grafts can accurately mimic the multifunctionality of native tissues, and can be produced at a clinically relevant scale.

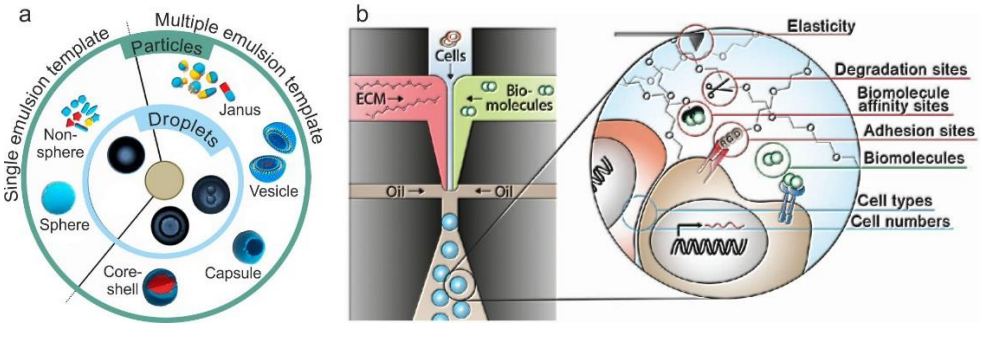

Figure 1.3. Droplet microfluidics for fabrication of tissue engineering building blocks. (a) Droplet microfluidics is an emulsion-based technology that is compatible with the production of a wide variety of droplets and particles. **(b)** Schematic representation of a microfluidic flow focusing droplet generator for the production of biochemically and biomechanically defined cell-laden microgels. Adapted from references.[34, 37]

1.2 Motivation: Challenges and Contributions

This thesis addresses a number of challenges that currently hamper the widespread application of droplet microfluidics-based modular tissue engineering. The **current chapter (1)** provides the reader with a short perspective on the emergence and pertinence of tissue engineering and specifically microfluidics-based modular approaches. In the following sections, we introduce the main challenges (underlined) and provide a per-chapter overview on how this thesis contributes to overcome these.

1.2.1 In-emulsion Enzymatic Crosslinking

The production of cell-laden microgels is typically based on the emulsification of a cell containing hydrogel precursor solution followed by an *in situ* crosslinking reaction. In contrast to widely exploited, but cytotoxic, ionic- and photo-based crosslinking strategies, enzymatic crosslinking enables the facile, cytocompatible, and rapid production of cell-laden hydrogels.[38-40] However, enzymatic crosslinking is not trivial in emulsion-based droplet microfluidics, as emulsions are typically multiphase immiscible systems where oil hampers the direct mixing of the hydrogel precursor and its crosslinker. There is currently only a limited number of micromanufacturing approaches that are compatible with the in-emulsion enzymatic crosslinking of cell-laden hydrogel particles, which has limited the widespread use of this promising class of biomaterials for cell microencapsulation.

Chapter 2 focuses on the enzymatic crosslinking of tyramine-functionalized polymer droplets using nanoemulsified crosslinker to form hydrogel particles that span multiple length scales. In particular, the in-emulsion enzymatic crosslinking strategy is leveraged to produce cell-laden microgels using droplet microfluidics.

1.2.2 Preventing Cell Escape

Modularity could be introduced into tissue engineered constructs using relatively large building blocks (≥100 μm).[41-44] However, cells covered by a thin layer of matrix are life's smallest functional eukaryotic units that can exist on their own. For modular tissue engineering approaches it is therefore intuitive to use building blocks composed of a single cell surrounded with a thin layer of matrix (e.g. microgels <40 μm). Droplet microfluidics technology is in principle ideally suited for the production of such (single-)cell-laden microgels.[45] However, currently explored single cell microencapsulation strategies have suffered from rapid cell escape caused by off-center cell encapsulation (**Figure 1.4a-c**).[34] This hampers all investigations and applications that require the long-term culture of individual cells in controlled 3D microenvironments.

In **chapter 3**, we reveal that cells are positioned on the outer edge of gel precursor droplets immediately after emulsification. Immediate gelation – which is the general exploited strategy in the microencapsulation field – thus results in off-center cell encapsulation. By delaying gelation, cells are allowed to reposition to the droplet's center. We present the first microfluidic approach that exploits on-chip delayed gelation

to enable long-term 3D single cell culture by centering cells in microgels in a facile, modular, and widely applicable manner.

1.2.3 *In Situ* Tunable Building Blocks

Native tissues are characterized by a dynamic nature. For example, tissue development is a multi-staged process that involves remodeling of the extracellular matrix.[46] Recapitulating such dynamicity in engineered tissues requires the temporal control over their biochemical composition. Although tissue engineers have recently started to integrate these complex functions into smart (i.e. instructive and responsive) biomaterials,[47-58] their use has remained limited to bulk constructs that do not recapitulate the modular design of native tissues. The modular tissue engineering toolbox is thus currently lacking *in situ* biochemically and biomechanically tunable building blocks, which are essential to incorporate both the dynamicity and multiscale modularity of native tissue into artificial tissue constructs.

In **chapter 4**, we introduce 'direct on-cell crosslinking' (DOCKING) of non-adhesive biomaterial onto stem cells, which is a bio-inspired technology that enables the transduction of biomechanical cues to the stem cells in a unique RGD-independent manner. We use DOCKING in combination with droplet microfluidics to demonstrate encapsulation of stem cells into microgels with *in situ* tunable stiffness. This strategy readily supports the investigation of single stem cell lineage commitment dynamics in 3D, which is a new feature in the field of mechanotransduction.

Chapter 5 covers the development of *in situ* biochemically tunable microgels for modular tissue engineering. Specifically, we introduce desthiobiotin/biotin displacement to engineer *in situ* tunable microgels that act as smart building blocks, thereby granting reversible and sequential spatiotemporal biochemical control over self-assembled living modular tissue constructs.

1.2.4 Beating Poisson

Single cell encapsulation strategies are typically challenged by Poisson-distributed cell encapsulation, which inherently results in many non-cell-laden microgels (**Figure 1.4d**).[59] Although high-yield deterministic single cell encapsulation in culture medium droplets has been demonstrated using inertial focusing,[60] these forces are too weak to obtain longitudinal cell ordering in comparatively viscous fluids such as hydrogel precursor solutions. Non-pure microgel fractions are highly inefficient and impede subsequent applications, including modular tissue engineering. Specifically, too many non-cell-laden microgels may result in modular constructs with non-physiological cell concentrations.

In **chapter 6**, we exploit droplet microfluidics-based single cell encapsulation followed by flow cytometry-based sorting to obtain >90% pure cell-laden microgel fractions.

1.2.5 Multifunctionality

The aim of modular tissue engineering is to create multifunctional tissue constructs that can simultaneously provide cell-centric microenvironments to support e.g. encapsulated cell survival and function, as well as host-centric macroenvironments to support e.g. integration, anastomosis, and mechanical integrity. Although it might seem trivial, multifunctional modular tissue constructs with distinct optimized cellular micro- and macro environments have remained elusive.

In **chapter 6**, modular bio-inks are created by combining purified (see section '1.2.4 Poisson distribution') single-cell-laden microgels with a distinct cell-laden injectable hydrogel to manufacture modular 3D constructs with optimized cellular micro- and macroenvironments. We demonstrate that such modular bio-inks readily enable the engineering of a construct with two clinically important yet normally incompatible characteristics, namely immunoprotection and angiogenesis. Furthermore, we demonstrate the compatibility of modular bio-inks with a multitude of standard biofabrication technologies including molding, spinning, and 3D printing.

1.2.6 Upscaling and Integration

Due to its high resolution and control, multiphase droplet microfluidics is widely applied for the production of tissue engineering building blocks.[34, 35] However, despite their success in lab-scale analysis and production, microfluidic chips also have intrinsic limitations that have hampered the extensive clinical and industrial translation of microfluidic concepts.[61-63]

Conventional droplet microfluidics' throughput is limited, as controlled microdroplet production is restricted to the dripping regime. For low-surface tension liquids such as biological or polymer solutions, this requires Capillary number $Ca \leq 0.1$,[64, 65] which typically corresponds to per-nozzle flow rates of 1-10 µl/min, as confirmed by data from literature (**Figure 1.4e**). In contrast, clinical and industrial scale applications require throughput of 1-1000 ml/min, thus at least 100x faster as compared to chip-based droplet microfluidics. Faster jet-based microfluidics ($Ca > 0.1$) results in polydisperse droplets (and thus particles) due Rayleigh-Plateau instabilities that cause spontaneous breakup.[66-68] Advanced strategies based on bubble-triggered jet breakup have been demonstrated to enable the on-chip production of monodisperse microdroplet production with more than tenfold higher rates.[65, 69] However, introducing air bubbles into microfluidic chip typically causes other issues such as flow instabilities.[70]

Microfluidic chips can only be operated with at least one non-solidifying co-flow, which is required to separate droplets, particles, or fibers from each other and the channel walls.[71, 72] This co-flow (e.g. oil) not only impairs clinical translation, it also interferes with the microfluidics' straightforward integration into rapid additive manufacturing processes. Specifically, chip-based microfluidic products are limited to suspensions and emulsions, which are incompatible with the direct manufacturing of larger 3D constructs.

Chapter 7 describes the invention of a platform technology called 'in-air microfluidics' (IAMF), which revolutionizes microfluidics-based manufacturing in several ways. IAMF is a chip-free method were liquid microjets are combined and controlled in a gaseous phase (e.g. air) to form monodisperse emulsions and suspensions at rates that are ~100x higher as compared to conventional chip-based microfluidics, while maintaining resolution. Furthermore, IAMF is compatible with solidifying co-flows; in-air and oil-free produced micromaterials can be directly jetted onto substrates to form larger modular 3D constructs in one step. We demonstrate that this integration of micro- and macromanufacturing effectively enables the clinical-scale manufacturing of 3D tissue-engineered constructs with an intrinsic structure that closely mimics the modularity of native tissues.

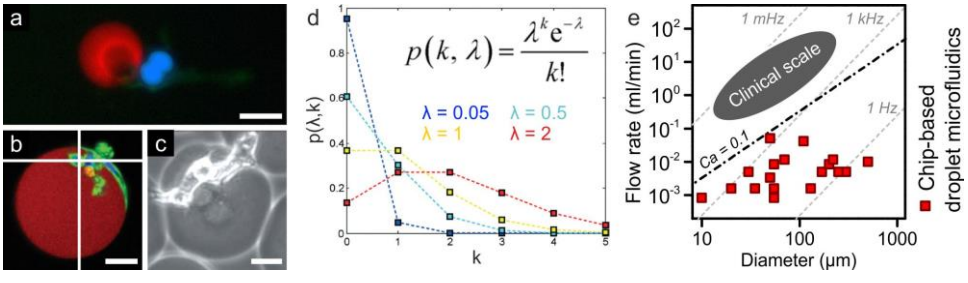

Figure 1.4. Limitations of conventional droplet microfluidics-based single-cell-laden tissue building block fabrication. (a-c) Investigation of various landmark papers in the field revealed consistent cell escape from microgels during *in vitro* culture within a few days from encapsulation. **(d)** The number of encapsulated cells per microdroplet or –gel can be described by the Poisson distribution and is often represented by plotting the chance '*p*' of finding a certain cell number '*k*' in a droplet as a function of the average number of cells per droplet '*λ*'. Importantly, the single cell encapsulation yield of random cell encapsulation strategies is inherently maximized to 37%. **(e)** Droplet microfluidic chips are typically operated in the dripping regime, which requires Ca ≤ 0.1,[64, 65] Plotting the per-nozzle flow rate as a function of the droplet diameter of various droplet microfluidics-based studies (red squares)[60, 64, 73-80] confirmed this upper limit and revealed typical throughputs of 1-10 µl/min and droplet frequencies in the 1-1000 Hz range. We anticipate that typical clinical applications require higher throughputs, in the order of ml/min. Subpanels (a-d) adapted from references.[59, 81-83]

1.2.7 Future Perspective

This thesis describes several novel biomaterial modifications and microfluidic concepts to further expand the modular tissue engineering toolbox. In short, it contributes to the field by improving the resolution, versatility, and throughput of tissue building block fabrication, as well as by pioneering integration of micro- and macromanufacturing strategies to aid widespread use and eventually clinical translation of modular tissue engineering.

Importantly, each of these contributions have their own limitations. **Chapter 8** reflects on these and provides possible directions for future research with respect to microfluidics-based modular tissue engineering.

References

1. Jovic, N.J. and M. Theologou, *The miracle of the black leg: E astern neglect of Western addition to the hagiography of Saints Cosmas and Damian.* Acta Med Hist Adriat, 2015. **13**(2): p. 329-44.
2. *Genesis*. Vol. 21. 2.
3. Kaul, H. and Y. Ventikos, *On the genealogy of tissue engineering and regenerative medicine.* Tissue Eng Part B Rev, 2015. **21**(2): p. 203-17.
4. Crubezy, E., et al., *False teeth of the Roman world.* Nature, 1998. **391**(6662): p. 29.
5. Nerlich, A.G., et al., *Ancient Egyptian prosthesis of the big toe.* Lancet, 2000. **356**(9248): p. 2176-9.
6. Meyer, U., *The History of Tissue Engineering and Regenerative Medicine in Perspective*, in *Fundamentals of Tissue Engineering and Regenerative Medicine*, U. Meyer, et al., Editors. 2009, Springer Berlin Heidelberg: Berlin, Heidelberg. p. 5-12.
7. Langer, R. and J.P. Vacanti, *Tissue engineering.* Science, 1993. **260**(5110): p. 920-6.
8. O'Brien, F.J., *Biomaterials & scaffolds for tissue engineering.* Materials Today, 2011. **14**(3): p. 88-95.
9. Drury, J.L. and D.J. Mooney, *Hydrogels for tissue engineering: scaffold design variables and applications.* Biomaterials, 2003. **24**(24): p. 4337-51.
10. Hollister, S.J., *Porous scaffold design for tissue engineering.* Nat Mater, 2005. **4**(7): p. 518-24.
11. Lenas, P., et al., *Modularity in developmental biology and artificial organs: a missing concept in tissue engineering.* Artificial Organs, 2011. **35**(6): p. 656-62.
12. Lakes, R., *Materials with structural hierarchy.* Nature, 1993. **361**(6412): p. 511-515.
13. http://www.pathpedia.com/education. 2017.
14. Liu, J.S. and Z.J. Gartner, *Directing the assembly of spatially organized multicomponent tissues from the bottom up.* Trends Cell Biol, 2012. **22**(12): p. 683-91.
15. Poole, C.A., M.H. Flint, and B.W. Beaumont, *Morphological and functional interrelationships of articular cartilage matrices.* J Anat, 1984. **138 (Pt 1)**: p. 113-38.
16. http://www.bbc.co.uk/schools. 2014.
17. Hill, M.A., *Embryology Cartilage histology 001.jpg*. 2017.
18. http://medpics.ucsd.edu/images, 2017.
19. Martiniakova, M., M. Vondrakova, and R. Omelka, *Manual preparation of thin sections from historical human skeletal material.* Timisoara Medical J, 2006. **56**: p. 15-17.
20. Werning, S., *Liver lobules*. 2007.
21. http://www.mun.ca/biology. 2012.
22. Nichol, J.W. and A. Khademhosseini, *Modular Tissue Engineering: Engineering Biological Tissues from the Bottom Up.* Soft Matter, 2009. **5**(7): p. 1312-1319.
23. Zorlutuna, P., N.E. Vrana, and A. Khademhosseini, *The expanding world of tissue engineering: the building blocks and new applications of tissue engineered constructs.* IEEE Rev Biomed Eng, 2013. **6**: p. 47-62.
24. Elbert, D.L., *Bottom-up tissue engineering.* Curr Opin Biotechnol, 2011. **22**(5): p. 674-80.
25. Nichol, J.W., et al., *Cell-laden microengineered gelatin methacrylate hydrogels.* Biomaterials, 2010. **31**(21): p. 5536-44.
26. Rivron, N.C., et al., *Tissue assembly and organization: developmental mechanisms in microfabricated tissues.* Biomaterials, 2009. **30**(28): p. 4851-8.
27. Lee, K.Y. and D.J. Mooney, *Hydrogels for Tissue Engineering.* Chemical Reviews, 2001. **101**(7): p. 1869-1880.
28. Wichterle, O. and D. LÍM, *Hydrophilic Gels for Biological Use.* Nature, 1960. **185**(4706): p. 117-118.
29. Cushing, M.C. and K.S. Anseth, *Materials science. Hydrogel cell cultures.* Science, 2007. **316**(5828): p. 1133-4.
30. Selimovic, S., et al., *Microscale Strategies for Generating Cell-Encapsulating Hydrogels.* Polymers (Basel), 2012. **4**(3): p. 1554.
31. Lima, A.C., P. Sher, and J.F. Mano, *Production methodologies of polymeric and hydrogel particles for drug delivery applications.* Expert Opin Drug Deliv, 2012. **9**(2): p. 231-48.
32. Oh, J.K., et al., *The development of microgels/nanogels for drug delivery applications.* Progress in Polymer Science, 2008. **33**(4): p. 448-477.
33. Xu, S., et al., *Generation of monodisperse particles by using microfluidics: control over size, shape, and composition.* Angew Chem Int Ed Engl, 2005. **44**(5): p. 724-8.

34. Rossow, T., P.S. Lienemann, and D.J. Mooney, *Cell Microencapsulation by Droplet Microfluidic Templating.* Macromolecular Chemistry and Physics, 2017. **218**(2): p. 1600380.
35. Chung, B.G., et al., *Microfluidic fabrication of microengineered hydrogels and their application in tissue engineering.* Lab on a Chip, 2012. **12**(1): p. 45-59.
36. Scott, E.A., et al., *Modular scaffolds assembled around living cells using poly(ethylene glycol) microspheres with macroporation via a non-cytotoxic porogen.* Acta Biomater, 2010. **6**(1): p. 29-38.
37. Wang, J., et al., *Droplet Microfluidics for the Production of Microparticles and Nanoparticles.* Micromachines, 2017. **8**(1): p. 22.
38. Teixeira, L.S., et al., *Enzyme-catalyzed crosslinkable hydrogels: emerging strategies for tissue engineering.* Biomaterials, 2012. **33**(5): p. 1281-90.
39. Henke, S., et al., *Enzymatic Crosslinking of Polymer Conjugates is Superior over Ionic or UV Crosslinking for the On-Chip Production of Cell-Laden Microgels.* Macromol Biosci, 2016. **16**(10): p. 1524-1532.
40. Roberts, J.J., et al., *A comparative study of enzyme initiators for crosslinking phenol-functionalized hydrogels for cell encapsulation.* Biomater Res, 2016. **20**: p. 30.
41. Du, Y., et al., *Sequential assembly of cell-laden hydrogel constructs to engineer vascular-like microchannels.* Biotechnol Bioeng, 2011. **108**(7): p. 1693-703.
42. McGuigan, A.P. and M.V. Sefton, *Vascularized organoid engineered by modular assembly enables blood perfusion.* Proc Natl Acad Sci U S A, 2006. **103**(31): p. 11461-6.
43. Huebsch, N., et al., *Matrix elasticity of void-forming hydrogels controls transplanted-stem-cell-mediated bone formation.* Nat Mater, 2015. **14**(12): p. 1269-77.
44. Levato, R., et al., *Biofabrication of tissue constructs by 3D bioprinting of cell-laden microcarriers.* Biofabrication, 2014. **6**(3): p. 035020.
45. Velasco, D., E. Tumarkin, and E. Kumacheva, *Microfluidic encapsulation of cells in polymer microgels.* Small, 2012. **8**(11): p. 1633-42.
46. Daley, W.P., S.B. Peters, and M. Larsen, *Extracellular matrix dynamics in development and regenerative medicine.* Journal of Cell Science, 2008. **121**(Pt 3): p. 255-64.
47. Place, E.S., N.D. Evans, and M.M. Stevens, *Complexity in biomaterials for tissue engineering.* Nat Mater, 2009. **8**(6): p. 457-70.
48. Anderson, D.G., J.A. Burdick, and R. Langer, *Materials science. Smart biomaterials.* Science, 2004. **305**(5692): p. 1923-4.
49. Mieszawska, A.J. and D.L. Kaplan, *Smart biomaterials - regulating cell behavior through signaling molecules.* Bmc Biology, 2010. **8**: p. 59.
50. Burdick, J.A. and W.L. Murphy, *Moving from static to dynamic complexity in hydrogel design.* Nature Communications, 2012. **3**: p. 1269.
51. Guvendiren, M. and J.A. Burdick, *Stiffening hydrogels to probe short- and long-term cellular responses to dynamic mechanics.* Nature Communications, 2012. **3**: p. 792.
52. Lee, T.T., et al., *Light-triggered in vivo activation of adhesive peptides regulates cell adhesion, inflammation and vascularization of biomaterials.* Nat Mater, 2015. **14**(3): p. 352-60.
53. Gandavarapu, N.R., M.A. Azagarsamy, and K.S. Anseth, *Photo-click living strategy for controlled, reversible exchange of biochemical ligands.* Advanced Materials, 2014. **26**(16): p. 2521-6.
54. Takezawa, T., Y. Mori, and K. Yoshizato, *Cell culture on a thermo-responsive polymer surface.* Biotechnology (N Y), 1990. **8**(9): p. 854-6.
55. Khetan, S. and J.A. Burdick, *Patterning network structure to spatially control cellular remodeling and stem cell fate within 3-dimensional hydrogels.* Biomaterials, 2010. **31**(32): p. 8228-34.
56. DeForest, C.A., B.D. Polizzotti, and K.S. Anseth, *Sequential click reactions for synthesizing and patterning three-dimensional cell microenvironments.* Nat Mater, 2009. **8**(8): p. 659-64.
57. Seidlits, S.K., C.E. Schmidt, and J.B. Shear, *High-Resolution Patterning of Hydrogels in Three Dimensions using Direct-Write Photofabrication for Cell Guidance.* Advanced Functional Materials, 2009. **19**(22): p. 3543-3551.
58. Shih, H. and C.-C. Lin, *Tuning stiffness of cell-laden hydrogel via host–guest interactions.* J. Mater. Chem. B, 2016. **4**(29): p. 4969-4974.
59. Collins, D.J., et al., *The Poisson distribution and beyond: methods for microfluidic droplet production and single cell encapsulation.* Lab on a Chip, 2015. **15**(17): p. 3439-59.
60. Kemna, E.W., et al., *High-yield cell ordering and deterministic cell-in-droplet encapsulation using Dean flow in a curved microchannel.* Lab on a Chip, 2012. **12**(16): p. 2881-7.

61. Volpatti, L.R. and A.K. Yetisen, *Commercialization of microfluidic devices.* Trends Biotechnol, 2014. **32**(7): p. 347-50.
62. Mashaghi, S., et al., *Droplet microfluidics: A tool for biology, chemistry and nanotechnology.* TrAC Trends in Analytical Chemistry, 2016. **82**: p. 118-125.
63. Duncombe, T.A., A.M. Tentori, and A.E. Herr, *Microfluidics: reframing biological enquiry.* Nat Rev Mol Cell Biol, 2015. **16**(9): p. 554-67.
64. Utada, A.S., et al., *Dripping to jetting transitions in coflowing liquid streams.* Phys Rev Lett, 2007. **99**(9): p. 094502.
65. Yan, Z., I.C. Clark, and A.R. Abate, *Rapid Encapsulation of Cell and Polymer Solutions with Bubble-Triggered Droplet Generation.* Macromolecular Chemistry and Physics, 2017. **218**(2): p. 1600297.
66. Nunes, J.K., et al., *Dripping and jetting in microfluidic multiphase flows applied to particle and fiber synthesis.* J Phys D Appl Phys, 2013. **46**(11).
67. Rayleigh, L., *On the Capillary Phenomena of Jets.* Proceedings of the Royal Society of London, 1879. **29**(196-199): p. 71-97.
68. Plateau, J., *Statique expérimentale et théorique des liquides soumis aux seules forces moléculaires*. 1873.
69. Abate, A.R. and D.A. Weitz, *Air-bubble-triggered drop formation in microfluidics.* Lab on a Chip, 2011. **11**(10): p. 1713-6.
70. Kohlheyer, D., et al., *Bubble-free operation of a microfluidic free-flow electrophoresis chip with integrated Pt electrodes.* Anal Chem, 2008. **80**(11): p. 4111-8.
71. Christopher, G.F. and S.L. Anna, *Microfluidic methods for generating continuous droplet streams.* J Phys D Appl Phys, 2007. **40**(19): p. R319.
72. Onoe, H., et al., *Metre-long cell-laden microfibres exhibit tissue morphologies and functions.* Nat Mater, 2013. **12**(6): p. 584-90.
73. Dendukuri, D. and P.S. Doyle, *The Synthesis and Assembly of Polymeric Microparticles Using Microfluidics.* Advanced Materials, 2009. **21**(41): p. 4071-4086.
74. Femmer, T., et al., *High-Throughput Generation of Emulsions and Microgels in Parallelized Microfluidic Drop-Makers Prepared by Rapid Prototyping.* Acs Applied Materials & Interfaces, 2015. **7**(23): p. 12635-12638.
75. Tumarkin, E., et al., *High-throughput combinatorial cell co-culture using microfluidics.* Integrative Biology, 2011. **3**(6): p. 653-662.
76. Yobas, L., et al., *High-performance flow-focusing geometry for spontaneous generation of monodispersed droplets.* Lab on a Chip, 2006. **6**(8): p. 1073-1079.
77. Liu, K., et al., *Shape-controlled production of biodegradable calcium alginate gel microparticles using a novel microfluidic device.* Langmuir, 2006. **22**(22): p. 9453-9457.
78. Zhang, H., et al., *Microfluidic production of biopolymer microcapsules with controlled morphology.* Journal of the American Chemical Society, 2006. **128**(37): p. 12205-12210.
79. Lin, Y.S., et al., *Microfluidic synthesis of tail-shaped alginate microparticles using slow sedimentation.* Electrophoresis, 2013. **34**(3): p. 425-431.
80. Utech, S., et al., *Microfluidic Generation of Monodisperse, Structurally Homogeneous Alginate Microgels for Cell Encapsulation and 3D Cell Culture.* Advanced Healthcare Materials, 2015. **4**(11): p. 1628-1633.
81. Mao, A.S., et al., *Deterministic encapsulation of single cells in thin tunable microgels for niche modelling and therapeutic delivery.* Nat Mater, 2017. **16**(2): p. 236-243.
82. Allazetta, S., et al., *Cell-Instructive Microgels with Tailor-Made Physicochemical Properties.* Small, 2015. **11**(42): p. 5647-56.
83. Ma, S., et al., *Monodisperse collagen–gelatin beads as potential platforms for 3D cell culturing.* Journal of Materials Chemistry B, 2013. **1**(38): p. 5128.

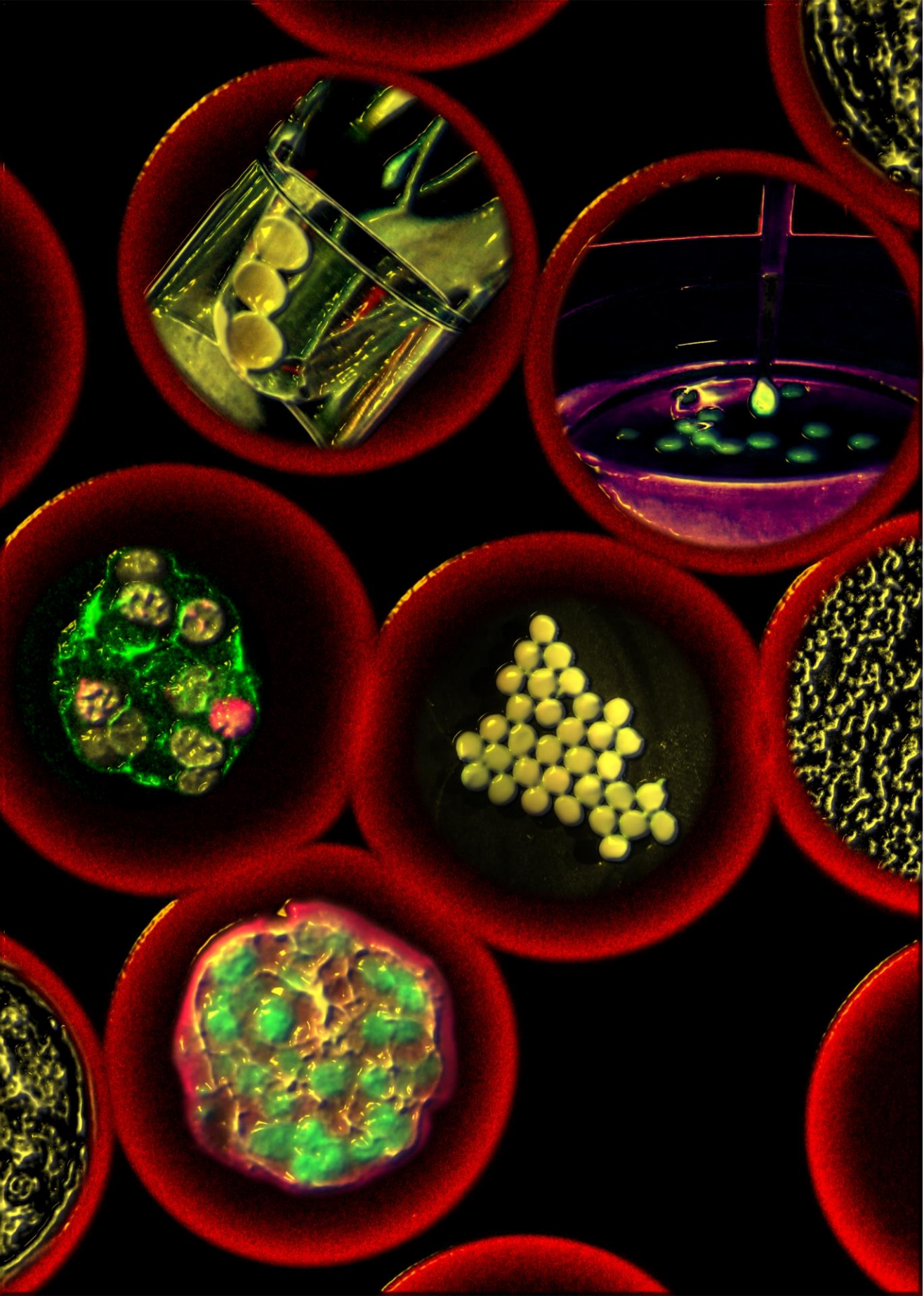

2

Nanoemulsion-induced Enzymatic Crosslinking of Tyramine-functionalized Polymer Droplets

In situ gelation of water-in-oil polymer emulsions is a key method to produce hydrogel particles. Although this approach is in principle ideal for encapsulating bioactive components such as cells, the oil phase can interfere with straightforward presentation of crosslinker molecules. Several approaches have been developed to induce in-emulsion gelation by exploiting the triggered generation or release of crosslinker molecules. However, these methods typically rely on photo- or acid-based reactions that are detrimental to cell survival and functioning. In this work, we demonstrate the diffusion-based supplementation of small molecules for the in-emulsion gelation of multiple tyramine-functionalized polymers via enzymatic crosslinking using a H_2O_2/oil nanoemulsion. This strategy is compatible with various emulsification techniques, thereby readily supporting the formation of monodisperse hydrogel particles spanning multiple length scales ranging from the nano- to the millimeter. As proof of principle, we leveraged droplet microfluidics in combination with the cytocompatible nature of enzymatic crosslinking to engineer hollow cell-laden hydrogel microcapsules that support the formation of viable and functional 3D microtissues. The straightforward, universal, and cytocompatible nature of nanoemulsion-induced enzymatic crosslinking facilitates its rapid and widespread use in numerous food, pharma, and life science applications.

Tom Kamperman†, Sieger Henke†, Bram Zoetebier, Niels Ruiterkamp, Rong Wang, Behdad Pouran, Harrie Weinans, Marcel Karperien, and Jeroen Leijten**

*† authors contributed equally to this work; * shared senior authorship.*

Contribution TK: conception, experimental design, experimental performance, and manuscript writing.

Published in J. Mater. Chem. B, 2017, DOI: 10.1039/C7TB00686A.

2.1 Introduction

Hydrogels are key to many applications in food, pharmacy, cosmetics, and tissue engineering.[1-5] These structurally stable water-swollen polymer networks have been proven ideally suited for the nano- and microencapsulation of bioactive components including cells and drugs.[6, 7] The encapsulating particles are typically produced via molding, atomization, or emulsification of the hydrogel precursor solution followed by an *in situ* gelation strategy.[8-10] In particular, emulsions can be continuously produced at high rates while stabilizing surfactants make them compatible with relatively slow (seconds to minutes) gelation mechanisms such as Michael-type addition,[11] temperature-dependent gelation,[12] and enzyme-based crosslinking approaches.[13] The majority of polymer gelation strategies however requires the presence of crosslinker molecules such as ions and radicals,[14] which is not trivial in emulsions, as these are typically multiphase immiscible systems where oil hampers the direct mixing of the hydrogel precursor and its crosslinker.

The most straightforward solution to crosslink hydrogel precursor droplets in an oil phase is by adding the crosslinker immediately before emulsification.[11, 15, 16] However, this strategy reduces the control over the emulsification process due to increasing liquid viscosity and may result in inhomogeneous polymeric networks because the crosslinking is induced before the hydrogel precursor and its crosslinker are homogeneously mixed.[13] Furthermore, coupling gelation and emulsification frequently causes device clogging and off-center cell encapsulation, which hampers the long-term applications of cell-laden hydrogel particles.[17] Consequently, it is often desirable to sequentially perform the emulsification and gelation processes, which requires the in-emulsion generation or release of crosslinker molecules. A number of advanced strategies has been developed to enable the *in situ* presentation of a crosslinker upon a chemical or physical trigger, such as changing pH, irradiation, and temperature.[6, 18-21] However, the commonly used acid-, photo-, and heat-triggered crosslinking strategies are detrimental to cell survival and function, or are technically challenging as they require the formation of labile crosslinker-laden complexes.[13, 22, 23] Alternatively, gelation of emulsified hydrogel precursor droplets can be induced via the diffusion-based supplementation of crosslinker molecules, which does not depend on technically challenging or cytotoxic triggers. For example, alginate microspheres have been formed by supplementing the oil phase with crosslinker nanoparticles[24, 25] and nanodroplets[26] that diffuse through the oil phase and induce crosslinking of the emulsified polymer droplets. Unfortunately, studies that reported on the in-emulsion crosslinking through diffusion of crosslinker molecules have remained limited and nearly exclusively focused on the production of alginate microparticles. Expanding the portfolio of in-emulsion diffusion-based crosslinkable materials would facilitate numerous hydrogel-based applications.

In this work, we demonstrated the in-emulsion enzymatic crosslinking of three distinct tyramine-functionalized polymers using horseradish peroxidase (HRP) and H_2O_2 that was supplemented by diffusion from a H_2O_2/oil nanoemulsion. The crosslinker

nanoemulsion was combined with various emulsification techniques to produce homogeneously crosslinked monodisperse nano-, micro-, and millimeter-sized hydrogel particles. Combining the crosslinker nanoemulsion with droplet microfluidics readily enabled the production of hollow dextran-based microcapsules that supported functional 3D microtissue formation. This confirmed the cytocompatible nature of the nanoemulsion-induced enzymatic crosslinking strategy and proved its value for 3D cell culture applications.

2.2 Materials and Methods

2.2.1 Materials

Dex-TA, HA-TA, and PEG-TA were synthesized as previously described.[27-29] The resulting Dex-TA and HA-TA contained 15 and 3 tyramine moieties per 100 repetitive units, respectively. PEG-TA contained 5 tyramine moieties per 8-armed PEG molecule. Horseradish peroxidase (HRP, type VI), H_2O_2 (with inhibitor), hexadecane, Span 80, peroxide color indicator strips (Quantofix), fetal bovine serum (FBS), iodixanol (OptiPrep), Calcein-AM, ethidium homodimer-1 (EthD-1), buffered formalin, Triton X-100, Tween 20, and bovine serum albumin (BSA) were purchased from Sigma-Aldrich. Catalase (from bovine liver) was purchased from Wako. Phosphate-buffered saline (PBS) was purchased from Lonza. Dulbecco's Modified Eagle's Medium (DMEM), Minimal Essential Medium α with nucleosides (αMEM), Penicillin and Streptomycin, GlutaMAX, 2-mercaptoethanol, HEPES, and trypsin-EDTA were purchased from Gibco. Basic fibroblast growth factor (ISOKine bFGF) was purchased from Neuromics. Anti-KI67-FITC (556026) was purchased from BD Biosciences. Anti-insulin (AB7842) was purchased from Abcam. Fluorescently labeled phalloidin and secondary antibodies were purchased from purchased from Molecular Probes. DAPI was purchased from Invitrogen. Polydimethylsiloxane (PDMS, Sylgard 184) was purchased from Dow Corning. Aquapel was purchased from Vulcavite.

2.2.2 Preparation and Characterization of Crosslinker Nanoemulsion

Crosslinker emulsion was prepared by mixing 30% (w/v) H_2O_2 and 1% (v/v) Span 80 containing hexadecane in a 1:5 volume ratio using a p1000 micropipette, and subsequent sonication for 5 minutes (Engisonic 200, 30 W, 47 kHz), mixing by shaking, and again 5 minutes sonication. To obtain a pure nanoemulsion, microdroplets were removed by 5 minutes centrifugation at 2000g. The size distribution of the obtained nanoemulsion was analyzed by measuring a 100 times diluted sample using dynamic light scattering (Zetasizer Nano ZS, Malvern). As a blank control, we measured surfactant containing hexadecane that was not emulsified with H_2O_2. The H_2O_2 concentration of the nanoemulsion was quantified using a color indicator strip that was pre-wetted with demineralized water.

2.2.3 Preparation and Characterization of Solid Hydrogel Particles

Millimeter-sized particles were produced by dripping 10 µl hydrogel precursor polymer droplets that consisted of 10% (w/v) tyramine-functionalized polymer and 11 U/ml HRP in PBS into H_2O_2/oil nanoemulsion. Alternatively, millimeter-sized particles were produced by putting 10 µl hydrogel precursor droplets that contained premixed 10% (w/v) Dex-TA and 11 U/ml HRP on a polystyrene substrate and subsequently covering them with 1 g/l H_2O_2 nanoemulsion. Millimeter-sized particles were also produced by mixing 10% (w/v) Dex-TA, 11 U/ml HRP, and 0.06% (w/v) H_2O_2 in 10 µl droplets using at least 10 times vigorous pipetting on a polystyrene substrate on ice, followed by a post-cure with 0.06% (w/v) H_2O_2 in PBS. Nanoparticles were produced by mixing H_2O_2/oil nanoemulsion with hydrogel precursor nanoemulsion that were prepared using the same sonication and centrifugation protocol. Microparticles were produced using a microfluidic droplet generator, where hydrogel precursor solution and H_2O_2/oil nanoemulsion were used as the dispersed and continuous phase at a 1:8 flow ratio, respectively. Alternatively, the continuous phase was 1% (v/v) Span 80 containing hexadecane and crosslinking was induced by introduction of H_2O_2/oil nanoemulsion using a separate inlet in the delay channel downstream of the droplet generator. Solidified hydrogel particles were separated from the oil phase by washing with surfactant-free oil in the presence of PBS. To retrieve the nanoparticles, a small amount of 2-propanol was added to the PBS. Crosslinked tyramines (i.e. dityramines) autofluoresce under ultraviolet (UV) light with excitation maximum at 315 nm and emission maximum at 405 nm.[30] To analyze the internal structure of millimeter-sized hydrogels, 10 µl hydrogel precursor droplets on flat polystyrene substrates were crosslinked and visualized using inverted phase contrast (PC) and fluorescence microscopy (EVOS FL with DAPI light cube). The relative UV intensity (i.e. intensity / average intensity) across hydrogels was measured using ImageJ. For nanoindentation, millimeter-sized hydrogels were placed on a glass stage in PBS and measured on at least four locations using a probe with a cantilever stiffness of 18.7 N/m and a diameter of 214 µm (Piuma, Optics11). Effective Young's moduli were determined by applying the Oliver-Pharr theory on the unloading part of indentation curves that were obtained using the following piezo indentation sweep settings (relative to piezo position set point at start): D[Z1] = 0 nm, t[1] = 2.0 s; D[Z2] = 15,000 nm, t[2] = 1.0 s (loading); D[Z3]= 15,000 nm, t[3] = 7.0 s (holding); D[Z4] = 0 nm, t[4] = 20.0 s (unloading); D[Z5] =0 nm, t[5] 2.0 s. To determine the variation in stiffness (coefficient of variation), matrix indentation was performed on at least 16 positions spaced 300 µm apart using the same indentation protocol and a probe with a cantilever stiffness of 24.5 N/m and a diameter of 70 µm. Size distributions of nano- and micro-, and millimeter-sized particles were determined using dynamic light scattering and phase contrast microscopy in combination with a Matlab function for circle size analysis (imfindcircles.m), respectively.

2.2.4 Preparation of Microfluidic Chips

Microfluidic chip designs were made using CAD software (Clewin, WieWeb) and chips with 100 µm high channels were manufactured from PDMS and glass using standard soft

lithography techniques. Aquapel was introduced in the chips before usage to ensure channel wall hydrophobicity. Chips were connected to gastight syringes (Hamilton) using fluorinated ethylene propylene (FEP, inner diameter 250 µm, DuPont), which were controlled by low pressure syringe pumps (neMESYS, Cetoni).

2.2.5 Preparation of (Cell-laden) Microcapsules

Hydrogel precursor solution that consisted of 5% (w/v) Dex-TA, 22 U/ml HRP, and 83,000 U/ml catalase in PBS was emulsified with 1% (v/v) containing hexadecane using a microfluidic droplet generator at a 1:6 precursor/oil flow ratio. The non-cell-laden precursor droplets were crosslinked by the influx of crosslinker nanoemulsion at a 1:8 nanoemulsion/oil flow ratio further downstream the delay channel, resulting in Dex-TA microcapsules through competitive enzymatic crosslinking. For cell-laden microcapsule production, mouse insulinoma MIN6-B1 cells were cultured in MIN6 proliferation medium, consisting of 10% (v/v) FBS, 100 U/ml Penicillin and 100 µg/ml Streptomycin, and 71 µM 2-mercaptoethanol (added fresh) in DMEM. Cells were cultured under 5% CO_2 at 37 °C and medium was replaced 3 times per week. When cell culture reached near confluence, the cells were detached using 0.25% (w/v) Trypsin-EDTA at 37 °C and subsequently subcultured or used for experimentation. For cell encapsulation, detached cells (passage 35) were washed with MIN6 proliferation medium, flown through a 40 µm cell strainer, and suspended in the hydrogel precursor solution (to which 8% (v/v) OptiPrep was added to obtain ρ = 1.05 g/l which reduces cell settling and aggregation) at a concentration of $7.5 \cdot 10^7$ cells/ml. The cell-laden hydrogel precursor solution was loaded into an ice-cooled gastight syringe where it was gently agitated every ten minutes using a magnetic micro stirring bar. The cell-laden precursor droplets were crosslinked by the influx of crosslinker nanoemulsion at various nanoemulsion/oil flow ratios as indicated in Figure 2.5. The resulting microcapsules were collected in MIN6 proliferation medium supplemented with 0.02 M HEPES or in surfactant containing hexadecane. To break the emulsion and retrieve the microcapsules from the oil phase, microcapsules were washed with surfactant-free oil in the presence of PBS or MIN6 proliferation medium. Retrieved cell-laden microcapsules were cultured in MIN6 proliferation medium which was refreshed three times per week.

2.2.6 Staining and Visualization

Millimeter-sized particles were imaged using a standard digital photo camera. On-chip droplets and microgels were visualized using a stereomicroscope set-up (Nikon SMZ800 equipped with Leica DFC300 FX camera). Nanoparticles were washed with water, air-dried and subsequently imaged using scanning electron microscopy (Zeiss Merlin HR-SEM) at 0.65 kV. Collected microemulsions and -particles were imaged using phase contrast microscopy. Microcapsules were analyzed by selectively labeling crosslinked Dex-TA with EthD-1 and visualization using confocal microscopy (Nikon A1+). Optical cross sections were analyzed using ImageJ. Viability of encapsulated cells was analyzed by staining with 2 µM calcein-AM and 4 µM EthD-1 in PBS, visualization using fluorescence microscopy (EVOS FL), and artisan counting of > 300 cells per condition.

For additional analyses, cell-laden microgels were first washed with PBS and fixated using 10% buffered formalin. For immunohistochemistry, samples were permeabilized with 0.1% Triton X-100, blocked with 5% (w/v) bovine serum albumin and 0.05% (v/v) Tween 20, and stained with 1:100 anti-KI67-FITC (556026, BD Biosciences), 1:100 anti-insulin (AB7842, Abcam), in combination with 1:400 AF647-labeled secondary antibodies, and 2.5 U/ml phalloidin-AF488 and DAPI to counterstain F-actin, and nuclei, respectively. MIN6 aggregate size distributions were determined by measuring the surface area of >50 aggregates per condition using ImageJ, represented as box plots, and analyzed for statistical significance using one-way ANOVA.

2.3 Results and Discussion

2.3.1 Preparation and Characterization of Crosslinker Nanoemulsion

Tyramine-functionalized polymers can be crosslinked *in situ* via the formation of tyramine-tyramine bonds using horseradish peroxidase (HRP) as catalyst and low levels of H_2O_2 as oxidizer (**Figure 2.1a**). However, this conventionally requires the mixing of these reactive components prior to emulsification, which significantly reduces the control over the emulsification process and typically results in deformed particles or bulk gel formation that causes device clogging (**Figure S2.1**). We therefore set out to develop a facile strategy to achieve in-emulsion crosslinking of tyramine-functionalized polymers. However, this is not trivial as the oil phase prevents the direct mixing of tyramine-functionalized polymer, HRP, and H_2O_2. We hypothesized, that in-emulsion crosslinking could be achieved by combining pre-emulsified enzyme containing precursor droplets with a H_2O_2 containing oil. In concept, enzymatic crosslinking of water-in-oil precursor droplets would be induced by the diffusion-based supplementation of H_2O_2 into the enzyme containing precursor droplet, while the surfactant containing oil would prevent precursor droplet merging and ensure spherically shaped particles (**Figure 2.1b**). To realize this, we emulsified H_2O_2 nanodroplets in oil. Compared to microdroplets, nanodroplets are more stable and have higher surface-to-volume ratios, which ensures an adequate and constant source of H_2O_2 molecules, allowing for sustained and complete gelation of precursor droplets. We exploited sonication-based emulsification followed by centrifugation to prepare the crosslinker nanoemulsion (**Figure 2.1c**). Specifically, 30% H_2O_2 and hexadecane with 1% Span 80 surfactant were mixed and sonicated to produce an emulsion. Using a subsequent centrifugation step, we obtained a transparent nanoemulsion (i.e. supernatant) by separating out the microdroplets and non-emulsified aqueous phase (i.e. sediment). Analyzing the supernatant using dynamic light scattering revealed that the obtained nanoemulsion was composed of two droplet populations with diameters ranging from 1 to 10 nm and 100 to 1000 nm (**Figure 2.1d**). The 1 to 10 nm population, which has also been reported by others,[31] was also present in non-emulsified surfactant containing oil and likely caused by micellar formation of Span 80 surfactant. We consequently deduced that the 100 to 1000 µm fraction consisted of H_2O_2 nanodroplets or -micelles. As shown in **Figure 2.1e**, the presence of H_2O_2 in the nanoemulsion was

confirmed using a quantitative colorimetric peroxide assay, which revealed a H_2O_2 concentration of ~1 g/l (**Figure S2.2**).

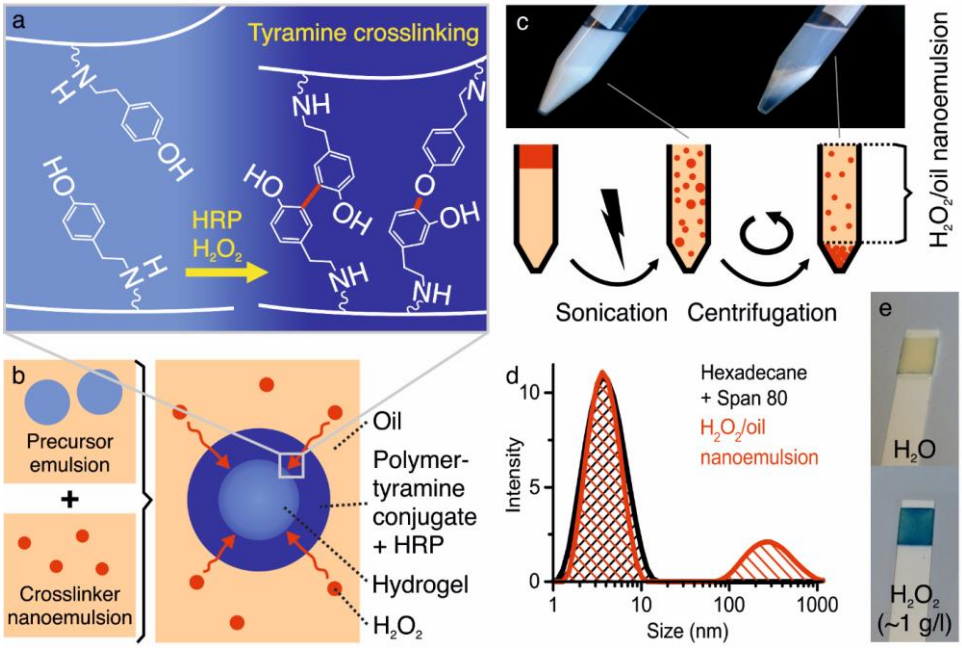

Figure 2.1. Preparation and characterization of crosslinker nanoemulsion. (a) Tyramine moieties are crosslinked by the enzyme HRP in the presence of H_2O_2. **(b)** Concept of in-emulsion crosslinking HRP containing hydrogel precursor droplets using a H_2O_2/oil nanoemulsion. **(c)** The nanoemulsion is prepared and purified by sonication-mediated emulsification of H_2O_2 in oil and subsequent centrifugation. **(d, e)** The presence of 1 g/l H_2O_2 containing nanoemulsion was confirmed using dynamic light scattering and a quantitative colorimetric peroxide assay.

2.3.2 Crosslinker Nanoemulsion for Homogeneous Enzymatic Crosslinking of Spherical Nano-, Micro-, and Millimeter Particles Made from Various Tyramine-functionalized Polymers

Leveraging the H_2O_2/oil nanoemulsion, we set out to demonstrate in-emulsion crosslinking of various tyramine-functionalized materials droplets for the production of monodisperse spherical particles. To extend the material compatibility of our nanoemulsion-induced crosslinking strategy, we conjugated the enzymatically crosslinkable moiety tyramine to dextran (Dex-TA), hyaluronic acid (HA-TA), and polyethylene glycol (PEG-TA), which are three distinct polymers that have been proven successful in various biomedical applications.[32-35] A facile production method based on dripping HRP containing hydrogel precursor droplets from a micropipette into a crosslinker bath was used to assess in-emulsion crosslinking of these polymer conjugates (**Figure 2.2a**). Dripping the polymer solutions in the H_2O_2/oil nanoemulsion resulted in the formation of shape stable spheres for all tested biomaterials (**Figure 2.2b-d**). Conversely, dripping in an aqueous bath (i.e. water) that had similar H_2O_2 concentration

(i.e. ~ 1 g/l) resulted in amorphously shaped gel particles, confirming the important shape stabilizing role of the immiscible oil phase during crosslinking (**Figure 2.2e**). The structural and mechanical properties of in-emulsion crosslinked (i.e. by H_2O_2 diffusion) Dex-TA hydrogels were then compared to Dex-TA hydrogels that had been prepared using the conventional crosslinking approach (i.e. by H_2O_2 mixing) (**Figure 2.2f**). To evaluate the internal hydrogel structure, gel precursor droplets were cured on flat substrates and visualized using inverted phase contrast (PC) and ultraviolet (UV) fluorescence microscopy. Analyzing the relative UV intensity across the hydrogels, as a measure for dityramine (i.e. crosslinked tyramine) distribution,[30] revealed that diffusion-based crosslinking resulted a more homogeneously crosslinked hydrogel interior as compared to samples that were prepared by mixing. Moreover, nanoindentation measurements demonstrated that diffusion-based crosslinking resulted in a significantly stiffer hydrogel surface (i.e. E-modulus) as compared to the mixing strategy (**Figure 2.2g**). This observation was corroborated by matrix scanning indentation of the hydrogel surface, which revealed that in-emulsion crosslinking Dex-TA resulted in ~3-fold less variation in stiffness (**Figure 2.2h**). These observations are likely to be explained by the fact that H_2O_2 induces relatively rapid gelation that prevents thorough mixing of all reactive components, thereby resulting in an inhomogeneous polymer network when applying the conventional mixing approach, whereas nanoemulsion-based crosslinking relies on the diffusion-based gelation of a premixed gel precursor solution.

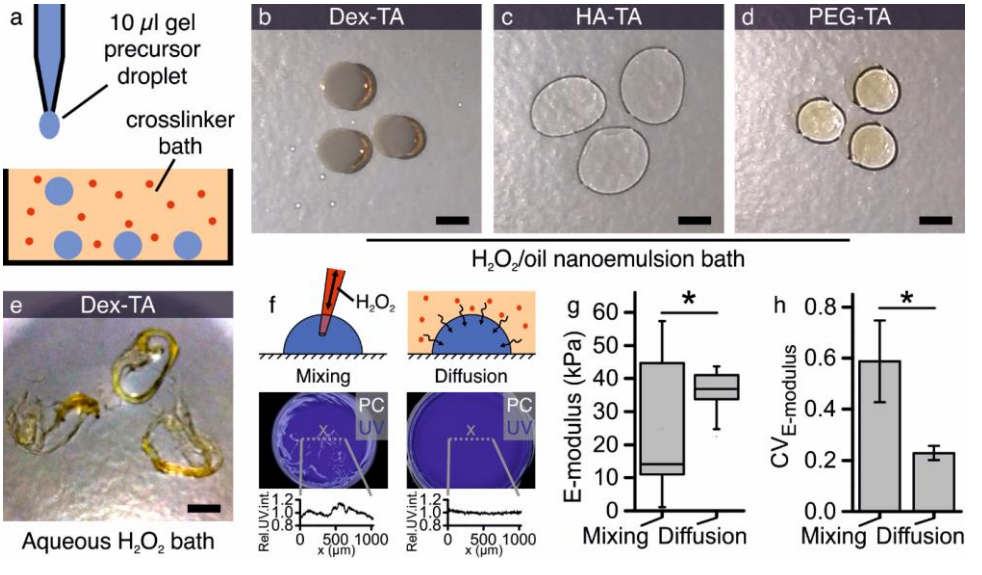

Figure 2.2. Spherical and homogeneous particle production using nanoemulsion-induced enzymatic crosslinking. (**a**) Dripping HRP containing tyramine-functionalized hydrogel precursor solutions from a micropipette into a H_2O_2/oil nanoemulsion bath resulted in spherical (**b**) Dex-TA, (**c**) HA-TA, and (**d**) PEG-TA particles, (**e**) which was in sharp contrast to the amorphously shaped particles that formed upon dripping the same Dex-TA precursor solution into an aqueous bath with similar H_2O_2 concentration as the H_2O_2/oil nanoemulsion bath. (**f**) The conventional hydrogel preparation method

(i.e. mixing) was compared to diffusion-based crosslinking. To study the intrinsic hydrogel crosslinking (i.e. dityramine) distribution, hydrogels were prepared on top of flat substrates and analyzed in a cross-sectional manner sectional using inverted phase contrast (PC) and ultraviolet (UV) fluorescence microscopy. Nanoemulsion-induced crosslinking resulted in a more homogeneously crosslinked hydrogel interior as compared to mixing. Furthermore, (**g**) hydrogels prepared using diffusion-based crosslinking were significantly stiffer and (**h**) characterized by a significantly less heterogeneous network (coefficient of variation; CV) than hydrogels prepared by directly mixing the gel precursor with a non-emulsified H_2O_2 solution. * indicates significance between populations with $p<0.05$. Scale bars indicate 2 mm.

As the precursor droplets and crosslinker nanoemulsion are produced separately, the nanoemulsion-induced crosslinking is readily compatible with a wide variety of emulsion-based droplet production technologies. Indeed, spherical particles ranging from the nano- to the millimeter scale could be produced by combining various existing emulsion-based droplet production technologies using a chemically identical crosslinker nanoemulsion. In particular, we used sonication (**Figure 2.3a, b**), droplet microfluidics (**Figure 2.3c-e**), and dripping (**Figure 2.3f, g**) in combination with nanoemulsion based enzymatic crosslinking to demonstrate the production of monodisperse spherical Dex-TA particles with diameters spanning at least four orders of magnitude (**Figure 2.3h**). The generic nature of this crosslinking strategy facilitates its application in various fields that rely on the use of emulsion-based particle production including pharma, tissue engineering, and food technology.[36-40]

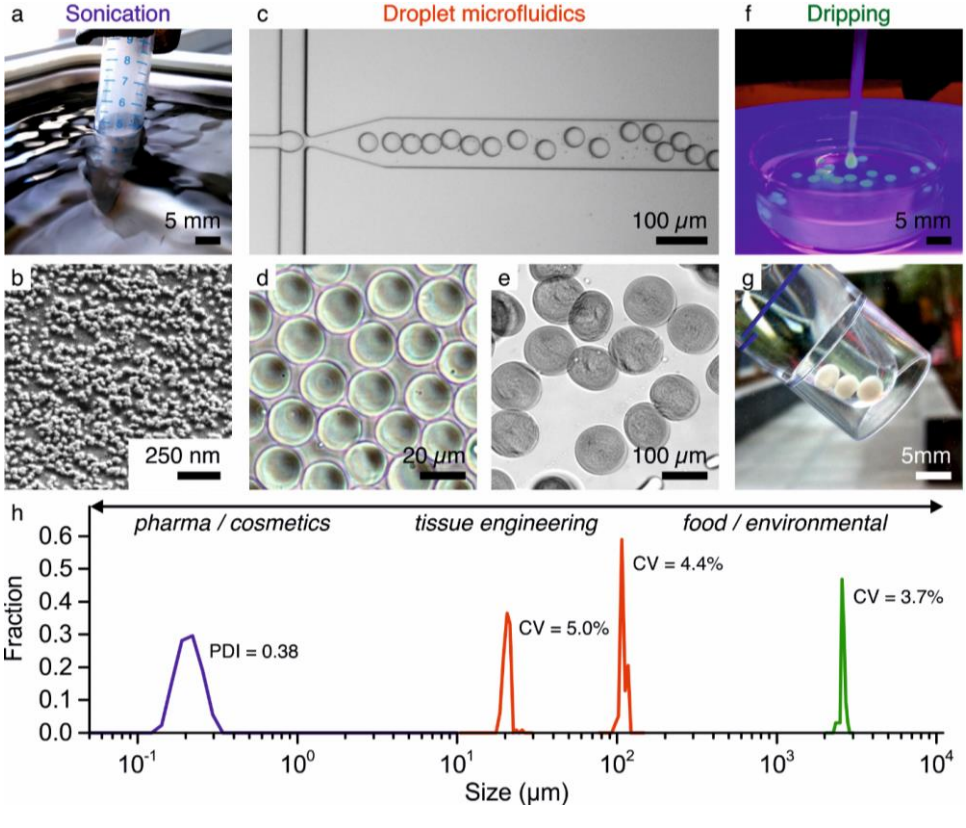

Figure 2.3. Monodisperse nano-, micro-, and millimeter particle production using nanoemulsion-induced enzymatic crosslinking. (**a**) Mixing HRP and Dex-TA containing nanoemulsion prepared using sonication resulted in (**b**) Dex-TA nanoparticles when mixed with H_2O_2/oil nanoemulsion, as confirmed with scanning electron microscopy. (**c**) Droplet microfluidics was used to generate (**d**) 20 μm and (**e**) 100 μm Dex-TA microparticles using H_2O_2/oil nanoemulsion as the continuous phase. (**f**) Dripping hydrogel precursor solution into a H_2O_2/oil nanoemulsion bath resulted in (**g**) spherical millimeter-sized particles. (**h**) Size distributions of Dex-TA particles produced with various emulsification-based technologies in combination with in-emulsion enzymatic crosslinking using crosslinker nanoemulsion. PDI indicates polydispersity index. CV indicates coefficient of variation.

2.3.3 Producing Hollow Hydrogel Microcapsules using Nanoemulsion-induced Enzymatic Crosslinking

Nanoemulsion-induced enzymatic crosslinking is intrinsically an outside-in process; H_2O_2 diffuses from the oil phase into the gel precursor droplet where it drives the HRP-mediated crosslinking of tyramines (**Figure 2.4a**). Inhibiting this crosslinking mechanism from the inside (i.e. the aqueous phase) using the H_2O_2 neutralizing enzyme catalase is a proven strategy to form hollow particles or capsules (**Figure 2.4b**).[41, 42] We set out to exploit this approach in combination with droplet microfluidics to realize the production of hollow Dex-TA microcapsules. To this end, we designed and manufactured a dedicated microfluidic chip from polydimethylsiloxane (PDMS) and glass (**Figure 2.4c**). The microfluidics chip contained several filters to prevent any particles larger than ~50 μm in the oil phase (e.g. remaining PDMS particles from inlet punching) from interfering with the droplet generation or crosslinking processes (**Figure 2.4d**). Furthermore, the aqueous phase inlet contained a previously reported pillar structure [13] that ensured particle homogenization to aid evenly distributed encapsulation of particles (e.g. cells) (**Figure 2.4e**). The flow focusing droplet generator (**Figure 2.4f**) was positioned a few millimeters upstream of the crosslinker nanoemulsion inlet (**Figure 2.4g**). This separation between droplet production and crosslinking initiation effectively prevented flow instabilities and clogging by preventing polymer gelation at the nozzle. First, we assessed the production of non-laden (i.e. without cells) hydrogel microcapsules. After Dex-TA, HRP, and catalase containing gel precursor droplets were stabilized, on-chip enzymatic crosslinking was induced by introducing H_2O_2/oil nanoemulsion (~1 g/l) in the serpentine-shaped delay channel with an nanoemulsion/oil flow ratio of 1:8 (**Figure 2.4h**). The nanoemulsion's slightly diffuse appearance was no longer observed after four channel turns (i.e. 20 mm), which indicated its homogenous distribution across the microfluidic delay channel. The resulting 75±1 μm spherical particles were retrieved by washing the collected emulsion with surfactant-free oil and breaking it in the presence of phosphate-buffered saline (PBS) (**Figure 2.4i**). Analyzing these particles using confocal microscopy revealed the presence of homogeneously crosslinked shells of even thickness (8±1 μm) surrounding a non-crosslinked core, confirming the controlled production of hollow Dex-TA microcapsules (**Figure 2.4j**).

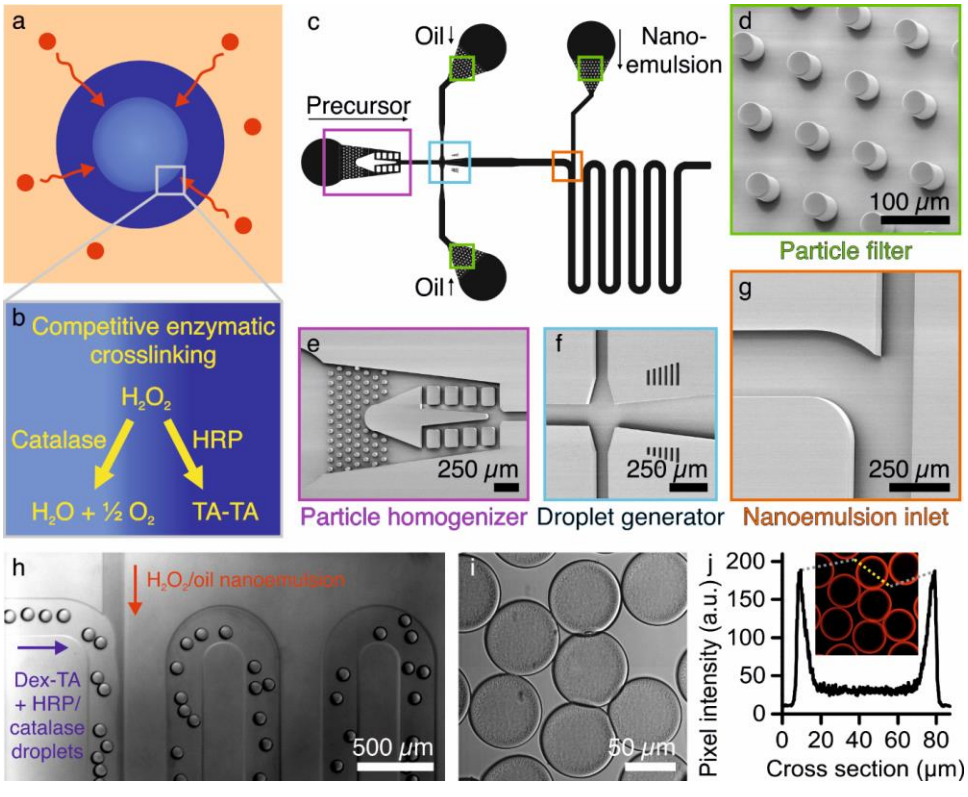

Figure 2.4. Hollow microcapsules production using nanoemulsion-induced enzymatic crosslinking. (**a**) Nanoemulsion-induced crosslinking is an outside-in process where small H_2O_2 molecules diffuse from the nanoemulsion through the oil phase into the gel precursor droplet to induce enzymatic crosslinking. (**b**) The enzyme catalase consumes H_2O_2 and can be incorporated in the gel precursor to achieve competitive enzymatic crosslinking that results in hollow hydrogel capsule formation. (**c**) The microfluidic microcapsule production chip containing (**d**) oil inlets with particle filters, (**e**) a gel precursor inlet with particle homogenizer, (**f**) a flow focusing droplet generator, and (**g**) an inlet for the crosslinker nanoemulsion, as shown by a schematic depiction and scanning electron microscopy images, respectively. (**h**) Microphotograph of the microfluidic chip in action, where Dex-TA, HRP, and catalase containing precursor droplets in oil (blue arrow) are solidified after the influx of H_2O_2/oil nanoemulsion (red arrow) into (**i**) robust microcapsules with (**j**) non-crosslinked centers, as confirmed by confocal imaging of the retrieved hydrogels.

2.3.4 Engineering Functional 3D Microtissues in Hollow Hydrogel Microcapsules via Nanoemulsion-induced Crosslinking

Hollow microcapsules are ideally suited for the controlled formation of 3D microtissues,[25, 26, 43] which serve multiple purposes in fundamental biological, pharmacological, and tissue engineering applications.[44-46] For example, controlled aggregation of cells is key to bottom-up engineering of islets of Langerhans for the treatment of diabetes.[47, 48] To investigate the potential of nanoemulsion-induced enzymatic crosslinking for 3D cell cultures, we set out to encapsulate the pancreatic beta cell line MIN6 to form insulin producing microtissues. First, we aimed to identify the

smallest amount of H_2O_2 containing nanoemulsion that still resulted in robust cell encapsulating microcapsules, as even a small excess of H_2O_2 (order 1 to 10 mg/l) has been proven detrimental to cell functioning.[49] The separated configuration of droplet generator and nanoemulsion inlet enabled straightforward screening of increasing amounts of crosslinker without affecting droplet size. Specifically, cell-laden gel precursor droplets were produced using a constant water/oil ratio of 1:8, while the nanoemulsion/oil ratio was stepwise increased from 1:16 to 1:2 (**Figure 2.5a**). Collecting the on-chip formed samples in an off-chip aqueous bath (i.e. cell culture medium) resulted in <25% encapsulated cells in all tested nanoemulsion/oil ratios (**Figure 2.5b**). This poor cell encapsulation was most likely the result of incomplete on-chip crosslinking and immediate demulsification upon collection in the serum-containing aqueous bath. However, by collecting the emulsion in an oil bath, immediate demulsification could be prevented. This approach effectively increased the enzymatic crosslinking time of cell-laden droplets from seconds (on-chip) to minutes (in-suspension) resulting in robust Dex-TA microcapsules that encapsulated ~90% of the cells while using minimal amounts of H_2O_2. Using this optimized encapsulation strategy, we compared viability rates of encapsulated to non-encapsulated (i.e. syringe control) cells using a live/dead assay (**Figure 2.5c**). This revealed that the encapsulation procedure had no detrimental effect on cell survival (**Figure 2.5d**). The encapsulated cells autonomously assembled into 3D microtissues within a single day (**Figure 2.5e**) and continued to proliferate during subsequent *in vitro* culture (**Figure 2.5f**), which significantly increased the cell aggregates' size (**Figure 2.5g**). KI67 staining revealed that MIN6 cells intensively proliferated as early as day 1 post encapsulation, which underlined the cytocompatible nature of the nanoemulsion-induced enzymatic crosslinking strategy (**Figure 2.5h**). Importantly, encapsulated and aggregated MIN6 cells remained positive for insulin staining throughout the culture period, indicating that the MIN6 cells remained functional during encapsulation and subsequent culture, further confirming the mild and cytocompatible nature of the procedure (**Figure 2.5i**).

2.4 Conclusion

In conclusion, we demonstrated the successful preparation and application of nanoemulsified H_2O_2 for the in-emulsion enzymatic crosslinking of tyramine-functionalized polymers including dextran (Dex-TA), hyaluronic acid (HA-TA), and polyethylene glycol (PEG-TA). In-emulsion enzymatic crosslinking readily enabled monodisperse spherical particle formation over a size range spanning at least 4 orders (nm to mm). Furthermore, diffusion-based crosslinking resulted in more homogenously crosslinked Dex-TA hydrogels that yielded higher and more consistent Young's moduli as compared to the conventional hydrogel preparation method. Lastly, we introduced the crosslinker nanoemulsion in a microfluidic chip and leveraged its cytocompatible nature to produce cell-laden hollow microcapsules that facilitated the controlled formation of viable and functional 3D microtissues. In short, we demonstrated that a H_2O_2/oil nanoemulsion enabled facile, homogeneous, and cytocompatible in-emulsion

enzymatic crosslinking of multiple distinct hydrogel precursor polymer droplets to form solid and hollow spherical particles with diameters ranging from the nano- to the millimeter scale.

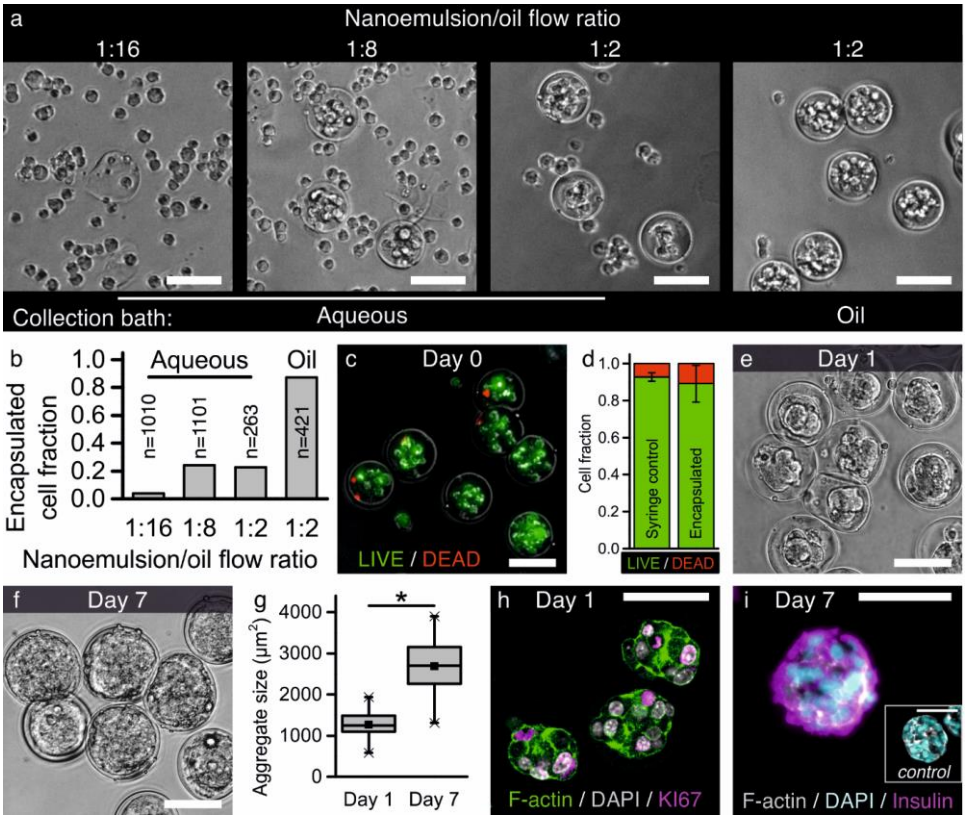

Figure 2.5. Functional 3D microtissue formation in hollow microcapsules. (**a**) Hollow microcapsule formation was optimized by tuning the nanoemulsion/oil flow ratio and changing the off-chip collection bath from aqueous culture medium to surfactant containing oil, (**b**) while quantifying the fraction of encapsulated cells in collected samples. (**c**) The viability of microencapsulated MIN6 cells was (**c**) visualized and (**d**) quantified using live/dead staining and compared to non-encapsulated cells (i.e. syringe control). (**e**) Within one day, encapsulated MIN6 cells formed microaggregates that (**f, g**) significantly grew during subsequent *in vitro* culture as a result of (h) cell proliferation, which was confirmed by (**h**) KI67-positive cells in the 3D microtissues on day 1. (**i**) The MIN6 cells remained viable and functional throughout the encapsulation procedure and subsequent culture, as confirmed by insulin-positive 3D microtissues on day 7. Scale bars indicate 50 μm. * indicates significance with $p<0.001$.

2.5 Supplementary Information

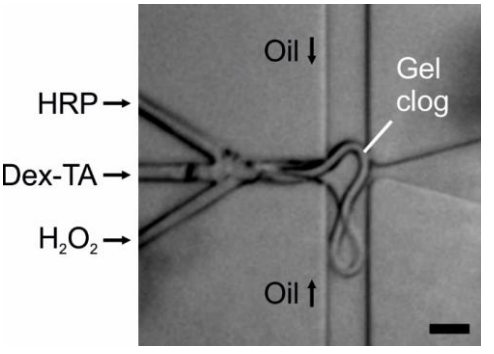

Figure S2.1. Mixing HRP, Dex-TA, and H_2O_2 typically results in clogging of the microfluidic droplet generator, thereby hampering its further use for hydrogel microparticle production.

Figure S2.2. H_2O_2/oil nanoemulsion contained ~1 g/l H_2O_2, as determined using a 100x diluted emulsion on a quantitative peroxide color indicator strip.

References

1. Hoffman, A.S., *Hydrogels for biomedical applications.* Adv Drug Deliv Rev, 2012. **64**: p. 18-23.
2. Liu, L.S., et al., *Hydrogels from Biopolymer Hybrid for Biomedical, Food, and Functional Food Applications.* Polymers, 2012. **4**(4): p. 997-1011.
3. Yu, L. and J. Ding, *Injectable hydrogels as unique biomedical materials.* Chem Soc Rev, 2008. **37**(8): p. 1473-81.
4. Peppas, N.A., et al., *Hydrogels in Biology and Medicine: From Molecular Principles to Bionanotechnology.* Advanced Materials, 2006. **18**(11): p. 1345-1360.
5. Van Tomme, S.R., G. Storm, and W.E. Hennink, *In situ gelling hydrogels for pharmaceutical and biomedical applications.* International Journal of Pharmaceutics, 2008. **355**(1-2): p. 1-18.
6. Tan, W.H. and S. Takeuchi, *Monodisperse Alginate Hydrogel Microbeads for Cell Encapsulation.* Advanced Materials, 2007. **19**(18): p. 2696-2701.
7. Hamidi, M., A. Azadi, and P. Rafiei, *Hydrogel nanoparticles in drug delivery.* Adv Drug Deliv Rev, 2008. **60**(15): p. 1638-49.
8. Selimovic, S., et al., *Microscale Strategies for Generating Cell-Encapsulating Hydrogels.* Polymers (Basel), 2012. **4**(3): p. 1554.
9. Lima, A.C., P. Sher, and J.F. Mano, *Production methodologies of polymeric and hydrogel particles for drug delivery applications.* Expert Opin Drug Deliv, 2012. **9**(2): p. 231-48.
10. Oh, J.K., et al., *The development of microgels/nanogels for drug delivery applications.* Progress in Polymer Science, 2008. **33**(4): p. 448-477.
11. Rossow, T., et al., *Controlled synthesis of cell-laden microgels by radical-free gelation in droplet microfluidics.* Journal of the American Chemical Society, 2012. **134**(10): p. 4983-9.
12. Kumachev, A., et al., *High-throughput generation of hydrogel microbeads with varying elasticity for cell encapsulation.* Biomaterials, 2011. **32**(6): p. 1477-83.
13. Henke, S., et al., *Enzymatic Crosslinking of Polymer Conjugates is Superior over Ionic or UV Crosslinking for the On-Chip Production of Cell-Laden Microgels.* Macromol Biosci, 2016. **16**(10): p. 1524-1532.
14. Hennink, W.E. and C.F. van Nostrum, *Novel crosslinking methods to design hydrogels.* Adv Drug Deliv Rev, 2012. **64**: p. 223-236.
15. Ma, Y., et al., *Artificial microniches for probing mesenchymal stem cell fate in 3D.* Biomater. Sci., 2014. **2**(11): p. 1661-1671.
16. Griffin, D.R., et al., *Accelerated wound healing by injectable microporous gel scaffolds assembled from annealed building blocks.* Nat Mater, 2015. **14**(7): p. 737-44.
17. Kamperman, T., et al., *Centering Single Cells in Microgels via Delayed Crosslinking Supports Long-Term 3D Culture by Preventing Cell Escape.* Small, 2017. **13**(22): p. 1603711-n/a.
18. Johansen, A. and J.M. Flink, *Immobilization of yeast cells by internal gelation of alginate.* Enzyme and Microbial Technology, 1986. **8**(3): p. 145-148.
19. Utech, S., et al., *Microfluidic Generation of Monodisperse, Structurally Homogeneous Alginate Microgels for Cell Encapsulation and 3D Cell Culture.* Adv Healthc Mater, 2015. **4**(11): p. 1628-33.
20. Kamperman, T., et al., *Single Cell Microgel Based Modular Bioinks for Uncoupled Cellular Micro- and Macroenvironments.* Adv Healthc Mater, 2017. **6**(3).
21. Ma, S., et al., *Monodisperse collagen–gelatin beads as potential platforms for 3D cell culturing.* Journal of Materials Chemistry B, 2013. **1**(38): p. 5128.
22. Gu, T., et al., *Droplet microfluidics with a nanoemulsion continuous phase.* Lab on a Chip, 2016. **16**(14): p. 2694-700.
23. Ren, C.D., et al., *Liposomal delivery of horseradish peroxidase for thermally triggered injectable hyaluronic acid–tyramine hydrogel scaffolds.* J. Mater. Chem. B, 2015. **3**(23): p. 4663-4670.
24. Paques, J.P., et al., *Alginate submicron beads prepared through w/o emulsification and gelation with CaCl2 nanoparticles.* Food Hydrocolloids, 2013. **31**(2): p. 428-434.
25. Agarwal, P., et al., *One-step microfluidic generation of pre-hatching embryo-like core-shell microcapsules for miniaturized 3D culture of pluripotent stem cells.* Lab on a Chip, 2013. **13**(23): p. 4525-33.
26. Sakai, S., et al., *Peroxidase-catalyzed cell encapsulation in subsieve-size capsules of alginate with phenol moieties in water-immiscible fluid dissolving H2O2.* Biomacromolecules, 2007. **8**(8): p. 2622-6.

27. Wang, R., *Macromolecular engineering of in-situ forming hydrogels*, in *Department of Developmental BioEngineering*. 2016, University of Twente: Enschede. p. 180.
28. Jin, R., et al., *Enzyme-mediated fast in situ formation of hydrogels from dextran-tyramine conjugates.* Biomaterials, 2007. **28**(18): p. 2791-800.
29. Wennink, J.W.H., et al., *Injectable Hydrogels by Enzymatic Co-Crosslinking of Dextran and Hyaluronic Acid Tyramine Conjugates.* Macromolecular Symposia, 2011. **309-310**(1): p. 213-221.
30. Sakharov, D.V., et al., *Photodynamic treatment and H2O2-induced oxidative stress result in different patterns of cellular protein oxidation.* European Journal of Biochemistry, 2003. **270**(24): p. 4859-65.
31. Solomon, B.R., M.N. Hyder, and K.K. Varanasi, *Separating oil-water nanoemulsions using flux-enhanced hierarchical membranes.* Sci Rep, 2014. **4**: p. 5504.
32. Lin, C.C. and K.S. Anseth, *PEG hydrogels for the controlled release of biomolecules in regenerative medicine.* Pharm Res, 2009. **26**(3): p. 631-43.
33. Cadee, J.A., et al., *In vivo biocompatibility of dextran-based hydrogels.* Journal of Biomedical Materials Research, 2000. **50**(3): p. 397-404.
34. Portalska, K.J., et al., *Boosting angiogenesis and functional vascularization in injectable dextran-hyaluronic acid hydrogels by endothelial-like mesenchymal stromal cells.* Tissue Eng Part A, 2014. **20**(3-4): p. 819-29.
35. Burdick, J.A. and G.D. Prestwich, *Hyaluronic acid hydrogels for biomedical applications.* Advanced Materials, 2011. **23**(12): p. H41-56.
36. Shewan, H.M. and J.R. Stokes, *Review of techniques to manufacture micro-hydrogel particles for the food industry and their applications.* Journal of Food Engineering, 2013. **119**(4): p. 781-792.
37. Joscelyne, S.M. and G. Trägårdh, *Membrane emulsification — a literature review.* Journal of Membrane Science, 2000. **169**(1): p. 107-117.
38. Freitas, S., H.P. Merkle, and B. Gander, *Microencapsulation by solvent extraction/evaporation: reviewing the state of the art of microsphere preparation process technology.* J Control Release, 2005. **102**(2): p. 313-32.
39. Teh, S.Y., et al., *Droplet microfluidics.* Lab on a Chip, 2008. **8**(2): p. 198-220.
40. Khademhosseini, A. and R. Langer, *Microengineered hydrogels for tissue engineering.* Biomaterials, 2007. **28**(34): p. 5087-92.
41. Ashida, T., S. Sakai, and M. Taya, *Competing two enzymatic reactions realizing one-step preparation of cell-enclosing duplex microcapsules.* Biotechnol Prog, 2013. **29**(6): p. 1528-34.
42. Khanmohammadi, M., et al., *Production of hyaluronic-acid-based cell-enclosing microparticles and microcapsules via enzymatic reaction using a microfluidic system.* Journal of Applied Polymer Science, 2016. **133**(16): p. n/a-n/a.
43. Sakai, S., et al., *Cell-enclosing gelatin-based microcapsule production for tissue engineering using a microfluidic flow-focusing system.* Biomicrofluidics, 2011. **5**(1): p. 13402.
44. Occhetta, P., et al., *High-Throughput Microfluidic Platform for 3D Cultures of Mesenchymal Stem Cells, Towards Engineering Developmental Processes.* Sci Rep, 2015. **5**: p. 10288.
45. Tung, Y.C., et al., *High-throughput 3D spheroid culture and drug testing using a 384 hanging drop array.* Analyst, 2011. **136**(3): p. 473-8.
46. Wolf, F., et al., *Cartilage tissue engineering using pre-aggregated human articular chondrocytes.* Eur Cell Mater, 2008. **16**: p. 92-9.
47. Toyoda, T., et al., *Cell aggregation optimizes the differentiation of human ESCs and iPSCs into pancreatic bud-like progenitor cells.* Stem Cell Res, 2015. **14**(2): p. 185-97.
48. Hilderink, J., et al., *Controlled aggregation of primary human pancreatic islet cells leads to glucose-responsive pseudoislets comparable to native islets.* J Cell Mol Med, 2015. **19**(8): p. 1836-46.
49. Duan, J., et al., *Irreversible cellular senescence induced by prolonged exposure to H2O2 involves DNA-damage-and-repair genes and telomere shortening.* Int J Biochem Cell Biol, 2005. **37**(7): p. 1407-20.

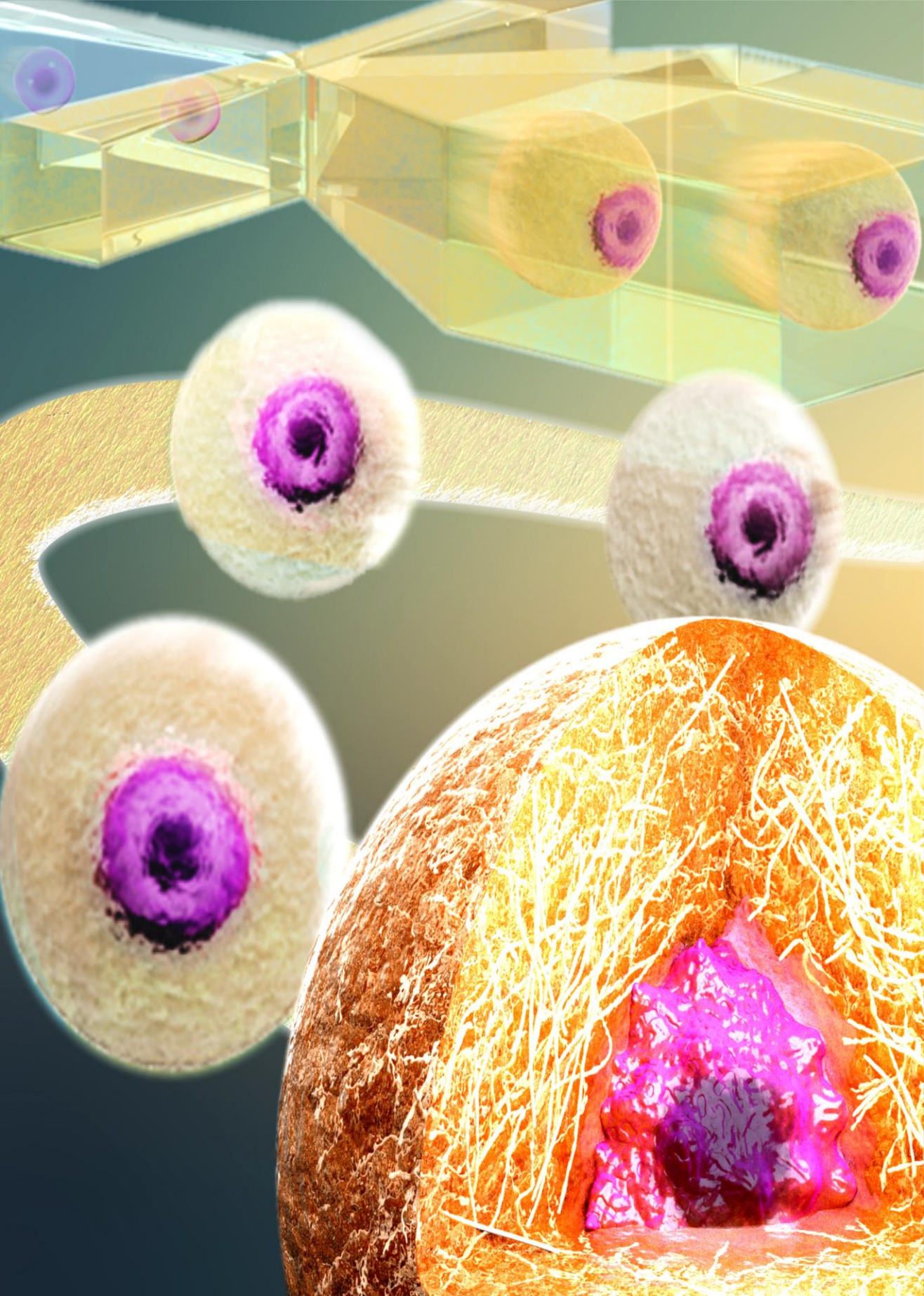

3

Centering Single Cells in Microgels via Delayed Crosslinking Supports Long-term 3D Cell Culture by Preventing Cell Escape

Single-cell-laden microgels support physiological 3D culture conditions while enabling straightforward handling and high-resolution readouts of individual cells. However, their widespread adoption for long-term cultures is limited by cell escape. In this work, we demonstrate that cell escape is predisposed to off-center encapsulated cells. High-speed microscopy reveals that cells are positioned at the microgel precursor droplets' oil/water interface within milliseconds after droplet formation. In conventional microencapsulation strategies the droplets are typically gelled immediately after emulsification, which traps cells in this off-center position. By delaying crosslinking, we succeed to drive cells towards the centers of microgels. The centering of cells in enzymatically crosslinked microgels prevents their escape during at least 28 days. It thereby uniquely enables the long-term culture of individual cells within <5 μm thick 3D uniform hydrogel coatings. Single cell analysis of mesenchymal stem cells in enzymatically crosslinked microgels reveals unprecedented high cell viability (>90%), maintained metabolic activity (>70%), and multilineage differentiation capacity (>60%) over a period of 28 days. The facile nature of this microfluidic cell centering method enables its straightforward integration into many microencapsulation strategies and significantly enhances control, reproducibility, and reliability of 3D single cell cultures.

Tom Kamperman, Sieger Henke, Claas Willem Visser, Marcel Karperien, and Jeroen Leijten**

Contribution TK: conception, experimental design, experimental performance, and manuscript writing.

** shared senior authorship.*

Published in Small, 2017, DOI: 10.1002/smll.201603711.

3.1 Introduction

Encapsulating cells into biomaterials such as hydrogels provides cells with an extracellular environment that can be tuned to mimic natural microenvironments *in vitro*.[1-3] Engineering the physicochemical and biofunctional properties of a biomaterial provides control over cellular behavior including migration, survival, proliferation, and differentiation.[4-6] Consequently, cell-laden hydrogels have a great potential to contribute to fundamental biological studies, pharmacological screenings, and cell-based therapies.[7-9] Although the size of cell encapsulating biomaterials is typically in the millimeter to centimeter range, it has been recognized that downsizing hydrogel constructs to the micrometer scale, called microgels, has the potential to advance numerous applications. Such cell-laden microgels can, for example, advance the high-throughput screening of cell-material combinations by allowing for facile single cell analysis.[10] Furthermore, cell-laden microgels could function as modular building blocks for engineering tissues with intrinsic multiscale hierarchy, which is essential for the functioning of native tissues.[11, 12] Ultimately, encapsulating individual cells in a hydrogel coating that is only a few micrometers thick offers unique advantages. Such microconstructs are readily compatible with standard visualization techniques including confocal microscopy without the need for optical or physical processing such as sectioning due to their minimal size. They also offer most efficient material-to-cell volume ratios and improved diffusion rates of solutes, which facilitates real-time pharmacological screenings and regenerative medicine applications while offering all advantages of 3D cell culture conditions.[12-14]

Droplet microfluidics technology is ideally suited for the production of (single-)cell-laden microgels with narrow size distributions.[15] However, current systems lock the encapsulated cell in an asymmetrical position within the microgel. This results in partial cell encapsulation and even escape of cells upon gelation and during subsequent culture.[14, 16-21] Moreover, incomplete encapsulation exposes cells asymmetrically to biochemical and biomechanical stimuli and counteracts possible microgel functions such as immunoprotection.[22] Encapsulation of single-cell-laden microgels in a second biomaterial layer has been explored to prevent cell escape and guarantee immunoprotection.[19, 23] However, this laborious two-step approach increases the microgels' size, while the cells are still exposed to a polarized microenvironment. Developing a facile strategy to center cells in microgels would thus prevent stimuli polarization and cellular escape, which would facilitate the use of single-cell-laden microgels in numerous research and clinical applications that require long-term 3D culturing.

Here, we confirm that off-center encapsulation results in cell escape, and present a novel and facile microfluidics-based approach to center single cells in microgels which enables their long-term 3D culture. Based on our observation that cells take position at the droplets' water/oil interface immediately after emulsification, we delayed on-chip crosslinking and thereby succeeded in repositioning cells from the droplet water/oil

interface to the droplet center. In this work, we specifically focused on delaying enzymatic crosslinking, as enzymatically crosslinked hydrogels and microgels support cell function and tissue formation in both *in vitro* and *in vivo* applications, and have consistently been reported to outperform widely used physical and photocrosslinking hydrogels systems such as alginate and polyethylene glycol diacrylate (PEGDA) in terms of cell survival and metabolic activity.[24-27] However, delayed enzymatic crosslinking of droplets in oil is not trivial as it requires the gel precursor to be in direct contact with a crosslinker. We have therefore developed a novel microfluidic device that enables *in situ* enzymatic crosslinking of a continuous stream of tyramine-conjugated hydrogel precursor droplets in oil via the controlled diffusion of small crosslinker molecules. This approach to delay crosslinking of cell-laden microdroplets was demonstrated to be of key importance to achieve cell centering and thereby prevent cell escape. The modular nature of our delayed crosslinking strategy makes it readily compatible with widely used standard droplet microfluidics technology, which facilitates its straightforward integration into conventional encapsulation procedures.

3.2 Materials and Methods

3.2.1 Materials

Dex-TA and HA-TA were synthesized as previously described [28, 29]. The resulting Dex-TA and HA-TA contained 15 and 3 tyramine moieties per 100 repetitive units, respectively. Horseradish peroxidase (HRP, type VI), H_2O_2 (with inhibitor), fetal bovine serum (FBS), ascorbic acid, iodixanol (OptiPrep), insulin (human), 3-Isobutyl-1-methylxanthine (IBMX), indomethacin, dexamethasone, β-glycerol phosphate disodium salt pentahydrate (β-GP), Calcein AM, ethidium homodimer-1 (EthD-1), Thiazolyl Blue Tetrazolium Blue (MTT), dextran-FITC (2000 kDa), Oil Red O, 2-propanol, Alizarin Red S, buffered formalin, Triton X-100, and 10-Acetyl-3,7-dihydroxyphenoxazine (Amplex Red) were purchased from Sigma-Aldrich. Phosphate-buffered saline (PBS) was purchased from Lonza. Dulbecco's Modified Eagle's Medium (DMEM), Minimal Essential Medium α with nucleosides (αMEM), Penicillin and Streptomycin, GlutaMAX, 2-mercaptoethanol, and trypsin-EDTA were purchased from Gibco. Basic fibroblast growth factor (ISOKine bFGF) was purchased from Neuromics. Phalloidin-AF488 was purchased from Molecular Probes. DRAQ5 was purchased from Thermo Scientific. Polydimethylsiloxane (PDMS, Sylgard 184) was purchased from Dow Corning. Aquapel was purchased from Vulcavite. Pico-Surf 1 in Novec 7500 Engineered Fluid and Pico-Break 1 were purchased from Dolomite. Surfactant-free fluorocarbon oil (Novec 7500 Engineered Fluid) was kindly provided by the BIOS Lab-on-a-Chip group. Gastight syringes (Hamilton), fluorinated ethylene propylene tubing (FEP, inner diameter 250 μm, DuPont) and connectors were purchased from IDEX Health and Science. Low pressure syringe pumps (neMESYS) were purchased from Cetoni.

3.2.2 Cell Isolation and Expansion

Human mesenchymal stem cells (MSCs) were isolated from fresh bone marrow samples and cultured as previously described.[30] The use of patient material was approved by the local ethical committee of the Medisch Spectrum Twente and informed written consent was obtained for all samples. In short, nucleated cells in the bone marrow aspirates were counted, seeded in tissue culture flasks at a density of 500,000 cells/cm^2 and cultured in MSC proliferation medium, consisting of 10% FBS, 100 U/ml Penicillin and 100 µg/ml Streptomycin, 1% GlutaMAX, 0.2 mM ascorbic acid, and 1 ng/ml bFGF (added fresh) in αMEM. Mouse insulinoma MIN6-B1 cells (provided by Dr. P. Halban, University Medical Center, Geneva, Switzerland) were cultured in MIN6 proliferation medium, consisting of 10% (v/v) FBS, 100 U/ml Penicillin and 100 µg/ml Streptomycin, and 71 µM 2-mercaptoethanol (added fresh) in DMEM. When cells reached near confluence, the cells were detached using 0.25% (w/v) Trypsin-EDTA at 37 °C and subsequently subcultured or used for experimentation.

3.2.3 Microgel Production and Culture

All microfluidic chips were manufactured from PDMS and glass using standard soft lithography techniques. The droplet generator and H_2O_2 diffusion-based crosslinking chips were fabricated with ~25 µm, and ~100 µm high channels, respectively. Aquapel was introduced in the chips before usage to ensure channel wall hydrophobicity. Chips were connected to gastight syringes using FEP tubing, which were controlled by low pressure syringe pumps. All emulsions were produced using 2% Pico-Surf 1 containing Novec 7500 Engineered Fluid. The conventional microgel production platform was operated as previously described, using flow rates of 0.5, 0.11, 0.11, and 2.8 µl/min for Dex-TA, HRP, H_2O_2, and oil, respectively.[25] To uncouple emulsification and gelation, a standard microfluidic flow focusing droplet generator was connected to the H_2O_2 diffusion-based crosslinking chip. In this modular microfluidic set-up, tyramine-conjugated polymer and HRP containing hydrogel precursor microemulsion was flown through the diffusion platform, which was also fed with H_2O_2 flowing in opposite direction at a rate of 30 µl/min. The H_2O_2 diffused from the feed channel through the PDMS walls into the gel precursor microemulsion, thereby triggering enzymatic crosslinking of tyramine-conjugated polymer. Hydrogel precursor solution contained 10% Dex-TA or 5% Dex-TA + 5% HA-TA, 44 U/ml HRP, and 8% OptiPrep (i.e. to obtain ρ = 1.05 g/l) in PBS and was emulsified in surfactant containing oil at a 1:6 flow ratio. To produce cell-laden microgels, detached cells (passage 2 to 5) were washed with medium, flown through a 40 µm cell strainer, and suspended in the hydrogel precursor solution at a concentration of 10^7 cells per ml. The cell-laden hydrogel precursor solution was loaded into an ice-cooled gastight syringe where it was gently agitated every ten minutes using a magnetic micro stirring bar. The microemulsion was broken by washing three times with surfactant-free fluorocarbon oil and subsequent supplementation of Pico-Break 1 in the presence of PBS or serum containing proliferation medium. Retrieved single-cell-laden microgels were cultured in MSC proliferation medium, MSC adipogenic differentiation medium, consisting of 10% FBS, 100 U/ml Penicillin and 100 µg/ml

Streptomycin, 1% GlutaMAX, 0.2 mM ascorbic acid, 10 mg/l insulin, 0.5 mM IBMX, 200 µM indomethacin, and 1 µM dexamethasone (added fresh) in DMEM, or MSC osteogenic differentiation medium, consisting of 10% FBS, 100 U/ml Penicillin and 100 µg/ml Streptomycin, 1% GlutaMAX, 0.2 mM ascorbic acid, 10 nM dexamethasone (added fresh), and 10 mM β-GP (added fresh) in αMEM, which were refreshed three times per week. As a negative control, encapsulated MSCs were also cultured in MSC proliferation medium substituted with 10 nM β-GP.

3.2.4 Staining and Visualization

On-chip droplets and microgels were visualized using a stereomicroscope set-up (Nikon SMZ800 equipped with Leica DFC300 FX camera). The position of cells in microdroplets or microgels was analyzed using ImageJ software. Collected microemulsions were imaged using phase contrast microscopy. Cells touching and protruding the microgels' wall, and cell escape were quantified by artisan counting of >90 cells per time point. To exclude cell proliferation, cell escape was only quantified until day 8 and cell colonies on tissue culture plastic were counted as 1 escape event. Viability and metabolic activity of cells was analyzed by staining with 2 µM calcein AM (live), 4 µM EthD-1 (dead), and 0.5 g/l MTT (metabolically active) in PBS and visualization using brightfield and fluorescence microscopy (EVOS FL). For additional analyses, cell-laden microgels were first washed with PBS and fixated using 10% neutral buffered formalin. Adipogenic differentiation was analyzed by staining samples with a filtered (0.45 µm) 1.8 g/l Oil Red O in a 2-propanol/PBS mixture (6:4) and visualization using brightfield microscopy. Osteogenic differentiation was analyzed by staining samples with a filtered (0.45 µm) 20 g/l Alizarin Red S in saline demineralized H_2O and visualization using brightfield microscopy. For fluorescence confocal microscopy (Nikon A1+), samples were permeabilized using 0.1% Triton X-100 and subsequently stained with 2.5 U/ml phalloidin-AF488, 50 µM DRAQ5, and 4 µM EthD-1 to stain F-actin, nuclei, and Dex-TA, respectively.

3.2.5 H_2O_2 Detection

To quantify H_2O_2, microemulsions were broken as described before, immediately diluted 10^5 times with PBS, and mixed 1:1 with 100 µM Amplex Red, 0.2 U/ml HRP in PBS. After 30 minutes incubation at room temperature, fluorescence intensities were measured using a plate reader (Victor X3, ex. 545/10 nm, em. 590/10 nm) and correlated to H_2O_2 concentrations using a standard curve.

3.2.6 Statistical Analysis

Meta-analysis of encapsulated cell position was performed on all available single cell encapsulation studies with a selection criterion of >20 displayed single cell encapsulation events. Cell positions in microdroplets and microgels were analyzed for statistical significance using ANOVA with Bonferroni's post hoc test with n>20. Escaped cell fraction and H_2O_2 detection data are shown as average ± standard deviation of technical

triplicates. Live/dead, metabolic activity, and differentiation analyses were performed via artisan counting of >125 cells per condition per time point.

3.3 Results and Discussion

3.3.1 Conventional Single Cell Encapsulation Methods Result in Frequent Cell Escape due to Off-center Encapsulation

We observed that single cell encapsulation in microgels using droplet microfluidics is typically challenged by off-center cell encapsulation, which causes cell escape during subsequent culture. We set out to confirm this limitation by encapsulating single cells into enzymatically crosslinkable microgels using a conventional encapsulation approach in which cells, prepolymer, and crosslinkers are mixed on-chip just before droplet formation. To this end, we down-sized the multi-cell enzyme-based microfluidic encapsulation platform that we have recently reported.[25] In concept, a tyramine-conjugated hydrogel precursor is crosslinked on-chip via the formation of tyramine-tyramine bonds using horseradish peroxidase (HRP) enzyme as catalyst and low levels of H_2O_2 as oxidizer (**Figure 3.1a**). Using this conventional production approach, we succeeded to encapsulate individual mesenchymal stem cells (MSCs) – which were used as multipotent model cells – in gelating dextran-tyramine (Dex-TA) precursor microdroplets of 44±3 µm (**Figure 3.1b**). Notably, close observation of the microfluidic encapsulation procedure revealed that cells take position at the droplets' water/oil interface immediately after emulsification. In a typical encapsulation approach as demonstrated here, emulsification and gelation processes happen within milliseconds (i.e. virtually coupled), and consequently cells become trapped in an off-center position. As a result, the majority of cells was positioned on the outer edge of the microgels (**Figure 3.1c**). This induced frequent cell escape from the microgels during subsequent handling and culture (**Figure 3.1d, Figure S3.1**). After one week, more than 25% of the cells had escaped from the microgels, while the fraction of cells that touched and protruded the outer edge of microgels had decreased, which indicated that off-center encapsulation was the major cause for cell escape (**Figure 3.1e**). Consequently, off-center cell encapsulation and escape impairs long-term cell-based studies, prevents immunoprotection, and presents polarized biochemical and biomechanical stimuli to the semi-encapsulated cells, which significantly reduces the control over the engineered 3D cell microenvironment (**Figure 3.1f**).[14, 19, 23]

To assess the prevalence of asymmetric cell encapsulation – as the underlying cause for cell escape – we quantified the positions of cells within microgels for all reported single-cell encapsulation systems that displayed at least 20 single-cell-laden microgels. The cell's distance from the center x was normalized as $x/(r_{gel}-r_{cell})$, with r_{gel} and r_{cell} as the diameters of the gel and cell, respectively (**Figure 3.1g**). Interestingly, this meta-analysis revealed near identical encapsulation deficiencies for all analyzed studies, including our own microencapsulation attempt from **Figure 3.1b** (**Figure 3.1h** refs: a[17], b[22], c[31], d[32], e[20], f[16], g[19]; **Figure S3.2**). In particular, the analyzed studies are

consistently characterized by off-center cell encapsulation (i.e. median of $x/(r_{gel}-r_{cell})$ > 0.5), which therefore does not seem to depend on the cell type (yeast or mammalian), cell size (3 to 30 µm), cell encapsulating material (synthetic or natural, degradable or non-degradable), crosslinking strategy (physical or chemical), or droplet generator type (T-junction or flow focusing). Importantly, all analyzed studies were performed using encapsulation methods in which emulsification and gelation happened within milliseconds, thus near simultaneously (i.e. coupled). High-speed microscopic visualization of our own microencapsulation procedure confirmed that cells position at the droplets' water/oil interface almost immediately (i.e. < 10 ms) after emulsification (**Figure S3.3**). Therefore, we hypothesized that immediate gelation of the microgel precursor droplet traps the cell in this off-center position, whereas delayed gelation could provide time for repositioning of the cell towards the droplet center, which would result in centered, complete, and uniform encapsulation of single cells in microgels and thereby prevent cell escape.

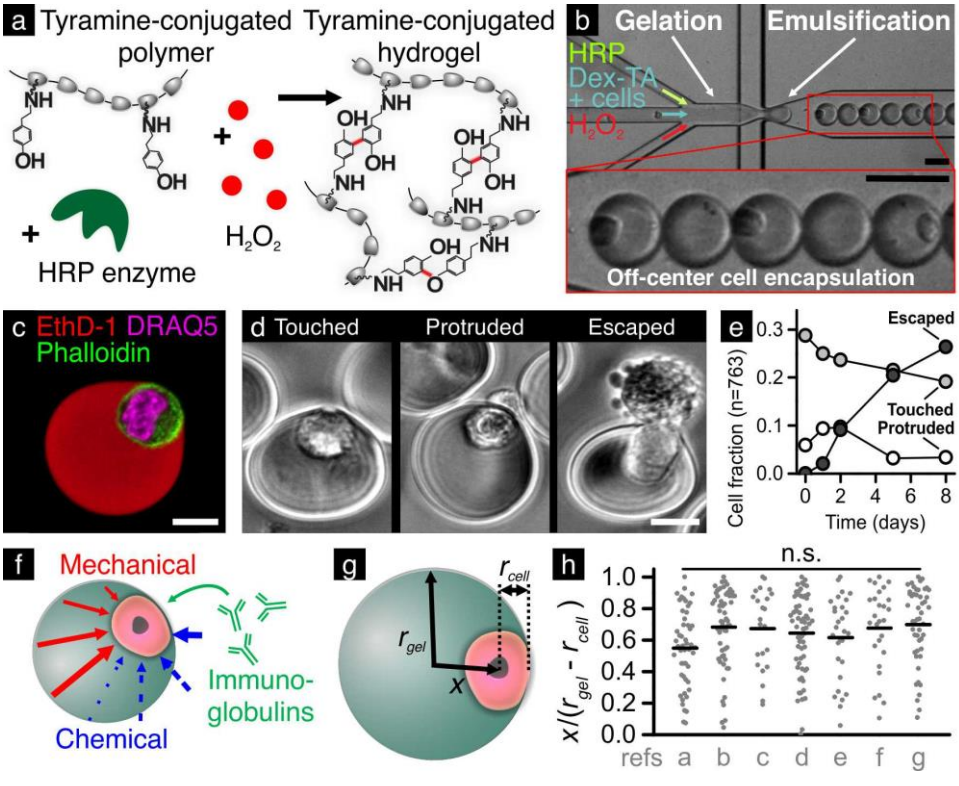

Figure 3.1. Conventional single cell encapsulation methods result in off-center encapsulation and subsequent cell escape. (**a**) Tyramine-conjugated polymer is crosslinked by HRP in the presence of H_2O_2. (**b**) Conventional microfluidic microgel generator with coupled on-chip gelation and emulsification forced cells in an off-center position, (**c**) as confirmed by fluorescence confocal microscopy. (**d,e**) Off-center encapsulated cells that touched the outer microgel boundary often protruded and subsequently escaped during subsequent culture. (**f**) This hampers the microgel's potential immunoprotective capacity and may induce asymmetrical polarized presentation of

biochemical and biomechanical stimuli. (**g**) The cell position in microgels was quantified by $x/(r_{gel}-r_{cell})$, with x, r_{gel} and r_{cell} as the distance from the cell's center to the microgel's wall, and diameters of the microgel and cell, respectively. (**h**) Meta-analyses of cells' positions in microgels produced using previously reported microfluidic encapsulation platforms. A value of 0 corresponds to the microgel center and a value of 1 to the edge of the microgel, as drawn in panel (g). n.s. indicates 'not significant with $p<0.05$'. Refs: a[17], b[22], c[31], d[32], e[20], f[16], g[19]. Black scale bars: 50 µm, white scale bar: 10 µm.

3.3.2 Modular Microfluidic Diffusion Chip Enables Delayed Enzymatic Crosslinking of Hydrogel Precursor Microdroplets

To achieve delayed enzymatic crosslinking, we had to develop a novel strategy to supplement yet emulsified hydrogel precursor droplets with the crosslinker. Inspired by sensor technology, we leveraged the permselective nature of silicone rubber towards H_2O_2 to enable *in situ* enzymatic crosslinking of hydrogel precursor droplets.[33] Specifically, we designed a dedicated microfluidic chip that consisted of three equally long (35 cm) and high (100 µm) parallel channels: one center channel for Dex-TA and HRP containing gel precursor droplets, and two aligning channels that contained H_2O_2 feed solution (**Figure 3.2a**). The chip was fabricated from polydimethylsiloxane (PDMS), a silicone rubber that enables the diffusion of H_2O_2 from the feed channels towards the gel precursor microemulsion and on-chip initiation of outside-in enzymatic crosslinking (**Figure 3.2b**). Various combinations of different wall thicknesses and channel widths were assessed to identify the design that enabled robust on-chip crosslinking of Dex-TA and HRP containing microdroplets. The microfluidic chips were fabricated using standard soft lithography techniques and connected to a standard microfluidic flow focusing droplet generator in a modular fashion. All chip designs were tested for their ability to crosslink Dex-TA and HRP containing microdroplets into microgels (**Figure S3.4**). Chips with 25 µm thin PDMS walls could be produced, but proved fragile as the thin walls often collapsed, which prevented numerous chips (>90%) from being reliably used (**Figure S3.5**). In contrast, thicker channel walls of 50 µm did not collapse and readily supported the crosslinking of Dex-TA microdroplets. However, robust microgel production in center channels of 50 µm in widths was hampered by occasional droplet merging, which resulted in clogging by the formation of gel plugs that caused in continual stagnations of the flow (**Figure 3.2c**). Such stagnation caused differences in diffusion-based H_2O_2 supplementation, which is time and concentration dependent. This resulted in a variation of crosslinking densities among microgels, causing a polydisperse size distribution ($D/D_{average}$) of differently swollen microgels (**Figure 3.2d**). Widening the channel to 300 µm could prevent clogging-induced flow instabilities, but still resulted in varying crosslinking densities. This was likely caused by the presence of a H_2O_2 gradient over the relatively wide (~10 droplet diameters) center channel (**Figure 3.2e**). Chips with a 100 µm wide center channel (~3 droplet diameters) allowed for robust and undisturbed flow of microgel precursor droplets at all times, while supplementing all microdroplets across the channel with equal amounts of H_2O_2 (**Figure 3.2f**, **Figure S3.4**). On-chip crosslinking of Dex-TA precursor microdroplets using this specific design uniquely resulted in microgels with a narrow size distribution and identical swelling rates, which corroborated that the microgels had received equal amounts of crosslinker

(i.e. H_2O_2) (**Figure 3.2g**). This particular chip design consistently enabled delayed enzymatic crosslinking of hydrogel precursor microdroplets and was therefore used for all subsequent experiments.

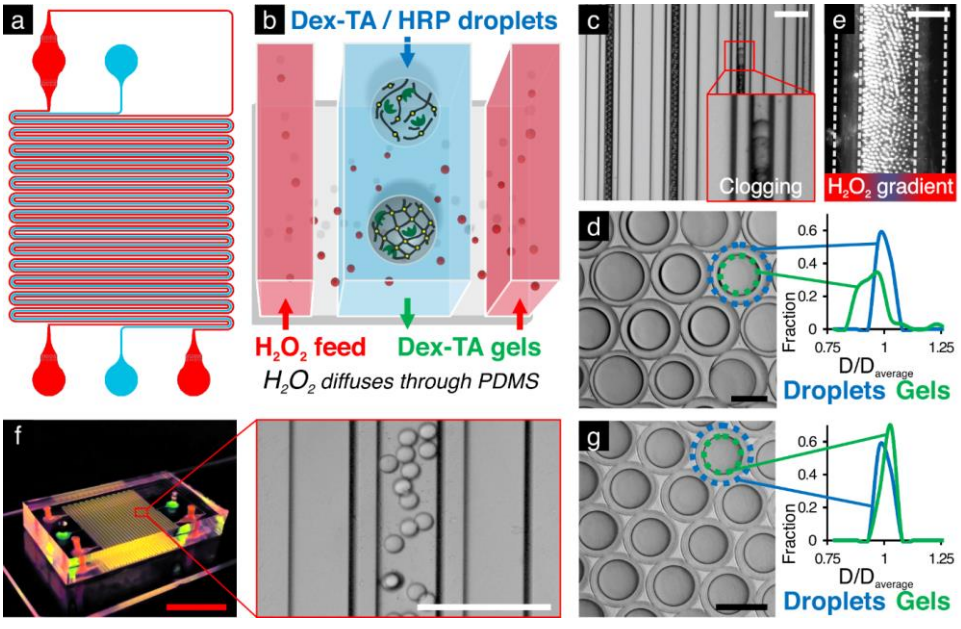

Figure 3.2. Design and optimization of the novel microfluidic diffusion-based enzymatic crosslinking platform. (**a**) In concept, the crosslinking platform chip consists of parallel microfluidic channels separated by a thin PDMS wall (**b**) which enables the controlled supplementation of H_2O_2 to initiate on-chip enzymatic crosslinking of Dex-TA gel precursor droplets in oil. (**c**) Narrow (50 µm) center channels caused flow instabilities due to droplet merging, resulting in (**d**) varying crosslinking densities among microgels. (**e**) Wide (300 µm) center channels also resulted in varying crosslinking densities, likely due to a H_2O_2 gradient over the channel. (**f**) The final chip design supported stable flow and cured all microgels equally, resulting in (**g**) monodisperse Dex-TA microgels. Black scale bars: 25 µm, white scale bars: 250 µm, red scale bar: 1 cm.

3.3.3 Delayed On-chip Crosslinking Enables Centering of Single Cells in Microgels

The development of a strategy to delay on-chip gelation readily allowed us to position cells in the centers of enzymatically crosslinked microgels, which was confirmed using fluorescence confocal imaging (**Figure 3.3a**). Here, individual MSCs (18±4 µm) were encapsulated within Dex-TA microgels (27±2 µm), effectively resulting in uniform 3D single cell coatings of less than 5 µm (**Figure 3.3b**). To analyze the dynamics of cell centering within the microgel precursor droplets, the relative position of single cells in non-gelating (i.e. without H_2O_2 feed) Dex-TA precursor droplets was measured at three different positions along the modular microfluidic chip setup: (t1) immediately after the droplet generator; (t2) at the start of the crosslinking chip; and (t3) at the end of the crosslinking chip (**Figure 3.3c**). Similar to previous observations (**Figure 3.1b**, **Figure S3.3**), cells were positioned at the droplets' oil/water interface almost immediately after encapsulation, which was <10 ms after droplet generation (**Figure 3.3d**). In contrast, at

the end of the crosslinking chip (~25 s after droplet generation), most cells were repositioned to the centers of microdroplets (**Figure 3.3e**). Quantification of the cell position within microdroplets along the modular microfluidic setup validated on-chip cell centering, as indicated by the blue data points in **Figure 3.3f**. Importantly, delayed induction of on-chip enzymatic crosslinking (i.e. with H_2O_2 feed) did not affect the centering behavior and indeed resulted in near perfectly centered single cells in Dex-TA microgels, as indicated by the green data points in **Figure 3.3f**. Moreover, delayed crosslinking significantly improved cell centering as compared to all analyzed studies including our own previous single cell microencapsulation experiment where emulsification and gelation were coupled (grey and red data points).

We then aimed to confirm that cell centering via delayed crosslinking can be universally applied with respect to the hydrogel material, crosslinking mechanism, and cell type. To this end, we first encapsulated MSCs in enzymatically crosslinkable microdroplets with a distinct composition. In particular, MSCs were encapsulated in microgels that consisted of Dex-TA and hyaluronic acid-tyramine (HA-TA) in a 1:1 ratio.[29] We quantified the cells' positions within delayed crosslinked Dex-HA-TA microgels and compared these to single-cell-laden Dex-TA microgels. **Figure 3.3g** shows that cells were equally centered in delayed crosslinked Dex-TA (green circles) and Dex-HA-TA microgels (light blue circles), and significantly more centered as compared to enzymatically crosslinked Dex-TA microgels that were produced using the conventional strategy where emulsification and gelation were coupled (red circles). Furthermore, encapsulating a different cell type of smaller size (pancreatic beta cell line MIN6; 12±2 µm) into delayed crosslinked Dex-HA-TA microgels (light blue crosses) also significantly increased centering as compared to the immediate crosslinking approach. To prove that cell centering is not limited to enzymatic crosslinking approaches only, we also encapsulated individual MSCs in photocrosslinkable PEGDA. Initiating photocrosslinking at the end of a previously reported microencapsulation platform's delay channel (i.e. ~3 s after emulsification) resulted in near perfectly centered MSCs in PEGDA microgels (yellow circles; **Figure S3.6**).[12] In fact, comparing PEGDA encapsulated cells' positions to those in enzyme-based delayed crosslinked microgels did not reveal a significant difference, while exploiting different hydrogel precursor solutions (i.e. PEG *vs* Dex/HA), crosslinking mechanisms (i.e. photo- *vs* enzymatic crosslinking), and microgel sizes (38±1 µm *vs* 27±2 µm). In addition, we investigated the effect of droplet size on cell position by performing regression analyses on all presented cell position data (including data from the meta-analysis). This revealed no relationship between droplet size and cell position ($R^2 \leq 0.5$). Together, these results prove that the cell position in microgels is independent of the cells, encapsulation material, crosslinking strategy, or droplet generator, and can be tuned via a universal and facile delayed on-chip crosslinking approach.

It is of note that relatively slow (minutes to hours) off-chip crosslinking via, for example, thiol-Michael addition – albeit delayed – may still result in asymmetric cell encapsulation and cell escape.[34] Delayed gelation of non-moving emulsions is likely to

result in asymmetrical cell encapsulation due to gravitational repositioning of cells towards the bottom of the hydrogel precursor droplets. We anticipate that cell centering is an active process that requires continuous movement of the droplets. This idea is corroborated by a recent study where cells were centered in microgels by crosslinking cell-laden hydrogel precursor droplets off-chip on an orbital shaker.[35] Investigating the physical mechanism that underlies cell centering in gelating microdroplets will be the focus of future studies.

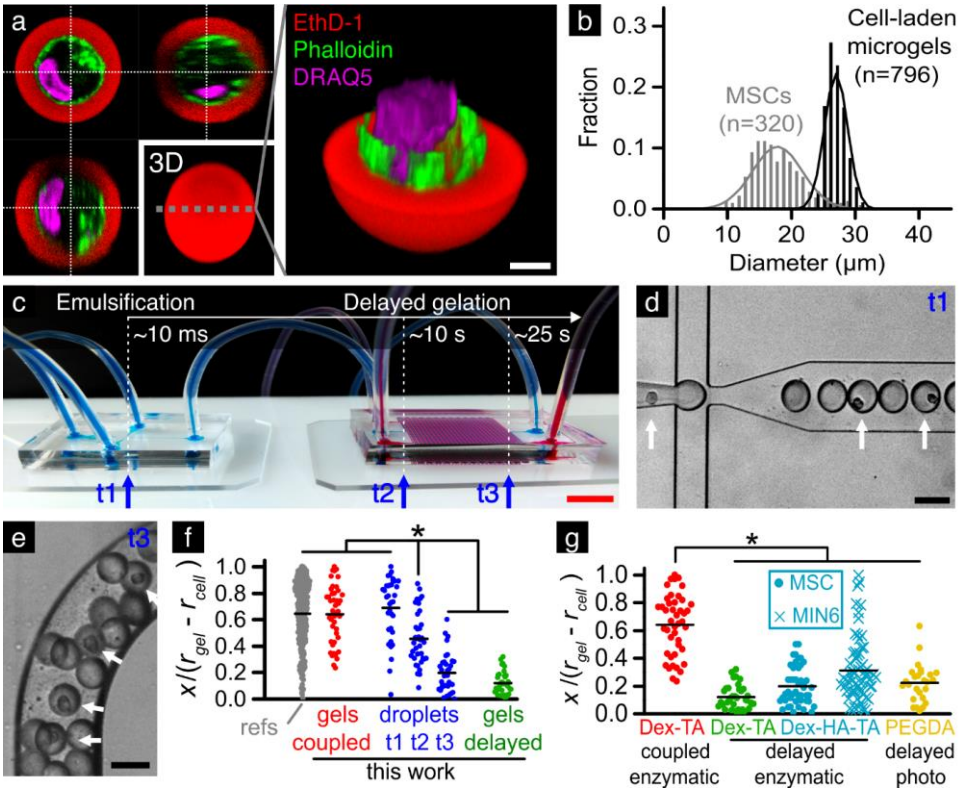

Figure 3.3. Delayed on-chip crosslinking enables centering of single cells in microgels. (**a**) Fluorescence confocal imaging confirmed that delayed enzymatic crosslinking enabled centering of single MSCs in Dex-TA microgels. (**b**) On average, cell-laden microgels were only 9 µm larger than the encapsulated MSCs, effectively resulting in 3D hydrogel coatings of less than 5 µm. (**c**) A standard microfluidic droplet generator was connected to the H_2O_2 diffusion-based crosslinking chip. The position of cells (white arrows) in non-crosslinking microgel precursor droplets was analyzed (**d**) immediately after droplet generation (t1), at the start of the crosslinking chip (t2), and (**e**) at the end of the crosslinking chip (t3). (**f**) Cell positions within microgels produced using conventional microfluidic encapsulation systems (i.e. with coupled emulsification and gelation) are indicated with grey (i.e. references) and red (i.e. this work) data points. Cell positions within gel precursor droplets along the modular microfluidic setup are indicated with blue data points. Cell positions within delayed enzymatically crosslinked microgels are indicated with green data points. (**g**) Cell position analyses of various combinations of distinct hydrogel materials (i.e. Dex-TA, Dex-HA-TA, PEGDA), cell types (i.e. MIN6, MSC), and crosslinking methods (i.e. enzyme-based and photocrosslinking), revealed that delayed crosslinking consistently resulted in significantly increased cell centering as compared to the conventional

encapsulation approach where emulsification and gelation are coupled. * indicates 'significant with $p<0.05$'. White scale bars: 5 µm, black scale bars: 50 µm, red scale bar: 5 mm.

3.3.4 Cell Centering in Cytocompatible Microgels Enables Long-term Single Cell 3D Culture by Preventing Cell Escape

To enable long-term cell-based studies, we optimized the enzymatic crosslinking process to produce completely crosslinked microgels while maintaining cytocompatible levels of H_2O_2 (i.e. <10 µM), which would support maintained cell viability and function.[36] In the diffusion-based crosslinking platform, precursor droplets and crosslinker fluid flows are separated by a PDMS wall. This separation enabled straightforward screening of increasing amounts of crosslinker while leaving the droplet production process undisturbed. As the crosslinker chip has fixed dimensions and constant diffusivity, Fick's law dictates that the amount of H_2O_2 that diffuses from the feed channel through the PDMS wall and oil into the microdroplets is determined by both the concentration difference, which approximates the H_2O_2 feed concentration ($[H_2O_2]_{feed}$) and the diffusion time, which scales with the emulsion's flow rate ($Q_{emulsion}$). **Figure 3.4a** summarizes the crosslinker screening results, where blue, green, and red indicate incomplete crosslinking, complete crosslinking, and excessive H_2O_2 supplementation, respectively. The lower production limit of our gelation platform in terms of $[H_2O_2]_{feed}$ and $Q_{emulsion}$ was determined by qualifying the amount of microgel swelling. Incomplete crosslinking resulted in the absence of microgels (i.e. dissolved) or relatively large microgels with vague contours (i.e. swollen) as compared to completely crosslinked microgels (**Figure S3.7**). Conversely, excessive H_2O_2 supplementation did not affect microgel morphology, but was detrimental to cell survival (**Figure S3.8**). To determine a robust and cytocompatible microencapsulation window, we quantified the residual H_2O_2 concentration in collected microemulsions ($[H_2O_2]_{emulsion}$) using the fluorescence-based substrate Amplex Red, which is oxidized by H_2O_2 to form highly fluorescent resorufin (**Figure 3.4b**).[37] First, we validated this approach by measuring H_2O_2 concentrations in non-gelating microdroplets (i.e. without HRP). Indeed, increasing $[H_2O_2]_{feed}$ correlated with increased H_2O_2 concentrations in non-crosslinking HRP-free microemulsions (**Figure 3.4c**). Subsequent quantification of residual H_2O_2 in hydrogel precursor microdroplets that did contain HRP (which consumed H_2O_2 during crosslinking) revealed that only $[H_2O_2]_{feed}$ >10% resulted in detectable (i.e. potentially cytotoxic) levels, while $[H_2O_2]_{feed}$ ≤10% remained undetectable (i.e. <10 µM). Indeed, also the short-term viability of MSCs that were microencapsulated using $[H_2O_2]_{feed}$ = 5% and $Q_{emulsion}$ = 14 µl/min was unaffected as compared to that of non-encapsulated MSCs (i.e. syringe control). In fact, over 98% of the cells remained viable in both encapsulated and non-encapsulated samples on day 0, as measured using a live/dead assay comprised of calcein AM and ethidium homodimer-1 (EthD-1) (**Figure 3.4d**). Based on these findings, we considered $[H_2O_2]_{feed}$ = 5% and $Q_{emulsion}$ = 14 µl/min as optimal parameters for the production of well-crosslinked cytocompatible Dex-TA microgels. These production settings were used in all subsequent cell encapsulation experiments.

We then assessed whether our novel cell centering strategy would reduce cell escape during subsequent *in vitro* culture. Strikingly, the centered MSC/Dex-TA microconstructs demonstrated only 4±1% cell escape after 7 days, which was reached within 24 hours and did not further increase over time (**Figure 3.4e**). This was in sharp contrast to the 27±5% cell escape – which was still rising over time – from off-center single-cell-laden microconstructs that were produced using the conventional (i.e. coupled) encapsulation approach. Cell centering thus minimized cell escape, which makes our microencapsulation platform uniquely suited for long-term singe-cell-based studies. Quantifying the encapsulated cell fraction during long-term culture also revealed identical Poisson-distributed cell encapsulation on day 0 and 28 of *in vitro* culture, confirming inconsiderable amounts of cell escape of centered cells from microgels (**Figure 3.4f**).[38] Furthermore, this experiment proved the long-term cytocompatibility of the enzymatically crosslinked 3D microenvironments. Remarkably, over 90% of encapsulated MSCs remained alive (i.e. EthD-1 negative) of which 80% was metabolically active (i.e. MTT positive) throughout 28 days of *in vitro* culture (**Figure 3.4g-i**).

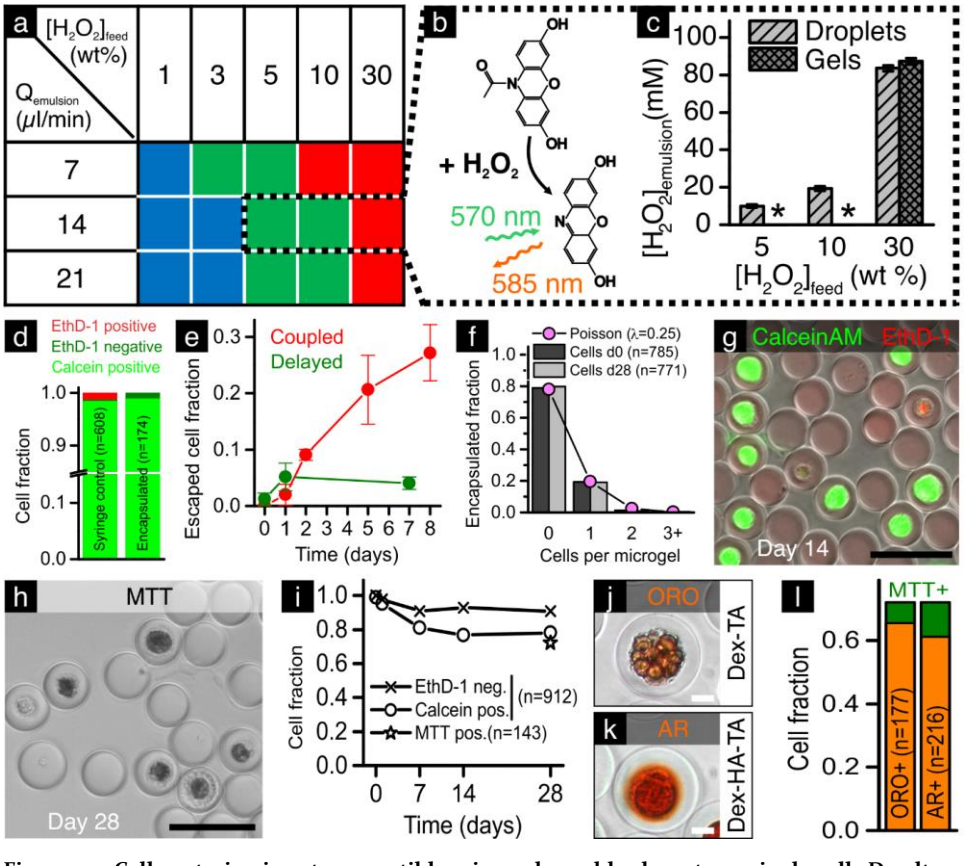

Figure 3.4. Cell centering in cytocompatible microgels enables long-term single cell 3D culture by preventing cell escape. (**a**) Qualification of Dex-TA microgel crosslinking as a function of the

microemulsion flow rate ($Q_{emulsion}$) and concentration of the H_2O_2 feed ($[H_2O_2]_{feed}$). Blue, green, and red indicate incomplete crosslinking, complete crosslinking, and H_2O_2 excess, respectively. (**b,c**) Amplex Red assay to quantify the concentration of residual H_2O_2 ($[H_2O_2]_{emulsion}$) in Dex-TA microgel precursor droplets and crosslinked microgels after their retrieval from the diffusion-based crosslinking platform. (**d**) The microencapsulation procedure had no detrimental effect on short-term cell survival. (**e**) Delayed crosslinking resulted in 4±1% cell escape after 7 days of *in vitro* culture, as compared to 27±5% cell escape when using coupled emulsification and gelation. (**f**) The number of encapsulated cells per microgel tightly followed the Poisson distribution and remained similar throughout long-term (28 days) of *in vitro* culture, which confirmed that cell centering prevents cell escape. (**g-i**) MSCs encapsulated in delayed enzymatically crosslinked microgels remained viable and metabolically active throughout 28 days of *in vitro* culture. (**j**) Positive Oil Red O and (**k**) Alizarin Red stainings confirmed that (**l**) more than 60% of the microencapsulated MSCs could differentiate into the adipogenic and osteogenic lineage, respectively. Black scale bars: 50 µm, white scale bars: 5 µm.

To assure complete cytocompatibility of our novel delayed enzymatic crosslinking mechanism, we aimed to assess the long-term function of encapsulated MSCs by probing their multipotent differentiation potential. To this end, single-cell-laden microgels were cultured 28 days in differentiation medium to induce adipogenic and osteogenic differentiation of the encapsulated MSCs. Interestingly, Dex-TA microenvironments readily supported adipogenic, but not osteogenic differentiation, indicated by positive Oil Red O (fat deposition) and negative Alizarin Red (calcium deposition) stainings, respectively (**Figure 3.4j**, **Figure S3.9**). We leveraged the universal nature of tyramine-based enzymatic crosslinking to endow the microgels with hyaluronic acid, which rendered the microgels osteoinductive.[39, 40] Specifically, HA-TA was readily incorporated into the microgels to effectively create single-cell-laden Dex-HA-TA microenvironments.[29] Culturing these constructs for 28 days in osteogenic differentiation medium resulted in complete osteogenic differentiation of the encapsulated MSCs, while adipogenic differentiation capacity was also maintained, as confirmed by positive Alizarin Red and Oil Red O stainings (**Figure 3.4k**, **Figure S3.10**). Quantifying adipogenic and osteogenic differentiation of MCSs in Dex-TA and Dex-HA-TA microgels, respectively, revealed that >60% of the individually encapsulated cells (i.e. ≥85% of metabolically active cells) remained multipotent throughout the encapsulation procedure and subsequent long-term *in vitro* culture (**Figure 3.4l**). This further confirmed the cytocompatible nature of the presented enzymatic crosslinking approach as well as its capability to contribute to single cell analysis within 3D microenvironments by preventing cell escape from microgels.

3.4 Conclusion

Encapsulation of single cells in microgels using conventional microfluidic approaches typically results in off-center cell encapsulation. Such off-center cell encapsulation causes frequent cell escape and consequently hampers long-term single-cell-based studies. This work revealed that asymmetrical positioning of cells within microgels occurs irrespective of the cell type, cell size, hydrogel material, crosslinking mechanism, and microfluidic droplet generator. Instead, off-center encapsulation is caused by near immediate gelation of cell-laden hydrogel precursor droplets, which traps cells in off-

center positions. Here, we showed that a delayed crosslinking approach enabled on-chip centering of cells within microgels. This method can be universally applied to center various cell types into various materials that are crosslinked via different mechanisms. Using a novel diffusion-based enzymatic crosslinking strategy, we demonstrated that cell centering prevented cell escape and thereby enabled long-term (28 days) culture and differentiation of MSCs in less than 5 µm thick dextran- and hyaluronic acid-based 3D hydrogel coatings. We anticipate that the generic and facile nature of this delayed crosslinking approach facilitates its straightforward integration into many conventional microencapsulation systems, thereby increasing reproducibility and reliability of cell-based studies.

3.5 Supplementary Information

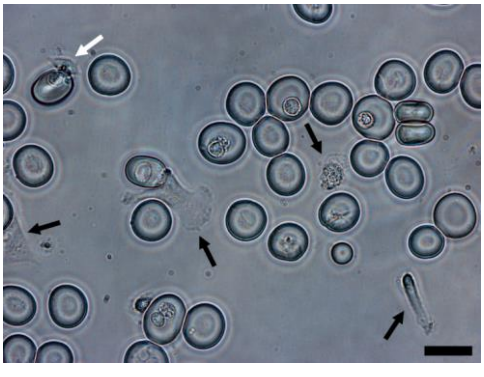

Figure S3.1. Off-center encapsulated MSCs escape from microgels. Single-cell-laden Dex-TA microgels produced using a conventional microencapsulation approach where emulsification and gelation were coupled. Off-center encapsulated MSCs protruded (white arrow) and escaped (black arrows) from the microgels during handling and *in vitro* culture. Scale bar: 50 µm.

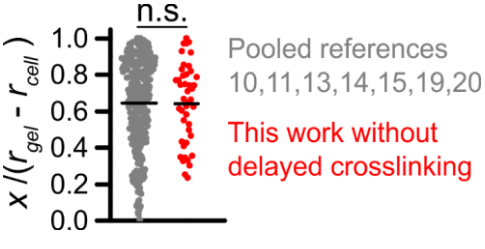

Figure S3.2. Near-immediate on-chip crosslinking resulted in off-center encapsulation. There was no significant difference in cell position between all analyzed references (grey data points) and our own data obtained using a conventional encapsulation system were reported encapsulation system (red data points). n.s. indicates 'not significant with $p<0.05$'.

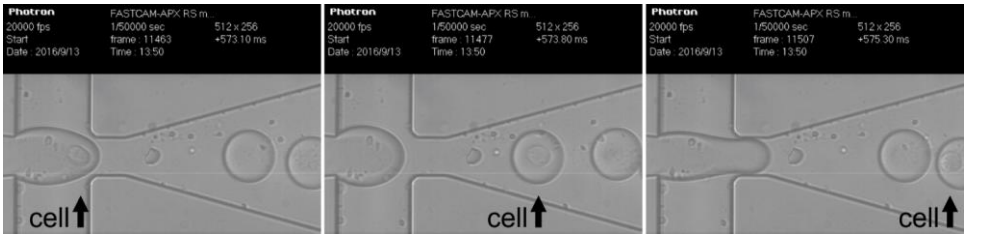

Figure S3.3. High-speed microscopy imaging of single-cell-laden hydrogel precursor microdroplet formation. A cell takes position at the droplet's water/oil interface within milliseconds after droplet formation.

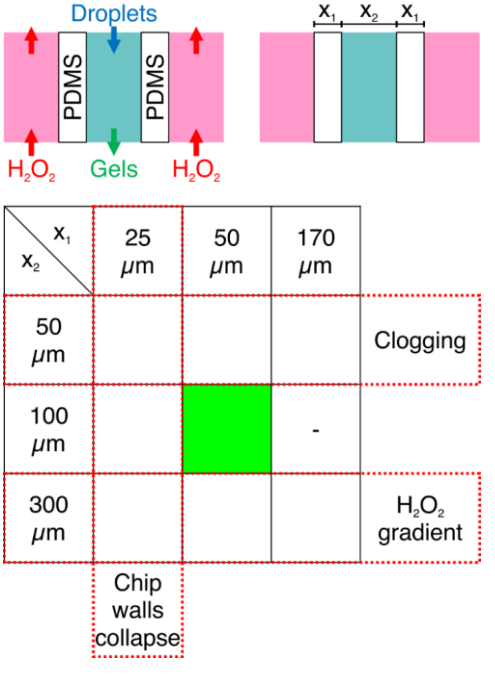

Figure S3.4. Design parameters for the H_2O_2 diffusion-based microgel crosslinking platform. Various combinations of different wall thicknesses (x_1) and center channel widths (x_2) were assessed to identify the optimal design for robust on-chip crosslinking of Dex-TA and HRP containing microdroplets. - indicates 'not tested'.

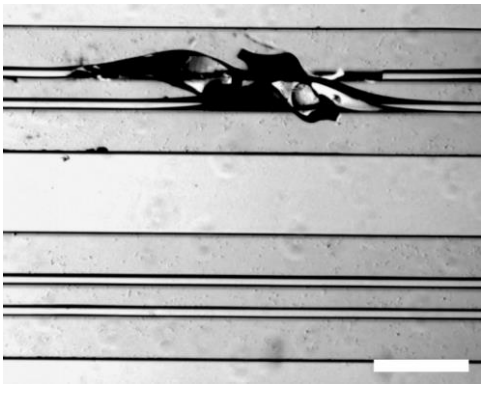

Figure S3.5. Collapsed PDMS walls. 25 µm thick PDMS walls frequently (>90%) collapsed during chip fabrication. Scale bar: 250 µm.

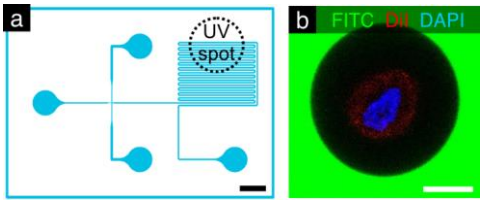

Figure S3.6. Delayed photocrosslinking to center cells in PEGDA microgels. (**a**) The microfluidic cell encapsulation platform consisted of a standard droplet generator and a delay channel that enabled delayed photocrosslinking of cell-laden microgel precursor using an external UV light spot. (**b**) Fluorescence confocal imaging revealed that on-chip delayed photocrosslinking resulted in centering of cells in PEGDA microgels. Black scale bar: 2 mm, white scale bar: 10 µm.

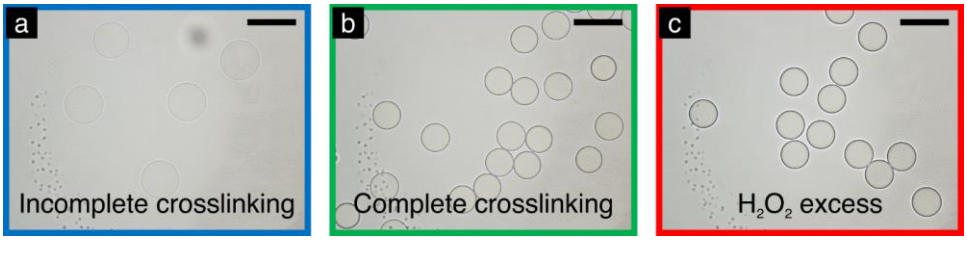

Figure S3.7: Optimizing microgel crosslinking. Increasing amounts of H_2O_2 were flown through the H_2O_2 feed channel to determine optimal crosslinking concentrations. Blue, green, and red indicate (**a**) incomplete crosslinking, (**b**) complete crosslinking, and (**c**) H_2O_2 excess, respectively. Scale bars: 50 µm.

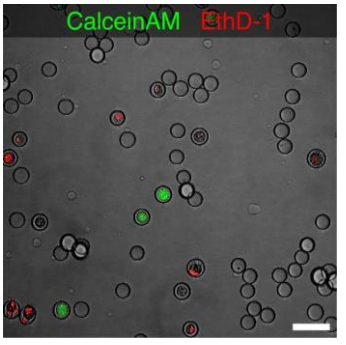

Figure S3.8: H_2O_2 excess is detrimental to cell survival. Live/dead analysis revealed that $[H_2O_2]_{feed}$ = 30% and $Q_{emulsion}$ = 14 µl/min resulted in well-crosslinked microgels, but also caused significant (~80%) cell dead. Scale bar: 50 µm.

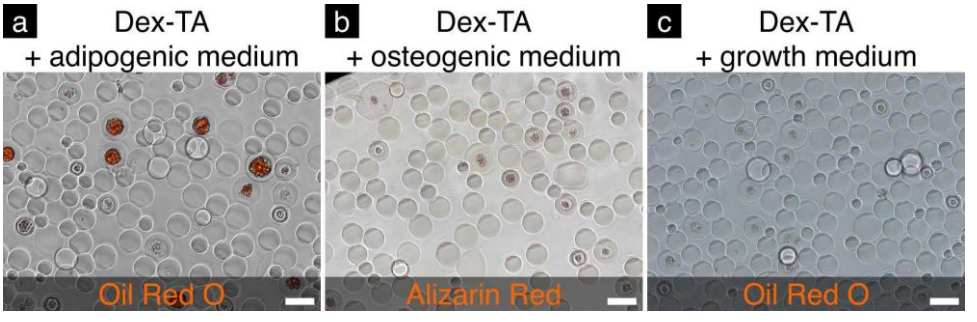

Figure S3.9. Multilineage differentiation of MSCs in Dex-TA microgels. MSCs differentiated into the (**a**) adipogenic lineage in the presence of adipogenic differentiation medium as visualized using Oil Red O staining, (**b**) but not into the osteogenic lineage in the presence of osteogenic medium as visualized using Alizarin Red staining. (**c**) MSCs did not differentiate into the adipogenic lineage in the presence of growth medium. Scale bars: 25 µm.

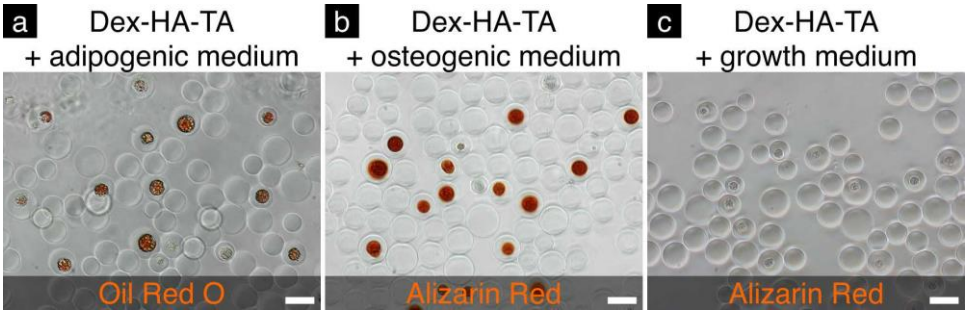

Figure S3.10. Multilineage differentiation of MSCs in Dex-HA-TA microgels. MSCs differentiated into the (**a**) adipogenic lineage in the presence of adipogenic differentiation medium as visualized using Oil Red O staining, (**b**) and into the osteogenic lineage in the presence of osteogenic medium as visualized using Alizarin Red staining. (**c**) MSCs did not differentiate into the osteogenic lineage in the presence of growth medium. Scale bars: 25 µm.

References

1. Leijten, J. and A. Khademhosseini, *From Nano to Macro: Multiscale Materials for Improved Stem Cell Culturing and Analysis.* Cell Stem Cell, 2016. **18**(1): p. 20-4.
2. Peppas, N.A., et al., *Hydrogels in Biology and Medicine: From Molecular Principles to Bionanotechnology.* Advanced Materials, 2006. **18**(11): p. 1345-1360.
3. Lee, K.Y. and D.J. Mooney, *Hydrogels for Tissue Engineering.* Chemical Reviews, 2001. **101**(7): p. 1869-1880.
4. Benoit, D.S., et al., *Small functional groups for controlled differentiation of hydrogel-encapsulated human mesenchymal stem cells.* Nat Mater, 2008. **7**(10): p. 816-23.
5. Lutolf, M.P., et al., *Synthetic matrix metalloproteinase-sensitive hydrogels for the conduction of tissue regeneration: engineering cell-invasion characteristics.* Proc Natl Acad Sci U S A, 2003. **100**(9): p. 5413-8.
6. Mann, B.K., R.H. Schmedlen, and J.L. West, *Tethered-TGF-beta increases extracellular matrix production of vascular smooth muscle cells.* Biomaterials, 2001. **22**(5): p. 439-44.
7. Leijten, J., et al., *Cell based advanced therapeutic medicinal products for bone repair: Keep it simple?* Adv Drug Deliv Rev, 2015. **84**: p. 30-44.
8. Sung, J.H. and M.L. Shuler, *A micro cell culture analog (microCCA) with 3-D hydrogel culture of multiple cell lines to assess metabolism-dependent cytotoxicity of anti-cancer drugs.* Lab on a Chip, 2009. **9**(10): p. 1385-94.
9. Bian, L., et al., *Hydrogels that mimic developmentally relevant matrix and N-cadherin interactions enhance MSC chondrogenesis.* Proc Natl Acad Sci U S A, 2013. **110**(25): p. 10117-22.
10. Ranga, A., et al., *3D niche microarrays for systems-level analyses of cell fate.* Nature Communications, 2014. **5**: p. 4324.
11. Liu, J.S. and Z.J. Gartner, *Directing the assembly of spatially organized multicomponent tissues from the bottom up.* Trends Cell Biol, 2012. **22**(12): p. 683-91.
12. Kamperman, T., et al., *Single Cell Microgel Based Modular Bioinks for Uncoupled Cellular Micro- and Macroenvironments.* Adv Healthc Mater, 2017. **6**(3).
13. Wang, H., et al., *The use of micro- and nanospheres as functional components for bone tissue regeneration.* Tissue Eng Part B Rev, 2012. **18**(1): p. 24-39.
14. Mao, A.S., et al., *Deterministic encapsulation of single cells in thin tunable microgels for niche modelling and therapeutic delivery.* Nat Mater, 2017. **16**(2): p. 236-243.
15. Velasco, D., E. Tumarkin, and E. Kumacheva, *Microfluidic encapsulation of cells in polymer microgels.* Small, 2012. **8**(11): p. 1633-42.
16. Ma, Y., et al., *Artificial microniches for probing mesenchymal stem cell fate in 3D.* Biomater. Sci., 2014. **2**(11): p. 1661-1671.
17. Kumachev, A., et al., *High-throughput generation of hydrogel microbeads with varying elasticity for cell encapsulation.* Biomaterials, 2011. **32**(6): p. 1477-83.
18. Utech, S., et al., *Microfluidic Generation of Monodisperse, Structurally Homogeneous Alginate Microgels for Cell Encapsulation and 3D Cell Culture.* Adv Healthc Mater, 2015. **4**(11): p. 1628-33.
19. Allazetta, S., et al., *Cell-Instructive Microgels with Tailor-Made Physicochemical Properties.* Small, 2015. **11**(42): p. 5647-56.
20. Ma, S., et al., *Monodisperse collagen–gelatin beads as potential platforms for 3D cell culturing.* Journal of Materials Chemistry B, 2013. **1**(38): p. 5128.
21. Rossow, T., P.S. Lienemann, and D.J. Mooney, *Cell Microencapsulation by Droplet Microfluidic Templating.* Macromolecular Chemistry and Physics, 2017. **218**(2): p. 1600380.
22. Novak, R., et al., *Single-cell multiplex gene detection and sequencing with microfluidically generated agarose emulsions.* Angew Chem Int Ed Engl, 2011. **50**(2): p. 390-5.
23. Bhujbal, S.V., et al., *A novel multilayer immunoisolating encapsulation system overcoming protrusion of cells.* Sci Rep, 2014. **4**: p. 6856.
24. Teixeira, L.S., et al., *Enzyme-catalyzed crosslinkable hydrogels: emerging strategies for tissue engineering.* Biomaterials, 2012. **33**(5): p. 1281-90.
25. Henke, S., et al., *Enzymatic Crosslinking of Polymer Conjugates is Superior over Ionic or UV Crosslinking for the On-Chip Production of Cell-Laden Microgels.* Macromol Biosci, 2016. **16**(10): p. 1524-1532.

26. Yung, C.W., et al., *Transglutaminase crosslinked gelatin as a tissue engineering scaffold.* J Biomed Mater Res A, 2007. **83**(4): p. 1039-46.
27. Ahmed, T.A., E.V. Dare, and M. Hincke, *Fibrin: a versatile scaffold for tissue engineering applications.* Tissue Eng Part B Rev, 2008. **14**(2): p. 199-215.
28. Jin, R., et al., *Enzyme-mediated fast in situ formation of hydrogels from dextran-tyramine conjugates.* Biomaterials, 2007. **28**(18): p. 2791-800.
29. Wennink, J.W.H., et al., *Injectable Hydrogels by Enzymatic Co-Crosslinking of Dextran and Hyaluronic Acid Tyramine Conjugates.* Macromolecular Symposia, 2011. **309-310**(1): p. 213-221.
30. Both, S.K., et al., *A rapid and efficient method for expansion of human mesenchymal stem cells.* Tissue Eng, 2007. **13**(1): p. 3-9.
31. Aikawa, T., et al., *Spherical phospholipid polymer hydrogels for cell encapsulation prepared with a flow-focusing microfluidic channel device.* Langmuir, 2012. **28**(4): p. 2145-50.
32. Liu, K., et al., *Generation of disk-like hydrogel beads for cell encapsulation and manipulation using a droplet-based microfluidic device.* Microfluidics and Nanofluidics, 2012. **13**(5): p. 761-767.
33. Posch, H.E. and O.S. Wolfbeis, *Optical Sensor for Hydrogen-Peroxide.* Mikrochimica Acta, 1989. **1**(1-2): p. 41-50.
34. Rossow, T., et al., *Controlled synthesis of cell-laden microgels by radical-free gelation in droplet microfluidics.* Journal of the American Chemical Society, 2012. **134**(10): p. 4983-9.
35. Lienemann, P.S., et al., *Single cell-laden protease-sensitive microniches for long-term culture in 3D.* Lab on a Chip, 2017. **17**(4): p. 727-737.
36. Duan, J., et al., *Irreversible cellular senescence induced by prolonged exposure to H2O2 involves DNA-damage-and-repair genes and telomere shortening.* Int J Biochem Cell Biol, 2005. **37**(7): p. 1407-20.
37. Mohanty, J.G., et al., *A highly sensitive fluorescent micro-assay of H2O2 release from activated human leukocytes using a dihydroxyphenoxazine derivative.* Journal of Immunological Methods, 1997. **202**(2): p. 133-141.
38. Collins, D.J., et al., *The Poisson distribution and beyond: methods for microfluidic droplet production and single cell encapsulation.* Lab on a Chip, 2015. **15**(17): p. 3439-59.
39. Zou, L., et al., *Effect of hyaluronan on osteogenic differentiation of porcine bone marrow stromal cells in vitro.* J Orthop Res, 2008. **26**(5): p. 713-20.
40. Chen, M., et al., *Improvement of Distribution and Osteogenic Differentiation of Human Mesenchymal Stem Cells by Hyaluronic Acid and beta-Tricalcium Phosphate-Coated Polymeric Scaffold In Vitro.* Biores Open Access, 2015. **4**(1): p. 363-73.

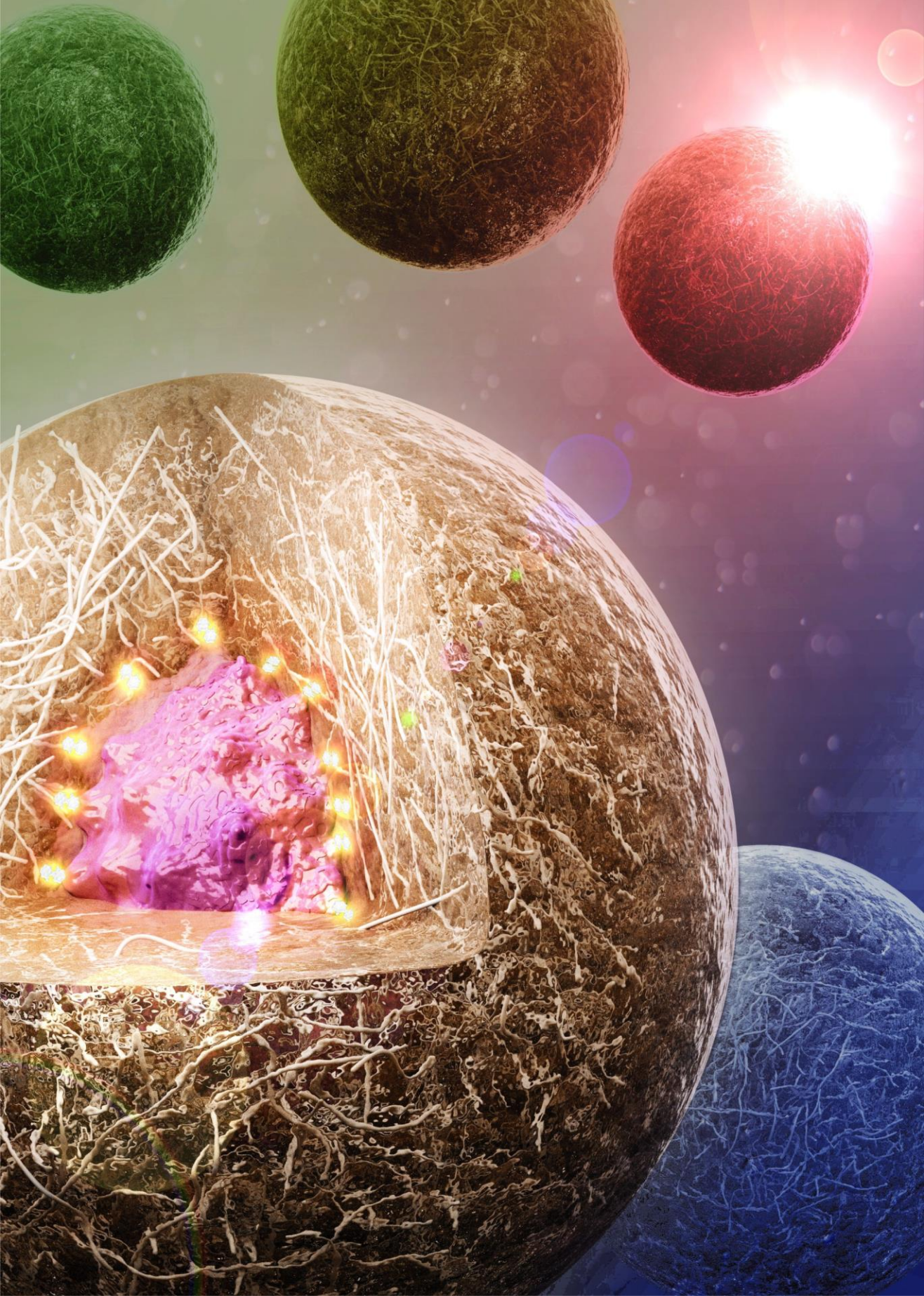

4

Direct On-cell Crosslinked Hydrogel Microniches with On-demand Tunable Stiffness to Program Single Stem Cell Fate

Hydrogels yield unprecedented control over cell culture by offering user-defined microenvironments. Tuning hydrogel characteristics such as the biomechanical properties effectively controls cell behavior via cell-material interactions. Yet, technologies to controllably convey biomechanical cues between biomaterials and cells have remained scarce. State-of-the-art 3D culture platforms are often static and rely nearly exclusively on RGD-based interactions. This limitation has hampered the unraveling and utilization of mechanotransduction pathways that, amongst others, underlie the stiffness-induced lineage commitment of stem cells. In this study, we introduce a novel bio-inspired technology called 'Direct On-cell CrosslinKing' (DOCKING) that directly and covalently tethers biomaterials onto cell membranes using a universal and cytocompatible enzymatic crosslinking reaction between polymers and cellular proteins. We reveal that DOCKING technology readily supports the transduction of biomechanical cues towards 3D encapsulated cells in a unique RGD-independent manner. By leveraging advanced droplet microfluidics, we achieve the long-term culture of individual stem cells within on-cell tethered hydrogel microniches. Using cytocompatible enzymatic post-curing, the microgel can be stiffened on demand within a physiological relevant range (~5-50 kPa) to control stem cell lineage commitment. Using on-demand stiffening, we reveal that early-stage biomechanical stimuli are crucial to program long-term stem cell fate. Single cell DOCKING thus readily supports the investigation of stem cell lineage commitment dynamics in 3D microniches with unprecedented temporal control and resolution.

Tom Kamperman, João Crispim, Sieger Henke, Wooje Lee, Herman Offerhaus, Martin Neubauer, Andreas Fery, Piet Dijkstra, Marcel Karperien, and Jeroen Leijten**

** shared senior authorship.*

Contribution TK: conception, experimental design, experimental performance, and manuscript writing.

Submitted

4.1 Introduction

A cell's behavior is intimately controlled through continuous interactions with its microenvironment. In fact, the biochemical and biophysical (i.e. biomechanical) cues that cells are exposed to, are essential for their survival and function.[1] For example, (stem) cells sense microelasticity by deforming themselves and the extracellular matrix, and respond to these stimuli via mechanotransduction pathways that control migration, proliferation, apoptosis, metabolism, and differentiation.[2, 3] Mechanotransduction is canonically mediated through transmembrane cell adhesion molecules (CAM; e.g. integrins, cadherins, and selectins), and transmitted through the intracellular actinomyosin cytoskeleton.[4]

To recapitulate these biological events in engineered tissues, biomaterials have typically been endowed with cell adhesive moieties that specifically bind to these CAMs. In particular, the integrin binding tripeptide arginine-glycine-aspartic acid (RGD) has been widely explored to this end.[5] Other, less frequently explored strategies, have been based on modifying biomaterials with, amongst others, CAM binding antibodies[6] or homing-CAM (CD44) binding hyaluronic acids.[7] However, none of these strategies explored the covalent coupling of cells and extracellular matrix. This is surprising, as covalent enzymatic coupling is common in nature. For example, the enzyme tissue transglutaminase (tTG) is able to stabilize extracellular matrix proteins through covalent coupling and supports cell adhesion in a RGD-independent manner via complexation with fibronectin, thereby playing a major role in wound healing.[8-10] Although enzymatic crosslinking has been harnessed to endow native tissues and biomaterials with biofunctional moieties such as RGD-type peptides,[11, 12] it has never been explored as a biomimetic approach to covalently couple biomaterials directly onto cells.

We hypothesized that tethering a non-adhesive biomaterial directly onto cells using a cytocompatible enzymatic crosslinking approach would readily support cell/biomaterial mechanotransduction in a novel, unique, and RGD-independent manner. As tTG-mediated cell adhesion not exclusively acts through transamidation (i.e. crosslinking), but also involves ternary complexation with integrins and fibronectin,[8-10] we opted for a highly specific enzymatic crosslinking mechanism based on tyrosine coupling, which is known to stabilize proteins in native tissues.[13] Tyrosines are abundantly present in the extracellular domains of transmembrane proteins[14] and can be coupled to other phenolic moieties using a cytocompatible enzymatic crosslinking reaction.[15] This bio-inspired crosslinking mechanism has been proven successful in tyramide signal amplification[16], peroxidase-mediated proteomic mapping strategies within cells,[17] and tissue engineering strategies,[18, 19] but has not yet been applied for the direct tethering of biomaterials onto living cells.

In this work, we set out to exploit a tyramine-functionalized polymer that could be simultaneously (i) enzymatically crosslinked to form a hydrogel and (ii) enzymatically co-crosslinked with the tyrosines of the cellular membrane. We then investigated whether this 'Direct On-cell CrosslinKing' (DOCKING) technology would enable the

mechanotransduction between cells and biomaterials in a novel RGD-independent manner. As a proof-of-concept, we leveraged an advanced microfluidic system to encapsulate individual mesenchymal stem cells (MSCs) in enzymatically crosslinked microgels. Through on-demand microgel stiffening via *in situ* enzymatic post-curing, we could program the lineage commitment of microencapsulated stem cells, which strongly suggested DOCKING-mediated mechanotransduction (**Figure 4.1**).

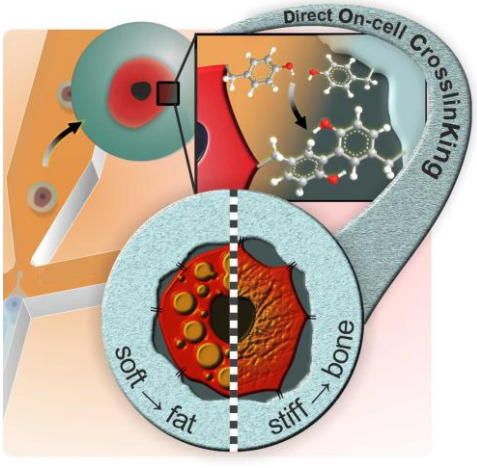

Figure 4.1. Schematic representation of 'Direct On-cell CrosslinKing' (DOCKING) in combination with droplet microfluidics to program the fate of 3D microencapsulated single stem cells. Individual stem cells can be encapsulated into microdroplets that contain tyramine-functionalized polymer (e.g. dextran-tyramine). Enzymatic crosslinking of phenolic tyramine moieties results in the formation of a stable microgel that is covalently bound to phenolic tyrosine proteins on the cell surface. Tuning the microgel's biomechanical properties can steer the fate of stem cells during multilineage differentiation.

4.2 Materials and Methods

4.2.1 Materials

Dextran (MW 15-25 kg/mol – M_n 16 kg/mol) was functionalized with tyramine, as previously described.[20] The resulting dextran-tyramine (Dex-TA) contained ~15 tyramine moieties per 100 repetitive monosaccharide units. Horseradish peroxidase (HRP, type VI), hydrogen peroxide (H_2O_2; with inhibitor), tyramine, tyrosine, fetal bovine serum (FBS), ascorbic acid, iodixanol (OptiPrep), insulin (human), 3-Isobutyl-1-methylxanthine (IBMX), indomethacin, dexamethasone, β-glycerol phosphate disodium salt pentahydrate (β-GP), Calcein AM, ethidium homodimer-1 (EthD-1), Thiazolyl Blue Tetrazolium Bromide (MTT), dextran-FITC (10, 40, 70, 150 kDa), Oil Red O, Alizarin Red S, buffered formalin, Triton X-100, and all other solvents were purchased from Sigma-Aldrich. Spin filter columns were purchased from Millipore. Cell strainers were purchased from Corning. Tyramide-AlexaFluor647 (AF647) and 4',6-diamidino-2-phenylindole (DAPI) were purchased from Thermo Scientific. Phosphate-buffered saline

(PBS) was purchased from Lonza. Minimal Essential Medium α with nucleosides (αMEM), Penicillin and Streptomycin, GlutaMAX, and trypsin-EDTA were purchased from Gibco. Basic fibroblast growth factor (ISOKine bFGF / FGF2) was purchased from Neuromics. Phalloidin-AF488 was purchased from Molecular Probes. Catalase (from bovine liver) was purchased from Wako. Polydimethylsiloxane (PDMS, Sylgard 184) was purchased from Dow Corning. Aquapel was purchased from Vulcavite. Pico-Surf 1 in Novec 7500 Engineered Fluid and Pico-Break 1 were purchased from Dolomite. Surfactant-free fluorocarbon oil (Novec 7500 Engineered Fluid) was kindly provided by the BIOS Lab-on-a-Chip group. Gastight syringes (Hamilton), fluorinated ethylene propylene tubing (FEP, inner diameter 250 µm, DuPont) and connectors were purchased from IDEX Health and Science. Low pressure syringe pumps (neMESYS) were purchased from Cetoni.

4.2.2 Cell Isolation and Expansion

Human mesenchymal stem cells (MSCs) were isolated from fresh bone marrow samples and cultured as previously described.[21] The use of patient material was approved by the local ethical committee of the Medisch Spectrum Twente and informed written consent was obtained for all samples. In short, nucleated cells in the bone marrow aspirates were counted, seeded in tissue culture flasks at a density of 500,000 cells/cm² and cultured in MSC proliferation medium, consisting of 10% (v/v) FBS, 100 U/ml Penicillin and 100 µg/ml Streptomycin, 1% (v/v) GlutaMAX, 0.2 mM ascorbic acid, and 1 ng/ml bFGF (added fresh) in αMEM. When cells reached near confluence, the cells were detached using 0.25% (v/v) Trypsin-EDTA at 37 °C and subsequently subcultured or used for experimentation.

4.2.3 Phenolic Crosslinking

To demonstrate enzymatic tyramine-tyrosine crosslinking, saturated tyramine and tyrosine solutions were prepared by overnight stirring 2.5 g/l in H_2O and subsequent filtration (0.22 µm). Saturated solutions were sequentially mixed with 44 U/ml HRP and 0.1% (w/v) H_2O_2 containing H_2O in a 1:1 ratio, resulting in final HRP and H_2O_2 concentrations of 22 U/ml and 0.05% (w/v), respectively. After 1 hour incubation on a roller mixer, the product was filtered using a spin filter column with 3 kDa molecular weight cut-off to remove the HRP, and analyzed using positive electron spray ionization mass spectrometry (Waters Micromass). Dex-TA bulk gel formation was achieved by mixing 10% (w/v) Dex-TA, 44 U/ml HRP, and 0.06% (w/v) H_2O_2 in PBS. Gelation was confirmed using the vial tilting method. To demonstrate direct on-cell enzymatic crosslinking of phenolic moieties, mesenchymal stem cells (MSCs) were fluorescently labeled with tyramide-AF647 by incubation with 4 U/ml HRP and 0.06% (w/v) H_2O_2 in PBS. Enzymatic crosslinking of MSCs onto Dex-TA hydrogel substrates was demonstrated by seeding formalin-fixed MSCs on a Dex-TA hydrogel substrate, inducing crosslinking by adding HRP and H_2O_2 containing PBS, and subsequently washing the substrate with PBS. For all phenolic crosslinking experiments, H_2O instead of H_2O_2 was used as a negative control.

4.2.4 Microgel Production and Culture

All microfluidic chips were manufactured from PDMS and glass using standard soft lithography techniques. The droplet generator and H_2O_2 diffusion-based crosslinking chips were fabricated with ~25 µm, and ~100 µm high channels, respectively. Aquapel was introduced in the chips before usage to ensure channel wall hydrophobicity. Using FEP tubing, chips were connected to each other and to gastight syringes, which were controlled by low-pressure syringe pumps. Hydrogel precursor solution contained 10% Dex-TA, 44 U/ml HRP, and 8% OptiPrep (i.e. to obtain ρ = 1.05 g/l) in PBS and was emulsified in 2% (w/w) Pico-Surf 1 containing Novec 7500 Engineered Fluid surfactant containing oil at a 1:6 (hydrogel:oil) flow ratio. To produce cell-laden microgels, detached cells (passage 2 to 5) were washed with medium, flown through a 40 µm cell strainer, and suspended in the hydrogel precursor solution at a concentration of 10^7 cells per ml. The cell-laden hydrogel precursor solution was loaded into an ice-cooled gastight syringe where it was gently agitated every ten minutes using a 2 mm long magnetic stirring bar. The microemulsion was broken by washing three times with surfactant-free fluorocarbon oil and subsequent supplementation of Pico-Break 1 in the presence of serum containing proliferation medium. Single-cell-laden microgels were cultured in MSC proliferation medium, MSC adipogenic differentiation medium, consisting of 10% FBS, 100 U/ml Penicillin and 100 µg/ml Streptomycin, 1% GlutaMAX, 0.2 mM ascorbic acid, 10 mg/l insulin, 0.5 mM IBMX, 200 µM indomethacin, and 1 µM dexamethasone (added fresh), MSC osteogenic differentiation medium, consisting of 10% FBS, 100 U/ml Penicillin and 100 µg/ml Streptomycin, 1% GlutaMAX, 0.2 mM ascorbic acid, 10 nM dexamethasone (added fresh), and 10 mM β-GP (added fresh) in αMEM, or a 1:1 mixture of adipogenic and osteogenic medium, which were refreshed three times per week. As a negative control, encapsulated MSCs were also cultured in MSC proliferation medium substituted with 10 nM β-GP. To stiffen microgels *in situ*, they were incubated 30 minutes with 44 U/ml HRP, after which H_2O_2 was added to a final concentration of 0.03% (w/v). After 90 s, the enzymatic post-cure was terminated by adding bovine catalase to a final concentration of 6 kU, which immediately consumed all remaining H_2O_2 through a competitive enzymatic reaction.[22]

4.2.5 Characterization of (Cell-laden) Microgels

On-chip droplets and microgels were visualized using a stereomicroscope set-up (Nikon SMZ800 equipped with Leica DFC300 FX camera). The position of cells in microdroplets or microgels was analyzed using ImageJ software. Microgels were imaged using phase contrast microscopy and the encapsulation and size distributions of cells and microgels were measured using Matlab software. Microgels were mechanically characterized using atomic force microscopy (JPK NanoWizard) combined with inverted optical microscopy (Zeiss Axio Observer Z1). Indentation measurements were performed in PBS using a cantilever (spring constant 0.151 N/m) with a glass colloidal probe (radius = 18.55 µm) attached to the tip. To extract the elastic modulus of the beads from the obtained force-deformation curves, the data was fitted assuming the Hertz model for the deformation of two spheres in contact. The mathematical expression is given below, with

F being the applied force, d deformation, E and R the relative Young's modulus and radius, respectively.

$$F = \frac{4}{3} E\, d^{\frac{3}{2}} \sqrt{R}$$

E and R are given as follows, with ν being Poisson's ratio (assumed to equal 0.5 for our samples) and the indices referring to the two spheres in contact.

$$\frac{1}{E} = \frac{1 - \nu_1^2}{E_1} + \frac{1 - \nu_2^2}{E_2}$$

$$\frac{1}{R} = \frac{1}{R_1} + \frac{1}{R_2}$$

To analyze permeability, microgels they were incubated with FITC-labeled dextran with molecular weights ranging from 10 to 150 kDa for six days, after which the fluorescent intensities across the microgels were measured using fluorescent confocal imaging (Zeiss LSM 510) and quantified using ImageJ software. A relative permeated intensity of 0.1 was arbitrarily chosen as the molecular weight cut-off (MWCO). Viability and metabolic activity of cells was analyzed by staining with 2 µM calcein AM (live), 4 µM EthD-1 (dead), and 0.5 g/l MTT (metabolically active) in PBS and visualization using brightfield and fluorescence microscopy (EVOS FL). For focused ion beam and scanning electron microscopy (FIB/SEM) samples were prepared and imaged as previously described.[23] For additional analyses, cell-laden microgels were first washed with PBS and fixated using 10% buffered formalin.

Adipogenic differentiation was analyzed by staining samples with a filtered (0.45 µm) 1.8 g/l Oil Red O in a 2-propanol/PBS mixture (6:4), visualizing using brightfield microscopy, and quantifying the per-cell intensity of the inverted blue color channel using ImageJ software. Osteogenic differentiation was analyzed by staining samples with a filtered (0.45 µm) 20 g/l Alizarin Red S in saline H_2O, visualizing using fluorescence microscopy, and quantifying the per-cell fluorescent intensity using ImageJ software. Label-free hyperspectral coherent anti-Stokes Raman (CARS) and spontaneous Raman microscopy were performed using in-house build setups, as previously described.[24, 25] For fluorescence confocal microscopy (Nikon A1+), samples were permeabilized using 0.1% Triton X-100 and subsequently stained with 2.5 U/ml phalloidin-AF488, 1 µg/ml DAPI, and 4 µM EthD-1 to stain F-actin, nuclei, and Dex-TA, respectively.

4.2.6 Statistics

The position of cells was determined in ≥35 droplets/microgels and reported as the average relative position (0: center, 1: edge) ± standard deviation. The encapsulated cell fraction was determined by analyzing >1200 microgels. Size distributions were obtained by measuring the diameters of >250 MSCs and >500 microgels. Linear regression analyses and AVOVA with Tukey's post hoc tests to analyze statistical significance were performed using OriginPro software.

4.3 Results and Discussion

4.3.1 Enzymatic Crosslinking of Phenolic Moieties Enables Simultaneous Gelation and On-cell Crosslinking of Polymers

We set out to exploit a biomaterial that could simultaneously polymerize and covalently bind to the plasma membrane of cells using a single facile crosslinking reaction. Inspired by nature and our previous work on self-attaching hydrogels,[18] we selected an enzymatic crosslinking strategy based on phenolic moieties for this purpose. Polyphenols can be formed by crosslinking the aromatic rings via C-C and C-O coupling using HRP as a catalyst and hydrogen peroxide (H_2O_2) as an oxidizer (**Figure 4.2a**). To demonstrate that tyramine can be crosslinked with itself (i.e. for gelation), as well as with tyrosine (i.e. for cell adhesion), tyramine and tyrosine were reacted in solution using HRP and H_2O_2. Electrospray ionization mass spectrometry confirmed the presence of uncoupled tyramine and tyrosine in the unreacted sample (i.e. without H_2O_2) and revealed tyramine-tyramine and tyramine-tyrosine products in the reacted sample (i.e. with H_2O_2) (**Figure 4.2b**).

Phenolic crosslinking between tyramine-functionalized molecules and cellular tyrosines was demonstrated by successfully labeling MSCs with fluorescently labeled tyramine (i.e. tyramide-AF647) using HRP and H_2O_2 (**Figure 4.2c**). Importantly, the staining remained present even after extensive washing, which suggested covalent coupling of the label to the cells rather than fouling due to precipitation. We leveraged this phenolic crosslinking strategy to establish DOCKING of biomaterials. To this end, we synthesized an injectable biomaterial that could enzymatically couple directly onto cells' membranes by chemically adding tyramine residues to a dextran, which is a cytocompatible and cell-resistant polymer.[26-28] Dextran-tyramine (Dex-TA) was synthesized as previously described.[20] HRP-mediated crosslinking of Dex-TA resulted in the formation of a hydrogel via di-tyramine formation (**Figure 4.2d**).

To demonstrate the direct coupling of Dex-TA to cells via polymerization of phenolic moieties, formalin-fixed MSCs were seeded onto preformed Dex-TA hydrogel sheets, after which they were exposed to a second enzymatic crosslinking reaction (i.e. post-cure). Enzymatic post-curing securely trapped the cells onto the intrinsically cell-resistant dextran-based hydrogel; vigorous washing did not remove the cells from the hydrogel's surface. In contrast, seeding fixated MSC's in the absence of an enzymatic post-cure resulted in a complete failure to trap any MSC. This strongly suggested the formation of tyramine-tyrosine bonds between the cells and the Dex-TA during enzymatic crosslinking (**Figure 4.2e**). The fact that cell-polymer and polymer-polymer crosslinks could be *in situ* formed during the same cytocompatible enzyme-based crosslinking reaction, primed Dex-TA as an ideal injectable material for covalently coupling 3D hydrogel microniches around and onto cells via DOCKING (**Figure 4.2f**).

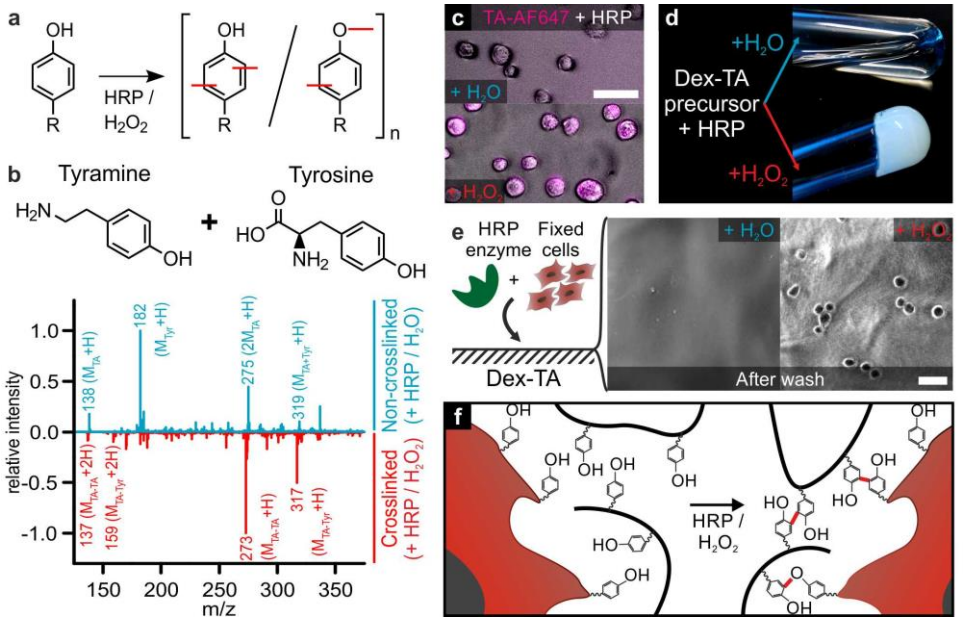

Figure 4.2. Enzymatic crosslinking of phenolic moieties for dextran gelation and cell adhesion. **(a)** Phenolic moieties can be enzymatically crosslinked using horseradish peroxidase and H_2O_2 via the formation of C-C and C-O bonds. **(b)** Electrospray ionization mass spectrometry confirmed the enzymatic crosslinking (red peaks) of tyramine to tyramine ($M_{TA\text{-}TA}$+H: 273, $M_{TA\text{-}TA}$+2H: 137), tyramine to tyrosine ($M_{TA\text{-}Tyr}$+H: 317, $M_{TA\text{-}Tyr}$+2H: 159). The enzyme-based crosslinking could also be leveraged to **(c)** couple fluorescently-labeled tyramine (TA-AF647) directly onto cells, **(d)** gel tyramine-functionalized dextran (Dex-TA), and **(e)** bind cells to a Dex-TA hydrogel substrate. **(f)** Consequently, *in situ* crosslinking of a cell embedded in Dex-TA hydrogel precursor would presumably result in the direct on-cell crosslinking (DOCKING) and gelation of dextran via the coupling of phenolic residues on the cell (i.e. tyrosine) and the dextran (i.e. tyramine). Scale bars: 50 µm.

4.3.2 DOCKING Supports the Production of 3D Single-cell-laden Hydrogel Microniches

To investigate if DOCKING could support covalent cell/biomaterial coupling in 3D, we encapsulated individual MSCs in Dex-TA microgels. To this end, we leveraged an advanced microfluidic encapsulation platform that we have recently developed.[29] This platform uniquely enables the long-term culture of single-cell-laden microgels by preventing cell escape; a typical problem within the microencapsulation field.[30] Specifically, Dex-TA polymer solution, HRP enzyme, and MSCs were emulsified with perfluorocarbon oil into monodisperse droplets of ~20 pl using a microfluidic droplet generator and subsequently crosslinked using a second microfluidic device via diffusion-based supplementation of H_2O_2 (**Figure 4.3a-d**). This resulted in the successful production of single-cell-laden Dex-TA microgels (**Figure 4.3e**). Analyzing the relative off-center cell position as a function of on-chip crosslinking delay time revealed that delayed gelation was instrumental to the centering of cells in microgels, as confirmed using confocal imaging (**Figure 4.3f,g**). In accordance to literature, the encapsulated cell

fraction closely followed the Poisson distribution (**Figure 4.3h**).[31] The retrieved cell-laden microgels (27±2 µm) were on average only 9 µm larger than the stem cells (18±4 µm) they encapsulated, thereby effectively providing single MSCs with a conformal 3D Dex-TA hydrogel coating with a thickness of less than 5 µm (**Figure 4.3i**). High resolution confocal imaging of single-cell-laden microgels suggested that parts of the cell membrane were physically attached to the microgel's interior surface(**Figure 4.3j**). This observation was corroborated by scanning electron microscopy images of microgels that were opened up using focused ion beam milling (i.e. FIB/SEM) (**Figure 4.3k**). Together, these data indicated that our DOCKING strategy had resulted in the crosslinking between cells and Dex-TA, which was most likely achieved via tyrosine-tyramine coupling.

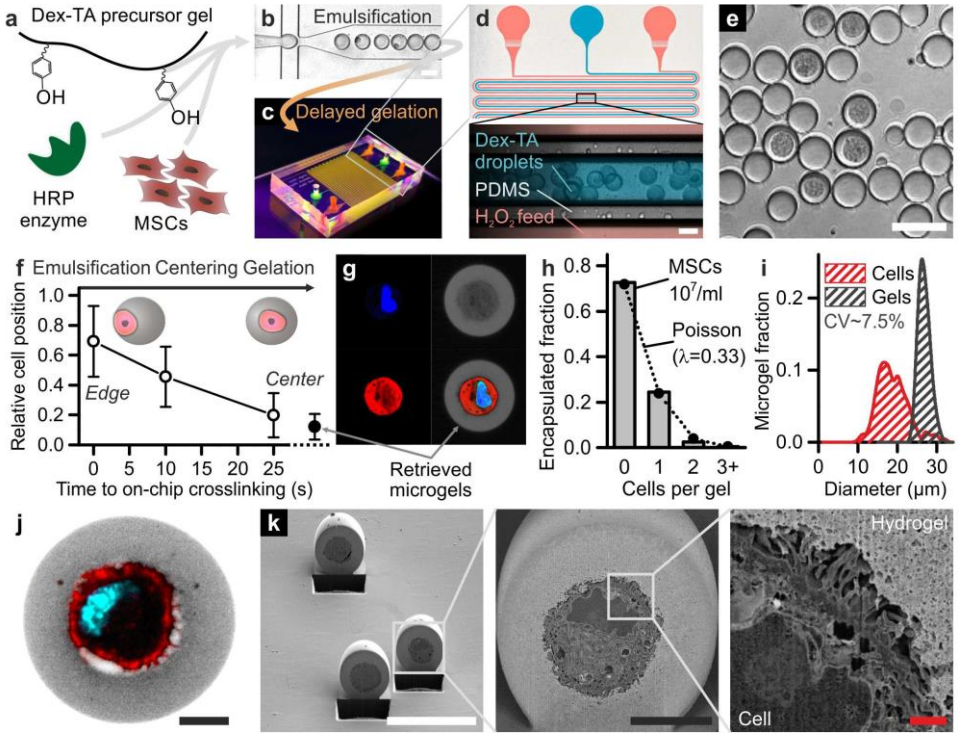

Figure 4.3. Producing 3D single stem cell microniches using the DOCKING technology. (a) Dex-TA, HRP, and MSCs were mixed, **(b)** emulsified using droplet microfluidics, and **(c,d)** reacted using a diffusion-based H_2O_2 supplementation platform into **(e)** single-cell-laden microgels. **(f,g)** Delayed gelation enabled centering of the cells within microgels. **(h)** The encapsulated cell fraction followed the Poisson distribution. **(i)** The Dex-TA microgels were characterized by a narrow size distribution and were just a few micrometers larger than the cells they encapsulated. **(j)** Confocal microscopy and **(k)** FIB/SEM strongly suggested that the DOCKING technology had resulted in the physical connection of MSCs to the Dex-TA microgel interior. White scale bars: 50 µm, black scale bars: 10 µm, red scale bars: 1 µm.

4.3.3 Single Stem Cell DOCKING of Soft and Stiff Microniches Enables Stiffness-imposed Multilineage Stem Cell Differentiation

We then aimed to tune the mechanical properties of the Dex-TA microgels. As biomaterial stiffness is correlated to its degree of enzymatic crosslinking,[32] microgel stiffness could be readily tuned by controlling the amount of crosslinker (i.e. H_2O_2). The diffusion-based microfluidic crosslinker platform allowed for high fidelity control over the amount of crosslinking by controlling the supplemented H_2O_2 concentration (**Figure S4.1**). Indeed, Dex-TA microgel stiffness linearly (R^2=0.99) correlated with the supplemented H_2O_2 concentration (**Figure 4.4a**). Following a titration experiment, we could robustly produce soft, medium, and stiff microgels with E-moduli of 6.7±0.4, 31.5±2.5, and 46.8±3.0 kPa, respectively. We validated that the changes in crosslinking density had a near-negligible effect on polymer network permeability by determining the molecular weight cut-off of soft, medium, and stiff microgels. (**Figure 4.4b**).

The short- and long-term effects of single cell DOCKING on cell survival were assessed using live/dead and metabolic assays. After 28 days of *in vitro* culture, approximately 90% of all encapsulated (i.e. soft, medium, and stiff) MSCs were viable and up to 70% of the MSCs were metabolically active, as indicated by negative ethidium homodimer-1 (EthD-1) and positive (i.e. reduced) MTT staining, respectively (**Figure 4.4c-e**). This proved that the microfluidic encapsulation procedure, the DOCKING procedure, and the different microenvironment stiffnesses were all cytocompatible and allowed for long-term cell survival.

We then investigated whether DOCKING enabled mechanotransduction between the microgels and the microencapsulated MSCs. As extracellular matrix stiffness has been proven to direct stem cell lineage commitment,[33] we assessed the multilineage differentiation capacity of individually encapsulated MSCs in the soft, medium, and stiff microgels. Culturing soft single-cell-laden Dex-TA microgels for 28 days in adipogenic differentiation medium resulted in their adipogenic differentiation, as indicated by MSCs with intracellular lipid vesicles accumulation (**Figure 4.4f**). This data was corroborated with label-free hyperspectral coherent anti-Stokes Raman spectroscopy (CARS) microscopy revealing a sharp peak at 2850 cm^{-1}, which is typical for lipids (**Figure 4.4g**).[34] Furthermore, long-term (28 days) culture of MSCs in stiff microgels in osteogenic differentiation medium resulted in the osteogenic differentiation MSCs, as determined by extracellular matrix calcification using histochemical analysis (**Figure 4.4h**). This data was corroborated with label-free hyperspectral spontaneous Raman microscopy revealing a sharp peak at 960 cm^{-1}, which is typical for phosphates and in particular hydroxyapatite (**Figure 4.4i**).[35]

The ability of DOCKING to convey mechanotransductional signals was further confirmed by validating that adipogenesis and osteogenesis of MSCs were intimately related with micromaterial stiffness. Specifically, the average lipid deposition within individual cells was significantly higher in soft than in medium and stiff microgels, which was corroborated by an adipogenic population fraction (i.e. ORO absorption > 50 a.u.)

of 64%, 35%, and 25% in soft, medium, and stiff microgels, respectively (**Figure 4.4j**). Moreover, the average quantity of deposited calcium phosphate matrix per individual cell was significantly higher in stiff than in medium and soft microgels, which was corroborated by an osteogenic population (i.e. AR fluorescence > 50 a.u.) of 0%, 44%, and 97% in soft, medium, and stiff microgels, respectively (**Figure 4.4k**). Together, our data thus indicated that DOCKING could facilitate the transduction of biomaterial mechanics onto stem cells to steer lineage commitment.

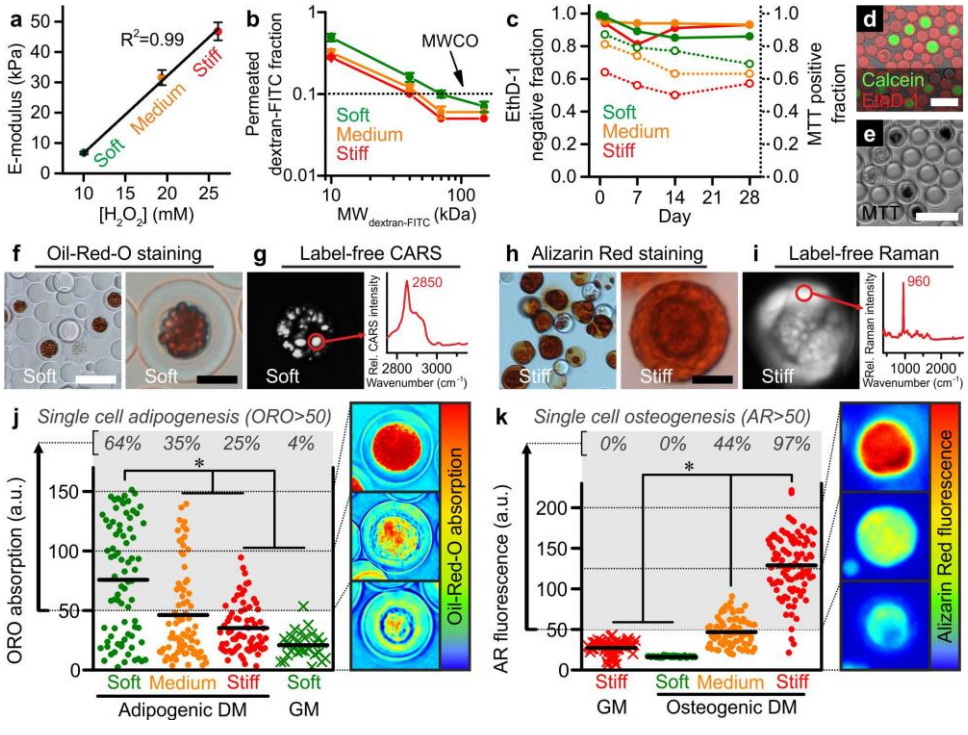

Figure 4.4. Single stem cell DOCKING of soft and stiff microniches enables stiffness-imposed multilineage stem cell differentiation. (a) The E-modulus of microgels could be tuned between approximately 5 and 50 kPa and linearly depended on the concentration of H_2O_2. **(b)** The molecular weight cut-off (MWCO; dotted line), and **(c)** the survived and the metabolically active cell fractions during 28 days of *in vitro* culture were determined using **(d)** live/dead and **(e)** MTT staining. In soft Dex-TA microgels, adipogenic differentiation after 4 weeks of culture in adipogenic differentiation medium (DM) was confirmed using **(f)** Oil-Red-O (ORO) staining and **(g)** label-free detection of lipids using hyperspectral coherent anti-Stokes Raman scattering (CARS; characteristic lipid peak at 2850 cm^{-1}). **(h)** In stiff Dex-TA microgels, osteogenic differentiation after 4 weeks of culture in osteogenic differentiation medium was confirmed using Alizarin Red (AR) staining and **(i)** label-free detection of calcium phosphates using hyperspectral spontaneous Raman (characteristic phosphate peak at 960 cm^{-1}). **(j)** Quantification of the per-cell adipogenic differentiation as a function of microgels stiffness and culture medium (GM: 'growth medium'). **(k)** Quantification of the per-cell osteogenic differentiation as a function of microgels stiffness and culture medium. * indicates 'significant with $p<0.01$'. White scale bars: 50 µm, black scale bars: 10 µm.

Given the profound differences in osteogenic differentiation and the near-identical MWCOs of the medium and stiff microgels, we reasoned that the biomechanical (i.e. stiffness) and not the biochemical (i.e. permeability) properties of the microgels were responsible for the stem cell differentiation. Although several studies have reported on stiffness-imposed stem cell differentiation in 3D microenvironments using RGD-dependent mechanisms,[3, 36-39] the osteogenic differentiation of MSCs within non-degradable and RGD-free hydrogels has not been demonstrated before. In fact, it has often been claimed that biomaterial degradation and RGD-integrin interaction are essential for mechanotransduction-mediated stem cell lineage commitment.[3, 36, 39] Our data advocates for the unique capacity of DOCKING to instruct cells via mechanotransduction through covalent cell/biomaterial interactions.

4.4.4 On-demand Stiffening On-cell Crosslinked Microgels Reveals Lineage Commitment Dynamics of 3D Microencapsulated Stem Cells

We then leveraged DOCKING to create 3D stem cell microniches with *in situ* (i.e. on-demand) tunable stiffness to further unravel the temporal role of mechanotransduction that acted through the covalent cell/biomaterial interactions. Specifically, we harnessed the free tyramines in soft microgels to enable their on-demand stiffening using a post-cure with HRP and H_2O_2, which is a novel strategy for this purpose. Nanoindentation measurements revealed that enzymatically post-curing soft microgels increased the stiffness of the microgels with an order of magnitude (from 6.7±0.4 to 46.1±3.9 kPa). Notably, the stiffness of on-demand stiffened microgels was not significantly different from that of as prepared stiff microgels (46.8±3.0 kPa) (**Figure 4.5a**). Furthermore, stiffening microgels did not change their MWCO, indicating that post-curing altered the microgels' biomechanical properties, but not their biochemical permeability (**Figure 4.5b**). Importantly, microgel stiffness could not spontaneously fluctuate during long-term culture, as mammalian cells do not produce dextranase[40] and Dex-TA has been proven to be hydrolytically resistant under similar conditions during several months.[41]

The on-demand stiffening of DOCKING-generated microgels was then used to investigate the dynamics of biomechanical-imposed stem cell lineage commitment. Specifically, single-cell-laden microgels were stiffened at various time points during their first week of *in vitro* culture (**Figure 4.5c**, top row). Lineage commitment was determined by analyzing adipogenic (i.e. intracellular lipids) and osteogenic (i.e. extracellular calcification) after two weeks of culture; the previous experiments demonstrated robust lineage specific matrix deposition within two weeks. On-demand stiffening DOCKING-generated single-cell-laden microgels cultured in osteogenic differentiation medium revealed that delayed stiffening significantly reduced osteogenic differentiation (**Figure 4.5d,e**). In fact, stiffening the microgels within the first week of culture was essential to induce osteogenic differentiation. These data were in line with a previous observation based on a RGD-depending 2D hydrogel system.[42] Our results thus suggested that, in 3D, osteogenic lineage commitment was dictated by biomaterial stiffness, but only during the first days after differentiation had been biochemically initiated (i.e. using differentiation medium). To verify this hypothesis, we validated that

osteogenic differentiation potential was not just diminished in soft microgels over time. To this end, we performed a (positive) control experiment where soft MSC-laden microgels were cultured for 7 days in growth medium, then *in situ* stiffened, followed by 2 weeks of culture in osteogenic differentiation medium (**Figure 4.5c**, bottom row). Calcified extracellular matrix deposition analysis revealed osteogenic differentiation, thereby confirming that soft microgels did not diminish MSCs' osteogenic potential when cultured in growth medium. Moreover, no osteogenic differentiation was observed in a (negative) control experiment where on-demand stiffened single-cell-laden microgels were cultured for two weeks in growth medium (**Figure 4.5d,e**). In short, these data confirmed that during the earliest phase of differentiation both biomechanical and biochemical stimuli are essential to commit stem cells to the osteogenic lineage.

Conventional *in vitro* differentiation of stem cells is achieved using media that is optimized to commit stem cells into a single specific lineage, while minimizing their multilineage differentiation. In contrast, the *in vivo* biochemical microenvironment often offers stem cells the possibility to differentiate into multiple lineages, while regional variances in stiffness may determine the stem cells' differentiation fate.[33] To assess the effects of DOCKING-mediated mechanotransduction on stem cell lineage commitment under more physiological conditions, we exposed on-demand stiffened single-cell-laden microgels to a bipotential (i.e. adipogenic + osteogenic) differentiation medium. Similar to on-demand stiffening in osteogenic medium, delayed post-curing microgels in bipotential differentiation medium on days 0, 1, 3, and 7 also resulted in a significant decrease in osteogenic differentiation and an increase in adipogenic differentiation (**Figure 4.5f-i**). Indeed, this confirmed that the encapsulation, DOCKING, and post-cure procedures had no detrimental effect on the multilineage differentiation potential of MSCs. Notably, MSCs committed even more rapidly to the osteogenic lineage in bipotential differentiation medium as compared to osteogenic differentiation medium. These data confirmed the pivotal importance of early-phase mechanotransduction on stem cell lineage commitment within biochemically complex 3D microenvironments.

We then investigated whether continuous biochemical stimulation was essential to obtain complete differentiation of osteogenic-lineage-committed MSCs by exposing stiffened (do) single-cell-laden microgels for specific periods of time (i.e. part-time) to bipotential differentiation medium (**Figure 4.5j**). Histological staining of extracellular calcified matrix revealed that the continuous (i.e. long-term) presence of differentiation medium was essential to obtain complete osteogenic differentiation of the MSCs (**Figure 4.5k**). In contrast to biomechanical stimuli, biochemical stimuli appeared to play a crucial during both the short- and long-term lineage commitment of microencapsulated MSCs.

The osteogenic lineage commitment of microencapsulated MSCs can be captured in a schematic model by describing the cellular responses to short- and long-term stimuli as Boolean operators. Specifically, short-term osteogenic lineage commitment depended

on the paired positive input of mechanical (i.e. stiff yes/no) and chemical (i.e. differentiation medium yes/no) stimuli, which can thus be represented by a logic AND gate. Long-term osteogenic differentiation, or maturation, required short-term lineage commitment and a continued long-term chemical (i.e. differentiation medium) stimulus, which can thus be represented by a subsequent logic AND gate. We therefore postulated that osteogenic differentiation of 3D microencapsulated MSCs is represented by two mechanically- and chemically-triggered logic AND gates that are connected in a serial manner, as depicted in **Figure 4.5l**. This model advocates that MSCs possess a conditional long-term mechanical memory that is functional during the presence of the appropriate biochemical stimuli. Indeed, previous work on RGD-dependent 2D stem cell culture on *in situ* softening hydrogel substrates has postulated the existence of mechanical memory, which possibly acts through YAP/TAZ translocation.[43] Yet, a complete understanding of the biological pathways that underlie mechanical stem cell memory and its role in lineage decision has remained elusive. As DOCKING uniquely offers a dynamic, 3D, and RGD-independent culture platform, it is primed to provide novel insights in mechanotransduction pathways of (stem) cells with single cell resolution.

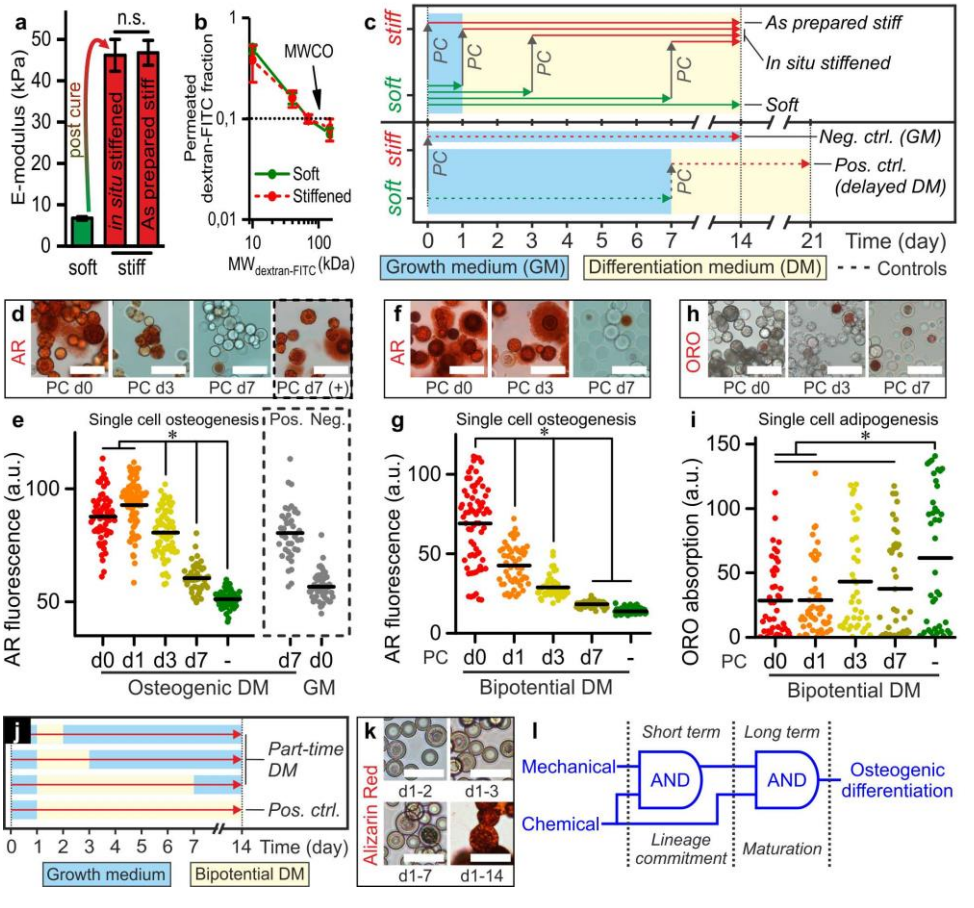

Figure 4.5. On-demand stiffening on-cell crosslinked microgels reveals lineage commitment dynamics of 3D microencapsulated stem cells. (a) Enzymatic post-curing enabled *in situ* (i.e. on-demand) stiffening of soft microgels. The E-modulus of post-cured (i.e. stiffened) microgels did not significantly differ from as prepared stiff microgels. **(b)** The permeability of stiffened microgels was similar to that of soft microgels, as indicated by comparable MWCOs (dotted line). **(c)** On-demand stiffening Dex-TA microgels on predefined time points was harnessed to study the underlying dynamics of stem cell lineage commitment. **(d-g)** This strategy revealed that short-term biomechanics steered long-term cell fate in the presence of bipotential differentiation medium (DM), where adipogenic and osteogenic differentiation were predisposed to late and early stiffened microgels, respectively. (**h,i**) Albeit delayed, a similar short-term lineage commitment was observed for *in situ* stiffened MSC-laden microgels in the presence of osteogenic differentiation medium. The osteogenic differentiation potential was maintained when soft microgels were cultured for 7 days in growth medium (GM; positive control). *In situ* stiffening did not result in osteogenic differentiation in the presence of growth medium (negative control). **(j,k)** Long-term biochemical stimulation (i.e. differentiation medium) was essential for osteogenic differentiation of MSCs in stiff microgels. **(l)** The osteogenic differentiation of MSCs could be described with Boolean logic using a model consisting of two AND gates in series that represent the short- and long-term cell responses as a function of mechanical and chemical stimuli. * indicates 'significant with $p<0.01$'. White scale bars: 50 μm.

4.4 Conclusion

In conclusion, we introduced 'Direct On-cell CrosslinKing' (DOCKING) technology to covalently tether polymers onto cells via the enzymatic coupling of phenolic moieties. Combining DOCKING technology with advanced droplet microfluidics readily supported the production of single-stem-cell-laden hydrogel microniches (i.e. microgels) that were compatible with long-term *in vitro* culture. Stem cell lineage commitment could be programmed by tuning the microgel stiffness, which underlined DOCKING's capability of enabling mechanotransduction via covalent crosslinks between the cell membrane and the biomaterial. A cytocompatible enzymatic post-curing procedure enabled the on-demand stiffening of cell-laden microgels. We harnessed these unique dynamic stem cell microniches to investigate the temporal aspects of stem cell differentiation in 3D on a single cell level. This has revealed the role of short- and long-term biochemical and biomechanical stimuli on the fate of 3D microencapsulated MSCs. Our DOCKING technology in combination with on-demand stiffening acts as a unique tool to further unravel the (dynamics of) biological mechanisms that underlie mechanotransduction of stem cells in 3D with unprecedented control and resolution.

4.5 Supplementary Information

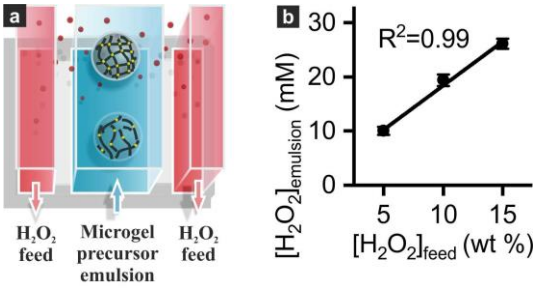

Figure S4.1. Microfluidic diffusion platform. (a) Schematic depiction of the microfluidic platform consisting of parallel microfluidic channels separated by semipermeable PDMS, which enables the diffusion-based supplementation of H_2O_2 to microgel precursor droplets. **(b)** The H_2O_2 concentration within droplets linearly (R^2 = 0.99) correlated to the H_2O_2 feed concentration.

To quantify H_2O_2, microemulsions were broken, immediately diluted 10^5 times with PBS, and mixed 1:1 with 100 µM Amplex Red (Sigma Aldrich) and 0.2 U/ml HRP in PBS. After 30 minutes incubation at room temperature, fluorescence intensities were measured using a plate reader (Victor X3, ex. 545/10 nm, em. 590/10 nm) and correlated to H_2O_2 concentrations using a standard curve.

References

1. Frisch, S.M. and H. Francis, *Disruption of epithelial cell-matrix interactions induces apoptosis.* J Cell Biol, 1994. **124**(4): p. 619-26.
2. Discher, D.E., P. Janmey, and Y.L. Wang, *Tissue cells feel and respond to the stiffness of their substrate.* Science, 2005. **310**(5751): p. 1139-43.
3. Huebsch, N., et al., *Harnessing traction-mediated manipulation of the cell/matrix interface to control stem-cell fate.* Nat Mater, 2010. **9**(6): p. 518-26.
4. Humphrey, J.D., E.R. Dufresne, and M.A. Schwartz, *Mechanotransduction and extracellular matrix homeostasis.* Nat Rev Mol Cell Biol, 2014. **15**(12): p. 802-12.
5. Hersel, U., C. Dahmen, and H. Kessler, *RGD modified polymers: biomaterials for stimulated cell adhesion and beyond.* Biomaterials, 2003. **24**(24): p. 4385-415.
6. Rafat, M., et al., *Dual functionalized PVA hydrogels that adhere endothelial cells synergistically.* Biomaterials, 2012. **33**(15): p. 3880-6.
7. Kim, Y. and S. Kumar, *CD44-mediated adhesion to hyaluronic acid contributes to mechanosensing and invasive motility.* Mol Cancer Res, 2014. **12**(10): p. 1416-29.
8. Griffin, M., R. Casadio, and C.M. Bergamini, *Transglutaminases: nature's biological glues.* Biochem J, 2002. **368**(Pt 2): p. 377-96.
9. Collighan, R.J. and M. Griffin, *Transglutaminase 2 cross-linking of matrix proteins: biological significance and medical applications.* Amino Acids, 2009. **36**(4): p. 659-70.
10. Zemskov, E.A., et al., *The role of tissue transglutaminase in cell-matrix interactions.* Front Biosci, 2006. **11**: p. 1057-76.
11. Ehrbar, M., et al., *Biomolecular hydrogels formed and degraded via site-specific enzymatic reactions.* Biomacromolecules, 2007. **8**(10): p. 3000-7.
12. Jones, M.E. and P.B. Messersmith, *Facile coupling of synthetic peptides and peptide-polymer conjugates to cartilage via transglutaminase enzyme.* Biomaterials, 2007. **28**(35): p. 5215-24.
13. Bailey, A.J., *The chemistry of natural enzyme-induced cross-links of proteins.* Amino Acids, 1991. **1**(3): p. 293-306.
14. Saidijam, M., S. Azizpour, and S.G. Patching, *Comprehensive analysis of the numbers, lengths and amino acid compositions of transmembrane helices in prokaryotic, eukaryotic and viral integral membrane proteins of high-resolution structure.* J Biomol Struct Dyn, 2017: p. 1-22.
15. Partlow, B.P., et al., *Dityrosine Cross-Linking in Designing Biomaterials.* ACS Biomaterials Science & Engineering, 2016. **2**(12): p. 2108-2121.
16. Schonhuber, W., et al., *Improved sensitivity of whole-cell hybridization by the combination of horseradish peroxidase-labeled oligonucleotides and tyramide signal amplification.* Appl Environ Microbiol, 1997. **63**(8): p. 3268-73.
17. Rhee, H.W., et al., *Proteomic mapping of mitochondria in living cells via spatially restricted enzymatic tagging.* Science, 2013. **339**(6125): p. 1328-31.
18. Moreira Teixeira, L.S., et al., *Self-attaching and cell-attracting in-situ forming dextran-tyramine conjugates hydrogels for arthroscopic cartilage repair.* Biomaterials, 2012. **33**(11): p. 3164-74.
19. Raia, N.R., et al., *Enzymatically crosslinked silk-hyaluronic acid hydrogels.* Biomaterials, 2017. **131**: p. 58-67.
20. Jin, R., et al., *Enzyme-mediated fast in situ formation of hydrogels from dextran-tyramine conjugates.* Biomaterials, 2007. **28**(18): p. 2791-800.
21. Both, S.K., et al., *A rapid and efficient method for expansion of human mesenchymal stem cells.* Tissue Eng, 2007. **13**(1): p. 3-9.
22. Kamperman, T., et al., *Nanoemulsion-induced enzymatic crosslinking of tyramine-functionalized polymer droplets.* Journal of Materials Chemistry B, 2017. **5**(25): p. 4835-4844.
23. Van Donselaar, E.G., et al., *Extremely thin layer plastification for dual-beam microscopy, an improved method to study cell surfaces and organelles of cultured cells (submitted)*. 2017, Utrecht University.
24. Garbacik, E.T., et al., *Rapid identification of heterogeneous mixture components with hyperspectral coherent anti-Stokes Raman scattering imaging.* Journal of Raman Spectroscopy, 2012. **43**(5): p. 651-655.
25. Kunstar, A., et al., *Recognizing different tissues in human fetal femur cartilage by label-free Raman microspectroscopy.* J Biomed Opt, 2012. **17**(11): p. 116012.

26. Cadee, J.A., et al., *In vivo biocompatibility of dextran-based hydrogels.* Journal of Biomedical Materials Research, 2000. **50**(3): p. 397-404.
27. De Groot, C.J., et al., *In vitro biocompatibility of biodegradable dextran-based hydrogels tested with human fibroblasts.* Biomaterials, 2001. **22**(11): p. 1197-203.
28. Massia, S.P., J. Stark, and D.S. Letbetter, *Surface-immobilized dextran limits cell adhesion and spreading.* Biomaterials, 2000. **21**(22): p. 2253-61.
29. Kamperman, T., et al., *Centering Single Cells in Microgels via Delayed Crosslinking Supports Long-Term 3D Culture by Preventing Cell Escape.* Small, 2017. **13**(22): p. 1603711-n/a.
30. Rossow, T., P.S. Lienemann, and D.J. Mooney, *Cell Microencapsulation by Droplet Microfluidic Templating.* Macromolecular Chemistry and Physics, 2017. **218**(2): p. 1600380.
31. Collins, D.J., et al., *The Poisson distribution and beyond: methods for microfluidic droplet production and single cell encapsulation.* Lab on a Chip, 2015. **15**(17): p. 3439-59.
32. Roberts, J.J., et al., *A comparative study of enzyme initiators for crosslinking phenol-functionalized hydrogels for cell encapsulation.* Biomater Res, 2016. **20**: p. 30.
33. Engler, A.J., et al., *Matrix elasticity directs stem cell lineage specification.* Cell, 2006. **126**(4): p. 677-89.
34. Masia, F., et al., *Quantitative chemical imaging and unsupervised analysis using hyperspectral coherent anti-Stokes Raman scattering microscopy.* Anal Chem, 2013. **85**(22): p. 10820-8.
35. Stewart, S., et al., *Trends in early mineralization of murine calvarial osteoblastic cultures: a Raman microscopic study.* Journal of Raman Spectroscopy, 2002. **33**(7): p. 536-543.
36. Khetan, S., et al., *Degradation-mediated cellular traction directs stem cell fate in covalently crosslinked three-dimensional hydrogels.* Nat Mater, 2013. **12**(5): p. 458-65.
37. Ma, Y., et al., *Artificial microniches for probing mesenchymal stem cell fate in 3D.* Biomater. Sci., 2014. **2**(11): p. 1661-1671.
38. Pek, Y.S., A.C. Wan, and J.Y. Ying, *The effect of matrix stiffness on mesenchymal stem cell differentiation in a 3D thixotropic gel.* Biomaterials, 2010. **31**(3): p. 385-91.
39. Parekh, S.H., et al., *Modulus-driven differentiation of marrow stromal cells in 3D scaffolds that is independent of myosin-based cytoskeletal tension.* Biomaterials, 2011. **32**(9): p. 2256-64.
40. Khalikova, E., P. Susi, and T. Korpela, *Microbial dextran-hydrolyzing enzymes: fundamentals and applications.* Microbiol Mol Biol Rev, 2005. **69**(2): p. 306-25.
41. Wennink, J.W.H., et al., *Injectable Hydrogels by Enzymatic Co-Crosslinking of Dextran and Hyaluronic Acid Tyramine Conjugates.* Macromolecular Symposia, 2011. **309-310**(1): p. 213-221.
42. Guvendiren, M. and J.A. Burdick, *Stiffening hydrogels to probe short- and long-term cellular responses to dynamic mechanics.* Nature Communications, 2012. **3**: p. 792.
43. Yang, C., et al., *Mechanical memory and dosing influence stem cell fate.* Nat Mater, 2014. **13**(6): p. 645-52.

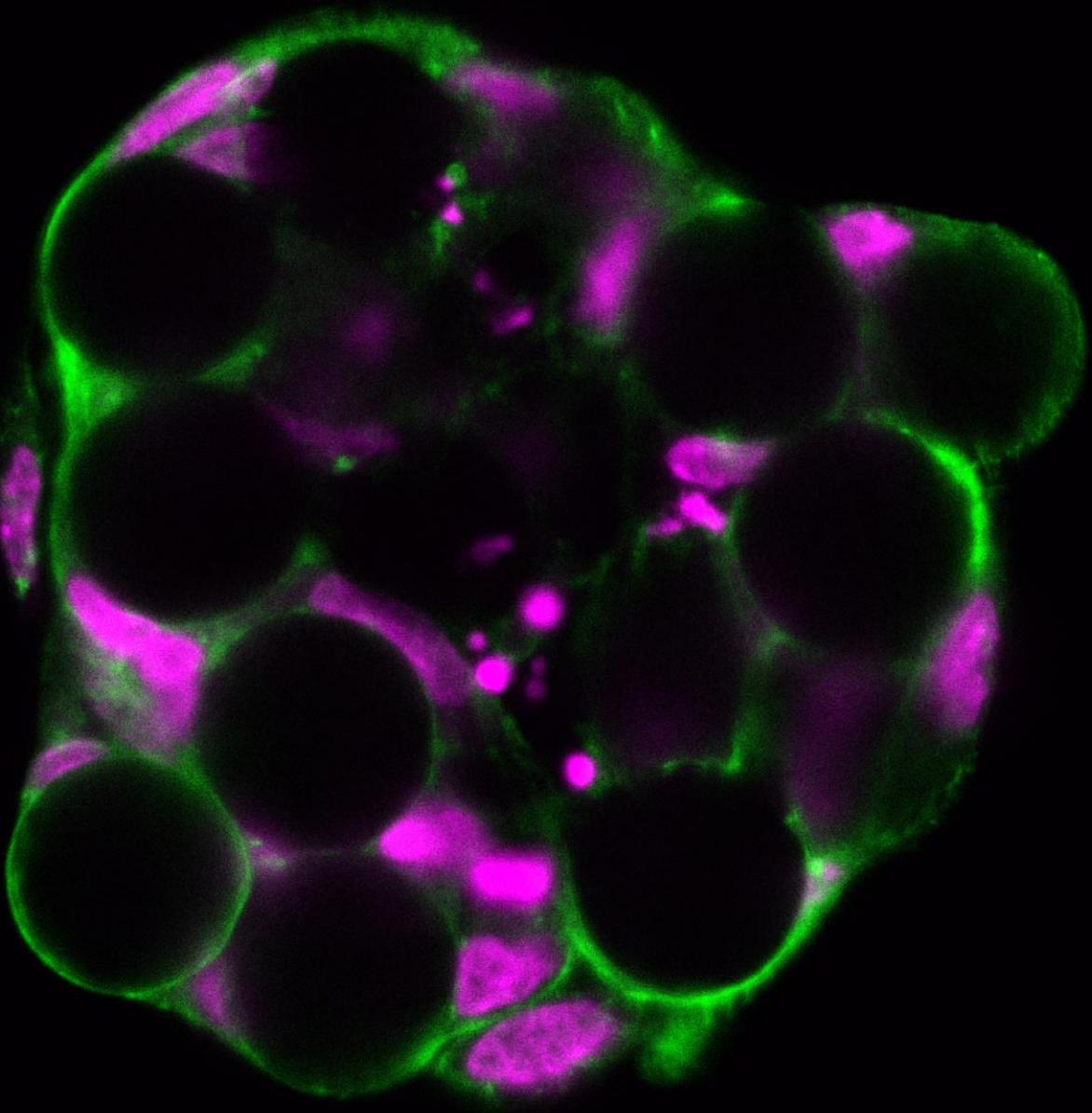

5

Smart Building Blocks for Modular Tissue Engineering Based on Sequential Desthiobiotin / Biotin Coupling

Modular tissue engineering enables the formation of 3D multiscale hierarchical tissues with high-resolution internal complexity that can act as functional replacements for damaged tissue and organs. This is typically accomplished by the assembly of building blocks composed of cells and/or (micro)materials (i.e. modules) into a larger engineered construct. However, the functionality of modular tissue constructs is limited by the current lack of smart building blocks. Indeed, current building blocks are designed as static elements that are not readily compatible with in situ biofunctionalization, which limits the spatiotemporal control over the engineered tissues. In this study, we introduce desthiobiotin/biotin displacement to engineer in situ tunable micrometer-sized hydrogels (microgels) that act as smart building blocks, thereby granting on-demand, reversible, and sequential spatiotemporal biochemical control over living modular tissues.

Tom Kamperman, Cindy Kelder, Michelle Koerselman, João Crispim, Jan Hendriks, Sieger Henke, Xandra de Peuter, Rong Wang, Piet Dijkstra, Marcel Karperien, and Jeroen Leijten**

** shared senior authorship.*

Contribution TK: conception, experimental design, experimental performance, and manuscript writing.

Submitted

5.1 Introduction

Conventional tissue engineering strategies are based on homogeneously combining cells with an isotropic supportive scaffold to form a substitute graft.[1-3] Although such top-down engineering results in grafts with clinically relevant sizes, they are often not effective in recapitulating the complex architecture of native tissues. Indeed, native tissues consist of repetitive functional modules that are organized into larger structures with a hierarchy that spans multiple length scales.[4, 5] This multiscale modularity is found throughout nature and is essential to combine multiple otherwise paradoxical biological functions (e.g. mechanical integrity, host integration, cell viability, and cell functioning) into a single construct. Inspired by nature, several modular, also referred to as bottom-up, tissue engineering strategies have been developed to enable the facile incorporation of multiscale modularity into man-made tissue constructs.[6-10] To produce a modular construct, functional subunits such as cell-, or drug-laden particles could be incorporated in the construct's precursor solution, thereby effectively creating a modular or hybrid precursor solution.[11-14] Alternatively, cells and/or microparticles can be self-assembled into larger modular tissue constructs by tuning their adhesive properties through exploiting, for example, electrostatic, supramolecular, or magnetic interactions.[15] The incorporation of micromaterials into artificial tissue constructs is an elegant approach to obtain clinical-sized grafts using fewer donor cells.[16-18] Furthermore, these constructs typically contain intrinsic porosity that could mitigate starvation-induced cell death by improving diffusion of nutrients and waste products and promoting vascularization.[17, 19, 20]

Modular tissue constructs can be biochemically and biomechanically tailored by combining various distinct functional building blocks via straightforward mixing and matching.[21] Growth factor-laden microcarriers can, for example, be integrated to stimulate maturation of the engineered tissue construct.[22] However, currently explored tissue engineering building blocks are limited to static non-responsive materials,[17, 18, 23, 24] which has prevented the development of dynamically tunable modular tissues. Importantly, native tissues are characterized by a dynamic nature. For example, tissue development is a multi-staged process that involves remodeling of the extracellular matrix.[25] Recapitulating such dynamicity in engineered tissues requires the temporal control over their biochemical composition. Although tissue engineers have recently started to integrate these complex functions into smart (i.e. instructive and responsive) biomaterials, their use has remained limited to bulk constructs that do not recapitulate the modular design of native tissues.[26-37] Creating smart building blocks from *in situ* tunable biomaterials is therefore expected to enable the incorporation of the dynamic nature as observed in native tissues into man-made tissue constructs via a facile modular tissue engineering approach.

In this study, we established the concept of smart microbuilding blocks to unlock the full potential of modular tissue engineering by enabling *in situ* spatiotemporal control over living constructs. Specifically, we aimed to develop hydrogel microparticles (i.e.

microgels) that could 1) self-assemble with cells into modular tissues and 2) allow for *in situ* inducible, reversible, and sequential presentation of instructive biochemical elements to temporarily control cell behavior (**Figure 5.1**). We hypothesize that the reversible nature of desthiobiotin/avidin complexation could be leveraged to this end. Desthiobiotin is a non-sulfur containing analog of biotin that also interacts with avidin, but with a substantially lower binding affinity than biotin ($K_{d,biotin}$~10^{-15} M vs $K_{d,desthiobiotin}$~10^{-13} M).[38] Consequently, desthiobiotin can be reversibly coupled to avidin and on-demand be replaced by biotin with a high level of specificity. This supramolecular displacement strategy has been proven effective for reversible labeling and affinity-based isolation of proteins.[39] Furthermore, it is fully cytocompatible, which is in contrast with photoresponsive strategies that typically rely on cytotoxic UV light.[31] Here, we pioneered desthiobiotin/biotin exchange as a novel strategy to create smart biomaterials. We leveraged this strategy to expand the modular tissue engineering toolbox by engineering smart building blocks that can readily grant man-made tissues with *in situ* tunable biochemical functions in a facile, cytocompatible, and highly specific manner.

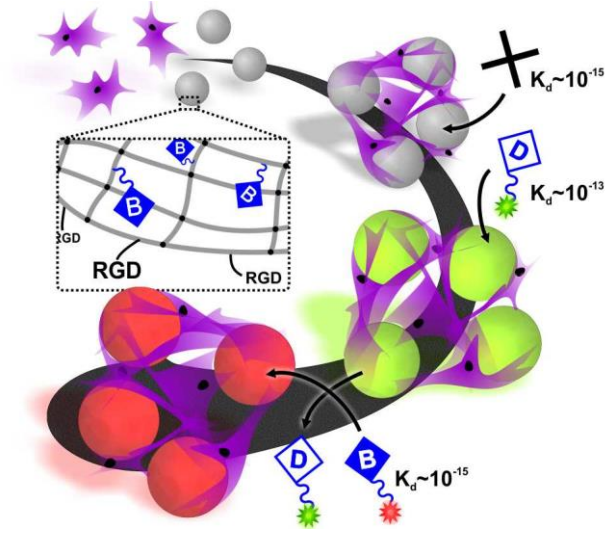

Figure 5.1. The concept of smart building blocks for engineering tunable 3D modular tissue constructs. The shell of biotinylated [B] dextran-based microgels are permanently functionalized with cell binding motives (RGD-type) to enable modular tissue engineering via the self-assembly of microgels (grey) and cells (magenta). The modular constructs can be further functionalized *in situ* via a two-step approach using tetravalent avidin [X] as the supramolecular linker between the microgels' free biotins and desthiobiotinylated [D] molecules of interest (green). Subsequently, the desthiobiotin can be displaced by biotinylated molecules of interest (red), thereby enabling on-demand biochemical tuning of the engineered modular tissue construct.

5.2 Materials and Methods

5.2.1 Materials

Dextran (Dex; MW 15 to 25 kg/mol – Mn 16 kg/mol; lyophilized before use), 4-nitrophenyl chloroformate (PNC; sublimated before use), LiCl (dried at 110 °C before use), tyramine (TA) anhydrous pyridine, anhydrous N,N-dimethylformamide (DMF), trifluoroacetic acid (TFA), sodium hydroxide (NaOH), N-Boc-1,4-butanediamine (NH_2-Boc), sodium bicarbonate ($NaHCO_3$), biotin-atto565, biotin-4-fluorescein (biotin-FITC), 6-aminofluorescein, horseradish peroxidase (HRP, type VI), hydrogen peroxide (H_2O_2; with inhibitor), fetal bovine serum (FBS), calcein AM, ethidium homodimer-1 (EthD-1), buffered formalin, Triton X-100, and all other solvents were purchased from Sigma-Aldrich. Succinimidyl 6-(biotinamido)hexanoate (biotin-LC-NHS) was purchase from ApexBio. N-hydroxysuccinimide-desthiobiotin (EZ-Link NHS-desthiobiotin) and 4',6-diamidino-2-phenylindole (DAPI) were purchased from Thermo Scientific. Phosphate-buffered saline (PBS) was purchased from Lonza. Minimal Essential Medium α with nucleosides (αMEM), Penicillin and Streptomycin, GlutaMAX, and trypsin-EDTA were purchased from Gibco. Basic fibroblast growth factor (ISOKine bFGF) was purchased from Neuromics. Phalloidin-AF647 was purchased from Molecular Probes. Polydimethylsiloxane (PDMS, Sylgard 184) was purchased from Dow Corning. Aquapel was purchased from Vulcavite. Pico-Surf 1 in Novec 7500 Engineered Fluid and Pico-Break 1 were purchased from Dolomite. Gastight syringes (Hamilton), fluorinated ethylene propylene tubing (FEP, inner diameter 250 µm, DuPont) and connectors were purchased from IDEX Health and Science. Low pressure syringe pumps (neMESYS) were purchased from Cetoni.

5.2.2 Dex-TA-biotin Synthesis and Characterization

First, dextran was functionalized with tyramine and 1,4-butanediamine, as previously described.[40, 41] In short, dextran was activated with PNC, which was subsequently substituted with tyramine and Boc-protected 1,4-butanediamine and, after using TFA and dialysis using a membrane with 3 kDa molecular weight cut-off, further functionalized with biotin by reacting the Dex-TA-NH_2 with a 20-fold excess of biotin-LC-NHS for at least 1 hour in 0.1 M bicarbonate buffer (pH ~ 8.5) (**Figure S5.1**, **Figure S5.2**). Dex-TA-biotin was then purified and concentrated using a spin filter column with 3 kDa molecular weight cut-off. The successful syntheses of Dex-PNC, Dex-TA-NH_2, and Dex-TA-biotin were confirmed using ^{1}H NMR (AVANCE III HD NanoBay 400 MHz, Bruker) in DMSO-d_6 or D_2O. The numbers of conjugated tyramine and butylamine moieties per 100 dextran anhydroglucose rings were determined by calculating the ratios of integrated signals from the dextran (δ 4.0 – 5.8 ppm) and the tyramine groups (δ 6.66 ppm and δ 6.98 ppm), and those of dextran and the the butylamine groups (δ 1.4 – 1.5 ppm), respectively. The number of conjugated biotin moieties per 100 dextran anhydroglucose rings was determined by calculating the ratio of integrated signals from the tyramine groups (δ 6.66 ppm and δ 6.98 ppm) and the coupled 6-aminocaproic spacer (δ 2.13).

5.2.3 Microgel Production and Characterization

All microfluidic chips were manufactured from PDMS and glass using standard soft lithography techniques. The microfluidic mixer, droplet generator, and H_2O_2 diffusion-based crosslinking chips were fabricated with ~100, ~25 µm, and ~100 µm high channels, respectively. Aquapel was introduced in the chips before usage to ensure channel wall hydrophobicity. Using FEP tubing, chips were connected to each other and to gastight syringes, which were controlled by low-pressure syringe pumps. All emulsions were produced using 2% (w/w) Pico-Surf 1 containing Novec 7500 Engineered Fluid. To generate hydrogel precursor microdroplets, PBS that contained 5% (w/v) Dex-TA-Biotin (~1 mM biotin) and 22 U/ml HRP in PBS, and PBS that contained 5% (w/v) Dex-TA (without biotin) and 22 U/ml HRP in PBS were combined in the microfluidic mixer and subsequently emulsified in the connected droplet generator using surfactant containing oil at a 1:6 flow ratio. The hydrogel precursor microemulsion was flown at a total rate of 14 µl/min through the connected diffusion platform, which was also fed with H_2O_2 flowing in opposite direction at a rate of 30 µl/min. The H_2O_2 diffused from the feed channel through the PDMS walls into the gel precursor microemulsion, thereby triggering enzymatic crosslinking of tyramine-conjugated polymer, as previously described.[42] The microemulsion was broken by washing three times with surfactant-free fluorocarbon oil and subsequent supplementation of Pico-Break 1 in the presence of PBS that contained 0.05% (w/v) NaN_3 for preservation and 1% (w/v) BSA to prevent aggregation and sticking. On-chip droplets were visualized using a stereomicroscope set-up (Nikon SMZ800 equipped with Leica DFC300 FX camera). Retrieved microgels were imaged using phase contrast microscopy and the size distribution was measured using Matlab software.

5.2.4 Microgel Functionalization and Characterization

After washing Dex-TA-biotin microgels three times with excessive washing buffer that consisted of 1% (w/v) BSA in PBS to remove NaN_3, they were consecutively incubated with 1 µM neutravidin in washing buffer, washed with washing buffer, incubated with 1 µM biotinylated or desthiobiotinylated molecule of interest in washing buffer, and washed again with washing buffer. If necessary, the functionalization protocol was repeated, for example, to create core-shell functionalized microgels, as further specified in **Figure 5.3d**. For fluorescence microscopy (EVOS FL), fluorescence confocal microscopy (Zeiss LSM 510 and Nikon A1+), and fluorescence recovery after photobleaching (FRAP; Zeiss LSM 510), the microgels were functionalized with biotin-atto565, biotin-FITC, and/or desthiobiotin-FITC that was produced in house by coupling desthiobiotin-NHS to 6-aminofluorescein in 1 M bicarbonate buffer (pH ~8). The FRAP curve was obtained by plotting, as a function of time, the fluorescent intensity of the bleach spot minus the background normalized for the bleach-rate corrected average intensity before bleaching, where the bleach rate was determined by normalizing the sample's fluorescent intensity besides the bleach spot normalized for its average intensity before bleaching. To characterize the desthiobiotin-biotin displacement, Dex-TA-biotin microgels were consecutively functionalized with neutravidin, washed,

functionalized with desthiobiotin-FITC, washed, and functionalized with biotin-atto565, while imaged using fluorescence confocal microscopy, as described above. Intensities of all fluorescent images were measured using ImageJ software.

5.2.5 Cell Isolation and Expansion

Human mesenchymal stem cells (MSCs) were isolated from fresh bone marrow samples and cultured as previously described.[43] The use of patient material was approved by the local ethical committee of the Medisch Spectrum Twente and informed written consent was obtained for all samples. In short, nucleated cells in the bone marrow aspirates were counted, seeded in tissue culture flasks at a density of 500,000 cells/cm² and cultured in MSC proliferation medium, consisting of 10% (v/v) FBS, 100 U/ml Penicillin and 100 µg/ml Streptomycin, 1% (v/v) GlutaMAX, 0.2 mM ascorbic acid, and 1 ng/ml bFGF (added fresh) in αMEM. When cells reached near confluence, the cells were detached using 0.25% (w/v) Trypsin-EDTA at 37 °C and subsequently subcultured or used for experimentation.

5.2.6 Modular Tissue Engineering

To produce modular tissue constructs, the shells of Dex-TA-biotin microgels that contained ~1 mM biotin were first permanently functionalized with c(RGDfK) peptide. To this end, the microgels were incubated for 30 minutes with 1 µM neutravidin in washing buffer (see previous section 'microgel functionalization and characterization'), washed, and subsequently incubated for 60 minutes with 1 µM biotinylated cyclic RGD peptide biotin-$(PEG)_2$-c(RGDfK) in washing buffer, as also depicted in **Figure 5.3d** in the results section. Dex-TA (i.e. without biotin) microgels that had been treated with the same functionalization protocol and Dex-TA-biotin microgels that had been functionalized with biotin-$(PEG)_2$-c(RADfK) were used as controls. The cell adhesive microgels were then co-seeded with cells into non-adherent microwell chips that were produced by casting 3% (w/v) sterile agarose in demineralized water on an in-house fabricated mold, as previously described.[44] In short, MSCs and microgels were homogenously seeded into agarose constructs (1.9 cm²) containing 3000 microwells (200 x 200 x 200 µm) at a seeding density of 50 units (i.e. cells + gels) per microwell. The modular microtissues were cultured in proliferation medium and visualized using fluorescence (confocal) microscopy. Viability and metabolic activity of cells was analyzed by staining with 2 µM calcein AM (live) and 4 µM EthD-1 (dead) in PBS and visualization using fluorescence microscopy. For additional fluorescent (confocal) analyses, constructs were first washed with PBS, fixated using 10% neutral buffered formalin, permeabilized using 0.1% Triton X-100 and subsequently incubated for 30 minutes with 2.5 U/ml phalloidin-AF647 and 1 µg/ml DAPI to stain F-actin and nuclei, respectively.

5.2.7 Statistics

The microgel size distribution was obtained by measuring the diameters of ≥275 microgels. The fluorescent confocal intensity measurements (except for FRAP measurements) were performed on ≥5 microgels per condition and reported as the average (cross sections of neutravidin diffusion experiment) or the average ± standard deviation (all other experiments) normalized for the highest average intensity. Cell seeding distributions were obtained by artisan counting of cells and microgels in ≥20 microwells per condition and reported as the average ± standard deviation normalized for the total average number of units (cells + microgels) per microwell. The diameter, area, circularity, and solidity of modular microaggregates were obtained from ≥10 constructs using the 'area' and 'shape descriptor' measurement functions of ImageJ and reported as the average ± standard deviation. Linear regression analyses and AVOVA with Bonferroni's post hoc tests to analyze statistical significance were performed using OriginPro software.

5.3 Results and Discussion

5.3.1 Engineering *in Situ* Biochemically Tunable Microgels Based on Sequential Desthiobiotin / Biotin Coupling

We set out to engineer micrometer-sized hydrogel particles (microgels) that could be biochemically tuned in a cytocompatible fashion. To this end, dextran was selected as a bio-inert, biocompatible, and easily modifiable polymer backbone, thereby acting as a perfect template material for further functionalization.[45, 46] Tyramine and biotin were selected as reactive side groups that could be enzymatically crosslinked and further functionalized via biotin/avidin interaction, respectively,[36, 41, 47] in a fully orthogonal and cytocompatible manner. The dextran polymer was endowed with tyramine and 1,4-butanediamine (i.e. Dex-TA-NH_2), as previously described,[40, 41] which was then further functionalized using amine-reactive biotin, which contained a long-chain spacer (biotin-LC-NHS) (**Figure 5.2a**). Successful Dex-TA-biotin synthesis was confirmed using ^{1}H NMR. The numbers of conjugated tyramine and biotin moieties per 100 dextran anhydroglucose rings were 13 and 6, respectively, as determined by calculating the ratios of integrated signals from the dextran (δ 4.0 – 5.8 ppm) and the tyramine (δ 6.66 ppm and δ 6.98 ppm) and those of tyramine and the coupled 6-aminocaproic spacer (δ 2.13) (**Figure 5,2b**, **Figure S5.1**, **Figure S5.2**). Tyramine-functionalized dextran could be crosslinked *in situ* via the formation of tyramine-tyramine bonds using horseradish peroxidase (HRP) as a catalyst and H_2O_2 as an oxidizer (**Figure S5.3**). A microfluidic droplet generator was used to generate microdroplets composed of 5% (w/v) Dex-TA-biotin (i.e. ~1 mM biotin) and 22 U/ml HRP (**Figure 5.2c**). These microgel precursor droplets were cured by controlled supplementation of H_2O_2 using a diffusion-based microfluidic crosslinking platform that we have recently reported (**Figure S5.4**).[42] This resulted in the formation of monodisperse Dex-TA-biotin microgels with a diameter of 20.7±0.6 μm (**Figure 5.2d,e**).

After enzymatic crosslinking, the biotin moieties remained available for subsequent orthogonal functionalization (i.e. without affecting the enzymatically crosslinked hydrogel network) via supramolecular biotin/avidin complexation. Specifically, the biotinylated microgels were further functionalized using a two-step approach by incubating them with tetravalent neutravidin (i.e. an avidin analog) and fluorescein-labeled biotin (biotin-FITC), respectively. Fluorescence confocal microscopy and fluorescence recovery after photobleaching (FRAP) confirmed that biotin-FITC was coupled to Dex-TA-biotin microgels, but not to non-functionalized (i.e. Dex-TA) microgels, which validated the successful generation and functionality of Dex-TA-biotin microgels (**Figure 5.2f,g**). The final degree of functionalization could be tuned by changing either the concentration of biotin in the microgels or the type and amount of biotinylated functional groups that were coupled via tetravalent neutravidin. To control the biotin concentration in the microgels, we varied the ratio of Dex-TA-biotin and Dex-TA hydrogel precursor solution using a microfluidic mix chip that was connected to the inlet of the droplet generator (**Figure S5.5**). The biotin concentration in the resulting microgels linearly correlated (R^2=0.99) to the final degree of functionalization, as measured by coupling either biotin-FITC (i.e. green) or biotin-atto565 (i.e. red) to the microgels (**Figure 5.2h**, **Figure S5.6**). Alternatively, the biochemical composition could be altered by varying the ratio of biotinylated FITC and atto565, while maintaining the same concentration of biotin in the microgels (**Figure S5.7**). In principle, both methods could be applied to tune the microgels' biochemical properties without altering their biomechanical properties.

We then aimed to create smart microgels that could reversibly and sequentially present molecules of interest. To this end, we leveraged the reversible nature of the supramolecular desthiobiotin/avidin complex by displacing desthiobiotin with biotin in a rapid and highly specific manner, as shown in **Figure 5.2i**. Microgels were first endowed with an abundant amount of neutravidin, which specifically bound to the free biotins in the microgels (K_d~10^{-15}). The microgels were then washed (t=0 min) and continually imaged using fluorescence confocal imaging to visualize and quantify the desthiobiotin binding and displacement in time (**Figure 5.2j**). The neutravidin-labeled microgels were incubated with 1 μM desthiobiotin-FITC (i.e. green), which could bind to the remaining free binding pockets of the tetravalent neutravidin in the microgels (K_d~10^{-13}). After the fluorescent intensity had reached a plateau (t~40 min), biotin-atto565 (i.e. red) was introduced to a final concentration of 1 μM. Biotin interacted more strongly with neutravidin (K_d~10^{-15}), which resulted in a rapid displacement of desthiobiotin by biotin. Over 80% of the desthiobiotin-FITC was replaced by the biotin-atto565 within the first 10 min after biotin addition and approximately 95% was replaced within 60 min.

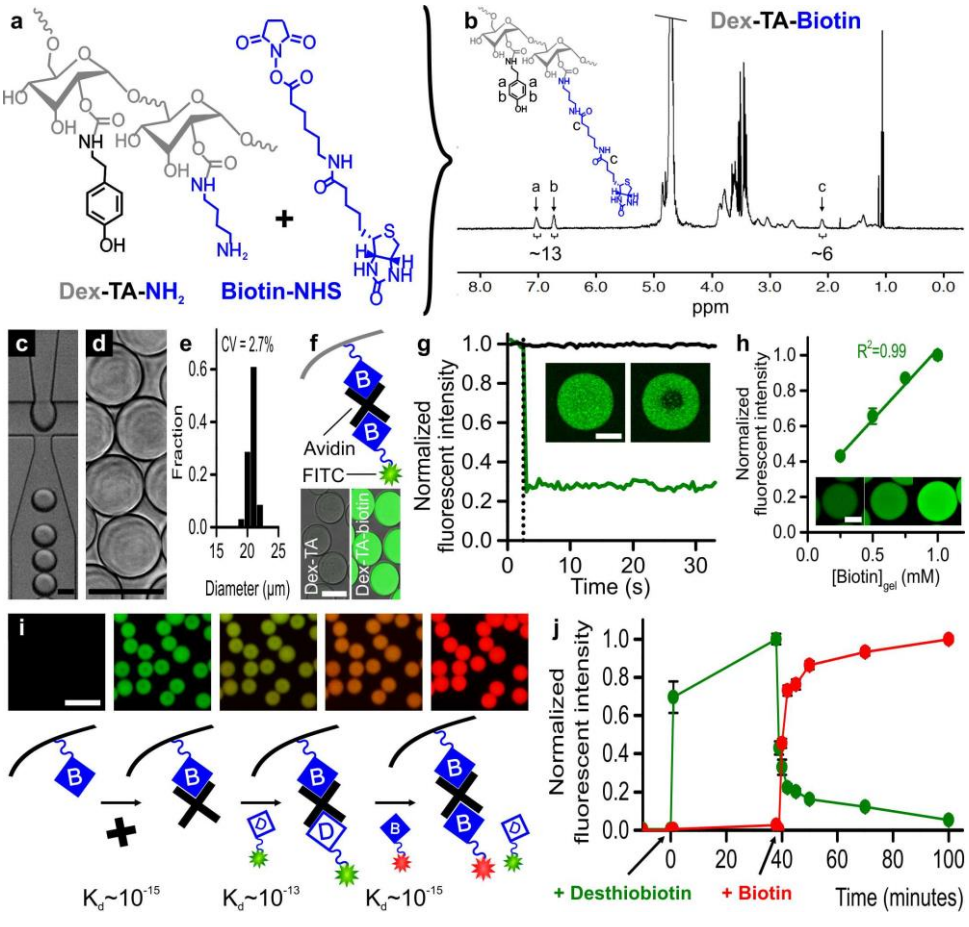

Figure 5.2. Engineering *in situ* biochemically tunable microgels based on sequential desthiobiotin/biotin coupling. (a,b) Tyramine- and biotin-functionalized dextran (Dex-TA-biotin) was synthesized by coupling amine-functionalized Dex-TA (Dex-TA-NH_2) to biotin-NHS. (**c-e**) Monodisperse dextran microgels were produced using droplet microfluidics. (**f**) Biotinylated microgels could be further functionalized with tetravalent avidin (or analog) and subsequently with a biotinylated molecule of interest, as demonstrated with biotinylated FITC. (**g**) The biotin/avidin/biotin coupling was confirmed by measuring fluorescence recovery after photobleaching (FRAP). (**h**) The amount of functional groups could be linearly tuned by controlling the concentration of biotinylated hydrogel precursor during Dex-TA-biotin microgel production. (**i**) The Dex-TA-biotin microgels could be reversibly functionalized using the facile desthiobiotin/biotin displacement strategy, as demonstrated by replacing desthiobiotin-FITC (i.e. green) by biotin-atto565 (i.e. red) (**j**) and characterized using time-lapse fluorescence confocal imaging. Black scale bars: 25 μm, white scale bars: 10 μm.

5.3.2 Enabling Self-assembly of Cells and Microgels using Cell Adhesive Shell Functionalization

To enable the self-assembly of smart microgels and cells into engineered modular tissue constructs, we aimed to endow the microgels with a permanent and spatially controlled cell adhesive coating. Specifically, we anticipated that functionalizing the

microgel's shell with biotinylated cyclic RGD peptide biotin-$(PEG)_2$-c(RGDfK) would enable the microgels to self-assemble with cells, while leaving the biotins in the microgel's core available for further *in situ* functionalization (**Figure 5.3a**). By tuning the concentration and incubation time of neutravidin, we could reproducibly control its penetration depth into the microgels. This strategy granted 2.5D control over the microgel's biochemical composition by determining the thickness of the neutravidin shell, which acted as the reactive substrate for subsequent coupling of biotinylated molecules. This diffusion-based spatial templating was visualized and quantified using biotin-FITC (i.e. green) labeling and subsequent fluorescence confocal imaging (**Figure 5.3b, c**, **Figure S5.8**). After shell functionalization, the microgels' cores still contained free biotins that could be endowed with another moiety by repeating the functionalization protocol with a prolonged neutravidin incubation step. For example, core-shell multifunctional microgels could be readily prepared by applying a shell functionalization using the multistep functionalization protocol as described in **Figure 5.3d**. After confirming the effectiveness of the core-shell functionalization protocol using fluorescent labels (**Figure 5.3e**), the same core-shell functionalization strategy was used to permanently endow the microgels' shells with c(RGDfK) peptides to enable integrin-mediated cell adhesion and promote bottom-up self-assembly. The concentration of biotin and consequently c(RGDfK) in the microgels was set to ~1 mM, as this has been proven to be effective to render hydrogels with cell adhesive properties.[48, 49]

Self-assembly of mesenchymal stem cells (MSCs) and c(RGDfK)-functionalized microgels into larger engineered modular tissues was achieved by co-seeding them in non-adherent microwell arrays, as previously described (**Figure S5.9**).[44, 50] Within a single day, the cells and gels self-assembled into modular microtissues with an average diameter of 110±10 μm (**Figure 5.3f**, **Figure S5.10**). In contrast, Dex-TA (i.e. without biotin) microgels that had been treated with neutravidin and biotin-$(PEG)_2$-c(RGDfK), and Dex-TA-biotin microgels that had been functionalized with neutravidin and biotin-$(PEG)_2$-c(RADfK) were not incorporated into the microtissues (**Figure 5.3g**, **Figure S5.11**). This confirmed that RGD-type peptides granted the Dex-TA-biotin microgels with the cell adhesive properties that are crucial for their self-assembly into modular microtissues.

To study the effect of aggregate composition on microtissue shape, self-assembled modular tissue constructs containing 0%, 50%, and 75% c(RGDfK)-functionalized microgels were produced by seeding 50 units (i.e. cells and microgels) per microwell (**Figure 5.3h**, **Figure S5.12**). It is of note that the effect of composition on modular tissue shape is cell- and microgel-size dependent. Here, we combined MSCs and microgels of almost equal size (~20 μm). Interestingly, increasing the microgel fraction resulted in significantly larger microtissues, and replacing 75% of the MSCs by cell adhesive microgels even resulted in more than 2-fold area increase (i.e. >8-fold volume) (**Figure S5.13**). The difference in microtissue size is presumably caused by cellular condensation; aggregated cells typically condensate over time,[50] whereas the non-degradable dextran-based microgels presumably remained their initial size and shape. This confirmed the

possibility of using modular tissue engineering strategies for engineering larger tissue constructs using fewer donor cells.[16] Using these specific cell and microgel types, the final construct's external shape was not affected up to a microgel fraction of 50%. However, incorporating 75% microgels into the construct affected its shape, as measured by a significant decrease in circularity and surface smoothness (**Figure S5.13**).

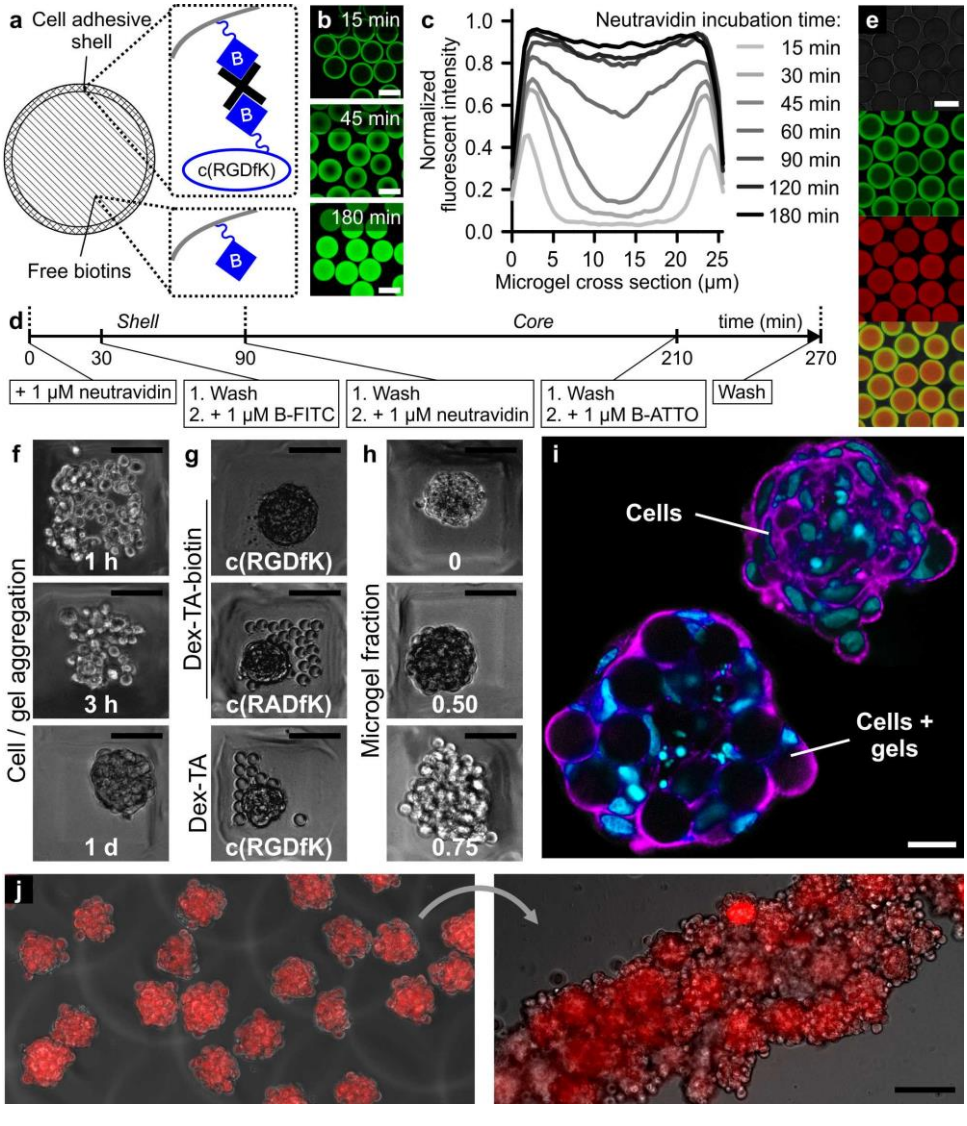

Figure 5.3. Cell adhesive shell functionalization enables the self-assembly of cells and microgels into 3D modular microtissues. (a) We set out to produce Dex-TA-biotin microgels with a cell adhesive shell by functionalizing the microgels with cyclic RGD-type peptides, while the biotin moieties in the cores remained free, which allowed for further *in situ* functionalization of the modular microtissues. **(b,c)** The thickness of the functionalized shells could be controlled by the diffusion of neutravidin, which acted as a reactive substrate for biotinylated moieties. **(d)** Using this facile multistep functionalization protocol,

the shells and cores of Dex-TA-biotin microgels could be endowed with distinct functional moieties, (**e**) as demonstrated using FITC- (i.e. green) and atto565-labeled (i.e. red) shells and cores, respectively. (**f,g**) Functionalizing Dex-TA-biotin microgels with a shell of c(RGDfK) peptides was essential to achieve self-assembly with MSCs. 3D modular microtissues were formed within a single day. (**h**) Microtissue composition and shape could be readily tuned by changing the ratio of cells and microgels. (**i**) Fluorescence confocal microscopy revealed that the microgels were completely incorporated in and homogeneously distributed throughout the modular tissue constructs. (**j**) Multiple preformed microtissues could be combined to form a larger, for example line-shaped modular tissue. Black scale bars: 100 μm, white scale bars: 20 μm.

Fluorescence confocal microscopy revealed that the c(RGDfK)-functionalized microgels were completely and homogeneously incorporated in the microtissues (**Figure 5.3i**). Live/dead staining of the modular microtissues revealed that neither the smart building blocks, nor the process of self-assembly caused any detrimental effect on cell survival (**Figure S5.14**). As expected, the living modular microtissues could self-assemble into larger structures by straightforwardly combining them into a mold to form, for example, a modular tissue fiber (**Figure 5.3j**).

5.3.3 Engineering Spatiotemporally Biochemically Tunable 3D Modular Microtissues using Smart Building Blocks

We then set out to demonstrate the tunable nature of smart building blocks in a living modular tissue by combining the optimized core-shell functionalization and desthiobiotin-based functionalization strategies. After self-assembly of the modular microtissues, the incorporated microgels where sequentially endowed with desthiobiotin-FITC (i.e. green) and biotin-atto565 (i.e. red). Fluorescence confocal microscopic imaging of the modular microtissues confirmed the *in situ* coupling of the desthiobiotin and its displacement by biotin, and thus the successful reversible and sequential functionalization of man-made living modular tissues (**Figure 5.4a**). This multimodal functionalization strategy also enabled the spatiotemporal controlled modification of microenvironments within the modular tissue constructs. To demonstrate this, we produced modular microtissues with biotin-FITC-labeled and non-labeled microgels that where subsequently seeded in various ratios in agarose microwells to form larger modular tissue constructs that consisted of 3 preformed microtissues. During culture, the construct could be spatiotemporally modified, as demonstrated by adding biotin-atto565 that specifically coupled to the non-labeled compartments within the modular microtissue (**Figure 5.4b**).

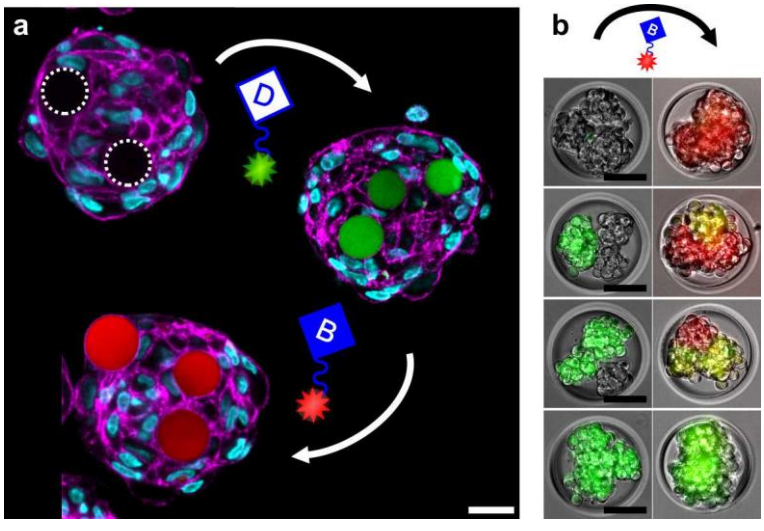

Figure 5.4. Engineering spatiotemporally biochemically tunable 3D modular microtissues using smart building blocks. (a) The concept of smart tissue engineering building blocks was demonstrated by the consecutive *in situ* modification of self-assembled cells and Dex-TA-biotin microgels with desthiobiotin-FITC and biotin-atto565. **(b)** Combining various 'smart microtissues' in different ratios readily enabled their self-assembly into a variety of larger complex modular microtissues with spatiotemporally controllable microenvironments. Black scale bars: 100 µm, white scale bars: 20 µm.

5.4 Conclusion

In conclusion, we have developed microgels that can on-demand, reversibly, and sequentially express molecules of interest using a desthiobiotin/biotin displacement strategy. These biochemically tunable microgels were leveraged as smart building blocks for modular tissue engineering applications by endowing the microgels with a permanent thin shell of RGD-type moieties by exploiting neutravidin diffusion kinetics. The resulting 3D modular living constructs could be readily biochemically modified in a spatiotemporal manner. The ability to endow man-made tissue constructs with *in situ* tunable spatiotemporal functionalization through the facile incorporation of smart building blocks aids the technologies rapid adoption in a variety of tissue engineering applications.

5.5 Supplementary Information

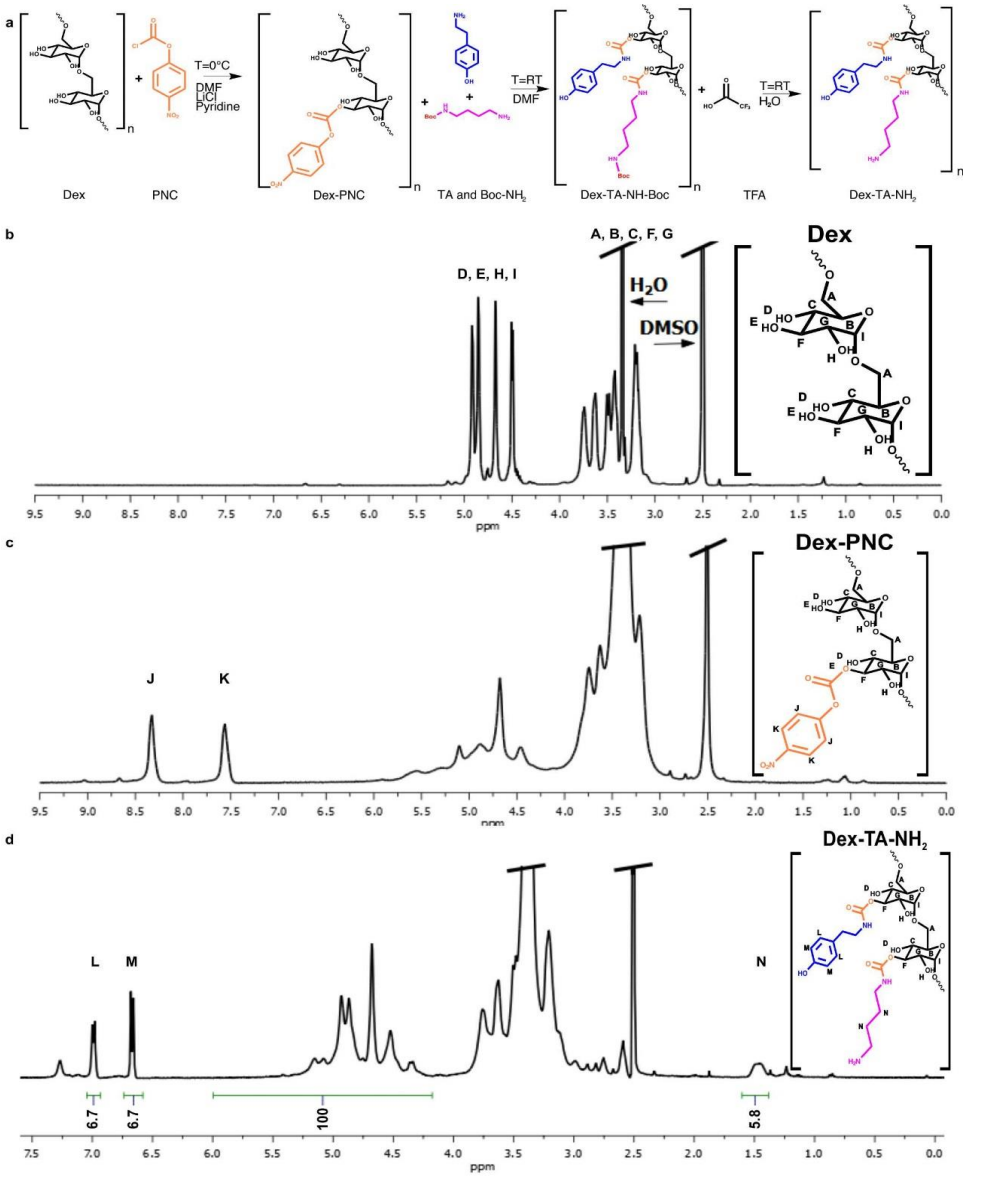

Figure S5.1. Synthesis and characterization of Dex-TA-NH₂. (a) Dextran (Dex) was first activated with 4-nitrophenyl chloroformate (PNC), which was then substituted with tyramine (TA) and Boc-protected 1,4-butanediamine (Boc-NH₂) that was subsequently deprotected using trifluoroacetic acid (TFA). **(b-d)** ^{1}H-NMR analysis was used to confirm the successful synthesis of Dex-PNC and Dex-TA-NH₂ and to quantify the numbers of conjugated tyramine and butylamine moieties per 100 dextran anhydroglucose rings by calculating the ratios of integrated signals from anomeric and hydroxylic protons of the dextran (δ 4.0 – 5.8 ppm), and aromatic protons of the tyramine groups (δ 6.66 ppm and δ 6.98 ppm) and methyl protons of the butylamine groups (δ 1.4 – 1.5 ppm), respectively.

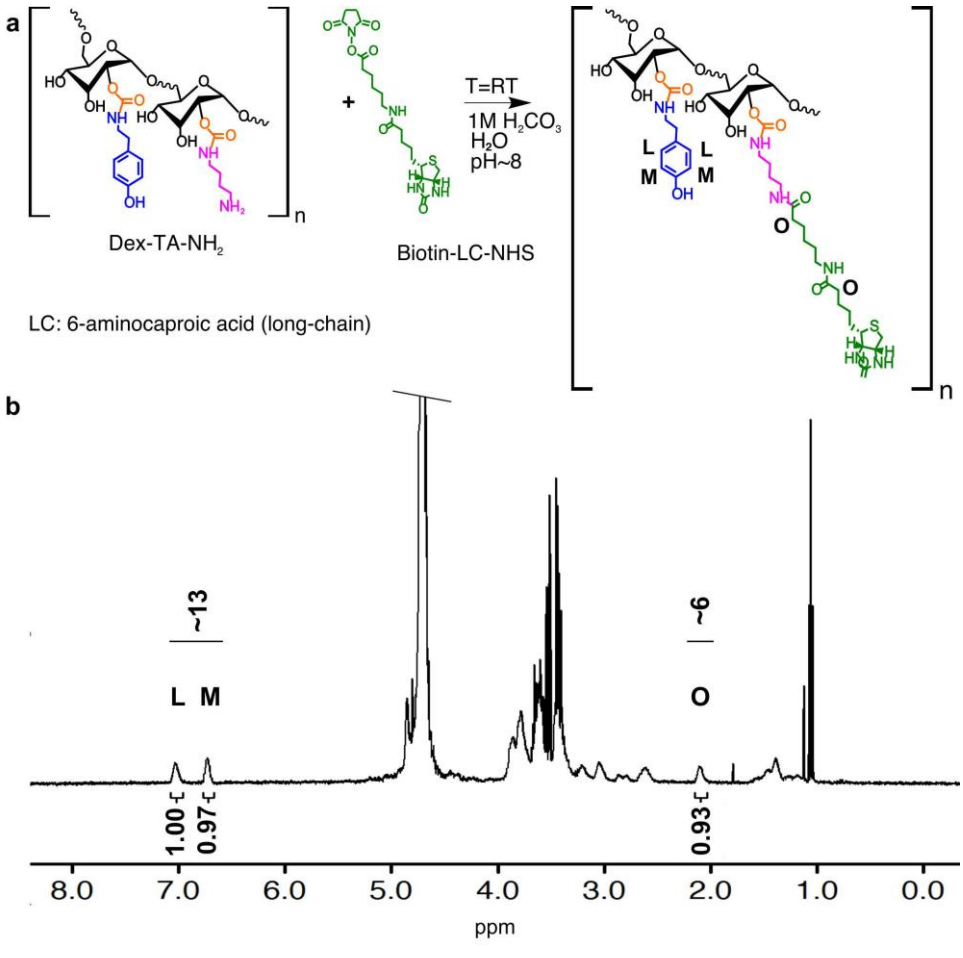

Figure S5.2. Synthesis and characterization of Dex-TA-biotin. (a) Dex-TA-NH_2 was functionalized with biotin using Succinimidyl 6-(biotinamido)hexanoate (biotin-LC-NHS; where LC is 6-aminocaproic acid (long-chain)). **(b)** ^{1}H-NMR analysis was used to confirm the successful synthesis of Dex-TA-biotin and to quantify the number of conjugated biotin moieties per 100 dextran anhydroglucose rings (as determined in Figure S1) by calculating the ratio of integrated signals from aromatic protons of the tyramine groups (δ 6.66 ppm and δ 6.98 ppm) and carboxylic amide protons of the coupled 6-aminocaproic spacer (δ 2.13).

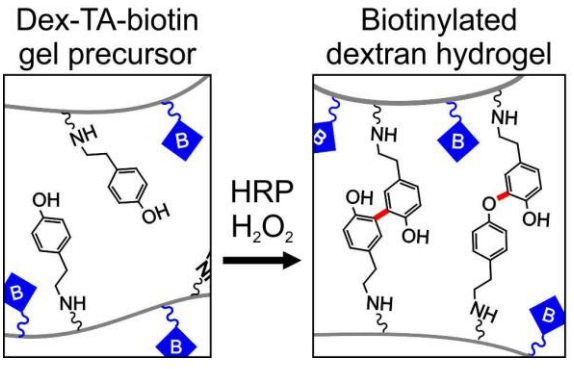

Figure S5.3. Dex-TA-biotin gelation. The phenolic hydroxyl groups in Dex-TA-biotin could be crosslinked *in situ* via the formation of C-C and C-O bonds (i.e. red) using horseradish peroxidase (HRP) as catalyst and H_2O_2 as oxidizer. This effectively results in a dextran-based hydrogel with free biotins.

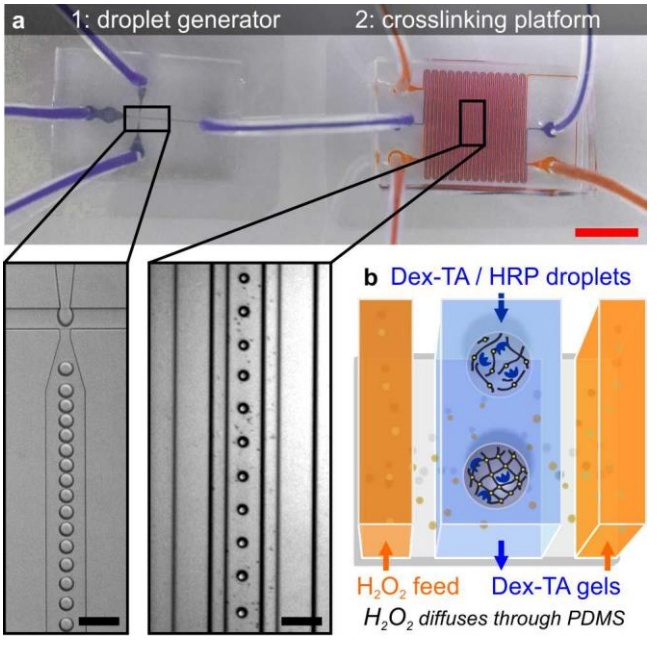

Figure S5.4. Droplet microfluidics-based microgel production. (a) To produce microgels, Dex-TA(-biotin) and HRP containing hydrogel precursor solution was emulsified using surfactant containing oil and a standard microfluidic droplet generator that was connected to a microfluidic crosslinking platform that consisted of 3 parallel channels separated by thin H_2O_2 permeable walls. **(b)** The crosslinking of hydrogel precursor microdroplets was induced with H_2O_2 that diffused from the outer channels through the polydimethylsiloxane (PDMS) walls and the oil phase into the center channel. Red scale bar: 5 mm, black scale bars: 100 µm.

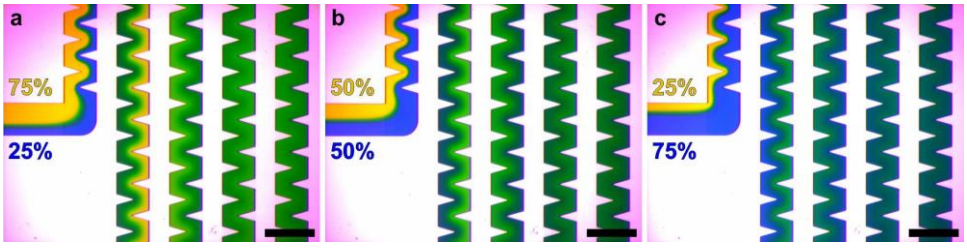

Figure S5.5. Microfluidic mixing. A microfluidic mixer was used to generate homogenous mixtures of Dex-TA and Dex-TA-biotin hydrogel precursor solution. **(a-c)** The mixer was characterized using various ratios of yellow and blue ink. Scale bars: 500 µm.

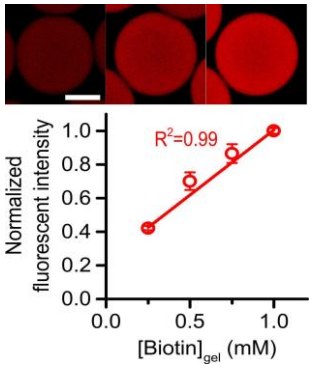

Figure S5.6. Tuning the biotin concentration in Dex-TA-biotin microgels. The biotin concentration in Dex-TA-biotin microgels was tuned by microfluidic mixing (Figure S5) of Dex-TA and Dex-TA-biotin hydrogel precursor solutions. Subsequent coupling of tetravalent neutravidin and fluorescently labeled biotin (biotin-atto565) revealed that the biotin concentration in the microgels linearly correlated (R^2=0.99) to the final degree of functionalization, as measured by the normalized fluorescent intensity. Scale bar: 10 µm.

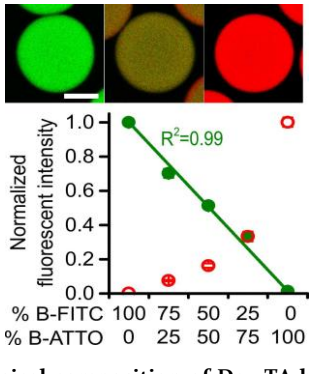

Figure S5.7. Tuning the biochemical composition of Dex-TA-biotin microgels. The biochemical composition of Dex-TA-biotin microgels could be altered by varying the ratio of biotinylated molecules of interest, as demonstrated using biotinylated FITC and atto565. Scale bar: 10 µm.

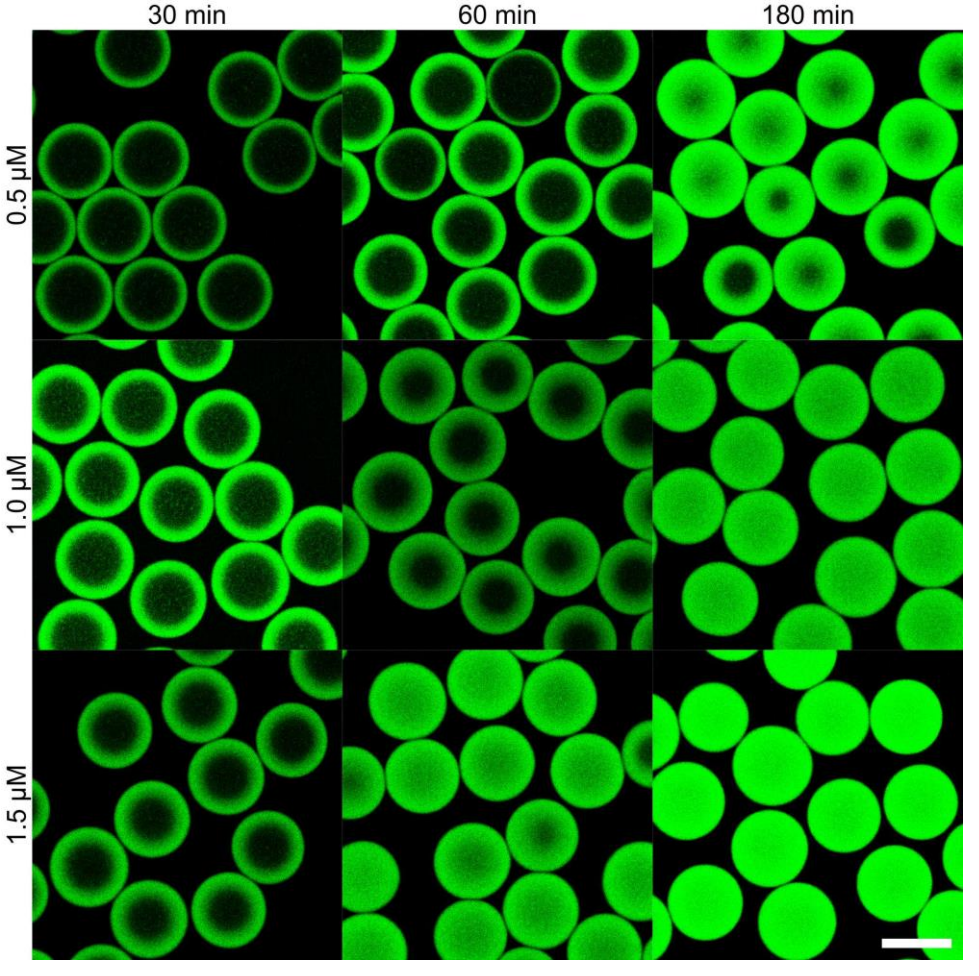

Figure S5.8. Controlling functionalized shell thickness. Dex-TA-biotin microgels could be endowed with a functional shell of tunable thickness by controlling the concentration and incubation time of neutravidin. In fact, the neutravidin acted as a template for subsequent tethering of biotinylated molecules of interest, as demonstrated using biotin-FITC (i.e. green). Scale bar: 20 µm.

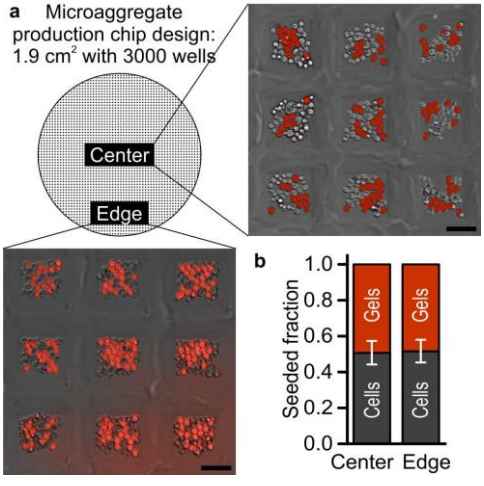

Figure S5.9. Homogeneous seeding of the microaggregate production chip. (a) To assess the seeding distribution of cells and microgels over the microwells, fluorescently labeled microgels (i.e. red) and cells were seeded on top of the microaggregate production chip. **(b)** Determining the per-well cell-to-gel ratios from microphotographs of the center and edge of the chip revealed that cells and gels were homogenously seeded in the microwels. Scale bars: 100 µm.

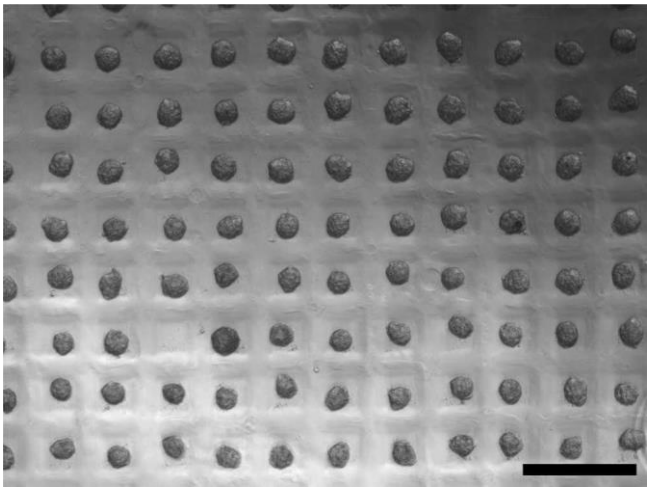

Figure S5.10. Modular microtissue formation. Representative microphotograph after one day of culturing c(RGDfK)-functionalized microgels and MSCs. In each microwell, all cells and microgels had self-assembled into modular microtissues. Scale bar: 500 µm.

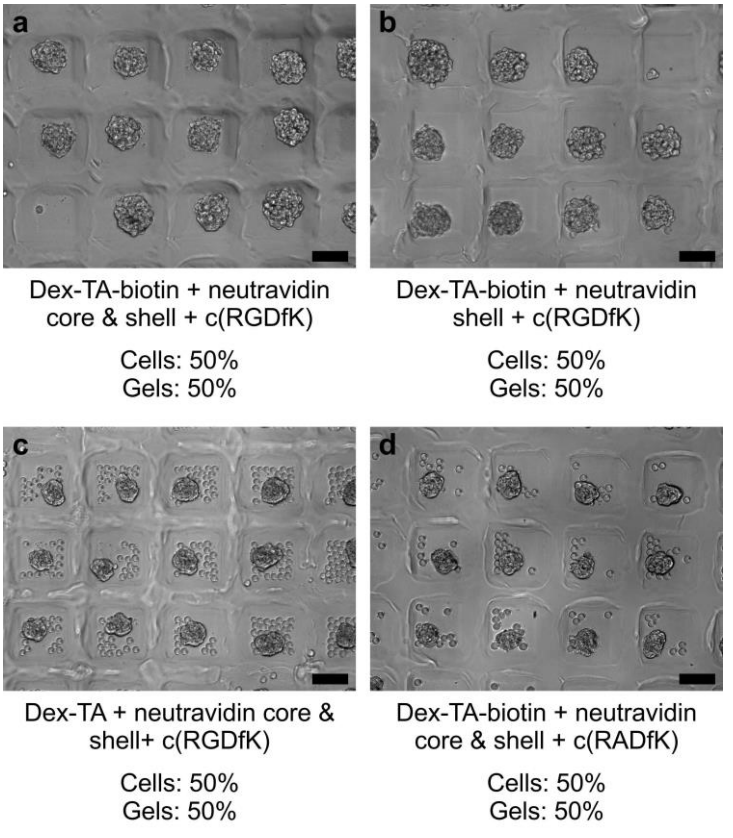

Figure S5.11. Tuning the microgels' cell adhesive properties. Dex-TA-biotin microgels that were **(a)** completely (i.e. core & shell) functionalized with c(RGDfK) peptides and **(b)** Dex-TA-biotin microgels of which only the shell was functionalized with c(RGDfK) peptides adhered good to cells, resulting in their complete incorporation into modular microtissues when seeded in a 50/50 ratio with MSCs. **(c)** Dex-TA (i.e. without biotin) microgels that were treated with the same neutravidin/c(RGDfK) functionalization protocol were not cell adhesive and could therefore not form self-assembled modular microtissues when seeded together with MSCs in a 50/50 ratio. **(d)** Also functionalization of Dex-TA-biotin microgels with c(RADfK) peptides did not result in sufficient cell adhesion to support the incorporation of all microgels into the modular microtissues, confirming that RGD-type peptides where essential to render the microgels with good cell adhesive properties. Scale bars: 100 μm.

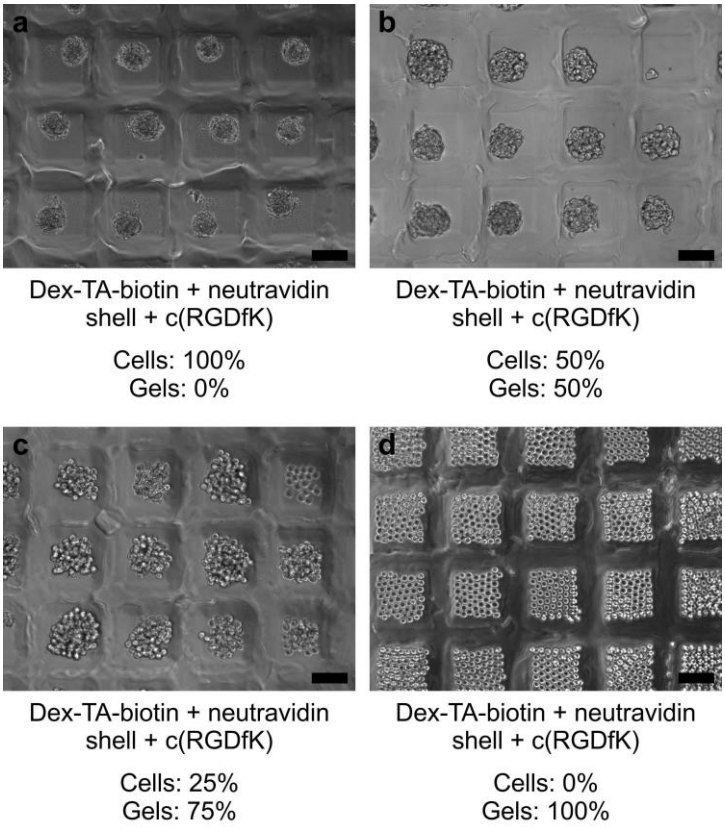

Figure S5.12. Tuning the modular microtissue composition. (a-d) Microtissues containing various ratios of c(RGDfK)-functionalized Dex-TA-biotin microgels and MSCs were formed to assess the effect of composition on tissue morphology. Scale bars: 100 μm.

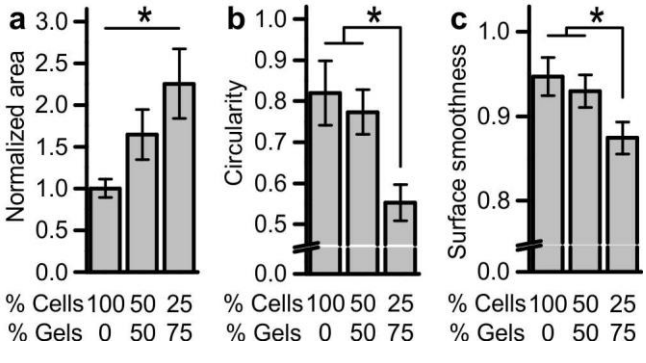

Figure S5.13. The effect of modular microtissue composition on morphology. (a) Increasing the microgel fraction resulted in significantly larger microtissues. **(b,c)** The circularity and surface smoothness of modular microtissues were significantly decreased when they consisted for more than 50% of microgels. * indicates 'significant with $p<0.01$'.

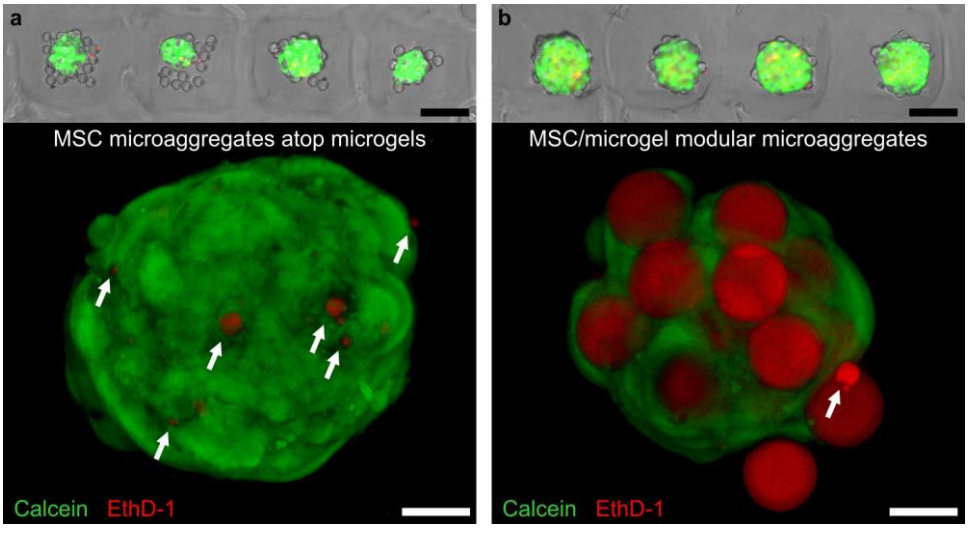

Figure S5.14. Microtissue viability. Both microtissues that consisted of (a) only MSCs and (b) MSCs and microgels (50/50 ratio) were characterized by > 90% cell viability, as demonstrated using live/dead stainings comprising of calcein (i.e. live cells in green) and homodimer-1 (EthD-1; i.e. dead cells in red). The top and bottom panels show representative live/dead stained microtissues as imaged using fluorescence microscopy and fluorescence confocal microscopy, respectively. Besides nuclei of dead cells, the EthD-1 also aspecifically stains the microgels. Dead cells are indicated with white arrows. Black scale bars: 100 μm, white scale bars: 20 μm.

References

1. O'Brien, F.J., *Biomaterials & scaffolds for tissue engineering.* Materials Today, 2011. **14**(3): p. 88-95.
2. Drury, J.L. and D.J. Mooney, *Hydrogels for tissue engineering: scaffold design variables and applications.* Biomaterials, 2003. **24**(24): p. 4337-51.
3. Hollister, S.J., *Porous scaffold design for tissue engineering.* Nat Mater, 2005. **4**(7): p. 518-24.
4. Lenas, P., et al., *Modularity in developmental biology and artificial organs: a missing concept in tissue engineering.* Artificial Organs, 2011. **35**(6): p. 656-62.
5. Lakes, R., *Materials with structural hierarchy.* Nature, 1993. **361**(6412): p. 511-515.
6. Liu, J.S. and Z.J. Gartner, *Directing the assembly of spatially organized multicomponent tissues from the bottom up.* Trends Cell Biol, 2012. **22**(12): p. 683-91.
7. Zorlutuna, P., N.E. Vrana, and A. Khademhosseini, *The expanding world of tissue engineering: the building blocks and new applications of tissue engineered constructs.* IEEE Rev Biomed Eng, 2013. **6**: p. 47-62.
8. Elbert, D.L., *Bottom-up tissue engineering.* Curr Opin Biotechnol, 2011. **22**(5): p. 674-80.
9. Nichol, J.W., et al., *Cell-laden microengineered gelatin methacrylate hydrogels.* Biomaterials, 2010. **31**(21): p. 5536-44.
10. Rivron, N.C., et al., *Tissue assembly and organization: developmental mechanisms in microfabricated tissues.* Biomaterials, 2009. **30**(28): p. 4851-8.
11. Kamperman, T., et al., *Single Cell Microgel Based Modular Bioinks for Uncoupled Cellular Micro- and Macroenvironments.* Adv Healthc Mater, 2017. **6**(3).
12. Huebsch, N., et al., *Matrix elasticity of void-forming hydrogels controls transplanted-stem-cell-mediated bone formation.* Nat Mater, 2015. **14**(12): p. 1269-77.
13. Levato, R., et al., *Biofabrication of tissue constructs by 3D bioprinting of cell-laden microcarriers.* Biofabrication, 2014. **6**(3): p. 035020.
14. Santo, V.E., et al., *Enhancement of osteogenic differentiation of human adipose derived stem cells by the controlled release of platelet lysates from hybrid scaffolds produced by supercritical fluid foaming.* J Control Release, 2012. **162**(1): p. 19-27.
15. Oliveira, S.M., R.L. Reis, and J.F. Mano, *Towards the design of 3D multiscale instructive tissue engineering constructs: Current approaches and trends.* Biotechnol Adv, 2015. **33**(6 Pt 1): p. 842-55.
16. Georgi, N., C. van Blitterswijk, and M. Karperien, *Mesenchymal stromal/stem cell-or chondrocyte-seeded microcarriers as building blocks for cartilage tissue engineering.* Tissue Eng Part A, 2014. **20**(17-18): p. 2513-23.
17. Matsunaga, Y.T., Y. Morimoto, and S. Takeuchi, *Molding cell beads for rapid construction of macroscopic 3D tissue architecture.* Advanced Materials, 2011. **23**(12): p. H90-4.
18. Leferink, A., et al., *Engineered micro-objects as scaffolding elements in cellular building blocks for bottom-up tissue engineering approaches.* Advanced Materials, 2014. **26**(16): p. 2592-9.
19. McGuigan, A.P. and M.V. Sefton, *Vascularized organoid engineered by modular assembly enables blood perfusion.* Proc Natl Acad Sci U S A, 2006. **103**(31): p. 11461-6.
20. Griffin, D.R., et al., *Accelerated wound healing by injectable microporous gel scaffolds assembled from annealed building blocks.* Nat Mater, 2015. **14**(7): p. 737-44.
21. Scott, E.A., et al., *Modular scaffolds assembled around living cells using poly(ethylene glycol) microspheres with macroporation via a non-cytotoxic porogen.* Acta Biomater, 2010. **6**(1): p. 29-38.
22. Dikina, A.D., et al., *Engineered cartilaginous tubes for tracheal tissue replacement via self-assembly and fusion of human mesenchymal stem cell constructs.* Biomaterials, 2015. **52**: p. 452-62.
23. Tasoglu, S., et al., *Untethered micro-robotic coding of three-dimensional material composition.* Nature Communications, 2014. **5**: p. 3124.
24. Qi, H., et al., *DNA-directed self-assembly of shape-controlled hydrogels.* Nature Communications, 2013. **4**: p. 2275.
25. Daley, W.P., S.B. Peters, and M. Larsen, *Extracellular matrix dynamics in development and regenerative medicine.* Journal of Cell Science, 2008. **121**(Pt 3): p. 255-64.
26. Place, E.S., N.D. Evans, and M.M. Stevens, *Complexity in biomaterials for tissue engineering.* Nat Mater, 2009. **8**(6): p. 457-70.
27. Anderson, D.G., J.A. Burdick, and R. Langer, *Materials science. Smart biomaterials.* Science, 2004. **305**(5692): p. 1923-4.

28. Mieszawska, A.J. and D.L. Kaplan, *Smart biomaterials - regulating cell behavior through signaling molecules.* Bmc Biology, 2010. **8**: p. 59.
29. Burdick, J.A. and W.L. Murphy, *Moving from static to dynamic complexity in hydrogel design.* Nature Communications, 2012. **3**: p. 1269.
30. Guvendiren, M. and J.A. Burdick, *Stiffening hydrogels to probe short- and long-term cellular responses to dynamic mechanics.* Nature Communications, 2012. **3**: p. 792.
31. Lee, T.T., et al., *Light-triggered in vivo activation of adhesive peptides regulates cell adhesion, inflammation and vascularization of biomaterials.* Nat Mater, 2015. **14**(3): p. 352-60.
32. Gandavarapu, N.R., M.A. Azagarsamy, and K.S. Anseth, *Photo-click living strategy for controlled, reversible exchange of biochemical ligands.* Advanced Materials, 2014. **26**(16): p. 2521-6.
33. Takezawa, T., Y. Mori, and K. Yoshizato, *Cell culture on a thermo-responsive polymer surface.* Biotechnology (N Y), 1990. **8**(9): p. 854-6.
34. Khetan, S. and J.A. Burdick, *Patterning network structure to spatially control cellular remodeling and stem cell fate within 3-dimensional hydrogels.* Biomaterials, 2010. **31**(32): p. 8228-34.
35. DeForest, C.A., B.D. Polizzotti, and K.S. Anseth, *Sequential click reactions for synthesizing and patterning three-dimensional cell microenvironments.* Nat Mater, 2009. **8**(8): p. 659-64.
36. Seidlits, S.K., C.E. Schmidt, and J.B. Shear, *High-Resolution Patterning of Hydrogels in Three Dimensions using Direct-Write Photofabrication for Cell Guidance.* Advanced Functional Materials, 2009. **19**(22): p. 3543-3551.
37. Shih, H. and C.-C. Lin, *Tuning stiffness of cell-laden hydrogel via host–guest interactions.* J. Mater. Chem. B, 2016. **4**(29): p. 4969-4974.
38. Green, N.M., *Avidin.* Adv Protein Chem, 1975. **29**: p. 85-133.
39. Hirsch, J.D., et al., *Easily reversible desthiobiotin binding to streptavidin, avidin, and other biotin-binding proteins: uses for protein labeling, detection, and isolation.* Analytical Biochemistry, 2002. **308**(2): p. 343-57.
40. Wang, R., *Macromolecular engineering of in-situ forming hydrogels*, in *Department of Developmental BioEngineering*. 2016, University of Twente: Enschede. p. 180.
41. Jin, R., et al., *Enzyme-mediated fast in situ formation of hydrogels from dextran-tyramine conjugates.* Biomaterials, 2007. **28**(18): p. 2791-800.
42. Kamperman, T., et al., *Centering Single Cells in Microgels via Delayed Crosslinking Supports Long-Term 3D Culture by Preventing Cell Escape.* Small, 2017. **13**(22): p. 1603711-n/a.
43. Both, S.K., et al., *A rapid and efficient method for expansion of human mesenchymal stem cells.* Tissue Eng, 2007. **13**(1): p. 3-9.
44. Moreira Teixeira, L.S., et al., *High throughput generated micro-aggregates of chondrocytes stimulate cartilage formation in vitro and in vivo.* Eur Cell Mater, 2012. **23**: p. 387-99.
45. Cadee, J.A., et al., *In vivo biocompatibility of dextran-based hydrogels.* Journal of Biomedical Materials Research, 2000. **50**(3): p. 397-404.
46. De Groot, C.J., et al., *In vitro biocompatibility of biodegradable dextran-based hydrogels tested with human fibroblasts.* Biomaterials, 2001. **22**(11): p. 1197-203.
47. Segura, T., et al., *Crosslinked hyaluronic acid hydrogels: a strategy to functionalize and pattern.* Biomaterials, 2005. **26**(4): p. 359-71.
48. Chaudhuri, O., et al., *Hydrogels with tunable stress relaxation regulate stem cell fate and activity.* Nat Mater, 2016. **15**(3): p. 326-34.
49. Burdick, J.A. and K.S. Anseth, *Photoencapsulation of osteoblasts in injectable RGD-modified PEG hydrogels for bone tissue engineering.* Biomaterials, 2002. **23**(22): p. 4315-23.
50. Leijten, J., et al., *Bioinspired seeding of biomaterials using three dimensional microtissues induces chondrogenic stem cell differentiation and cartilage formation under growth factor free conditions.* Sci Rep, 2016. **6**: p. 36011.

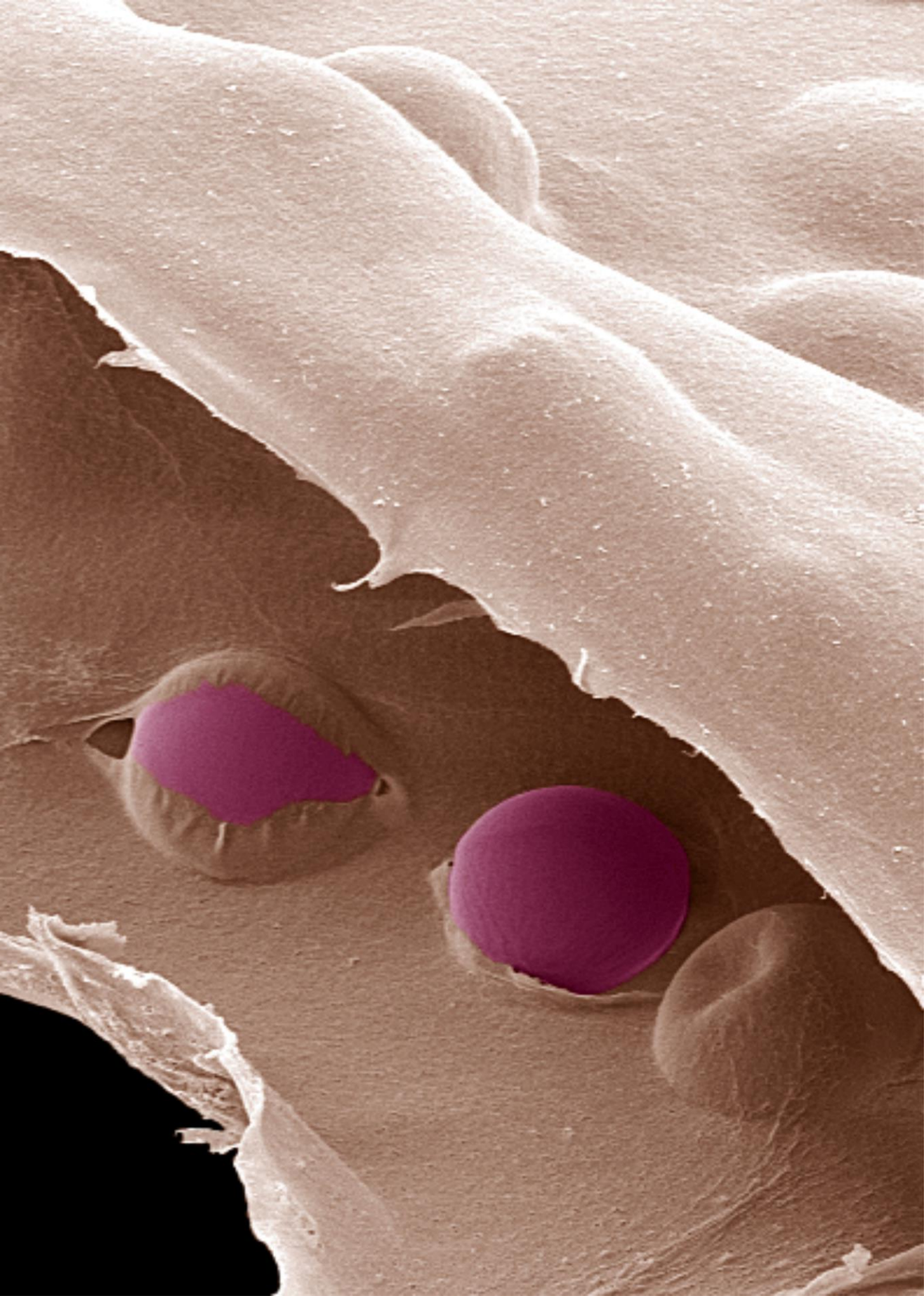

6

Single Cell Microgel Based Modular Bio-inks for Uncoupled Cellular Micro- and Macroenvironments

Multiscale hierarchy is found throughout nature and is essential for proper tissue functioning. It is based on combining multiple modular units with distinct functions into a single well-organized structure. Mimicking such designs in engineered tissues represents a promising approach to achieve the multifunctionality that is archetypal for native tissues. Here, we develop modular bio-inks to engineer three-dimensional (3D) multifunctional biomaterials by leveraging single-cell-laden microgels as building blocks. The microgels are efficiently produced using droplet-based microfluidics, and subsequent flow cytometry-based sorting yields near pure (>90%) cell-laden microgel populations. Microgels are mixed and matched with a wide variety of injectable biomaterials to form various modular bio-inks that are compatible with a variety of biofabrication techniques. Our modular approach enables independent control over the cellular micro- and macroenvironments within the biomaterials, which allows for the engineering of 3D multifunctional tissue constructs with unprecedented single cell resolution. Using this approach, we endow a construct with two clinically important yet normally incompatible functions: immunoprotection and angiogenesis. In short, bio-inks with a modular design based on single-cell-laden microgels within a distinct prepolymer can render engineered tissues with the multifunctionality that underlies the behavior of native tissues.

Tom Kamperman, Sieger Henke, Albert van den Berg, Su Ryon Shin, Ali Tamayol, Ali Khademhosseini, Marcel Karperien, and Jeroen Leijten**

** shared senior authorship.*

Contribution TK: experimental design, experimental performance, and manuscript writing.

Published in Adv. Healthcare Mater., 2017, 10.1002/adhm.201600913.

6.1 Introduction

Native tissues are characterized by a multiscale modular design.[1] The cells and matrices within are spatially organized into repetitive three-dimensional (3D) building blocks endowed with biochemical and biophysical ques having functional impact down to the single cell level.[2, 3] In fact, these modules enable uncoupling of cellular and tissue micro- and macroenvironments, which is key to obtain the multifunctionality that is essential for proper tissue performance. Uncoupling the micro- and macroenvironments by integrating modularity is also expected to improve construct functionality of engineered tissues.[4] To this end, modularity has already been successfully incorporated in a number of bioengineering approaches, for example by incorporating porogens or cell-laden microcarriers into an injectable biomaterial.[5-10] Here, we aim to engineer multifunctional tissues via a modular approach using bio-ink that comprises single-cell-laden microgels in an injectable macrogel. As cells covered by a thin layer of matrix are life's smallest functional units that can exist on their own, it is intuitive to create modular building blocks with single cell resolution. To this end, the encapsulation of single cells into micrometer-sized hydrogels, also called microgels, holds great promise. In particular, the combination of single-cell-laden microgels with distinct prepolymers would allow the development of modular bio-inks that can create 3D multifunctional biomaterials of which the cellular micro- and macroenvironments are individually tunable. This biomimetic design is expected to provide biomaterials with the multifunctionality that is typically found in native tissues.

Various techniques have been exploited for the encapsulation of cells in microgels, including droplet microfluidics, printing, micromolding, and stop-flow lithography.[11] Of these, droplet microfluidics has proven most suitable for the continuous high-throughput production of monodisperse spherical microgels. This approach has been widely used for the efficient encapsulation of multiple cells in microgels with a diameter as small as 100 micrometer.[12-15] By making use of the Poisson distribution, it has even been possible to encapsulate single cells into such microgels.[16, 17] However, due to their size and low cell-to-volume ratio, these gel particles have remained incapable of acting as modular building blocks for the creation of tissues with physiological cell concentrations. To address this need, subsequent studies with advanced approaches have attempted to encapsulate cells in microgels with sub 100 μm diameters. However, merely downsizing the microgels has typically been insufficient for enhancing cell encapsulation. Specifically, single cells take position at the droplet's water/oil interface resulting in partial cell encapsulation or even the 'escape' of cells upon gelation.[18, 19]. Developing a facile fabrication strategy to produce single-cell-laden microgels that would be just micrometers larger than the cell size thus represents a key stepping stone for creating modular bio-inks that can be used to engineer tissues with uncoupled cellular micro- and macroenvironments at a single cell level.

Here, we report on the development of such modular bio-inks by enabling the high-throughput fabrication of microgels that fully encapsulate single cells, which are as small

as 35 µm in diameter. In short, single-cell-laden microgels were produced by emulsifying a cell-laden hydrogel precursor solution in an immiscible oil phase using a microfluidic flow focusing device and subsequently photocrosslinking the resulting emulsion in a delay channel (**Figure 6.1a**). These microgels possess a vastly improved cell-to-volume ratio compared to microgels with a diameter of e.g. 100 µm, making them highly suitable as high-resolution building blocks for modular tissue engineering. To demonstrate this, we incorporated the microgels into multiple distinct injectable macromaterials to effectively create several modular bio-inks (**Figure 6.1b**), which were used for the biofabrication of various 3D constructs with an uncoupled micro- and macroenvironment (**Figure 6.1c**).

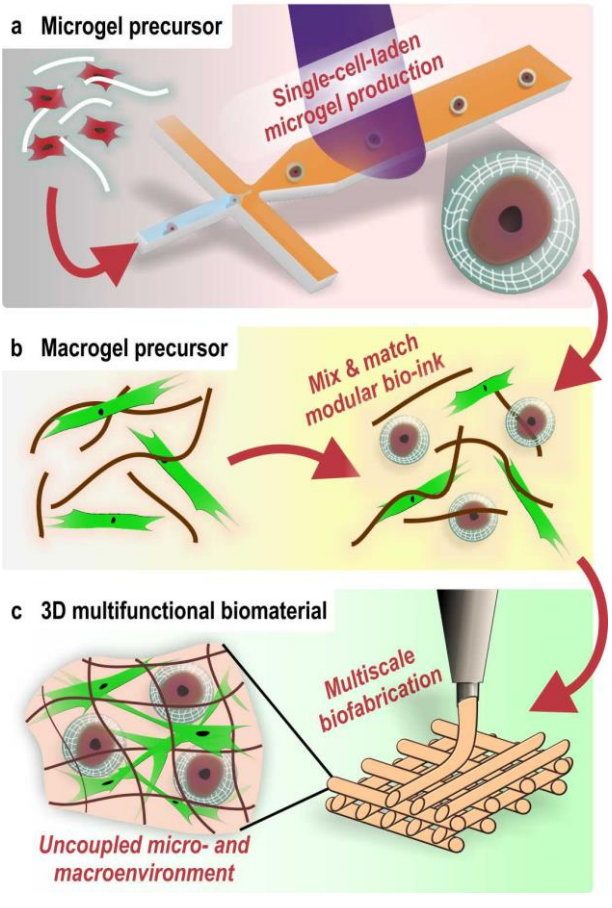

Figure 1. Schematic depiction of the creation of modular bio-inks and fabrication of 3D multifunctional biomaterials, which possess uncoupled micro- and macroenvironments. (a) Single-cell-laden microgels are produced by emulsifying and subsequent photocrosslinking cell-laden gel precursor microdroplets. **(b)** Modular bio-ink is prepared by mixing the single-cell-laden microgels in a distinct injectable macrogel precursor. The macrogel's composition can be optimized independently from the microgels to provide the construct with multiple functions, for example supporting the culture of different cell types. **(c)** The injectable nature of the modular bio-ink makes it compatible with a variety of standard biofabrication techniques such as 3D bioprinting.

6.2 Materials and Methods

6.2.1 Single-cell-laden Microgel Production

Microfluidic chips with 25.8 µm high structures were fabricated from polydimethylsiloxane (PDMS, Sylgard 184, Dow Corning) and glass using standard soft lithography techniques. Aquapel (Vulcavite) was introduced in the chips before usage to ensure channel wall hydrophobicity. Hydrogel precursor solution was prepared by mixing 10% (w/v) polyethylene glycol diacrylate (PEGDA 3400; Laysan Bio, Inc.), 0.1% (w/v) 2-hydroxy-4′-(2-hydroxyethoxy)-2-methylpropiophenone (Irgacure 2959, Sigma-Aldrich) and 33% (v/v) Percoll (Sigma-Aldrich), which was then filtered through a 0.22 µm pore size filter (Millex, Millipore). For photoinitiator system comparison, either hexadecane supplemented with 1% (v/v) Span 80, or hexadecane supplemented with 1% (v/v) Span 80, 0.1% (w/v) 2,2-dimethoxy-2-phenylacetophenone (Irgacure 651, Sigma-Aldrich) and 0.3% (v/v) N-Vinylpyrrolidone (Sigma-Aldrich) was used for emulsification. To produce cell-laden microgels, cells (maximally passage 4) were washed with phosphate-buffered saline (PBS, Gibco) and suspended in hydrogel precursor solution at a concentration of 9 million cells per ml. The cell-laden hydrogel precursor solution was loaded into an ice-cooled gastight syringe where it was continually agitated. All syringes were controlled by low pressure syringe pumps (neMESYS, Cetoni). The hydrogel precursor solution and oil were emulsified in the microfluidic chip at typical flow rates of 1 µl/min and 6 µl/min, respectively. The microdroplets were cured in an on-chip delay channel using 365 nm UV-light (~5s at ~100 mW/cm^2; LC8 Lightningcure L9588, Hamamatsu). Emulsions were broken by multiple hexadecane washes in the presence of serum containing proliferation medium. Viability of encapsulated cells was analyzed post encapsulation using a live/dead assay (Molecular Probes) following manufacturer's protocol and was visualized using a fluorescence microscope set-up (Nikon Eclipse E600 with Nikon DS-Fi1c camera). Images were analyzed using ImageJ software.

6.2.2 Cell Isolation and Expansion

Bovine chondrocytes were isolated from patellar-femoral groove cartilage of calf legs as previously reported.[20] In short, the cells were isolated via enzymatic digestion using Dulbecco's Modified Eagle's Medium (DMEM; Gibco) supplemented with 10% (v/v) fetal bovine serum (FBS; Lonza), 100 U/ml Penicillin with 100 µg/ml Streptomycin (Gibco) and 0.2% (w/v) collagenase type II (Worthington). Isolated chondrocytes were suspended in chondrocyte proliferation medium, consisting of 10% (v/v) FBS, 100 U/ml Penicillin with 100 µg/ml Streptomycin, 1% (v/v) MEM Non-Essential Amino Acid solution (Sigma-Aldrich), 0.35 mM L-Proline (Sigma-Aldrich) and 0.2 mM ascorbic acid (Sigma-Aldrich) in DMEM. The resulting cell suspension was seeded in tissue culture flasks (Nunc) at a density of 2500 cells/cm^2. Medium was replaced twice a week. Human mesenchymal stem cells (MSCs) were isolated from fresh bone marrow samples as previously described.[21] The use of patient material was approved by the local ethical committee of the Medisch Spectrum Twente and informed written consent was obtained for all samples. In short, nucleated cells in the bone marrow aspirates were counted,

seeded in tissue culture flasks at a density of 500,000 cells/cm² and cultured in MSC proliferation medium, consisting of 10% (v/v) FBS, 100 U/ml Penicillin with 100 µg/ml Streptomycin, 2 mM L-Glutamine (Gibco), 0.2 mM ascorbic acid and 1 ng/ml basic fibroblast growth factor (ISOKine bFGF, Neuromics) in Minimal Essential Medium (MEM) α with nucleosides (Gibco). Human umbilical vein endothelial cells (Lonza) were cultured in endothelial growth medium (EGM-2 BulletKit, Lonza). When either chondrocyte, MSC or endothelial cell culture reached near confluence, the cells were detached using 0.25% (w/v) Trypsin-EDTA (Gibco) at 37 °C and subsequently subcultured or used for experimentation.

6.2.3 Size Distributions and Permselectivity

The distribution of cell sizes was measured using laser diffraction at a concentration of 10^7 cells/ml (Mastersizer Hydro 2000S, Malvern). Microgel size distributions were measured using brightfield microscopy and Matlab software. Microgels were incubated with FITC-labeled dextran with molecular weights ranging from 10 to 70 kDa and proteins (bovine serum albumin and immunoglobulin G) for six days, after which the fluorescent intensities across the microgels were measured using fluorescent confocal imaging and quantified using ImageJ software.

6.2.4 Fluorescence-activated Cell Sorting (FACS)

Cell membranes were fluorescently labeled with 0.5% (v/v) Vybrant DiO (Molecular Probes) following manufacturer's protocol. A FACSAria II (BD Biosciences) was used to sort the cell-laden microgels fraction. To prevent clogging of the FACS nozzle, the cell-laden microgel solution was pipetted through a 100 µm mesh cell strainer (Fisherbrand, Fisher Scientific) prior to sorting. We acquired 50,000 data points for all samples to determine gate settings and used a 100 µm diameter nozzle at a liquid pressure of 20 psi. Cell encapsulation distributions were measured via artisan counting using phase contrast microscopy.

6.2.6 Interconnected Endothelial Networks

Fibrin precursor solution was prepared by suspending FITC-labeled PEGDA microgels, human umbilical vein endothelial cells and MSCs into EGM-2 without FBS supplemented with 10 mg/ml fibrinogen (Sigma-Aldrich). Just before producing the constructs, 5% FBS was added to the fibrin precursor solution. Modular constructs were formed by injecting and mixing 9.2 µl fibrin precursor solution and 0.8 µl 50 U/ml thrombin (Sigma-Aldrich) in a 10 µl microwell (µ-Slide Angiogenesis, Ibidi). After 5 minutes at room temperature, the constructs were incubated for 20 minutes at 37 °C to complete polymerization, after which warm EGM-2 was added on top. The hydrid constructs were cultured for one week in EGM-2 medium, which was refreshed every 2-3 days. The constructs were then fixated using 10% formalin and stained using phalloidin, anti-CD31 (AB76533, Abcam) and DAPI or DRAQ5 as counter stainings for subsequent fluorescent (confocal) imaging.

6.2.7 Biofabrication of 3D Modular Constructs

Modular biomaterials were produced by mixing cell-laden PEGDA microgels into a gelating 2% (w/v) agarose (Eurogentec) solution. Alternatively, fluorescently labeled PEGDA microgels were homogeneously mixed in various distinct fluorescently labeled in situ crosslinkable prepolymers and subsequently processed into a 3D hybrid construct using a variety of biofabrication techniques. For PEGDA photopatterning, PEGDA microgels were mixed with 5% (w/v) PEGDA 3400 and 0.5% (w/v) Irgacure 2959 in PBS. The modular bio-ink was injected between stacked microscopy slides that where spaced using #1 thickness cover glasses. Photopatterning was performed by UV-curing through a black sheet containing a pattern of transparent triangles. Subsequently, uncured PEGDA was washed followed by an injection of 1 µm fluorescent beads (Sigma-Aldrich). For dextran-tyramine emulsification, PEGDA microgels were mixed with 5% (w/v) in-house synthesized dextran-tyramine conjugates and 22 U/ml horseradish peroxidase (Sigma-Aldrich) in PBS. The modular bio-ink was mixed with hydrogen peroxide (Sigma-Aldrich) to a final concentration of 0.05% (w/v) and immediately emulsified with hexadecane that contained 1% hexadecane using a microfluidic droplet generator. After gelation, the emulsion was broken by multiple hexadecane washes in the presence of albumin containing PBS. For collagen injection molding, the PEGDA microgels were mixed with 5 mg/ml collagen type I (Collagen G1, Matrix BioScience) in PBS supplemented with 35 mM NaOH (Sigma-Aldrich). The modular bio-ink was injected into an in-house made bone-shaped PDMS mold and incubated over night to complete gelation. For alginate/gelatin methacryloyl (GelMA) 3D printing, the PEGDA microgels were mixed with 4% (w/v) alginate (FMC Biopolymers) and 4.5% (w/v) in-house synthesized GelMA. The modular bio-ink was coextruded with 0.3 M $CaCl_2$ with a deposition speed of 4 mm/s using microfluidic syringe pumps (Harvard Apparatus) and patterned using a NovoGen MMX Bioprinter™ (Organovo). For alginate wet spinning, the PEGDA microgels were mixed with 2% alginate in PBS. The modular bio-ink was extruded through a 30 gauge needle into a 0.1 M $CaCl_2$ bath to form fibers, which were subsequently weaved manually. All 3D constructs were visualized using fluorescent confocal imaging and microphotography under a black light source.

6.3 Results and Discussion

6.3.1 Droplet Microfluidics, Dual Photoiniated Crosslinking, and Flow Cytometry-based Purification Enables High-yield Single Cell Encapsulation

First, we aimed to encapsulate single cells into sub 50 µm microgels. To this end, we tested two different primary mammalian cell types (multipotent human mesenchymal stem cells (MSCs) and bovine chondrocytes) and selected polyethylene glycol diacrylate (PEGDA) as a model hydrogel. PEGDA allows for incorporation of a wide range of biomimetic elements and thus conforms as a template material for potential customization, which supports facile creation of user-defined cellular microenvironments.[22-25] Cell-laden PEGDA microdroplets were formed at a rate of ~1

kHz using a microfluidic droplet generator (**Figure 6.2a**). Nozzle size was a key parameter in determining the hydrogel precursor droplet diameter, as we mainly utilized the flow focusing device in geometry-controlled or 'squeezing' mode.[26, 27] Therefore, the nozzle dimensions were minimized to approximately 20 by 25 µm, thus only slightly larger than the average diameter of primary mammalian cells that we encapsulated (17 µm). A conventional crosslinking approach using only photoinitiator in the gel precursor phase, resulted in droplet coalescence and even expulsion of the cells from the microgels (**Figure 6.2b**). Indeed, cell-laden emulsions are relatively unstable due to the rapid adsorption of biomolecules and cells to the droplets' water/oil interface.[28] We implemented a dual photoinitiator system to achieve fast on-chip stabilization of the cell-laden droplets' water/oil interface, which was essential to prevent droplet coalescence and cell release (**Figure 6.2c**).[29] By dissolving photoinitiators in both the disperse water (0.1% Irgacure 2959) and the continuous oil (0.1% Irgacure 651) phases, we could encapsulate single cells in monodisperse PEGDA microgels with diameters between 35 and 40 µm in a robust and reproducible manner with good encapsulation quality, as measured by the relative position of the (semi-)encapsulated cell within the microgel (**Figure 6.2d,e**). The lower microgel diameter limit was determined by the size of the encapsulated single cells (10 to 35 µm). The microdroplets were photocrosslinked in an on-chip delay channel using an external UV-light source. To retrieve the microgels and allow their subsequent use, emulsions were broken by diluting the surfactant with hexadecane in the presence of serum-containing cell culture medium. The retrieved cell-laden microgels could be handled identically to cells in suspension. Importantly, more than 70% of the encapsulated cells (n=220) remained viable throughout the encapsulation, gelation, and retrieval procedures, as shown by live/dead staining (**Figure 6.2f**). This indicates the cytocompatible nature of our microencapsulation strategy and supports its further use as a platform technology. Furthermore, this observation is in line with previously published reports, which crosslinked PEGDA off-chip into macroscale hydrogels.[30, 31] It is of note that the incorporation of bioactive materials will support long-term cell viability and function. Regardless, we purposely exploited unmodified PEGDA, which is a universal bio-inert template material that does not stimulate any specific cell functions by itself. Moreover, numerous biofunctional moieties to modify hydrogels such as PEGDA are readily available and compatible with our encapsulation platform, indeed enabling cell specific stimulation depending on the application of interest.[22-25] Scanning electron microscopy (SEM) revealed intact spherical microgels, indeed completely enclosing single cells (**Figure 6.2g**). This was corroborated by opening the microgels using focused ion beam (FIB) milling (**Figure 6.2h**). Furthermore, fluorescent confocal microscopy traced fluorescently labeled cells in the center of the microgels (**Figure 6.2i**). 3D visualization by z-stacking confocal images confirmed that the hydrogel indeed completely (i.e. without protrusions) enclosed the cells (**Figure S6.1**). Together, our dual photoinitiator approach enables droplet microfluidics technology to completely encapsulate single cells within a micrometer-thin hydrogel coating.

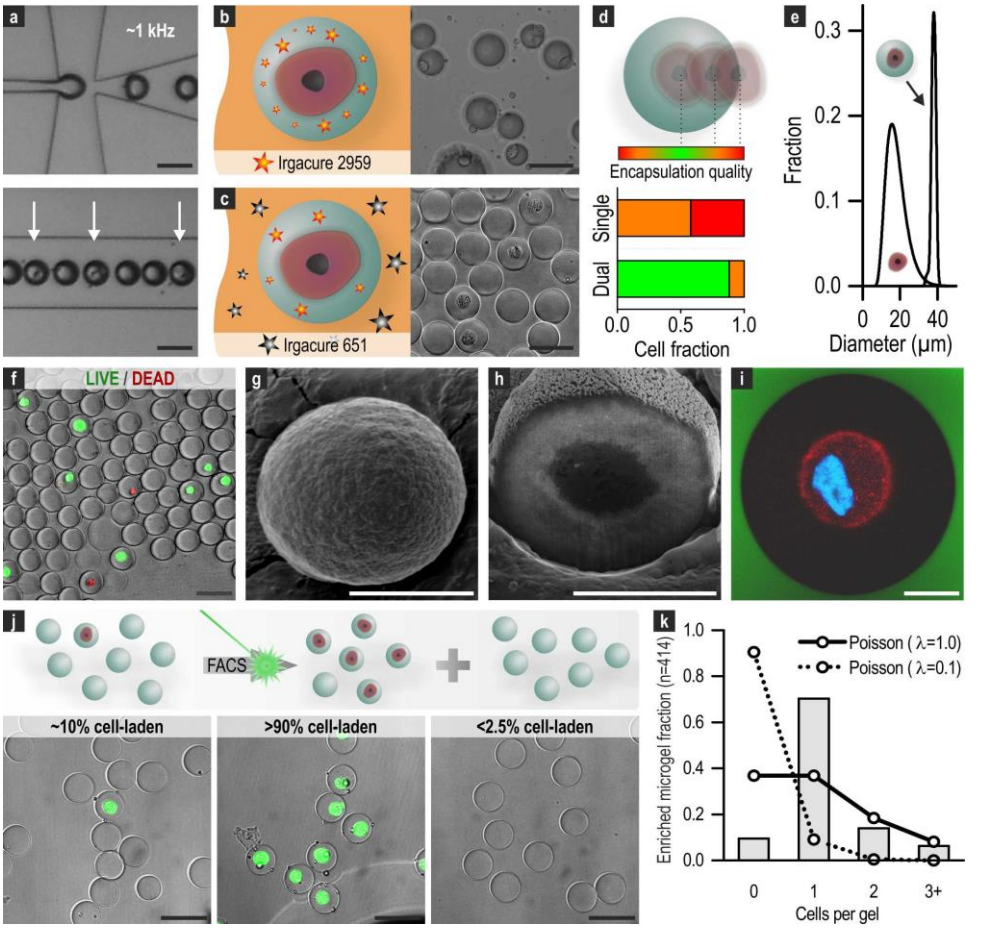

Figure 2. Single-cell-laden microgel production. **(a)** High-throughput encapsulation of single cells (white arrows) in PEGDA precursor microdroplets using droplet microfluidics. **(b)** Production of stable cell-laden microgels failed when using the gold standard single photoinitiator system, which relied on 0.1% Irgacure 2959 in the disperse phase. **(c)** Proficient cell encapsulation into PEGDA microgels using a double photoinitiator system that contained 0.1% Irgacure 2959 in the disperse phase and 0.1% Irgacure 651 in the continuous phase. **(d)** Histogram of the relative position of (semi-)encapsulated cells within microgels as a measure for cell encapsulation quality. **(e)** Single-cell-laden microgels have a monodisperse size distribution with diameters between 35 and 40 µm, which is just larger than the single cells they encapsulate (10 to 35 µm). **(f)** Live/dead staining of encapsulated chondrocytes post encapsulation. SEM images of a cell encapsulating microgel that is **(g)** left intact or **(h)** opened up using focused ion beam milling. **(i)** Fluorescent confocal microscopy image demonstrating complete encapsulation of a single chondrocyte (DiI: red) with stained nucleus (DAPI: blue) within a PEGDA microgel (black) residing in fluorescently labeled dextran solution (FITC: green). **(j)** The cell-laden microgel fraction was enriched by selectively separating cell-laden microgels from microgels containing no cells using flow cytometry-based sorting. **(k)** Distribution of encapsulated cells per microgel after flow cytometry-based enrichment (bars) and Poisson distributions (lines) with λ equal to 0.1 indicating the encapsulation yield of unsorted microgels and λ equal to 1.0 indicating the innate maximum single cell yield of random encapsulation. Black scale bars: 50 µm, white scale bars: 10 µm.

Although these data supported the proficient microencapsulation of cells, it had remained a random process that resulted in a mixed population of microgels containing no cell, a single cell, or multiple cells. Specifically, the number of encapsulated cells per microgel tightly fitted the Poisson distribution that was dependent on the cell concentration of the gel precursor solution.[32] We aimed to overcome this limitation of random encapsulation and thereby to maximize the fraction of single-cell-laden modular building blocks. Although high-yield deterministic single cell encapsulation in culture medium droplets has been shown using inertial focusing[33], these forces are too weak to obtain longitudinal cell ordering in comparatively viscous fluids such as hydrogel precursor solutions. Instead, we exploited fluorescence-activated cell sorting (FACS) to obtain a fraction with maximal single cell yield and minimal amounts of microgels containing no cell or multiple cells (**Figure 6.2j**). Flow cytometry has already been proven to be compatible with high-throughput analysis and sorting of cell-laden microgels.[34-36] Here, we used this technique to break through the paradigm of Poisson-distributed cell encapsulation. To limit the number of multiple-cell-laden microgels, we encapsulated cells at a concentration of 9 million cells per ml of hydrogel precursor. Indeed, our encapsulation strategy resulted in a relatively high amount of microgels containing a single cell and a minimized amount of microgels containing multiple cells. Specifically, the number of encapsulated cells per microgel innately followed the Poisson distribution with lambda (λ) equal to 0.1 (**Figure S6.2**). Consequently, we obtained a cell-laden microgel fraction of only ~10%, while the majority (~90%) of the microgels did not contain any cell (**Figure 6.2j** and **Figure S6.3**). Using flow cytometry, microgels encapsulating fluorescently labeled cells could be readily distinguished from microgels containing no cells (**Figure S6.4**). Labeled sorting increased the cell-laden microgel fraction from 10% to over 90% (**Figure 6.2j**, **Figure S6.5**). Further analysis of the cell number per microgel revealed over 70% single-cell-laden microgels in the enriched population, thereby amply transcending the maximal single cell yield of a Poisson-distributed random cell encapsulation process with λ equal to 1, which is intrinsically limited to ~37% (**Figure 6.2k**). As fluorescent labeling of cells might be suboptimal for some research applications and clinical translations, we explored label-free microgel sorting and demonstrated its feasibility. In particular, the presence of a cell within a microgel increased the forward-scattering and side-scattering of light, as compared to a microgel containing no cells (**Figure S6.6**). Exploiting this feature, we were able to enrich the population of cell containing microgels from 10% to almost 70% in a label-free manner, with a single cell yield of 50% (**Figure S6.7**). As cell expansion represents a major cost-determining factor in for example cell-based therapies, it is of importance to note that both sorting processes were nearly void of cell wastage. Almost none (<2.5%) of the cell-laden microgels were discarded, indicating the subtlety and precision of this enrichment method (**Figure 6.2j**, **Figure S6.8**). It is expected that by selecting more stringent sorting parameters, the percentage of single-cell-laden microgels could be even further increased, although it might be at the expense of increased cell wastage. Altogether, by incorporating our current sorting strategy in the production process, we

were able to generate single-cell-laden microgels with an encapsulation yield of 90% in a high-throughput manner.

6.3.2 Single Cell Microgel-based Modular Bio-inks

A plethora of materials and processing techniques are currently being developed for the fabrication of cell-based constructs.[37] Conventionally, these biomaterials are archetypal a homogenous matrix in which individual cells are dispersed. In contrast, natural tissues are characterized by a multiscale hierarchical design, which provides tissues with spatially distinct compositions. Oversimplifying engineered tissues by neglecting this modular design limits their functionality. Here, we leveraged our microgels as building blocks to create modular bio-inks that allow engineering of tissues with distinct material compositions at the micro- and macrolevel. This uncoupling enables novel material combinations and integration of multiple biochemical and biomechanical functions with single cell resolution. In order to expedite the translation of our multiscale modular approach, we have mixed our single cell building blocks with several clinically relevant materials and explored the compatibility of these bio-inks with various commonly used biofabrication processes. Specifically, microgels were incorporated in macroconstructs of PEGDA using photolithography, dextran-tyramine conjugates using emulsification, collagen using injection molding, alginate/gelatin methacryloyl (GelMA) mixtures using 3D printing, and alginate using wet spinning and subsequent weaving (**Figure 6.3a-e**). Homogeneous distribution of microgels within distinct macromaterial was observed for all biomaterial combinations and fabrication techniques using fluorescent confocal microscopy. This mix-and-match approach successfully produced 3D biomaterials for all tested combinations and fabrication techniques, which demonstrates the universal applicability of this novel form of high-resolution modular tissue engineering.

6.3.3 Controlling the Modular Construct Composition by Tuning the Microgel Concentration

An important design parameter of modular bio-inks when engineering tissues is the concentration of microgels per macrogel volume. This ratio determines several of the construct's biological and biomechanical properties. For example, a low concentration of microgels allows for a more dominant role of the macrogel, potentially providing tissue constructs with for example excellent mechanical properties (**Figure 6.4a**). This creates novel opportunities for engineering tissues that are characterized by a low cell density such as cartilaginous tissues, which contain a low density of individual cell niches with a large volume of mechanically stable ECM. Conversely, a high microgel concentration enables the macrogel to act as a biological glue, indeed confining the specialized microniches in minimal spatial manner (**Figure 6.4b**). Importantly, the single-cell-laden microgel concentration also determines the cell seeding density of the construct. Although cell concentrations are tissue dependent, their physiological range lies mostly between 10^6 and 10^8 cells per cm^3 tissue.[38-40] Concerning this, we would like to highlight the drastic impact of single-cell-laden microgels' size on the maximum

number of cells that can be seeded into a 3D construct. Therefore, we calculated the total number of cells in one cm^3 construct that contains only single-cell-laden microgels, as a function of microgel diameter. Importantly, we assumed that single-cell-laden microgels are produced with relatively low encapsulation yield (10%); a common strategy to prevent the formation of multi-cell microgels resulting from innate Poisson statistics.[32, 35]. Furthermore, we assumed a maximum sphere packing density of 75%, based on the theoretical limit of spheres packed in three dimensions.[41] **Figure 6.4c** clearly demonstrates that typically reported microgels with a diameter of 100 µm could barely result in 10^5 cells per cm^3 (black dashed line). Microgels with a diameter below 50 µm are required to reach natural densities of $\geq 10^6$ cells per cm^3. Opportunely, combining our microencapsulation platform with flow cytometry-based enrichment even boosted the theoretical maximum cell seeding density of constructs composed of these single cell building blocks to $>10^7$ per cm^3 (red dashed line). Attaining these cell concentrations enables the use of single-cell-laden microgels in cell-laden biomaterial-based therapies, which may require such high cell seeding concentrations to achieve proper clinical outcomes. Besides the cell seeding density argument, smaller single-cell-laden microgels are also favorable from a pharmacological perspective, as they are characterized by faster diffusion time of solutes (e.g. nutrients and cytokines) and relatively small gel to cell volume ratios, for example maximizing screening efficiency (**Figure S6.9**).

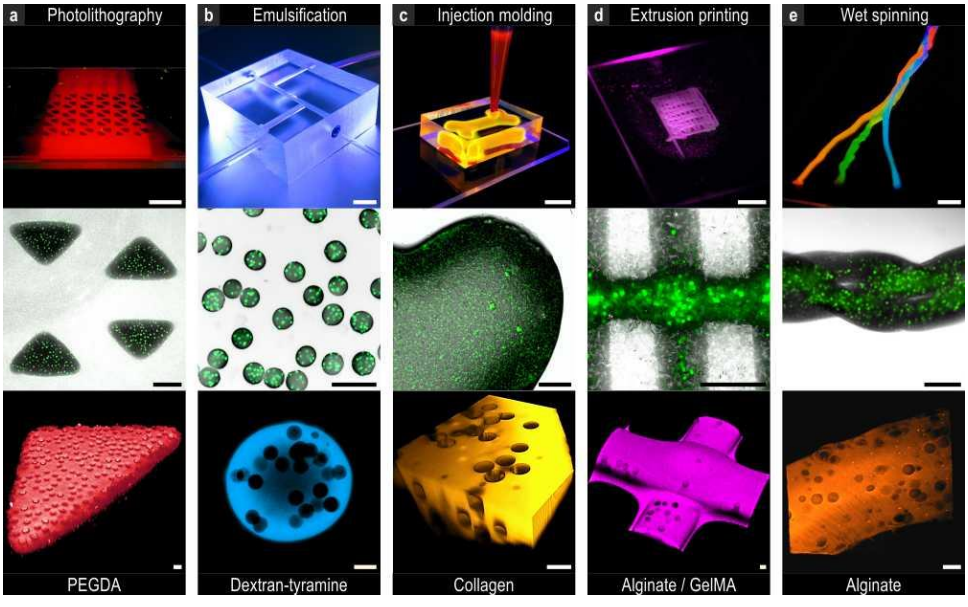

Figure 3. Biofabrication of 3D constructs using modular bio-inks. Standard biofabrication techniques (top) were exploited for the production of 3D constructs (middle) that contained PEGDA microgels as modular building blocks incorporated into a variety of injectable macromaterials (bottom). Fluorescent (confocal) imaging confirmed the homogeneous distribution of microgels throughout the constructs. The constructs were fabricated by **(a)** photopatterning PEGDA, **(b)** emulsifying dextran-tyramine, **(c)** injection molding collagen, **(d)** extruding alginate/GelMA, or **(e)** wet spinning and subsequent weaving alginate. Top scale bars: 5000 µm, middle scale bars: 500 µm, bottom scale bars: 50 µm.

Another major opportunity of modular biomaterials lies in the straightforward reduction of growth factor amount that is commonly required for tissue engineering applications. Conventionally, cell-based tissue-engineered constructs are homogeneously endowed with a supraphysiological payload of growth factors, peptides or small molecules. This is often necessitated by our desire to steer the encapsulated cells' proliferation, migration or function. However, in clinical trials these bulk loads of e.g. growth factors are frequently the main cause of adverse effects such as tissue inflammation, vessel leakage, and even cancer formation.[42, 43] The modular nature of our bio-inks allows for site-specific – or even cell-specific – growth factor incorporation in either the micro or macroenvironment, enabling considerable minimization of total growth factor amounts. To illustrate the significant potential of the modular bio-ink's uncoupled micro- and macroenvironments, we calculated the relative matrix composition of one cm^3 modular construct as a function of microgel number (**Figure 6.4d**). For example, by only administering cell stimulating growth factors to the microgels in implants with a single-cell-laden microgel load of 10^6 per cm^3, the required amount of growth factors could be reduced by >99%. In short, the use of single cell microgel-based bio-inks could reduce the amount of incorporated growth factor by two orders of magnitude while maintaining physiological concentrations around the cells. This may not only prevent potential adverse effects, but also lower therapy costs without affecting the biological performance of the construct, thus supporting clinical translation on several fronts.

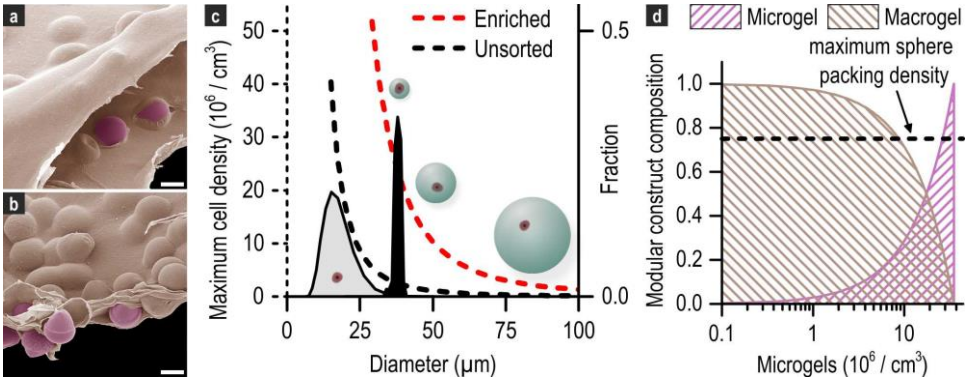

Figure 4. Effects of microgel concentration on modular construct composition. PEGDA microgels were seamlessly incorporated into an agarose bulk hydrogel at both **(a)** low and **(b)** high concentrations and imaged using SEM. SEM images were pseudo-colored, showing PEGDA in pink and agarose in beige. **(c)** The maximum cell seeding density is determined by the microgel diameter (i.e. black dashed line). Importantly, microgels smaller than 50 µm are required to yield cell seeding densities above one million per cm^3 construct. Enriching the cell-laden microgel fraction using flow cytometry-based sorting tremendously increased the theoretical cell seeding density of a construct packed with single cell microgels (i.e. red dashed line) to more than 20 million cells per cm^3 of construct, compared to a mere 2 million in case of using unsorted single-cell-laden microgels of 38 µm. The size distributions of single cells and single-cell-laden microgels are indicated in black and gray, respectively. **(d)** The microgel concentration determines the volume ratio of micro- and macromaterial. When using 38 µm single-cell-laden microgels at a typical concentration for tissue-engineered implants of one million per cm^3, the micromaterial merely makes up 1% of the total construct volume. Scale bars: 10 µm.

Finally, we demonstrated that our modular bio-inks integrate the functions of multiple biomaterials into a single 3D construct. In particular, we aimed to fabricate a 3D construct providing both biomaterial-based immunoprotection and vascularization. Although these two characteristics are not compatible in conventional approaches, using modular bio-ink both functions could be readily incorporated in a single construct through its uncoupled micro- and macroenvironments.

6.3.4 Modular Bio-ink to Uncouple Cellular Micro- and Macroenvironments

Currently, cell transplantations almost exclusively rely on autologous and allogeneic sources, which are typically only available in limited quantities.[44] Genetically modified xenogeneic sources could offer an alternative and are available in relatively copious quantities.[45] However, non-autologous cell transplantations are still hampered by the host-versus-graft immune response and therefore require constant immunosuppressive treatments. Shielding non-autologous cells from the host's immune system can be achieved by encapsulating the cells in a specific permselective microgel. PEGDA hydrogels have previously been demonstrated to render the construct with such immunoprotective properties.[46, 47] However, PEGDA cannot be remodeled in vivo and thus impedes blood vessel invasion, host integration and implant survival. A modular approach using PEGDA-based single cell building blocks inside a distinct biomaterial enables the engineering of a multifunctional tissue construct that provides both immunoprotective and pro-angiogenic functions. Using diffusion assays with fluorescently labeled dextran and proteins, we confirmed that micrometer-sized PEGDA gels provide similar immunoprotective capacity as the previously reported larger constructs (**Figure 6.5a**, **Figure S6.10**). In particular, they blocked the penetration of molecules with a hydrodynamic diameter larger than approximately 10 nm (**Figure 6.5b**). Besides controlling the cell's microenvironment, our bio-ink's multiscale modularity enables the independent engineering of the construct's macromaterial. Due to the spherical nature of the microgels, the macromaterial maintains an interconnected network. Therefore, it can function as a conduit for cellular ingrowth and thus act, for example, as a highway for vascularization, enabling all microgels to be located within micrometers of a vascular network. To demonstrate this, we formed a modular bio-ink composed of immunoprotective single cell PEGDA microgels, endothelial cells, MSCs and pro-angiogenic fibrinogen macromaterial solution, which was solidified using thrombin to form 3D multifunctional constructs. Within one week of culturing these constructs, the angiogenic cells in the macromaterial assembled into a CD31-positive prevascular network that permeated throughout the construct (**Figure 6.5c**). We observed bridging and encapsulation of microgels by the endothelial network in the macromaterial (**Figure 6.5d,e**). The single-cell-laden microgels were seamlessly integrated within the macrogel, while maintaining their immunoprotective capacity, proving the construct's multifunctionality (**Figure 6.5f,g**). Importantly, confocal microscopy confirmed that none of the cells in the macromaterial penetrated any of the microgels, corroborating the existence of the immunoprotective microenvironments within a prevascularized macromaterial (**Figure 6.5h**). We leveraged this approach by

coculturing different cell types in the uncoupled micro- and macroenvironments of these 3D multifunctional constructs. Specifically, MSCs were encapsulated in immunoprotective PEGDA microgels, which were then incorporated in endothelial cell and MSC containing fibrin (**Figure 6.5i**). In principle, this approach prevents exposure of the microencapsulated cells to the host's immunoglobulins, while preserving the diffusion of their nutrients, waste products and signaling molecules, such as growth factors (**Figure 6.5j**). The microgels' small diameter enables the vascular network to establish within micrometers of the microencapsulated cells, enabling fast response to cytokines in the blood, as well as unhampered diffusion of nutrients and waste, thereby abating necrosis that is often observed in scaffolds offering immunoprotection.[48] Potentially, non-autologous cells encapsulated in an immunoprotective microenvironment can be utilized in a variety of standard transplantation procedures, such as stem cell therapies. In short, modular bio-inks can simultaneously provide cell-centric microenvironments, for example immunoprotection for non-autologous cells, as well as host-centric macroenvironments such as integration, anastomosis, and implant survival.

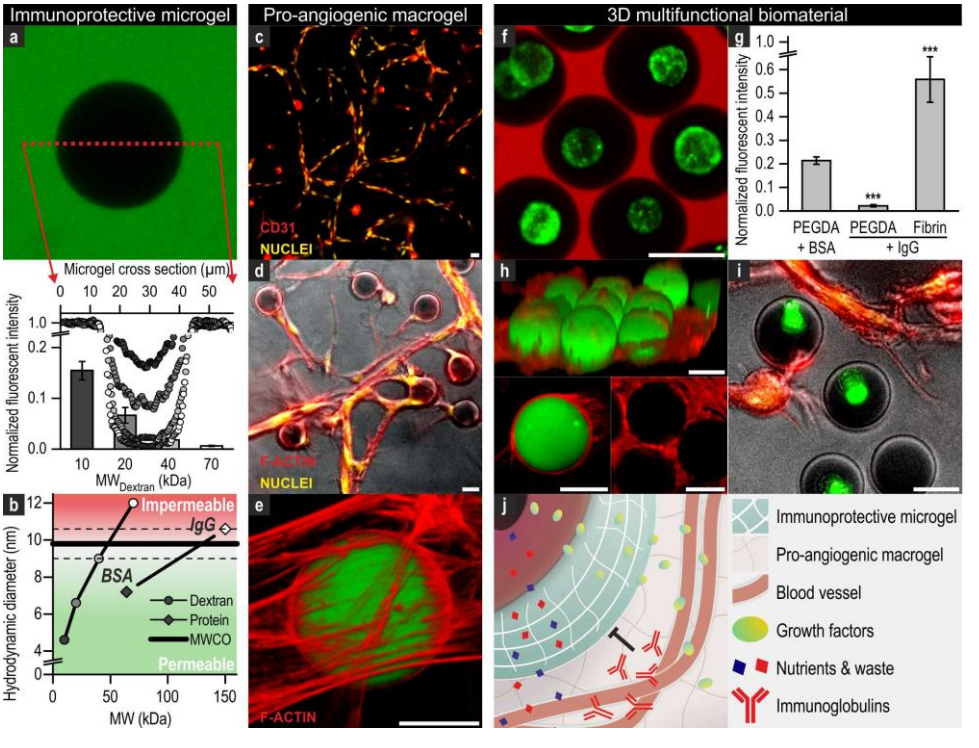

Figure 5. Multifunctional biomaterials with uncoupled micro- and macroenvironments fabricated using modular bio-ink. **(a)** The micromaterial's permselectivity was determined by measuring fluorescent intensities across PEGDA microgels (circles) using fluorescent confocal microscopy after six days of incubation in solutions with fluorescently labeled dextrans of various molecular weights, with darker data points representing lower molecular weights. The bars represent the average intensities of the microgels' centers. **(b)** Dextran and protein diffusion assays indicated that the microgels are permeable

to molecules with a hydrodynamic diameter below 10 nm. Multifunctional modular biomaterial was produced by embedding the immunoprotective PEGDA microgels in a pro-angiogenic fibrin macrogel. The endothelial cells in the macromaterial formed a **(c)** CD31-positive interconnected network that **(d)** bridged and **(e)** encapsulated the microgels. **(f)** Single cell (green) PEGDA microgels seamlessly integrated with fibrin macrogel, while maintaining immunoprotective properties, demonstrated by impermeability to fluorescently labeled 70 kDa dextran (red) and **(g)** IgG, while allowing permeation of BSA. **(h)** Confocal imaging confirmed that endothelial cells spread throughout the macrogel, but did not penetrate any of the microgels. **(i)** Proof-of-concept of a 3D multifunctional modular biomaterial with an uncoupled cellular micro- and macroenvironment where microencapsulated MSCs (green) are immunoprotected, while cocultured with endothelial cells and MSCs (red with yellow nuclei) in a pro-angiogenic macroenvironment. **(j)** Schematic depicting the concept of a multifunctional biomaterial that contains immunoprotective single-cell-laden microgels embedded in a pro-angiogenic macromaterial. *** $p < 0.001$. Scale bars: 25 μm.

6.4 Conclusion

In summary, high-throughput microfluidics and flow cytometry-based sorting technologies enabled the production of small (<40 μm) single-cell-laden microgels with near pure (>90%) encapsulation yield. These microgels could be mixed-and-matched with numerous biomaterials to create multiple modular bio-inks, which were proven to be compatible with various standard biofabrication techniques to fabricate 3D multifunctional biomaterials. Uniquely, this approach could exploit the individual materials' advantages, while limiting or omitting their drawbacks. Specifically, the use of modular bio-inks enabled uncoupled optimization of the biomaterials bulk and the cell's microenvironment with a single cell resolution, which was thus far impossible. Finally, the modular bio-ink-based approach's throughput, versatility, straightforward, and cost-effective nature primes it for rapid adoption in a myriad of clinically relevant applications.

6.5 Supplementary Information

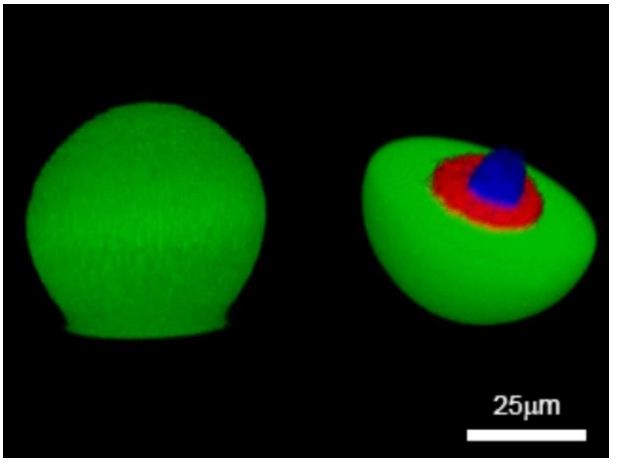

Figure S6.1. Three-dimensional reconstruction of a single-cell-laden microgel. Confocal microphotographs of a PEGDA microgel (green) encapsulating a single fluorescently labeled cell (DiI: red; DAPI: blue) were reconstructed by z-stacking using ImageJ software. The partially flattened bottom of the intact microgel (left) is an optical artefact caused by autofluorescence of the wells plate.

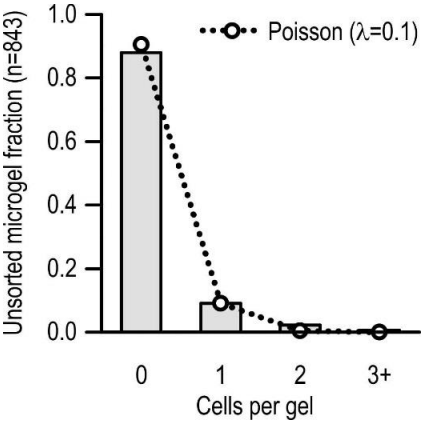

Figure S6.2. The unsorted microgel fraction tightly followed the Poisson distribution with λ equal to 0.1.

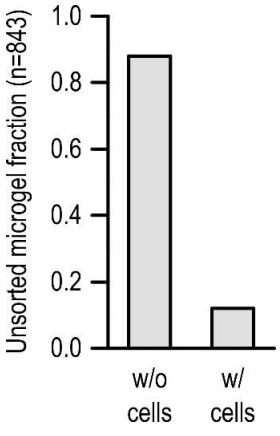

Figure S6.3. Before flow cytometry-based sorting, only ~10% of the microgels contained cells, while the majority (~90%) of microgels contained no cells.

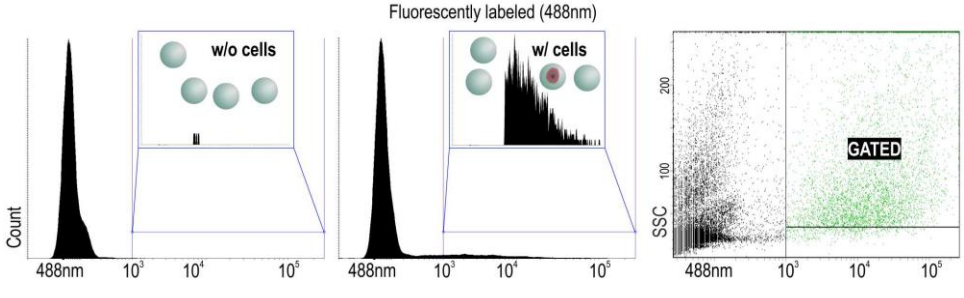

Figure S6.4. FACS histograms and dot plots of empty vs fluorescently labeled cell-laden microgel suspensions. Microgels encapsulating fluorescently labeled cells could be sorted based on their fluorescent intensity by gating the fluorescent detector channel.

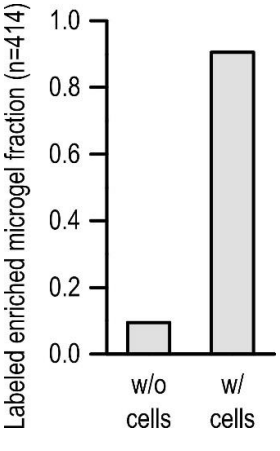

Figure S6.5. Fluorescence-based sorting increased the cell-laden microgel fraction to >90%.

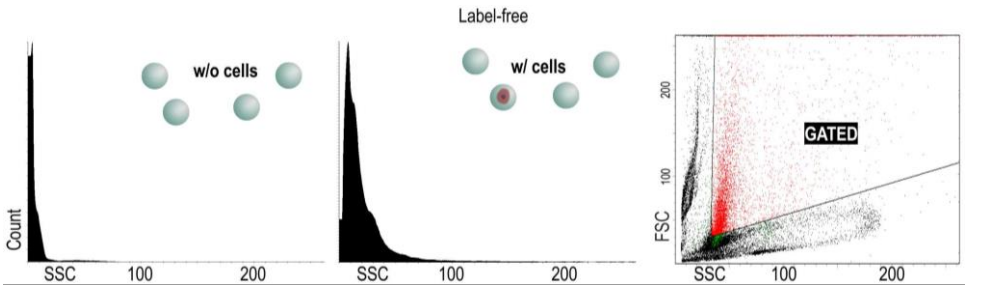

Figure S6.6. FACS histograms and dot plots of empty vs cell-laden microgel suspensions. Label-free sorting could be achieved by exploiting the difference in forward-scattering (FSC) and side-scattering (SSC) of empty vs cell-laden microgel suspensions.

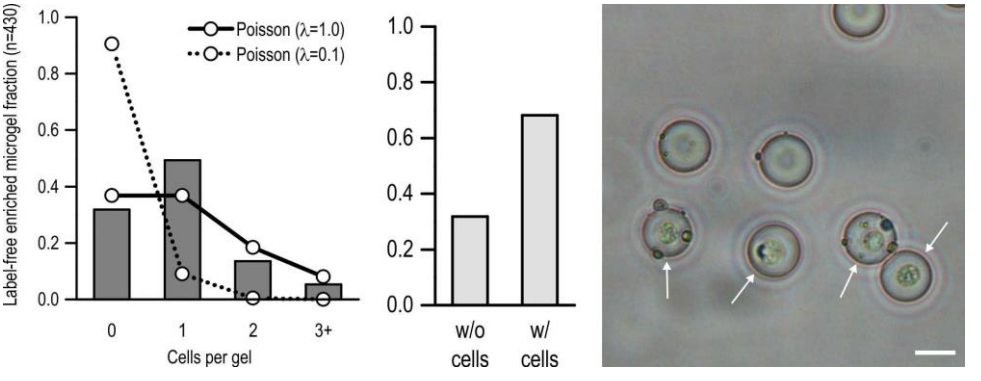

Figure S6.7. Label-free sorting increased the single cell yield by ~500%, as compared to the unsorted microgel fraction that tightly followed the Poisson distribution with λ equal to 0.1. The single cell yield of the enriched microgel fraction even amply transcended the innate limitation (~37%) of a Poisson-distributed cell encapsulation process with λ equal to 1. After label-free sorting, ~70% of the microgels contained cells (white arrows). Scale bar 25 µm.

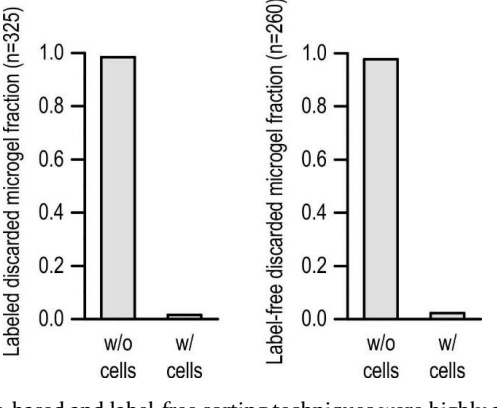

Figure S6.8. Fluorescence-based and label-free sorting techniques were highly accurate, since with both methods >97.5% of the discarded microgels did not contain a cell.

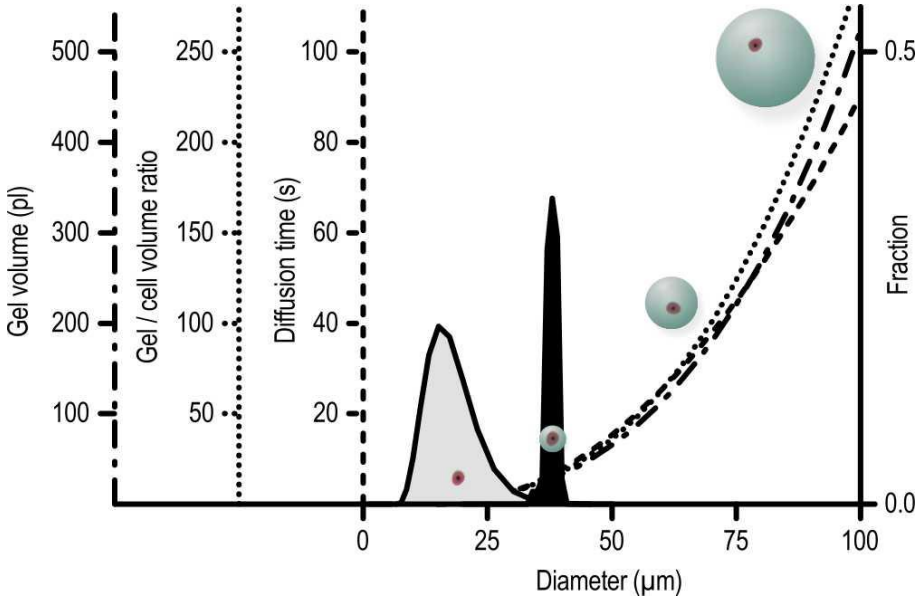

Figure S6.9. Increasing the microgel diameter drastically affects its volume, the gel to cell volume ratio and the estimated diffusion time of solutes ($D = 10^{-7}$). The lower single-cell-laden microgel diameter limit was determined by the size of single cells (10-35 µm). Our single-cell-laden microgels measured 35-40 µm in diameter.

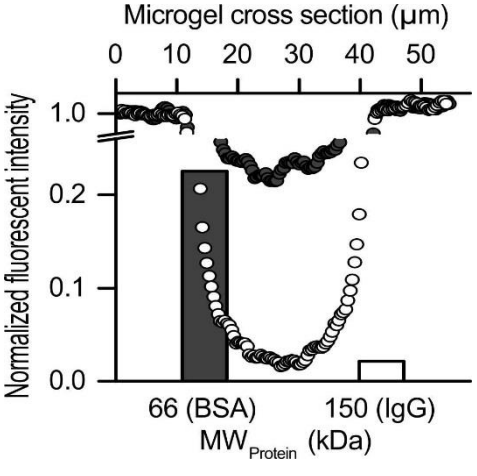

Figure S6.10. The micromaterial's permselectivity was determined by measuring fluorescent intensities across PEGDA microgels (circles) using fluorescent confocal microscopy after six days of incubation in solutions with fluorescently labeled proteins BSA (grey) and IgG (white). The bars represent the average intensities of the microgels' centers.

References

1. Liu, J.S. and Z.J. Gartner, *Directing the assembly of spatially organized multicomponent tissues from the bottom up.* Trends Cell Biol, 2012. **22**(12): p. 683-91.
2. Macri, L., D. Silverstein, and R.A. Clark, *Growth factor binding to the pericellular matrix and its importance in tissue engineering.* Adv Drug Deliv Rev, 2007. **59**(13): p. 1366-81.
3. Hall, P.A. and F.M. Watt, *Stem cells: the generation and maintenance of cellular diversity.* Development, 1989. **106**(4): p. 619-33.
4. Hollister, S.J. and W.L. Murphy, *Scaffold translation: barriers between concept and clinic.* Tissue Eng Part B Rev, 2011. **17**(6): p. 459-74.
5. Du, Y., et al., *Sequential assembly of cell-laden hydrogel constructs to engineer vascular-like microchannels.* Biotechnol Bioeng, 2011. **108**(7): p. 1693-703.
6. Tiruvannamalai-Annamalai, R., D.R. Armant, and H.W. Matthew, *A glycosaminoglycan based, modular tissue scaffold system for rapid assembly of perfusable, high cell density, engineered tissues.* PLoS One, 2014. **9**(1): p. e84287.
7. McGuigan, A.P. and M.V. Sefton, *Vascularized organoid engineered by modular assembly enables blood perfusion.* Proc Natl Acad Sci U S A, 2006. **103**(31): p. 11461-6.
8. Huebsch, N., et al., *Matrix elasticity of void-forming hydrogels controls transplanted-stem-cell-mediated bone formation.* Nat Mater, 2015. **14**(12): p. 1269-77.
9. Santo, V.E., et al., *Enhancement of osteogenic differentiation of human adipose derived stem cells by the controlled release of platelet lysates from hybrid scaffolds produced by supercritical fluid foaming.* J Control Release, 2012. **162**(1): p. 19-27.
10. Levato, R., et al., *Biofabrication of tissue constructs by 3D bioprinting of cell-laden microcarriers.* Biofabrication, 2014. **6**(3): p. 035020.
11. Selimovic, S., et al., *Microscale Strategies for Generating Cell-Encapsulating Hydrogels.* Polymers (Basel), 2012. **4**(3): p. 1554.
12. Headen, D.M., et al., *Microfluidic-based generation of size-controlled, biofunctionalized synthetic polymer microgels for cell encapsulation.* Advanced Materials, 2014. **26**(19): p. 3003-8.
13. Rossow, T., et al., *Controlled synthesis of cell-laden microgels by radical-free gelation in droplet microfluidics.* Journal of the American Chemical Society, 2012. **134**(10): p. 4983-9.
14. Ashida, T., S. Sakai, and M. Taya, *Propagation of human iPS cells in alginate-based microcapsules prepared using reactions catalyzed by horseradish peroxidase and catalase.* Artif Cells Nanomed Biotechnol, 2015: p. 1-4.
15. Tan, W.H. and S. Takeuchi, *Monodisperse Alginate Hydrogel Microbeads for Cell Encapsulation.* Advanced Materials, 2007. **19**(18): p. 2696-2701.
16. Kumachev, A., et al., *High-throughput generation of hydrogel microbeads with varying elasticity for cell encapsulation.* Biomaterials, 2011. **32**(6): p. 1477-83.
17. Ma, Y., et al., *Artificial microniches for probing mesenchymal stem cell fate in 3D.* Biomater. Sci., 2014. **2**(11): p. 1661-1671.
18. Allazetta, S., et al., *Cell-Instructive Microgels with Tailor-Made Physicochemical Properties.* Small, 2015. **11**(42): p. 5647-56.
19. Aikawa, T., et al., *Spherical phospholipid polymer hydrogels for cell encapsulation prepared with a flow-focusing microfluidic channel device.* Langmuir, 2012. **28**(4): p. 2145-50.
20. Ma, B., et al., *Gene expression profiling of dedifferentiated human articular chondrocytes in monolayer culture.* Osteoarthritis Cartilage, 2013. **21**(4): p. 599-603.
21. Both, S.K., et al., *A rapid and efficient method for expansion of human mesenchymal stem cells.* Tissue Eng, 2007. **13**(1): p. 3-9.
22. Mann, B.K., et al., *Smooth muscle cell growth in photopolymerized hydrogels with cell adhesive and proteolytically degradable domains: synthetic ECM analogs for tissue engineering.* Biomaterials, 2001. **22**(22): p. 3045-51.
23. Moon, J.J., S.H. Lee, and J.L. West, *Synthetic biomimetic hydrogels incorporated with ephrin-A1 for therapeutic angiogenesis.* Biomacromolecules, 2007. **8**(1): p. 42-9.
24. Mann, B.K., R.H. Schmedlen, and J.L. West, *Tethered-TGF-beta increases extracellular matrix production of vascular smooth muscle cells.* Biomaterials, 2001. **22**(5): p. 439-44.

25. Lutolf, M.P., et al., *Synthetic matrix metalloproteinase-sensitive hydrogels for the conduction of tissue regeneration: engineering cell-invasion characteristics.* Proc Natl Acad Sci U S A, 2003. **100**(9): p. 5413-8.
26. Anna, S.L. and H.C. Mayer, *Microscale tipstreaming in a microfluidic flow focusing device.* Physics of Fluids, 2006. **18**(12): p. 121512.
27. Garstecki, P., H.A. Stone, and G.M. Whitesides, *Mechanism for flow-rate controlled breakup in confined geometries: a route to monodisperse emulsions.* Phys Rev Lett, 2005. **94**(16): p. 164501.
28. Holtze, C., et al., *Biocompatible surfactants for water-in-fluorocarbon emulsions.* Lab on a Chip, 2008. **8**(10): p. 1632-9.
29. Franco, C.L., J. Price, and J.L. West, *Development and optimization of a dual-photoinitiator, emulsion-based technique for rapid generation of cell-laden hydrogel microspheres.* Acta Biomater, 2011. **7**(9): p. 3267-76.
30. Alhadlaq, A., et al., *Adult stem cell driven genesis of human-shaped articular condyle.* Annals of Biomedical Engineering, 2004. **32**(7): p. 911-23.
31. Dhariwala, B., E. Hunt, and T. Boland, *Rapid Prototyping of Tissue-Engineering Constructs, Using Photopolymerizable Hydrogels and Stereolithography.* Tissue Eng, 2004. **10**(9): p. 1316-1322.
32. Collins, D.J., et al., *The Poisson distribution and beyond: methods for microfluidic droplet production and single cell encapsulation.* Lab on a Chip, 2015. **15**(17): p. 3439-59.
33. Kemna, E.W., et al., *High-yield cell ordering and deterministic cell-in-droplet encapsulation using Dean flow in a curved microchannel.* Lab on a Chip, 2012. **12**(16): p. 2881-7.
34. Tumarkin, E., et al., *High-throughput combinatorial cell co-culture using microfluidics.* Integr Biol (Camb), 2011. **3**(6): p. 653-62.
35. Eun, Y.J., et al., *Encapsulating bacteria in agarose microparticles using microfluidics for high-throughput cell analysis and isolation.* ACS Chem Biol, 2011. **6**(3): p. 260-6.
36. Li, C.Y., et al., *Flow-based pipeline for systematic modulation and analysis of 3D tumor microenvironments.* Lab on a Chip, 2013. **13**(10): p. 1969-78.
37. Hunt, N.C. and L.M. Grover, *Cell encapsulation using biopolymer gels for regenerative medicine.* Biotechnol Lett, 2010. **32**(6): p. 733-42.
38. Del Monte, U., *Does the cell number 10(9) still really fit one gram of tumor tissue?* Cell Cycle, 2009. **8**(3): p. 505-6.
39. Quinn, T.M., et al., *Cell and matrix morphology in articular cartilage from adult human knee and ankle joints suggests depth-associated adaptations to biomechanical and anatomical roles.* Osteoarthritis Cartilage, 2013. **21**(12): p. 1904-1912.
40. Miller, C.C., et al., *Validation of a morphometric method for evaluating fibroblast numbers in normal and pathologic tissues.* Experimental Dermatology, 2003. **12**(4): p. 403-11.
41. Hales, T.C., *A Proof of the Kepler Conjecture.* Annals of Mathematics, 2005. **162**(3): p. 1065-1185.
42. Vajanto, I., et al., *Evaluation of angiogenesis and side effects in ischemic rabbit hindlimbs after intramuscular injection of adenoviral vectors encoding VEGF and LacZ.* Journal of Gene Medicine, 2002. **4**(4): p. 371-80.
43. Carragee, E.J., E.L. Hurwitz, and B.K. Weiner, *A critical review of recombinant human bone morphogenetic protein-2 trials in spinal surgery: emerging safety concerns and lessons learned.* Spine Journal, 2011. **11**(6): p. 471-91.
44. Matsumoto, S., *Clinical allogeneic and autologous islet cell transplantation: update.* Diabetes Metab J, 2011. **35**(3): p. 199-206.
45. Reardon, S., *New life for pig-to-human transplants.* Nature, 2015. **527**(7577): p. 152-4.
46. Cruise, G.M., et al., *In vitro and in vivo performance of porcine islets encapsulated in interfacially photopolymerized poly(ethylene glycol) diacrylate membranes.* Cell Transplant, 1999. **8**(3): p. 293-306.
47. Pathak, C.P., A.S. Sawhney, and J.A. Hubbell, *Rapid photopolymerization of immunoprotective gels in contact with cells and tissue.* Journal of the American Chemical Society, 1992. **114**(21): p. 8311-8312.
48. Avgoustiniatos, E.S. and C.K. Colton, *Effect of external oxygen mass transfer resistances on viability of immunoisolated tissue.* Ann N Y Acad Sci, 1997. **831**: p. 145-67.

7

In-air Microfluidics Enables Rapid Fabrication of Emulsions, Suspensions, and 3D Modular (Bio)materials

Microfluidic chips provide unparalleled control over droplets and jets, which has advanced all natural sciences. However, focusing on a chip-based approach only limits the full potential of microfluidics. Microfluidic applications could be vastly expanded by increasing the per-channel throughput and directly exploiting the output of chips for rapid additive manufacturing. Here we unlock these features using in-air microfluidics, a new chip-free concept to manipulate microscale liquid streams in the air. By controlling the composition and impact of liquid microjets, we demonstrate the production of monodisperse emulsions, particles, and fibers at rates that are 10 to 100 times higher as compared to chip-based droplet microfluidics. Furthermore, in-air microfluidics uniquely enables module-based production of 3D multiscale (bio)materials in one step, as droplets can be solidified in-flight and immediately be deposited onto a substrate. Through its combination of in-line control, high throughput, and cytocompatibility, in-air microfluidics provides an enabling platform technology for science, industry, and health care.

Tom Kamperman†, Claas Willem Visser†, Lisanne Karbaat, Detlef Lohse, and Marcel Karperien

† authors contributed equally to this work.

Contribution TK: conception, experimental design, experimental performance, and manuscript writing.

Accepted for publication in Science Advances.

7.1 Introduction

The miniaturization of fluidics using microfluidic chips offers predictable flow behavior and in-line liquid manipulation and monitoring.[1, 2] The level of control and versatility of microfluidics has resulted in tremendous progress and integration of many research areas. Microfluidic chips have, for example, been proven perfectly suitable for the production of monodisperse emulsions and suspensions that encapsulate food, drugs and even cells.[3-6] By further leveraging microfluidics' high resolution and in-line control, microparticles and -fibers with a variety of compositions and shapes have been engineered.[7-11] However, despite their success in lab-scale applications, the conventional chip-based approach has also some intrinsic limitations that have been hampering microfluidics' widespread use in clinical and industrial settings.[12-14] First, on-chip emulsification is a relatively slow process. Conventional two-phase (i.e. water/oil) droplet generators smaller than 100 µm have a typical per-nozzle throughput of 1 to 10 µl/min, as monodisperse droplet generation is restricted to the non-jetting regime where the Capillary number Ca < 0.1.[15, 16] Second, the design, fabrication, and operation of microfluidic devices require advanced skills and specialized equipment, which are not always compatible with existing production processes or environments outside the lab.[2, 17] Third, microfluidic chips are closed systems that can only be operated using at least one non-solidifying flow. This co-flow is required to generate and separate droplets, particles, or fibers from each other and the microfluidic channel walls.[4, 18] However, as removing the co-flow (e.g. oil) is not trivial, it not only limits clinical translation, but also interferes with microfluidics' straightforward integration with additive manufacturing processes. An off-chip approach would unlock the full potential of microfluidics by omitting all these wall-induced limitations.

Here we present 'in-air microfluidics' (IAMF), a new concept that enables the chip-free manipulation of microfluidic streams. In concept, microfluidic channels are replaced by micrometer-sized liquid jets that can be combined in the air, thereby maintaining in-line control (**Figure 7.1**). Via the controlled impact of two microjets, this off-chip approach is readily compatible with the production of monodisperse droplets, particles, and fibers at per-nozzle rates that exceed conventional microfluidics up to a 100-fold for a wide range of particle diameters. Moreover, IAMF is compatible with solidifying co-flows, which aids the direct deposition of oil-free in-air formed particles. This capacity uniquely enables the one-step additive manufacturing of 3D multiscale modular (bio)materials. In contrast to chip-based microfluidics, IAMF does not require cleanroom technology, but solely relies on the spatial alignment of individual nozzles. Its facile and open nature primes IAMF for straightforward integration into numerous academic and industrial applications.

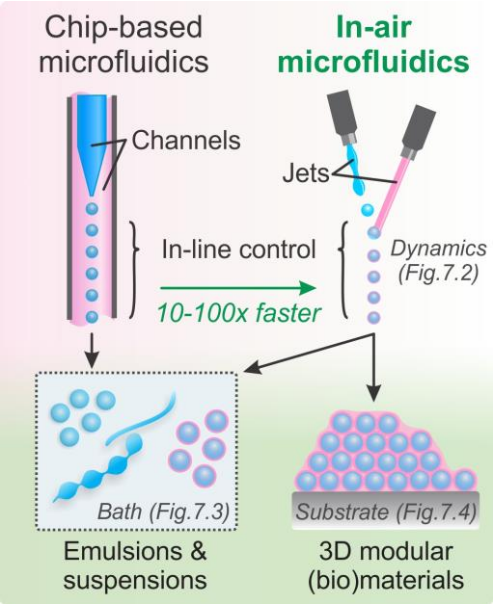

Figure 7.1. Chip-based *versus* in-air microfluidics (IAMF). In IAMF, liquid microjets are exploited as an alternative to microfluidic channels. By combining multiple jets, IAMF adopts the in-line control of conventional chip-based microfluidics while omitting all wall-induced drawbacks such as the limited per-nozzle throughput. As a result, monodisperse emulsions and suspensions could be generated at rates that exceed traditional microfluidics by at least one to two orders of magnitude. Furthermore, IAMF's open nature uniquely enables one-step additive manufacturing of 3D multiscale modular materials through the direct deposition of in-air and oil-free produced particles.

7.2 Materials and Methods

7.2.1 Device Preparation and Operation

Liquid jets were ejected from nozzles that consisted of 4±1 mm long fused silica tubing (Idex Health&Science) with an outer diameter of 360 µm and inner diameters of 20 µm, 50 µm, 100 µm, 150 µm, or 250 µm. The nozzles were cut using a Shortix capillary cutter (SGT), and glued into PEEK tubing (Idex Health&Science) with an inner diameter of 0.5 mm and an outer diameter of 1/16" using a quick-set epoxy adhesive (RS 850-956, RS components Ltd.). The PEEK tubing was mounted onto a piezo-electric actuator using two-sided tape (3M) and standard optical components (Thorlabs). The piezo was actuated using a 150 V sine wave. For various nozzle sizes and flow rates, jet break-up into droplets was monitored with a previously described stroboscopic visualization setup.[19] Unless otherwise specified, flow velocities of 1.3±0.2× the minimal flow velocity to obtain jetting were used. Nozzles were of equal diameter and were operated using equal flow velocities unless otherwise specified. Nozzles were aligned using a xyz-stage (Thorlabs), or using an in-house 3D printed hand-held device (**Figure S7.1**). To control the flow rate, a standard syringe pump (PhD 2000, Harvard Apparatus) and plastic syringes were used (5 ml or 10 ml, Luer-Lock, BD). A high-power syringe pump (Harvard

Apparatus) and steel syringes (9 ml, Harvard Apparatus) were used in case excessive pressure drops over the nozzle tip caused the standard syringe pump to stall (i.e. for the 20 µm nozzles). Threaded adapters (Idex Health&Science) were used to connect the syringes to the nozzles. **Table 7.1** provides a per-experiment overview of the used liquids. Small amounts (<0.1%) of dextran-FITC (2000kDa, Sigma-Aldrich) or Rhodamine B (Sigma-Aldrich) were added to enable visualization of the jets, emulsions, and suspensions using fluorescence microscopy.

Table 7.1. Per-experiment overview of used liquids.

Experiment	Fig.	Liquid 1	Liquid 2	Liquid 3 / substrate
Single-phase solid particles	7.2g 7.3d ,g-q	0.5% (w/v) sodium alginate (80 to 120 cP, Wako Chemicals)	0.1 M $CaCl_2$ in a 10% (v/v) ethanol	0.03 – 0.1 M $CaCl_2$ liquid bath
Water-oil single emulsions	7.3b	Water	2% Pico-Surf 1 in Novec 7500, (Dolomite)	Novec 7500 + one drop Pico-Surf 1 liquid bath
Water-oil-water double emulsions	7.3c	Water	2% Pico-Surf 1 in Novec 7500	1% (v/v) sodium dodecyl sulphate (SDS) liquid bath
Single-phase core-shell particles	7.3e	0.2 M $CaCl_2$ + 5 % (v/v) polyethylene glycol (PEG) 400	0.4% (w/v) sodium alginate (5 to 40 cP, Sigma-Aldrich) + 20% (v/v) ethanol	0.03 – 0.1 M $CaCl_2$ liquid bath
Multi-phase core-shell particles	7.3f	5% (w/v) in-house synthesized[20] dextran-tyramine (Dex-TA, 15-30 kDa, DS 15) + 22.5 U/ml horseradish peroxidase + 0.2 M $CaCl_2$	0.4% (w/v) sodium alginate (5 to 40 cP) + 20% (v/v) ethanol + 0.1% (w/v) H_2O_2	20% (v/v) ethanol + 0.05% (w/v) H_2O_2 liquid bath
Liquid-filled foams	7.4b ,c	0.2M $CaCl_2$ + 10% (v/v) PEG 400	0.5% – 2% (w/v) sodium alginate (80 to 120 cP, Sigma-Aldrich) + 20% – 50% (v/v) ethanol	Glass substrate

Multi-material solid freeforms	7.4d	10% (w/v) Dex-TA+34 U/ml horseradish peroxidase+0.2 M $CaCl_2$	0.4% sodium alginate (5 to 40 cP) + 20% (v/v) ethanol + 0.1% (w/v) H_2O_2	Glass substrate
Multimaterial injectables	7.4f-i	5% (w/v) sodium alginate (80 to 120 cP) + 10% (w/v) PEG 12000 + 0.1% (w/v) HO	5% (w/v) dextran-tyramine + 22.5 U/ml horseradish peroxidase + 0.06M CaCl + 10% ethanol	3rd jet: fibrin precursor solution (see section 7.2.3.) Substrate: polydimethyl siloxane (PDMS, Sylgard 184, Dow Corning) mold

7.2.2 Surface Tension

The surface tension of ethanol containing $CaCl_2$ solutions was measured using the hanging drop method on an optical contact angle measuring system (OCA15Pro, Dataphysics). The results overlap with previously reported measurements of ethanol/water mixtures within the experimental error (5%),[21] indicating that $CaCl_2$ had no significant effect on the surface tension (**Figure S7.2**).

7.2.3. Cell Isolation, Expansion, and Encapsulation

Human mesenchymal stem cells (MSCs) were isolated from fresh bone marrow samples and cultured as previously described.[22] The use of patient material was approved by the local ethical committee of the Medisch Spectrum Twente (Enschede, The Netherlands) and informed written consent was obtained for all samples. In short, nucleated cells in the bone marrow aspirates were counted, seeded in tissue culture flasks at a density of $5 \cdot 10^5$ cells/cm² and cultured in MSC proliferation medium, consisting of 10% (v/v) fetal bovine serum (FBS, Sigma-Aldrich), 100 U/ml Penicillin with 100 µg/ml Streptomycin (Gibco), 1% (v/v) GlutaMAX (Gibco), 0.2 mM ascorbic acid (Sigma-Aldrich), and 1 ng/ml basic fibroblast growth factor (ISOkine bFGF, Neuromics, added fresh) in Minimal Essential Medium (MEM) α with nucleosides (Gibco). Cells were cultured under 5% CO2 at 37 °C and medium was replaced 2 to 3 times per week. When cell culture reached near confluence, the cells were detached using 0.25% (w/v) Trypsin-EDTA (Gibco) at 37 °C and subsequently subcultured or used for experimentation. For cell encapsulation, MSCs were suspended in MSC proliferation medium and mixed with 1% (w/v) sodium alginate (80 to 120 cP, Wako Chemicals) in phosphate-buffered saline (PBS, Gibco) in a 1:1 ratio. The cell-laden hydrogel precursor solution was loaded into a disposable syringe and connected to the IAMF setup for encapsulation. After encapsulation, cell-laden microgels were cultured in 6-wells plates (Nunc) with MSC proliferation medium under 5% CO at 37 °C, which was refreshed three times per week. The viability of encapsulated MSCs was analyzed using a live/dead assay

(Molecular Probes) following manufacturer's protocol and visualization using a fluorescence microscope (EVOS FL, Thermo Fisher Scientific). Images were analyzed using ImageJ software and cell viability was quantified via artisan counting. Endothelial cell-laden modular constructs were formed by adding a third jet to the system, which contained fibrin precursor solution and 50 U/ml thrombin solution (Sigma-Aldrich) that were mixed immediately before jetting using a T-junction. Fibrin precursor solution was prepared by suspending HUVECs and MSCs into EGM-2 without FBS supplemented with 10 mg/ml fibrinogen (Sigma-Aldrich). Just before producing the constructs, 5% (v/v) FBS was added to the fibrin precursor solution as previously described.[23] After 5 minutes incubation at room temperature, the constructs were incubated for 20 minutes at 37 C to complete polymerization, after which a 1:1 mixture of MIN6 proliferation medium and EGM-2 was added on top. The constructs were cultured for one week and medium was refreshed every 2 to 3 days. The constructs were then fixated using 4% (w/v) formaldehyde (Sigma-Aldrich), permeabilized using 0.1% (v/v) Triton-X (Sigma-Aldrich), blocked using 10% (w/v) bovine serum albumin (Sigma-Aldrich), and stained using 1:100 anti-CD31 (AB32457, Abcam), 1:100 anti-insulin (AB7842, Abcam), in combination with 1:400 AF488-, TRITC-, or AF647-labeled secondary antibodies, and DAPI as counter staining. All staining solutions were prepared using Hank's Balanced Salt Solution (Sigma-Aldrich), as PBS dissolves the alginate. Alternatively, constructs were impregnated in cryo-matrix (Shandon), cryo-sectioned (7 µm, Leica cryostat), and stained as described. Subsequent imaging was performed using a fluorescence confocal microscope (Nikon A1+).

7.3 Results

7.3.1 Physical Principles of In-air Microfluidics

In IAMF, liquid microjets are manipulated and combined in a gaseous phase (e.g. air). Through controlled jet-breakup using superimposed vibration,[24] IAMF is readily compatible with the generation of monodisperse droplets at jet speed. To prevent the issue of synchronizing continuous droplet streams, we exploited at least one intact jet, which resulted in two distinct collisional modes: i.e. 'drop-jet' (**Figure 7.2a**) and 'jet-jet' (**Figure 7.2b**). The key physical mechanisms of colliding jets are impact, encapsulation, and solidification.

In 'drop-jet' mode, a droplet first impacts onto a jet (**Figure 7.2c**). Importantly, impact must result in coalescence, while droplet bouncing, stretching, or splashing must be prevented.[25] Furthermore, the production of spherical particles requires that the droplet maintains its shape during impact. Both conditions are met if capillary forces dominate inertia, i.e. for impact Weber numbers $We_{impact} \lesssim \rho_1 V_{impact}^2 D_d/\sigma \lesssim 1$, with ρ_1, σ_1, and D_d the droplet density, surface tension, and diameter, respectively.[25] The impact velocity $V_{impact} = V_1 sin\theta$ depends on the impact angle θ and the ejection velocity V_1 of jet 1. Since a significant ejection velocity is required for jet formation (**Figure S7.3**), a relatively small impact angle $\theta = 25° \pm 5°$ was chosen to ensure a low impact Weber

number. High-speed fluorescent imaging confirmed that the droplets maintained virtually spherical during impact onto an intact jet (**Figure 7.2d**) For $We_{impact} \lesssim 1$, the coalescence of the droplets is capillary-driven and therefore occurs at a capillary time scale $\tau_{cap} = \sqrt{\rho_1 D_1^3 \sigma_1 / \mu_1}$,[26] in which μ_1 is the droplet's viscosity.

Rapid in-air stabilization of the compound droplets is essential to prevent them from merging again during flight or upon collection.[27] We therefore encapsulated the droplets using a jet of immiscible (e.g. oil) or reacting (e.g. crosslinker) liquid. To drive this in-air encapsulation, the surface tension of the encapsulating (jet) liquid was reduced with respect to that of the droplet by adding a small amount of ethanol. As a result, a Marangoni flow (i.e. driven by surface tension gradients) pulls a thin film of the low surface-tension liquid around the high surface-tension liquid, as depicted in **Figure 7.2c**. This mechanism allows for encapsulation by both miscible and immiscible liquids,[26, 28, 29] while limiting droplet deformations. The encapsulation process is shown in **Figure 7.2e**, and occurs on a numerically validated time scale $\tau_e \sim \sigma_1 \mathrm{Oh}_1 \tau_{cap} / \Delta\sigma$,[26] with Oh_1 the Ohnesorge number and $\Delta\sigma = \sigma_1 - \sigma_2$. For our experimental conditions, τ_e was comparable to the impact time scale τ_{cap}. Therefore, both impact and encapsulation were completed in the air, prior to collection or deposition which happened typically ~100 ms after in-air impact.

Surface-tension-driven droplet stabilization was demonstrated using a stream of alginate-containing droplets that were solidified via ionotropic crosslinking with $CaCl_2$, which was added to the jet. Impacting these liquids without tuning the surface tension ($\Delta\sigma$ = 0 mN/m) did not induce Marangoni-driven encapsulation and resulted in irregularly shaped alginate microparticles (**Figure 7.2f**). Conversely, introducing a surface tension gradient $\Delta\sigma$ between the aqueous gel precursor and crosslinker liquids enabled in-air encapsulation with minimal mixing and resulted in spherical microparticles (**Figure 7.2g**). **Figure 7.2h** shows the alginate particle shape as a function of the surface tension gradient and the nozzle size. This demonstrated that the IAMF has a level of in-line control that can be leveraged for the all-aqueous (i.e. without oil) production of spherical particles. The regime transition from irregular to spherical particles is observed for $\Delta\sigma \approx 5$ mN/m, as achieved by adding a minimal amount of 0.3% ethanol.

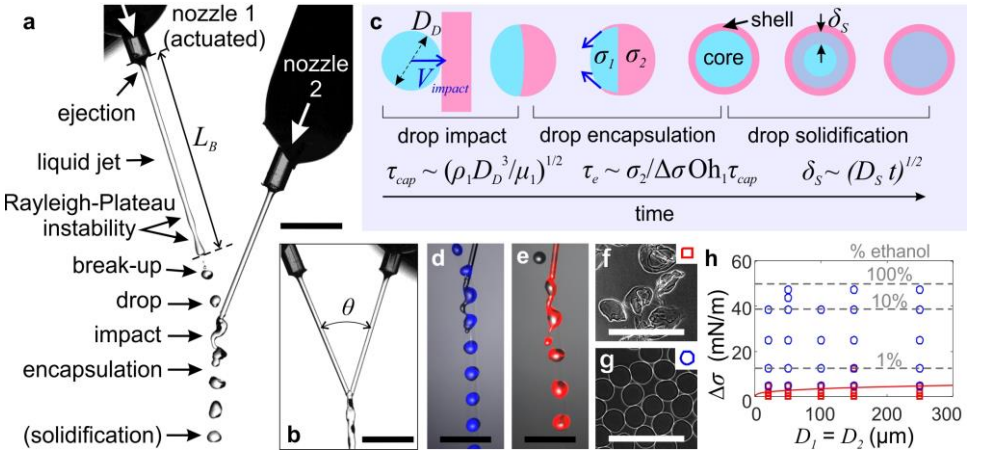

Figure 7.2. Physical principles of IAMF. (a) High-speed photograph of IAMF operated in 'drop-jet' mode. Here, a droplet train is ejected from actuated nozzle 1 and collides with a jet that is ejected from nozzle 2. **(b)** IAMF operated in 'jet-jet' mode. **(c)** Schematic representation of in-air impact, encapsulation, and solidification mechanisms. Different surface tensions ($\sigma_1 > \sigma_2$) result in Marangoni-driven encapsulation of the droplet. **(d,e)** High-speed photographs of the 'drop-jet' mode, in which **(d)** the droplets and **(e)** the jet are selectively labelled with a fluorescent dye. The droplets maintain a spherical shape during impact and encapsulation, while the jet spreads around the droplet within a few diameters of travel. **(f,g)** Alginate microparticles produced **(f)** without and **(g)** with Marangoni-driven encapsulation. **(h)** Phase diagram of particle shape as a function of surface tension gradient $\Delta\sigma$ and the nozzle diameter $D_1 = D_2$. Symbols indicate spherical (○) or irregular (□) particles. The solid line refers to a basic model for the transition between these shape regimes. Black scale bars: 1 mm, white scale bars: 0.4 mm.

It is surprising that the particle shape can be controlled by combining surface-tension-driven encapsulation and solidification, as even a thin solid front could potentially inhibit the Marangoni flow. To provide a first rationalization of this observation, we hypothesize that encapsulation is achieved if the surface tension gradient exceeds the strength of the solidifying film. The thickness of this film is estimated as $\delta_s \sim \sqrt{D_S \tau_e}$, with $D_S \approx 10^{-9}$ m²s⁻¹ the diffusion constant of the $CaCl_2$ into the gel.[30] The strength of the film is estimated as $\sigma_f \delta_S$, where $\sigma_f \approx 10^4$ Pa is the fracture stress of a 0.5% alginate gel.[31] By equating $\sigma_f \delta_S = \Delta\sigma$ and solving for $\Delta\sigma$, one obtains the solid line in **Figure 7.2h**. For the measured parameter regime, the expected film strength lies between 2 mN/m and 5 mN/m, which is remarkably close to the experimental threshold $\Delta\sigma \approx 5$ mN/m. However, the predicted dependence on the diameter is not observed, possibly because the initial solidification dynamics (e.g. time-dependent viscosity gradients) are ignored in our simplified model. Future research on this topic may be of interest, both for IAMF and alternative methods for particle formation.[26, 32, 33]

7.3.2 Engineering Droplets, Particles, and Fibers

By tuning the jets' composition and impact, IAMF can produce monodisperse microfluidic products with various compositions, sizes, and shapes with unparalleled throughputs while maintaining micrometer resolution First, different material

compositions were examined while operating in 'drop-jet' mode, using 100 µm nozzles and a per-nozzle flow rate of 1.3 ml/min (**Figure 7.3a**). Coalescing water droplets onto a surfactant-containing fluorocarbon oil jet (with $\Delta\sigma$ = 50±5 mN/m) readily enabled the production of monodisperse water-in-oil (w/o) emulsions (**Figure 7.3b**). Moreover, collecting these w/o droplets in surfactant-containing water resulted in w/o/w double emulsions (**Figure 7.3c**). IAMF also enabled the oil-free production of monodisperse solid particles such as alginate microspheres (**Figure 7.3d**). Alternatively, liquid-filled capsules were produced by coalescing $CaCl_2$ containing droplets onto an alginate jet with reduced surface tension (**Figure 7.3e**). Solid-filled capsules were made by adding an *in situ* crosslinkable dextran-based hydrogel precursor to the droplet and its crosslinker to the jet (**Figure 7.3f**). IAMF is also compatible with slower (i.e. not in-air) *in situ* solidifying materials, by leveraging alginate as structural template (**Figure S7.4**).[34]

The microfluidic product's size could be tuned by more than an order of magnitude by controlling the nozzle size and actuation frequency (**Figure 7.3g**). Monodisperse alginate microgels with diameters ranging from 20 to 300 µm were produced using nozzles with different diameters (**Figure 7.3h-j**). The droplet or particle diameter could be fine-tuned by altering the actuation frequency f (**Figure 7.3k**). Measuring the particles' size distributions revealed monodisperse (coefficient of variation <5%) products (**Figure 7.3k**, **Figure S7.5**).

The particle shape could be controlled by altering the velocity ratio between the jets (**Figure 7.3l**). Increasing the speed of the crosslinker jet (V_2) while maintaining the same gel precursor droplet speed (V_1) resulted the formation of elongated particles (**Figure 7.3m,n**. Details on the dynamics of particle elongation are provided in **Section S7.1** and **Figure S7.6**. Microfibers were readily produced by operating the same setup in the 'jet-jet' mode, as enabled by simply moving the nozzles closer to each other (**Figure 7.3o**). Fibers of homogeneous thickness were produced as shown in **Figure 7.3p**, where the crosslinker solution impacts with the gel precursor solution close to nozzle 1. Interestingly, with nozzle actuation turned on while moving the jet's impact location closer to the break-up point (i.e. $L \rightarrow L_B$), we could produce a 'beaded' fiber (**Figure 7.3q**). Overview images of particles and fibers are provided in **Figure S7.7**.

The diameter and throughput of IAMF-based droplet and particle generation are compared to chip-based droplet microfluidics in **Figure 7.3r**. As discussed, the lower flow rate of IAMF is bounded by the Weber number We > 1, as IAMF relies on the ejection of liquid jets into the air (**Figure S7.3**). The upper production rate of IAMF is presumably limited by wind-induced breakup, which occurs for gas Weber numbers $We_g = \rho_g/\rho We$ > 0.2, with ρ_g the density of the gas.[35] In contrast, the production of monodisperse droplets using chip-based microfluidics requires We < 0.1 and Ca = $\mu_c V_c/\sigma \lesssim 0.1$, where μ_c and V_c denote the outer phase's viscosity and velocity, respectively, and σ the interfacial tension between the liquids.[15, 16] These constraints imply that IAMF is intrinsically much faster than chip-based droplet microfluidics. Comparing actual IAMF production rates (round markers in **Figure 7.3r**) to those of typical microfluidic droplet generators as reported in the literature (square markers) revealed that IAMF is typically

operated at least two orders of magnitude faster than droplet microfluidics. Noteworthy, a single IAMF nozzle is able to produce droplets at similar production rate as compared to an up-scaled microfluidic chip consisting of 256 parallelized droplet generators (i.e. ~5 ml/min using a ~100 µm nozzle).[36] The high throughput as well as its versatility makes IAMF an interesting new platform for producing droplets, particles, and fibers.

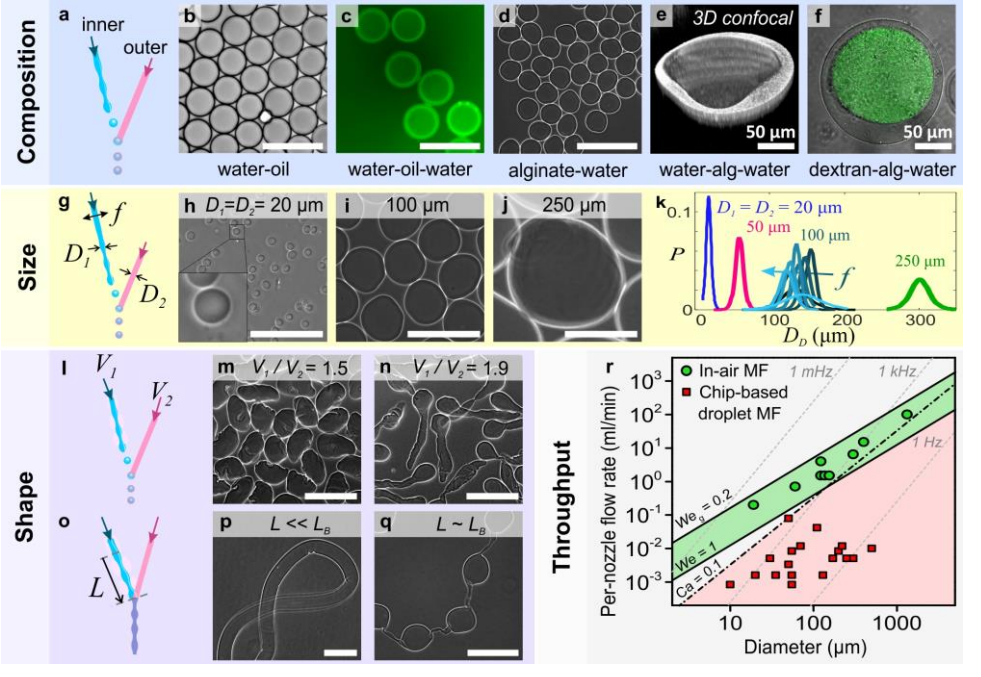

Figure 7.3. IAMF enables high-throughput production of monodisperse microemulsions and -suspensions with various compositions, sizes, and shapes. Schematic diagrams (left) indicate the relevant control parameters. **(a-f)** IAMF operated in 'drop-jet' mode enabled the production of monodisperse **(b)** water-in-oil emulsions, **(c)** double emulsions, **(d)** spherical particle suspensions, **(e)** single- and **(f)** multi-material core-shell particles. **(g-k)** The microparticle size could be tuned by controlling the nozzle size and actuation frequency. Colors from black to pale blue indicate increasing driving frequencies of [2.3, 3.5, 4, 4.5, 5, 6, 7, 8] kHz. **(l-n)** Elongated particles were made by increasing the relative jet velocity. **(o)** IAMF operated in 'jet-jet' mode enabled the production of **(p)** straight and **(q)** 'beaded' fibers **(r)** Throughput as a function of nozzle diameter for IAMF and chip-based droplet microfluidics (MF). The maximum per-nozzle throughput of monodispersed droplet production using chip-based microfluidics is limited by Ca = 0.1 and We = 1. The production throughput window of IAMF is determined by We = 1 (i.e. minimum) and We_g = 0.2 (i.e maximum). Green circles are data points obtained using our IAMF setup. Red squares are data points obtained from previously reported studies on droplet microfluidics.[37-46] Droplet production frequencies are indicated with grey dashed lines. Scale bars: 200 µm unless otherwise indicated.

7.3.3 IAMF Enables One-step Manufacturing of 3D Multiscale Modular Materials

In contrast to chip-based microfluidics, IAMF does not require a non-solidifying co-flow. It is therefore uniquely compatible with the one-step fabrication of 3D multiscale modular materials via the direct deposition of in-air formed particles or capsules onto a

substrate. To prove this concept, an alginate jet was impacted onto $CaCl_2$ droplets with higher surface tension, resulting in a stream of shape-stable core-shell alginate particles. Upon deposition onto a substrate, these partially crosslinked particles stick together such that a larger 3D modular freeform was formed (**Figure 7.4a**). As an example, we created a hollow hydrogel cylinder by the directed deposition of such core-shell particles onto a rotating substrate (**Figure 7.4b**, **Figure S7.8**). The microscale architecture of the modular freeform could be readily altered by tuning the microparticle composition. For example, single-material core-shell particles formed a liquid-filled foam (**Figure 7.4c**), whereas multi-material core-shell particles formed a multi-material solid construct (**Figure 7.4d**). Shape-stable constructs can also be formed onto substrates with an arbitrary inclination angle – and even upside-down – as demonstrated by omnidirectional deposition using a hand-held IAMF device (**Figure S7.9**).

Furthermore, IAMF could be readily used for the one-step generation of injectable modular materials by combining rapidly (i.e. in-air) solidifying droplet cores and slowly (i.e. after injection) solidifying droplet shells (**Figure 7.4e**). Upon deposition, particles or fibers are lubricated by their still-liquid shell that solidifies after the mold has been filled. As an example, we filled a bone-shaped mold with in-air formed particles (**Figure 7.4f,g**). The construct's micro- and mesoscale architectures consisted of stem cells encapsulated by alginate particles that were embedded in a dextran-based hydrogel matrix, respectively (**Figure 7.4h**). Alternative microarchitectures could be readily produced by, for example, tuning the building block's shape into a fiber (**Figure S7.10**).

Bottom-up module-based additive manufacturing has particular relevance for tissue engineering, as it is an effective approach to build constructs that structurally mimic the multiscale modularity of native tissues.[47-49] To investigate IAMF's potential in this regard, we analyzed both the effect of cell encapsulation on particle formation (**Figure S7.11**) and the influence of IAMF-based processing on the cells (**Figure S7.12**). The microparticle size and shape was not affected up to mesenchymal stem cell (MSC) concentrations of 10^6 cells/ml. In accordance to literature,[50] the amount of cells per particle tightly followed the Poisson distribution. For concentrations $>10^6$ cells/ml, the particles became more polydisperse and larger, as the jet's break-up was affected by the incorporated cells. More than 90% of the MSCs that had been encapsulated using 100 µm nozzles at a flow rate of 1.2 ml/min remained viable during at least one week of *in vitro* culture, irrespective of the nozzle-to-collector distance. When increasing the per-nozzle flow rate to 2 ml/min, the one-week cell survival remained over 80%. Moreover, the encapsulated MSCs remained functional as indicated by their maintained adipogenic differentiation capacity.

Leveraging the cytocompatible nature of IAMF, we then produced a multicellular and multimaterial 3D tissue construct (**Figure 7.4i**). Insulin-producing pancreatic beta cells (i.e. MIN6) were encapsulated in alginate microparticles that were surrounded by a co-culture of human endothelial cells and MSCs embedded in a pro-angiogenic fibrin gel. Within one week, proliferating insulin-positive MIN6 cells formed cell aggregates within the alginate microenvironments, while endothelial and stem cells organized into a

prevascular network that permeated throughout the fibrin gel and stained positive for vonWillebrand factor (**Figure S7.12**). As such, IAMF enabled one-step rapid manufacturing of 3D modular cell-laden biomaterials with distinct cellular micro- and macroenvironments, which is a promising, yet challenging direction in the field of tissue engineering.[49, 51, 52]

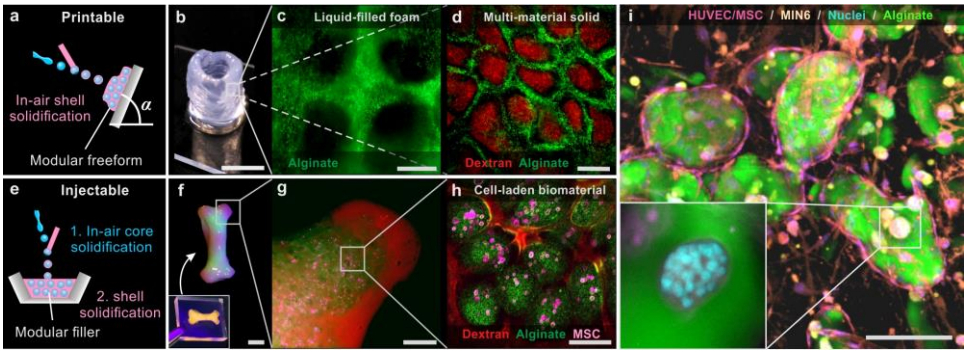

Figure 7.4. One-step fabrication of 3D multiscale modular (bio)materials. (a) To print modular freeforms, the flying droplets' shells are solidified from the inside out, which enables the deposition and stacking of shape stable core-shell particles. **(b-d)** A hollow cylinder was formed by deposition of the composite jet onto a rotating substrate. By altering the building blocks' composition, the resulting microarchitecture comprised of **(c)** a liquid-filled foam or **(d)** a multi-material modular solid, where the crosslinker for the core was added to the shell and *vice versa*. **(e)** To eject a modular filler, only the droplets' cores are solidified in the air, whereas the slower solidifying shells enable seamless filling of the mold. **(f-h)** A modular construct was produced by filling a bone-shaped mold. Inset: Hydrogel construct while still in the mold. The 3D multiscale modular material consisted of MCSs (pink), encapsulated in alginate microspheres (green) that are embedded in dextran-tyramine hydrogel (red). **(i)** The same one-step injection molding approach was leveraged to produce a multiscale modular tissue construct with optimized cellular micro- and macroenvironments. The construct consisted of insulin producing pancreatic beta cells (MIN6, beige with blue nuclei) that were encapsulated in alginate microparticles (green). The cell-laden microparticles were encapsulated within a pro-angiogenic fibrin network that contained human endothelial and stem cells (pink with blue nuclei). The microenvironments supported MIN6 cells proliferation, while the macroenvironment supported the formation of an endothelial cellular network within 7 days of *in vitro* culture. Scale bars (b,f) 1 cm, (g) 5 mm, (c,d,h,i) 100 μm.

7.4 Discussion and Conclusion

We here presented IAMF, a technical innovation that omits the wall-induced limitations of chip-based microfluidics through the controlled collision of liquid microjets. We demonstrated the production of various monodisperse microfluidic products with controlled composition, shape, and size, at per-nozzle rates that exceed conventional chip-based microfluidics by at least one to two orders of magnitude. We anticipate that IAMF's throughput can be readily scaled up even further by introducing additional liquid microjets. Furthermore, IAMF's open nature primes it readily suitable for integration with yet existing jet-based technologies such as impinging jet reactors[53] or on-the-fly droplet sorting technologies including fluorescence-activated cell sorting.[54] Another advantage of this jet-collision-based approach is that it only requires

straightforward nozzle alignment and does not rely on any cleanroom technology. This facilitates the application of microfluidics-based technologies in environments that are not readily compatible with microfluidic chips.[12] Furthermore, we foresee large potential for IAMF in cell microencapsulation strategies, as the technology is compatible with the oil-free production of cell-laden hydrogel particles and can be operated at relatively high throughputs, indeed both endorsing clinical translation.

As reported in this work, IAMF can also be directly integrated into additive manufacturing processes. Such integration might advance current fabrication approaches in several ways. For example, the controlled in-air gelation of microdroplets to form hydrogel bricks enables the one-step manufacturing of 3D multiscale modular materials. Furthermore, an in-air solidification strategy enables the uncoupling of material properties at the nozzle and substrate. Based on this feat, we demonstrated that low-viscosity inks can be ejected at high rates while both omitting shear stress-induced cell dead in the nozzle and ensuring shape stable construct formation on the substrate. In principle, in-air solidification thus circumvents the paradox between shape fidelity and printability/cytocompatibility that currently hampers biofabrication applications.[55] IAMF-based additive manufacturing could be further optimized by incorporating established 3D printing approaches. For example, IAMF nozzles could be readily mounted on automated xyz-stages to enable the direct 3D printing of multiscale modular materials with arbitrary shapes. Micrometer resolution is within reach when using a continuous inkjet printing approach,[35] where droplets can be precisely deposited as far as 1000 droplet diameters from the nozzle.[19] Incorporating drop-on-demand technology would even further improve spatial control over the printed product by enabling the precise placement of single modular building blocks.[56] In addition to such computer-aided manufacturing approaches, IAMF technology can also be adapted to enable hand-held device operation, as pioneered in this work. Especially tissue engineers and surgeons may benefit from this ability, as it might eventually enable, for example, the rapid *in situ* repair of wounds and defects using novel modular hydrogel filling strategies.

In conclusion, we demonstrated a novel disruptive manufacturing technology, called in-air microfluidics (IAMF). IAMF integrates the fields of microfluidics and additive manufacturing by enabling on-the-fly manipulation of liquids using controlled in-air coalescence of multiple microjets. In this work, we identified and described the essential physical principles underlying IAMF and demonstrated the potential of this platform for both microfluidic and additive manufacturing applications. Specifically, IAMF can be exploited as a chip-free alternative to conventional chip-based microfluidics for the production of monodisperse emulsions, particles, and fibers with controlled shape and size (10-1000 μm) at per-nozzle rates that match clinical- and industrial-level applications. In addition, IAMF offers new potential for 3D printing applications, as it enables uncoupling of material properties at the nozzle and substrate. In particular, we leveraged in-air solidification of low-viscosity (bio)inks, to form a variety of oil-free cell-laden micrometer-sized building blocks that can be directly combined into larger 3D modular freeforms. Using this approach, IAMF enabled the one-step biofabrication of a

viable and multifunctional engineered tissue construct with intrinsic hierarchy that spanned multiple length scales. Its straightforward and accessible (i.e. chip-free) nature will facilitate the rapid and widespread adoption of IAMF throughout microfluidics and biofabrication communities, as well as boosting its application in clinical and industrial settings.

7.5 Supplementary Information

Section S7.1. Shape Control

Shape-controlled microgels are produced by increasing the dimensionless jet velocity $\alpha = V_2/V_1$. As shown in Figure S7.6a-e, this approach results in elongation of the droplets in-flight. The collected particles closely mimic the shape of elongated droplets immediately after jet collision (Figure S7.6f-j), confirming that ionotropic gelation of the alginate containing droplets is rapid enough to freeze the particle shape before deposition in a bath or onto a substrate at 1-10 cm distance from the jets' collision point.

The extent of elongation is plotted as a function of the drop-jet velocity difference (Figure S7.6). Several trends can be observed. First, for jet velocity ratios ($1 < \alpha < 1.3$), the droplet hardly deforms, i.e. $L/D_{drop} \approx 1$. Here, the surface tension of the drop exceeds the inertia that corresponds to the tangential component of the drop-jet impact velocity, i.e. tangential Weber number $We_y = \rho_1 D_1 V_{y,d}^2/\sigma_2 < 1$ (the variables are drawn in Figure S7.6k). Inserting $V_{y,d} = V_1 - V_2 cos\theta = V_2(\alpha - cos\theta)$ in this equation readily results in a threshold value $\alpha_{th} = \cos\theta + \sqrt{\sigma_2/\rho_1 D_1 V_2^2} \approx 1.3$, which is in reasonable agreement with the experiments. Second, for high jet velocity ratios ($\alpha > 2.5$), a huge variation in the elongation is observed. This is the result of break-up of the microgel droplets into a head and a tail, as shown in the inset in Figure S7.6l. Finally, for $1.3 < \alpha < 2.5$, the elongation is observed to increase approximately linearly $L/L_{drop} \approx C_o\alpha$, with fitting constant $C_o = 5\pm1$.

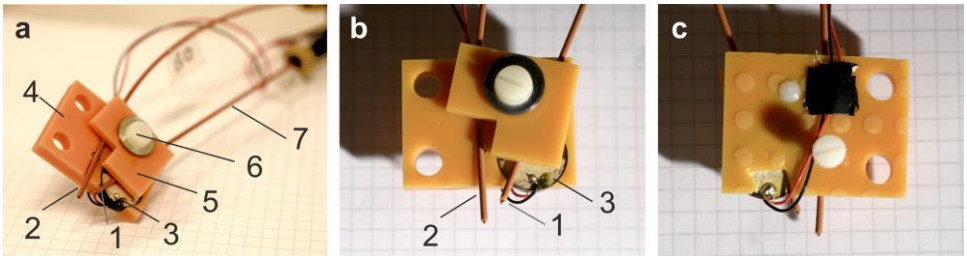

Figure S7.1. IAMF hand-held device. We used this device to produce particles and fibers, and to print the solid freeform structures onto surfaces with an arbitrary inclination angle, as shown in Figure S7.9**. (a)** Overview image. **(b)** Top view. **(c)** Bottom view. Numbers indicate (1) nozzle 1; (2) nozzle 2; (3) piezo-electric element; (4) base plate; (5) clamp; (6) screw; (7) tubing. Background grid: 5 mm squares.

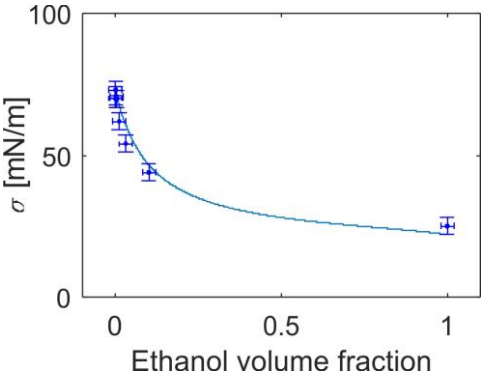

Figure S7.2. Surface tension of ethanol/water mixtures. The ethanol volume fraction is defined as $V_{ethanol}$ / ($V_{ethanol}$ + $V_{CaCl_2\ solution}$). Our measurements (data points) overlap with previously reported measurements of ethanol/water mixtures (line)[21] within the experimental error (5%).

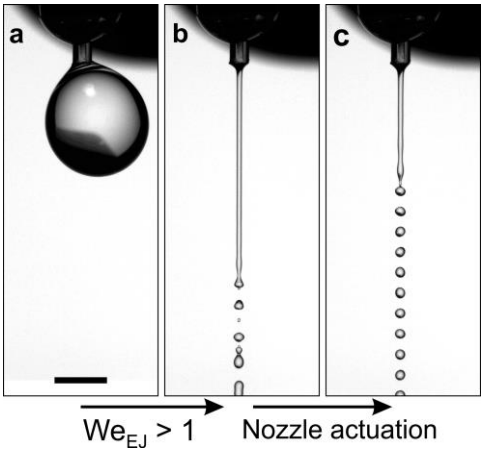

Figure S7.3. Ejection and break-up regimes. (a) Dripping is observed for slow flows, as, for example, observed for a slightly opened kitchen tap. **(b)** Chaotic jetting is observed for faster flows corresponding to higher Weber numbers $We_{ej} = \rho V_{ej} D/\sigma \gtrsim 1$. The exact value of this transition Weber number depends on additional parameters.[57] By default, the jet breaks up into droplets with a wide range of sizes. **(c)** However, a monodisperse droplet train is formed if the nozzle is vibrated. Controlled break-up is especially effective for nozzle vibrations close to the natural break-up frequency of the jet.[56] Scale bar: 1 mm.

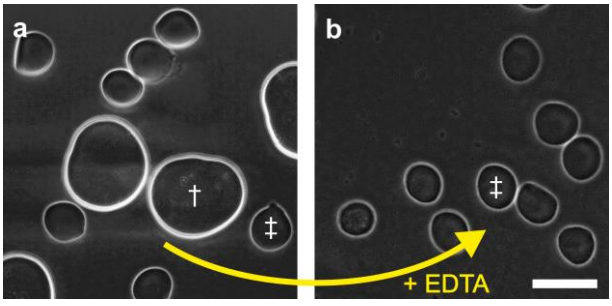

Figure S7.4. Hydrogel templating. (a) Suspension of small particles of alginate-dextran-tyramine interpenetrating networks (‡) and larger alginate particles (†). In all particles, the alginate was crosslinked in the air, whereas the slower solidifying Dex-TA in the small particles was crosslinked using horseradish peroxidase in a H_2O_2-containing bath. **(b)** Addition of the calcium chelator ethylenediaminetetraacetic acid (EDTA) removes the Ca^{2+} ions from the alginate networks, resulting in complete dissolution of the alginate particles and leaving only Dex-TA microparticles behind. This 'templating' approach is compatible with various materials.[34] Scale bar: 100 µm.

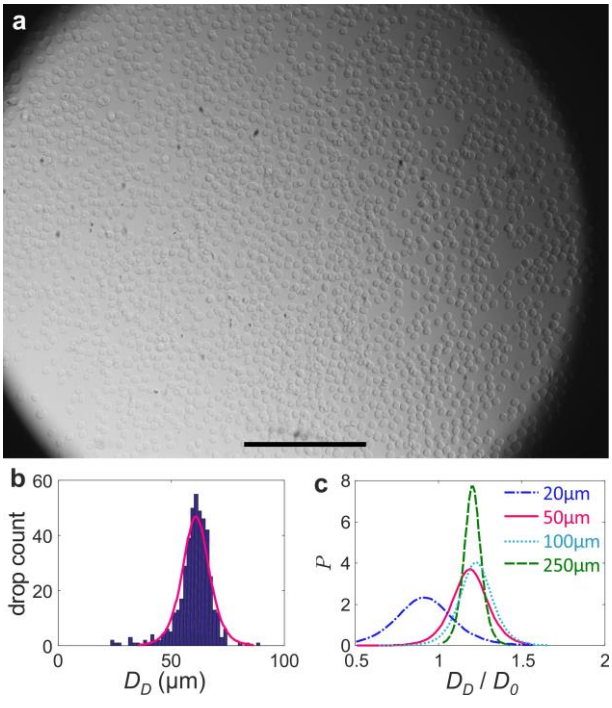

Figure S7.5. Particle size distributions. (a) Image of approximately 1100 particles as deposited by a D_1 = 50 µm nozzle. **(b)** Example size histogram of the particle diameter D_d, which was fitted by a logistic distribution fit. **(c)** Size distributions normalized by the nozzle diameter $D_1 = D_2$. Although the absolute size distribution increases for larger nozzles, the relative size distribution narrows. The average particle size is smaller than the nozzle for D = 20 µm, presumably because the size measurement was performed after two days in an ethanol containing liquid, which results in shrinking of the alginate. Scale bar: 1 mm.

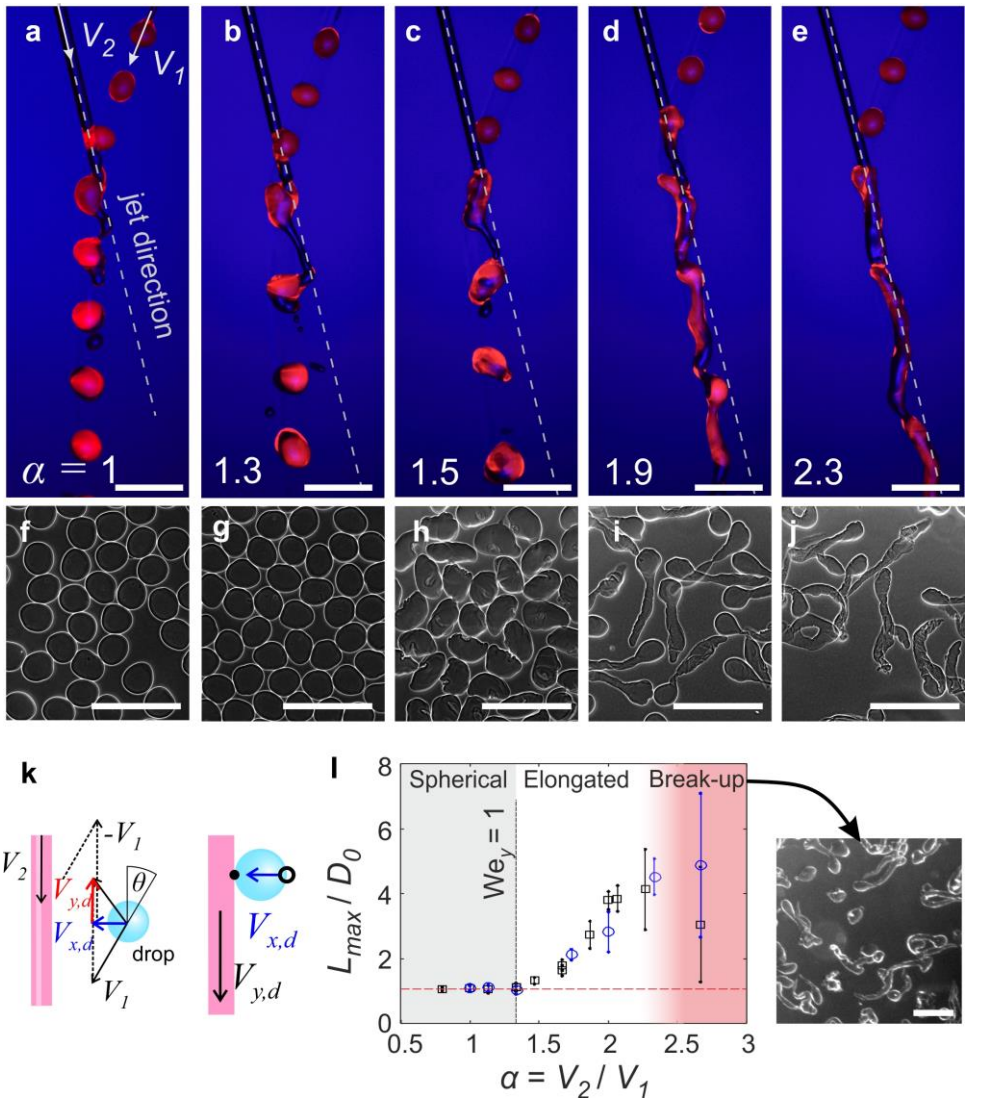

Figure S7.6. Elongation of droplets and particles. **(a-e)** High-speed fluorescence microscopy images of in-air drop (red) elongation for increasing relative jet (blue) velocities $\alpha = V_2/V_1$. **(f-j)** Collected particles corresponding to the top images. **(k)** Decomposition of the velocity vectors. **(l)** Particle elongation as a function of the relative jet velocity for $\theta = 17°$ (○) and $\theta = 30°$ (□). The shaded areas indicate regimes of no deformation (left, grey) and particle breakup into a head and a tail (pink, right) as shown in the inset. Scale bars: 500 μm.

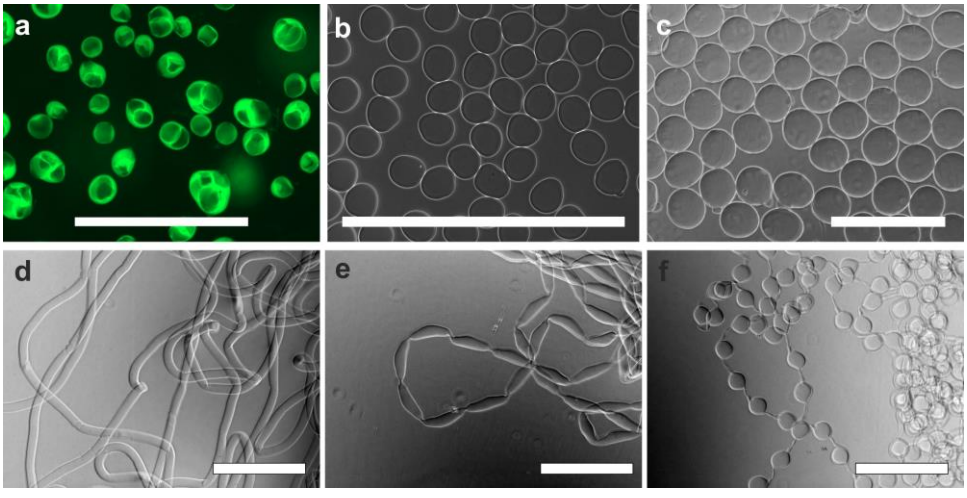

Figure S7.7. Overview of particles and fibers. (a) Overview of liquid-filled core-shell particles. Particles with 1, 2, 3, and 4 cores are observed. We hypothesize that the origin of these multi-core particles is in-air collision of partially-solidified shells, as observed in the live view of the droplet trains. Such inter-droplet collisions may be prevented by further homogenizing the speed and size of the droplets, for example by optimizing the nozzle design.[56] **(b-c)** Overview images corresponding to Figure 7.2i,j. **(d-f)** Transition from smooth to beaded fiber by tuning the impact position of gel precursor and crosslinker jets as shown in Figure 7.2o-q. Scale bars: 1 mm.

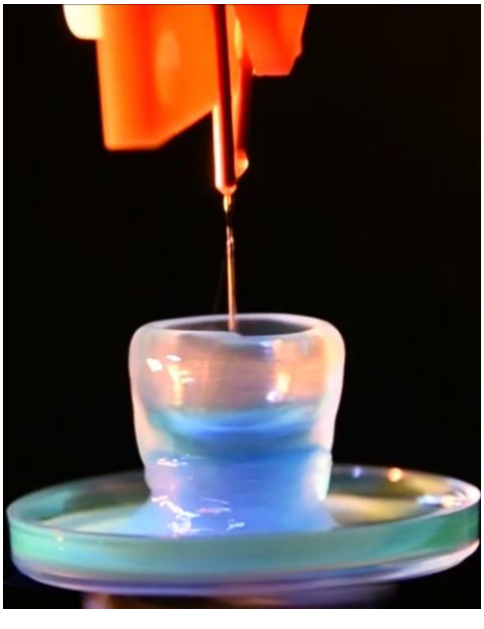

Figure S7.8. One-step 3D modular printing a solid freeform. A tube with an outer diameter of ~15 mm is printed in one step, by depositing core-shell alginate microparticles onto a rotating substrate.

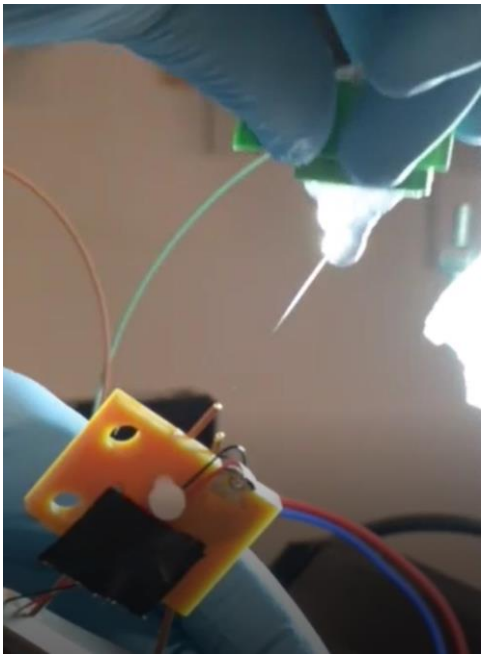

Figure S7.9. Omnidirectional printing using IAMF hand-held device. Through in-air solidification, IAMF enables on-step printing of 3D modular materials onto substrates with arbitrary inclination angles.

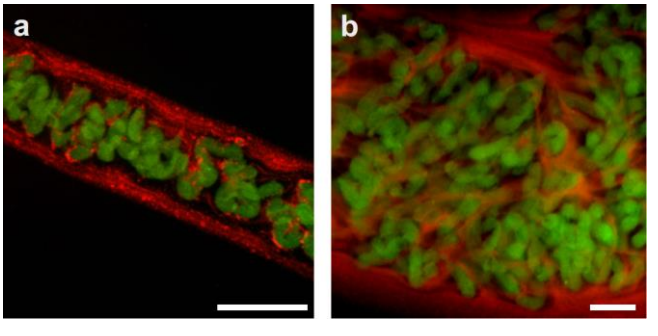

Figure S7.10. Fiber-based modular materials. (a) Line and **(b)** larger fiber-based modular constructs consisting of dextran-tyramine (green) and alginate (red) were deposited onto a glass substrate using nozzles with a diameter of 100 µm. Scale bars: 1 mm.

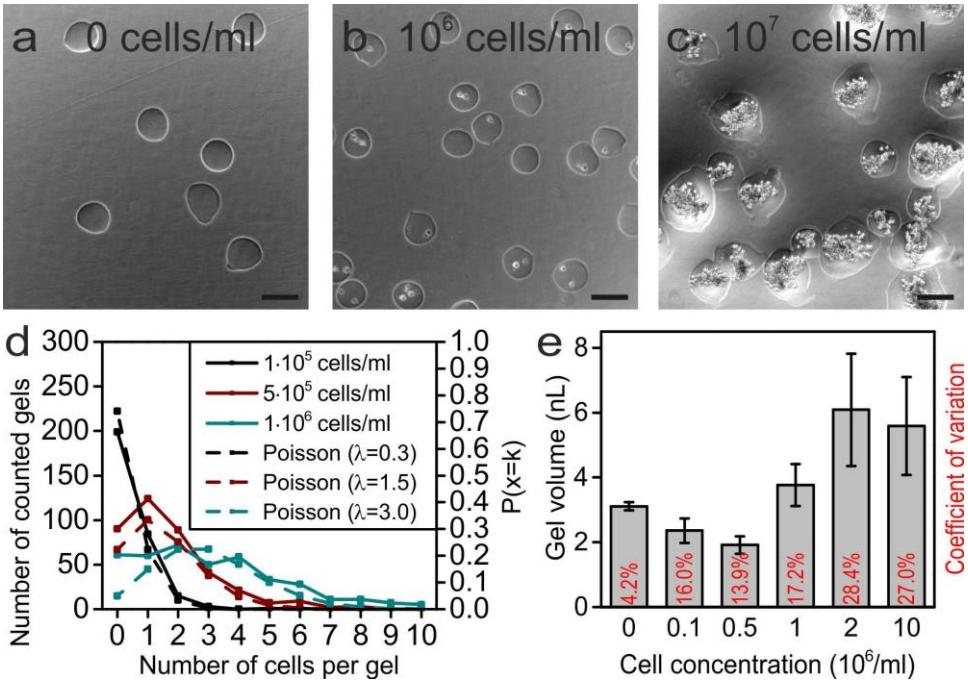

Figure S7.11. Characterization of IAMF-based cell microencapsulation. (a-c) IAMF was used with 100 µm nozzles in 'drop-jet' mode to encapsulate MSCs in alginate microparticles using increasing cell concentrations. **(d)** The number of encapsulated cells per gel (solid lines) tightly followed the Poisson distribution (dashed lines). **(e)** Cell concentrations of > 10^6 cells/ml resulted in larger and more polydisperse particles as compared to particles that were produced using lower cell concentrations or without cells. Scale bars: 100 µm.

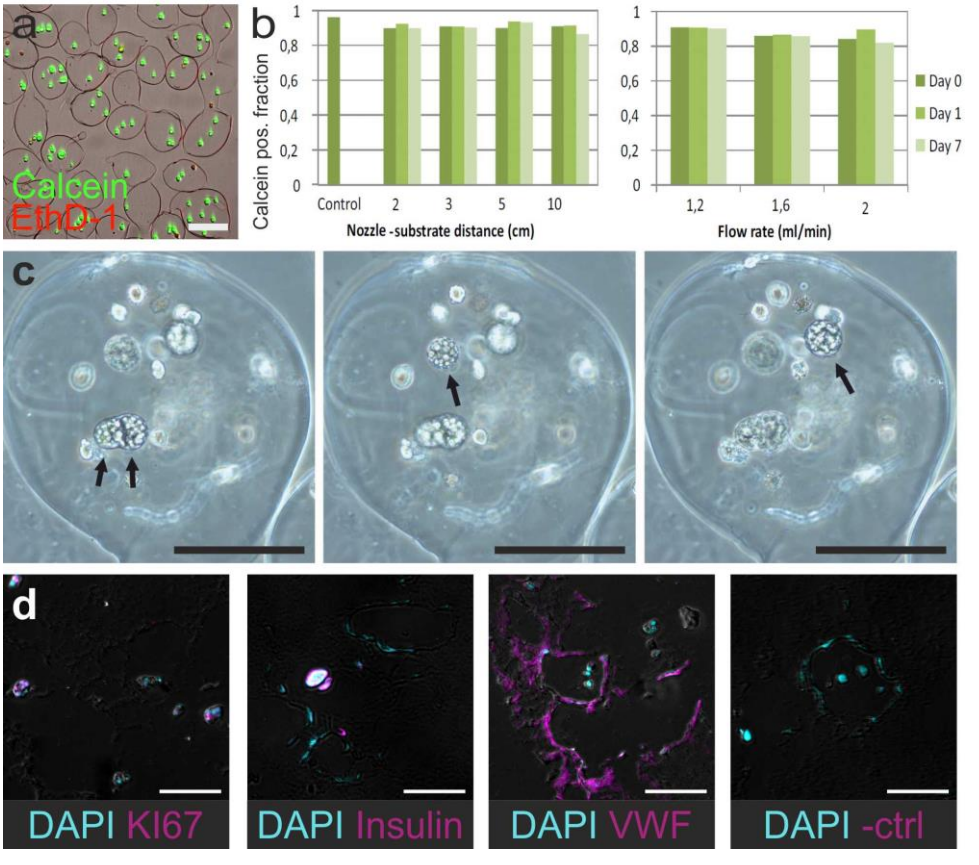

Figure S7.12. Viability and function of IAMF-processed cells. (a) Live/dead staining of encapsulated MSCs comprising calcein (green) and ethidium homodimer-1 (red). **(b)** Quantified cell viability of MSCs immediately, and 1 and 7 days after encapsulation using IAMF with various nozzle-to-collector distances (left) and flow rates (right). **(c)** Encapsulated MSCs differentiated into lipid droplet containing adipocytes (black arrows) after 7 days of *in vitro* culture in adipogenic differentiation medium. The different images correspond to different focal planes of a single alginate particle, revealing consistent differentiation throughout the microgel. **(d)** Immunofluorescent stainings confirmed maintained proliferation (KI67 positive) and function (Insulin positive) of MIN6 cells, and angiogenic network formation (von Willebrand factor; VWF) of endothelial cells and MSCs after IAMF-based manufacturing. Cell nuclei were counter-stained using DAPI. Scale bars: 100 μm.

References

1. Whitesides, G.M., *The origins and the future of microfluidics.* Nature, 2006. **442**(7101): p. 368-73.
2. Duncombe, T.A., A.M. Tentori, and A.E. Herr, *Microfluidics: reframing biological enquiry.* Nat Rev Mol Cell Biol, 2015. **16**(9): p. 554-67.
3. Seemann, R., et al., *Droplet based microfluidics.* Rep Prog Phys, 2012. **75**(1): p. 016601.
4. Onoe, H., et al., *Metre-long cell-laden microfibres exhibit tissue morphologies and functions.* Nat Mater, 2013. **12**(6): p. 584-90.
5. Dendukuri, D., T.A. Hatton, and P.S. Doyle, *Synthesis and self-assembly of amphiphilic polymeric microparticles.* Langmuir, 2007. **23**(8): p. 4669-74.
6. Kim, J.W., et al., *Fabrication of monodisperse gel shells and functional microgels in microfluidic devices.* Angew Chem Int Ed Engl, 2007. **46**(11): p. 1819-22.
7. Choi, A., et al., *Recent advances in engineering microparticles and their nascent utilization in biomedical delivery and diagnostic applications.* Lab on a Chip, 2017. **17**(4): p. 591-613.
8. Ma, S., et al., *Fabrication of microgel particles with complex shape via selective polymerization of aqueous two-phase systems.* Small, 2012. **8**(15): p. 2356-60.
9. Kang, E., et al., *Digitally tunable physicochemical coding of material composition and topography in continuous microfibres.* Nat Mater, 2011. **10**(11): p. 877-83.
10. Huang, G.Y., et al., *Microfluidic hydrogels for tissue engineering.* Biofabrication, 2011. **3**(1): p. 012001.
11. Xu, S., et al., *Generation of monodisperse particles by using microfluidics: control over size, shape, and composition.* Angew Chem Int Ed Engl, 2005. **44**(5): p. 724-8.
12. Volpatti, L.R. and A.K. Yetisen, *Commercialization of microfluidic devices.* Trends Biotechnol, 2014. **32**(7): p. 347-50.
13. Mashaghi, S., et al., *Droplet microfluidics: A tool for biology, chemistry and nanotechnology.* TrAC Trends in Analytical Chemistry, 2016. **82**: p. 118-125.
14. Kim, J.H., et al., *Droplet microfluidics for producing functional microparticles.* Langmuir, 2014. **30**(6): p. 1473-88.
15. Nunes, J.K., et al., *Dripping and jetting in microfluidic multiphase flows applied to particle and fiber synthesis.* J Phys D Appl Phys, 2013. **46**(11).
16. Yan, Z., I.C. Clark, and A.R. Abate, *Rapid Encapsulation of Cell and Polymer Solutions with Bubble-Triggered Droplet Generation.* Macromolecular Chemistry and Physics, 2017. **218**(2): p. 1600297.
17. Ching, S.H., N. Bansal, and B. Bhandari, *Alginate gel particles-A review of production techniques and physical properties.* Crit Rev Food Sci Nutr, 2017. **57**(6): p. 1133-1152.
18. Christopher, G.F. and S.L. Anna, *Microfluidic methods for generating continuous droplet streams.* J Phys D Appl Phys, 2007. **40**(19): p. R319.
19. Visser, C.W., et al., *Dynamics of high-speed micro-drop impact: numerical simulations and experiments at frame-to-frame times below 100 ns.* Soft Matter, 2015. **11**(9): p. 1708-22.
20. Jin, R., et al., *Enzyme-mediated fast in situ formation of hydrogels from dextran-tyramine conjugates.* Biomaterials, 2007. **28**(18): p. 2791-800.
21. Vazquez, G., E. Alvarez, and J.M. Navaza, *Surface Tension of Alcohol Water + Water from 20 to 50 .degree.C.* Journal of Chemical & Engineering Data, 1995. **40**(3): p. 611-614.
22. Both, S.K., et al., *A rapid and efficient method for expansion of human mesenchymal stem cells.* Tissue Eng, 2007. **13**(1): p. 3-9.
23. Verseijden, F., et al., *Adult human bone marrow- and adipose tissue-derived stromal cells support the formation of prevascular-like structures from endothelial cells in vitro.* Tissue Eng Part A, 2010. **16**(1): p. 101-14.
24. Whelehan, M. and I.W. Marison, *Microencapsulation using vibrating technology.* J Microencapsul, 2011. **28**(8): p. 669-88.
25. Chen, C., Lin, *Collisions of a string of water drops on a water jet of equal diameter.* Experimental Therman and Fluid Science, 2006. **31**: p. 6.
26. Blanchette, F., *Simulation of Mixing within Drops due to Surface Tension Variations.* Phys Rev Lett, 2010. **105**(7): p. 074501.
27. Brandenberger, H., et al., *Monodisperse particle production: A method to prevent drop coalescence using electrostatic forces.* Journal of Electrostatics, 1999. **45**(3): p. 227-238.

28. Planchette, C., E. Lorenceau, and G. Brenn, *Liquid encapsulation by binary collisions of immiscible liquid drops.* Colloids and Surfaces A: Physicochemical and Engineering Aspects, 2010. **365**(1): p. 89-94.
29. Chen, R.-H., *Diesel–diesel and diesel–ethanol drop collisions.* Applied Thermal Engineering, 2007. **27**(2): p. 604-610.
30. Skjåk-Bræk, G., H. Grasdalen, and O. Smidsrød, *Inhomogeneous polysaccharide ionic gels.* Carbohydrate Polymers, 1989. **10**(1): p. 31-54.
31. Zhang, J., C.R. Daubert, and E.A. Foegeding, *Fracture Analysis of Alginate Gels.* Journal of Food Science, 2005. **70**(7): p. e425-e431.
32. Levato, R., M.A. Mateos-Timoneda, and J.A. Planell, *Preparation of biodegradable polylactide microparticles via a biocompatible procedure.* Macromol Biosci, 2012. **12**(4): p. 557-66.
33. An, D., et al., *Mass production of shaped particles through vortex ring freezing.* Nature Communications, 2016. **7**: p. 12401.
34. Tamayol, A., et al., *Hydrogel Templates for Rapid Manufacturing of Bioactive Fibers and 3D Constructs.* Adv Healthc Mater, 2015.
35. van Hoeve, W., et al., *Breakup of diminutive Rayleigh jets.* Physics of Fluids, 2010. **22**(12): p. 122003.
36. Nisisako, T. and T. Torii, *Microfluidic large-scale integration on a chip for mass production of monodisperse droplets and particles.* Lab on a Chip, 2008. **8**(2): p. 287-93.
37. Dendukuri, D. and P.S. Doyle, *The Synthesis and Assembly of Polymeric Microparticles Using Microfluidics.* Advanced Materials, 2009. **21**(41): p. 4071-4086.
38. Femmer, T., et al., *High-Throughput Generation of Emulsions and Microgels in Parallelized Microfluidic Drop-Makers Prepared by Rapid Prototyping.* Acs Applied Materials & Interfaces, 2015. **7**(23): p. 12635-12638.
39. Tumarkin, E., et al., *High-throughput combinatorial cell co-culture using microfluidics.* Integrative Biology, 2011. **3**(6): p. 653-662.
40. Kemna, E.W., et al., *High-yield cell ordering and deterministic cell-in-droplet encapsulation using Dean flow in a curved microchannel.* Lab on a Chip, 2012. **12**(16): p. 2881-7.
41. Yobas, L., et al., *High-performance flow-focusing geometry for spontaneous generation of monodispersed droplets.* Lab on a Chip, 2006. **6**(8): p. 1073-1079.
42. Liu, K., et al., *Shape-controlled production of biodegradable calcium alginate gel microparticles using a novel microfluidic device.* Langmuir, 2006. **22**(22): p. 9453-9457.
43. Zhang, H., et al., *Microfluidic production of biopolymer microcapsules with controlled morphology.* Journal of the American Chemical Society, 2006. **128**(37): p. 12205-12210.
44. Lin, Y.S., et al., *Microfluidic synthesis of tail-shaped alginate microparticles using slow sedimentation.* Electrophoresis, 2013. **34**(3): p. 425-431.
45. Utech, S., et al., *Microfluidic Generation of Monodisperse, Structurally Homogeneous Alginate Microgels for Cell Encapsulation and 3D Cell Culture.* Advanced Healthcare Materials, 2015. **4**(11): p. 1628-1633.
46. Utada, A.S., et al., *Dripping to jetting transitions in coflowing liquid streams.* Phys Rev Lett, 2007. **99**(9): p. 094502.
47. Liu, J.S. and Z.J. Gartner, *Directing the assembly of spatially organized multicomponent tissues from the bottom up.* Trends Cell Biol, 2012. **22**(12): p. 683-91.
48. Nichol, J.W. and A. Khademhosseini, *Modular Tissue Engineering: Engineering Biological Tissues from the Bottom Up.* Soft Matter, 2009. **5**(7): p. 1312-1319.
49. Oliveira, S.M., R.L. Reis, and J.F. Mano, *Towards the design of 3D multiscale instructive tissue engineering constructs: Current approaches and trends.* Biotechnol Adv, 2015. **33**(6 Pt 1): p. 842-55.
50. Collins, D.J., et al., *The Poisson distribution and beyond: methods for microfluidic droplet production and single cell encapsulation.* Lab on a Chip, 2015. **15**(17): p. 3439-59.
51. Leijten, J., et al., *Advancing Tissue Engineering: A Tale of Nano-, Micro-, and Macroscale Integration.* Small, 2016. **12**(16): p. 2130-45.
52. Kamperman, T., et al., *Single Cell Microgel Based Modular Bioinks for Uncoupled Cellular Micro- and Macroenvironments.* Adv Healthc Mater, 2017. **6**(3).
53. Erni, P. and A. Elabbadi, *Free impinging jet microreactors: controlling reactive flows via surface tension and fluid viscoelasticity.* Langmuir, 2013. **29**(25): p. 7812-24.
54. Herzenberg, L.A., R.G. Sweet, and L.A. Herzenberg, *Fluorescence-Activated Cell Sorting.* Scientific American, 1976. **234**(3): p. 108-117.

55. Malda, J., et al., *25th anniversary article: Engineering hydrogels for biofabrication.* Advanced Materials, 2013. **25**(36): p. 5011-28.
56. Wijshoff, H., *The dynamics of the piezo inkjet printhead operation ☆.* Physics Reports, 2010. **491**(4-5): p. 77-177.
57. Clanet, C. and J.C. Lasheras, *Transition from dripping to jetting.* Journal of Fluid Mechanics, 1999. **383**: p. 307-326.

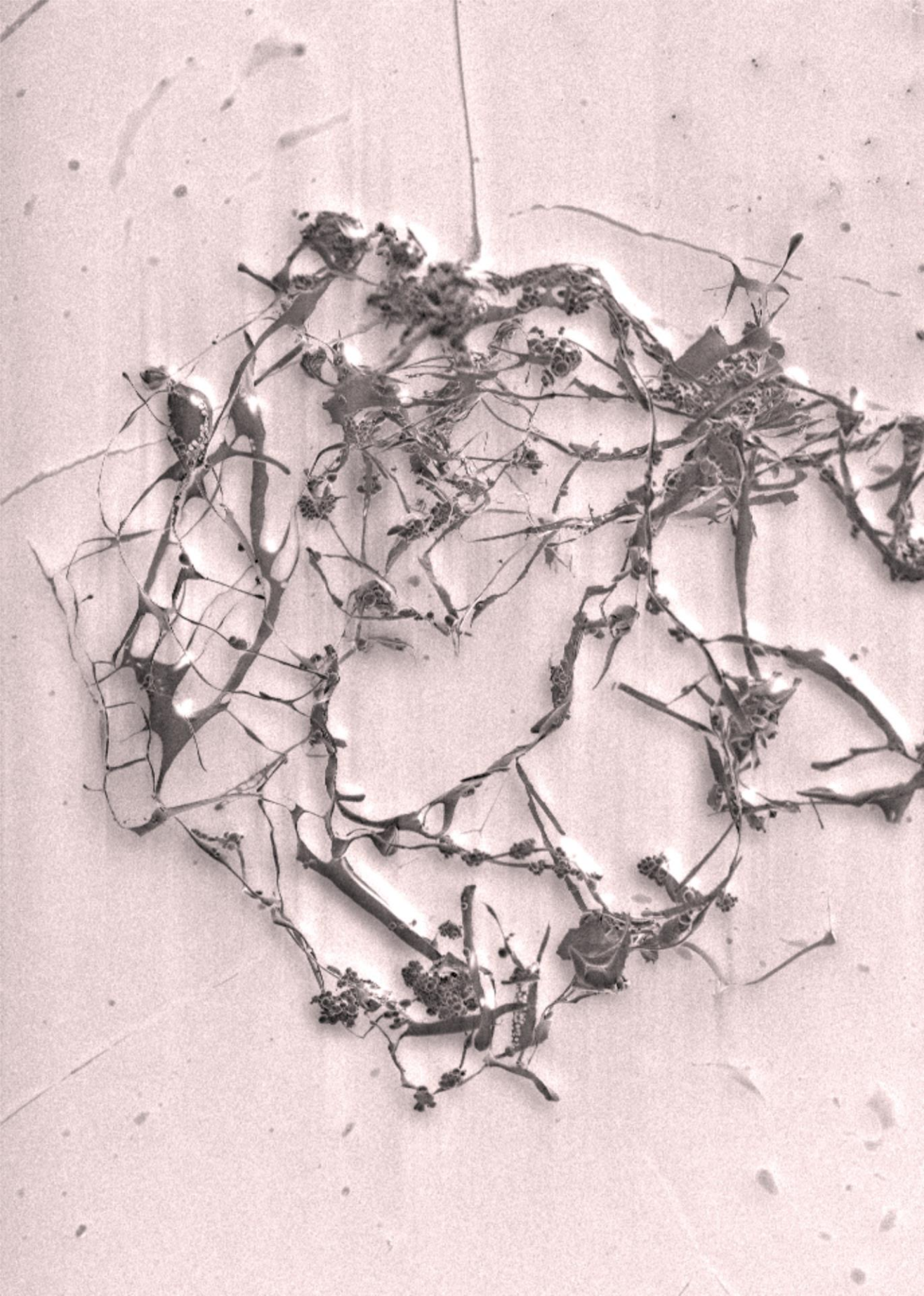

8

Reflection and Outlook

Conventional tissue engineering strategies rely on the bulk fabrication of isotropic scaffolds that act as functional substitutes for damaged or lost tissue. Although such top-down fabrication methods allow for the facile engineering of clinically-sized grafts, they do not recapitulate the intricate microstructural features of native tissues. The absence of this hierarchical organization limits the potential behavior of engineered tissues. Several bottom-up, or modular, manufacturing strategies have recently been developed that have the resolution to mimic the multiscale modular architecture as observed throughout natural tissues. This thesis significantly contributes to expanding the modular tissue engineering toolbox by: i) developing several enzymatic crosslinking strategies that are compatible with emulsion-based cell encapsulation; ii) enabling the long-term culture of single-cell-laden microgels by preventing cell escape through cell centering; iii) pioneering direct on-cell crosslinking (DOCKING) for RGD-free mechanotransduction to control cell fate in a novel manner; iv) producing smart building blocks through in situ spatiotemporal biomechanical and biochemical modifications of the microgels; v) facilitating facile modular biofabrication using single-cell-laden microgel-based modular bio-inks; vi) enabling faster production of microbuilding blocks using a novel chip-free microfluidic manufacturing technology called 'in-air microfluidics' (IAMF) and; vii) establishing one-step rapid manufacturing of 3D modular biomaterials using IAMF. However, to achieve the full potential of these innovations and further maturation of the field of modular tissue engineering additional research is needed, which is discussed in this chapter.

8.1 Alternatives to Dextran-tyramine

The majority of this thesis is based on the use of horseradish peroxidase (HRP) to enzymatically crosslink dextran-tyramine (Dex-TA) polymers. Dextran is a bio-inert natural polymer that acts as a template material for modification with functional moieties of interest. Indeed, dextran-based hydrogels have been proven to support cell survival and function in multiple *in vitro* and *in vivo* studies.[1-4] However, dextran matrices are not naturally occurring in the human body and, for example, cannot be remodeled through enzymatic degradation by cells. In principle, the tyramine-based crosslinking reaction can be leveraged to produce a variety of bioactive and/or degradable tyramine-conjugates that can be mixed and matched, acting as polymer building blocks. It would be intuitive to produce, for example, tyramine-conjugates of the native extracellular matrix components including collagen, hyaluronic acid, and heparan sulfate. Many of these tyramine-conjugated polymers have already been developed for the production of bulk hydrogels,[1] and are in principle readily compatible with the microfabrication strategies presented in this thesis. Future work could leverage this versatility to, for example, screen various microgel compositions to further optimize (single cell) microenvironments.

HRP-mediated Dex-TA crosslinking is a bio-inspired strategy to covalently couple polymers in a cytocompatible manner. However, it does not resemble the polymerization reactions that naturally occur during wound healing, which might induce arbitrary cell responses. Natural wound healing mechanisms involve, for example, the formation of fibrin matrix through crosslinking of fibrinogen using blood coagulation enzymes FIIa (i.e. thrombin) and FXIII (i.e. transglutaminase). We anticipate that a biomimetic strategy based on the enzymatic crosslinking of fibrinogen would result in fully natural cell-biomaterial interactions by effectively adopting one of nature's basic tissue repair strategies. A number of groups have recently begun to pioneer the FXIII-mediated manufacturing of microgels using polymers functionalized with FXIII substrate peptides, indicating the feasibility of this approach.[5, 6] Alternatively, from an engineering perspective it is very interesting to further explore cytocompatible bio-orthogonal crosslinking strategies that rely on highly specific bio-inert interactions, including Michael additions, thiol-ene coupling, and (copper-free) azide-alkyne cycloadditions.[7] In contrast to natural crosslinking strategies, bio-orthogonal systems allow for independent tuning of cell-polymer and polymer-polymer interactions, which provides an extra level of control over the final construct.

8.2 Mechanotransduction

We leveraged enzymatic crosslinking of tyramine and tyrosine to directly tether 3D dextran-tyramine polymer microniches onto single cells, which we called 'direct on-cell crosslinking' (DOCKING). Stem cell lineage commitment could be steered by tuning the microgels' microelasticity (i.e. stiffness), which indicated the successful transduction of biomechanical cues through tyramine-tyrosine bonds. In contrast to existing state-of-the art 3D cell culture platforms, our hydrogel was free of peptide sequences that can interact with integrins. This suggested that mechanotransduction in our model fully

relies on hardly described RGD-independent interactions. A possible biological role for such RGD-independent mechanotransduction is advocated by the natural occurrence of RGD-free cell adhesion through tissue transglutaminase/fibronectin complexes that occur in, for example, wound healing processes.[8] Future work should focus on unravelling how cells exactly sense and respond to their 3D microenvironment through on-cell crosslinked polymers. For example, inhibition of integrins, focal adhesion kinase, and the actinomyosin cytoskeleton during multilineage differentiation experiments would provide insight in the mechanism of mechanotransduction.[9, 10]

In this work, we exploited the same crosslinking reaction to achieve cell-biomaterial adhesion (i.e. DOCKING) and control microgel stiffness. Therefore the DOCKING density and material stiffness could not be independently tuned, which is an intrinsic limitation of this approach as cell-adhesion-ligand density and extracellular matrix stiffness could both influence cell behavior.[11] To uncouple DOCKING density from material stiffness, follow up research should exploit dual-orthogonal-functionalized polymers. An example of such material is dextran-tyramine-biotin, as presented in chapter 5. We hypothesize that the stiffness of this material could be modified post enzymatic crosslinking, via *in situ* coupling of biotins using tetravalent avidin.

In situ stiffening on-cell crosslinked microgels revealed the long-term lineage commitment of mesenchymal stem cells (MSCs) to early biomechanical stimuli in 3D. Specifically, a stiff microenvironment during the first week of differentiation was essential to induce long-term osteogenic differentiation. However, the long-term role of biomechanical cues during osteogenic differentiation of MSCs have remained unknown, as Dex-TA could only be irreversibly stiffened by post-curing of the hydrogel's unreacted tyramine residues. Developing a strategy to enable *in situ* softening of Dex-TA would provide a tool to study the long-term effect of microgel stiffness on stem cell differentiation. This is especially interesting, as 2D cultures on *in situ* softening substrates has potentially revealed a stiffness-induced mechanical memory of MSCs.[12] Although we attempted to soften our stiff Dex-TA using dextranase, this approach was not sufficiently efficient to cause significant *in situ* softening of microgels (data not shown). Future research should focus on the development of tyramine-modified hydrogels that can be reversibly stiffened. Such reversible stiffening could potentially be achieved with Dex-TA-desthiobiotin, by creating reversible crosslinks using the desthiobiotin/biotin displacement strategy presented in chapter 5.

8.3 Biochemical Tuning

In situ tuning of the biochemical composition of engineered tissues is key to mimic the dynamic nature of native tissues. We have developed smart building blocks that enable the facile integration of *in situ* modifiable microenvironments within modular tissues. Specifically, we pioneered desthiobiotin/biotin displacement on tetravalent avidin analogs to sequentially present molecules of interest onto Dex-TA-biotin microgels. This strategy readily enabled the orthogonal post-modification of modular tissues *in vitro*.

Potentially, desthiobiotin/biotin displacement is also compatible with a controlled *in vivo* modification or release strategy by displacing tethered desthiobiotin with endogenous biotin. For example, desthiobiotin/biotin displacement could trigger the release of bound molecules from nano- or microparticles in biotin-rich organs.[13] Moreover, there is a potential role for this approach to advance tumor-targeting therapies that rely on the overexpression of biotin-receptors on tumor cells.[14] Future research might thus focus on the biotin-rich-tumor-induced release of anticytostatica from microgels.

Conversely, some applications may require externally triggered post-modification of the implanted construct. For example, it has been demonstrated that photo-induced release of 'molecular cages' (i.e. protective groups) from cell adhesive RGD moieties after one week of *in vivo* implantation reduces fibrous capsule formation.[15] Such *in vivo* triggered modifications are not readily compatible with the desthiobiotin/biotin displacement strategy, due to the presence of ubiquitous endogenous biotin levels in many native tissues.[13] Therefore, it might be interesting to develop smart building blocks that rely on different *in situ* tunable modification strategies. Various alternative orthogonal chemistries have already been explored for the *in situ* modification of bulk materials, including click chemistry[16] and supramolecular interactions.[17] Photo-based approaches are of special interest for *in vivo* applications, as (near)infrared light can penetrate relatively deep into tissue.[18]

8.4 Modular Additive Manufacturing

Additive manufacturing of 3D cell-laden biomaterials with intrinsic multiscale modularity requires the integration of micro- and macrofabrication technologies.[19, 20] In this thesis, we pioneered two technologies that represent such integrated approach, namely modular bio-inks and in-air microfluidics (IAMF). The modular bio-inks are compatible with a wide variety of well-established biofabrication technologies such as drop-on-demand ink-jet, which supports high resolution placement of discrete liquid volumes.[21] However, the preparation of a modular bio-ink requires an additional manufacturing step. In contrast, IAMF enables the direct printing of in-air formed (cell-laden) microparticles into a 3D modular construct, which is a one-step process. As of yet, IAMF remains a continuous process that does not support on-demand printing and high-resolution placement of single voxels (i.e. microgels). Future work should focus on the integration of IAMF and drop-on-demand technology to eventually enable the rapid and controlled deposition of distinct microbuilding blocks with single droplet resolution.

Additive manufacturing technologies are challenged by a trade-off in printing resolution and cell survival, which originates from technical limitations in bio-ink design and processing strategies. Currently, 3D printers typically exploit a two-step approach, in which (cell-laden) solid precursor solution (i.e. ink) is sequentially deposited and crosslinked. This two-step approach requires highly viscous inks to maintain adequate shape fidelity. Consequently, the solidified constructs are typically comprised of non-

physiological high-density polymer networks that are not ideal for cell culture applications.[22] Moreover, rapid extrusion of high-viscous inks may cause shear stress-induced cell damage.[23] As shear stress is flow rate-dependent, this effectively limits high-throughput bio-printing applications, which are key to large scale clinical integration of the technology. IAMF might overcome these issues through in-air gelation of low-viscous bio-inks. Alternatively, cytocompatible cell-laden microgels could act as a shear-protective barriers in highly viscous but shape stable modular bio-ink. In this way, both modular bio-inks and IAMF-based printing could potentially enable rapid manufacturing of shape stable constructs by omitting shear stress-induced cell damage. Future research could focus on leveraging these integrated approaches to enable rapid and high-fidelity modular 3D printing while preventing shear-induced cell damage.

8.5 Single-cell-laden Microgel Applications

Besides modular tissue engineering, single-cell-laden microgels can be used for several other applications. Microgels are readily compatible with standard visualization techniques including confocal microscopy without the need for optical or physical processing such as sectioning due to their minimal size. They also offer most efficient material-to-cell volume ratios and improved diffusion rates of solutes, which facilitates real-time pharmacological screenings.

Among the applications that could potentially benefit from single cell microgel technologies are stem cell therapies. Although stem cells have great potential as anti-inflammatory and trophic mediators,[24] their therapeutic effect upon injection is hampered by fast cell clearance from the injection site and poor long-term cell survival.[25, 26] It has been proven that cell-laden microcarriers are characterized by improved retention after intra-myocardial injection as compared to bare cell suspensions.[27] We postulate that single-cell-laden microgels could further improve stem cell injection therapies by prolonging retention time, as well as improving cell survival by providing a protective microenvironment. As proof-of-concept, we have demonstrated the 3-week retention of single-MSC-laden Dex-TA microgels following intra-articular injection in a mouse knee. These promising results encourage future research in this direction.

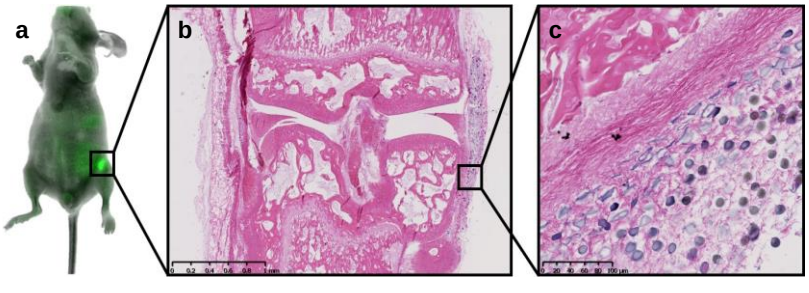

Figure 8.1. Encapsulation in Dex-TA microgels enables long-term intra-articular retention of stem cells. MSCs were microencapsulated in 30 µm near-infrared-labelled Dex-TA microgels and injected in the synovial cavity of a mouse knee. **(a)** After three weeks, the cell-laden microgels could still be traced in live animals using fluorescent imaging, and **(b,c)** post mortem using histological staining.

References

1. Teixeira, L.S., et al., *Enzyme-catalyzed crosslinkable hydrogels: emerging strategies for tissue engineering.* Biomaterials, 2012. **33**(5): p. 1281-90.
2. Henke, S., et al., *Enzymatic Crosslinking of Polymer Conjugates is Superior over Ionic or UV Crosslinking for the On-Chip Production of Cell-Laden Microgels.* Macromol Biosci, 2016. **16**(10): p. 1524-1532.
3. Cadee, J.A., et al., *In vivo biocompatibility of dextran-based hydrogels.* Journal of Biomedical Materials Research, 2000. **50**(3): p. 397-404.
4. De Groot, C.J., et al., *In vitro biocompatibility of biodegradable dextran-based hydrogels tested with human fibroblasts.* Biomaterials, 2001. **22**(11): p. 1197-203.
5. Lienemann, P.S., et al., *Single cell-laden protease-sensitive microniches for long-term culture in 3D.* Lab on a Chip, 2017. **17**(4): p. 727-737.
6. Allazetta, S., et al., *Cell-Instructive Microgels with Tailor-Made Physicochemical Properties.* Small, 2015. **11**(42): p. 5647-56.
7. Azagarsamy, M.A. and K.S. Anseth, *Bioorthogonal Click Chemistry: An Indispensable Tool to Create Multifaceted Cell Culture Scaffolds.* ACS Macro Lett, 2013. **2**(1): p. 5-9.
8. Griffin, M., R. Casadio, and C.M. Bergamini, *Transglutaminases: nature's biological glues.* Biochem J, 2002. **368**(Pt 2): p. 377-96.
9. Guvendiren, M. and J.A. Burdick, *Stiffening hydrogels to probe short- and long-term cellular responses to dynamic mechanics.* Nature Communications, 2012. **3**: p. 792.
10. McBeath, R., et al., *Cell shape, cytoskeletal tension, and RhoA regulate stem cell lineage commitment.* Dev Cell, 2004. **6**(4): p. 483-95.
11. Chaudhuri, O., et al., *Extracellular matrix stiffness and composition jointly regulate the induction of malignant phenotypes in mammary epithelium.* Nat Mater, 2014. **13**(10): p. 970-8.
12. Yang, C., et al., *Mechanical memory and dosing influence stem cell fate.* Nat Mater, 2014. **13**(6): p. 645-52.
13. Wang, H. and J. Pevsner, *Detection of endogenous biotin in various tissues: novel functions in the hippocampus and implications for its use in avidin-biotin technology.* Cell Tissue Res, 1999. **296**(3): p. 511-6.
14. Chen, S.Y., et al., *Mechanism-Based Tumor-Targeting Drug Delivery System. Validation of Efficient Vitamin Receptor-Mediated Endocytosis and Drug Release.* Bioconjugate Chemistry, 2010. **21**(5): p. 979-987.
15. Lee, T.T., et al., *Light-triggered in vivo activation of adhesive peptides regulates cell adhesion, inflammation and vascularization of biomaterials.* Nat Mater, 2015. **14**(3): p. 352-60.
16. van Dijk, M., et al., *Synthesis and applications of biomedical and pharmaceutical polymers via click chemistry methodologies.* Bioconjug Chem, 2009. **20**(11): p. 2001-16.
17. Park, K.M., et al., *In Situ Supramolecular Assembly and Modular Modification of Hyaluronic Acid Hydrogels for 3D Cellular Engineering.* Acs Nano, 2012. **6**(4): p. 2960-2968.
18. Gandavarapu, N.R., M.A. Azagarsamy, and K.S. Anseth, *Photo-click living strategy for controlled, reversible exchange of biochemical ligands.* Advanced Materials, 2014. **26**(16): p. 2521-6.
19. Leijten, J., et al., *Advancing Tissue Engineering: A Tale of Nano-, Micro-, and Macroscale Integration.* Small, 2016. **12**(16): p. 2130-45.
20. Oliveira, S.M., R.L. Reis, and J.F. Mano, *Towards the design of 3D multiscale instructive tissue engineering constructs: Current approaches and trends.* Biotechnol Adv, 2015. **33**(6 Pt 1): p. 842-55.
21. Wijshoff, H., *The dynamics of the piezo inkjet printhead operation ☆.* Physics Reports, 2010. **491**(4-5): p. 77-177.
22. Malda, J., et al., *25th anniversary article: Engineering hydrogels for biofabrication.* Advanced Materials, 2013. **25**(36): p. 5011-28.
23. Blaeser, A., et al., *Controlling Shear Stress in 3D Bioprinting is a Key Factor to Balance Printing Resolution and Stem Cell Integrity.* Adv Healthc Mater, 2016. **5**(3): p. 326-33.
24. Caplan, A.I. and J.E. Dennis, *Mesenchymal stem cells as trophic mediators.* J Cell Biochem, 2006. **98**(5): p. 1076-84.
25. Feyen, D.A., et al., *Stem cell-based therapy: Improving myocardial cell delivery.* Adv Drug Deliv Rev, 2016. **106**(Pt A): p. 104-115.

26. Ansboro, S., et al., *Strategies for improved targeting of therapeutic cells: implications for tissue repair.* Eur Cell Mater, 2012. **23**: p. 310-8; discussion 318-9.
27. van den Akker, F., et al., *Intramyocardial stem cell injection: go(ne) with the flow.* European Heart Journal, 2017. **38**(3): p. 184-186.

Description of Artwork

Chapter 1 (p. 0)

Multiscale modularity is an omnipresent concept in our universe. This artistic impression shows several multiscale modular phenomena that can be observed throughout nature and in daily life. Modular building blocks form the basis of, for example, galaxies, natural materials including bamboo and bone, man-made constructions such as the Eiffel tower and LEGO®.

Design: T. Kamperman and J. Klein Gunnewiek.

Chapter 2 (p. 12)

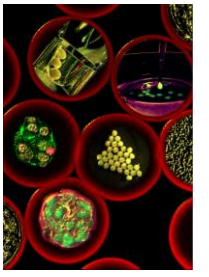

Compilation of nano-, micro-, and millimeter-sized hydrogel spheres produced using the nanoemulsion-induced enzymatic crosslinking method as described in chapter 2, displayed on top of a fluorescence confocal microscopy images of hollow hydrogel microcapsules. Some of the microcapsules contain fluorescent images of living cell microaggregates.

Design: T. Kamperman.

Chapter 3 (p. 30)

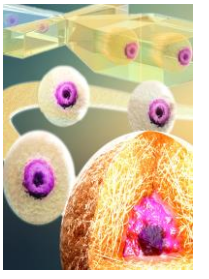

Schematic representation of a typical cell microencapsulation event using the delayed crosslinking approach as described in chapter 3. Immediately after microfluidic droplet generation, a cell is positioned at the outer edge of the droplet. By delaying on-chip crosslinking, the cell is allowed to move to the droplet's center. Subsequent crosslinking results in centered cell encapsulation.

Design: T. Kamperman, J. Leijten, and Demcon Nymus3D.

Chapter 4 (p. 52)

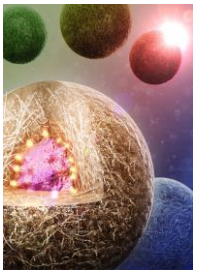

Schematic representation of single-cell-laden microgels produced using 'Direct On-cell CrosslinKing' (DOCKING), where biomaterial is covalently tethered onto cells via the crosslinking of phenolic moieties.

Design: T. Kamperman, J. Leijten, and Demcon Nymus3D.

Chapter 5 (p. 72)

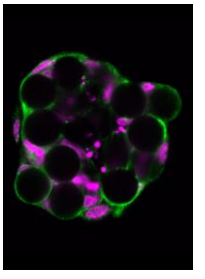

Confocal cross sectional image of a 3D modular microtissue produced by self-assembly of fluorescently labeled human mesenchymal stem cells (green cytoskeleton, magenta nuclei) and dextran-based microgels The microgels were functionalized with a cell adhesive peptide shell as described in chapter 5.

Design: T. Kamperman and C. Kelder.

Chapter 6 (p. 96)

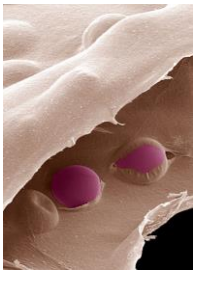

Pseudo-colored scanning electron microscopy photograph of solidified modular bio-ink that contains polyethylene glycol diacrylate microgels (pink) embedded in a distinct polymer matrix (beige).

Design: T. Kamperman and J. Leijten.

Chapter 7 (p. 118)

In-air microfluidics in 'drop-jet' mode as described in chapter 7. The fluid of the jet encapsulates each droplet, as it has a lower surface tension. Therefore, the compound droplet train flowing downwards contains spherical droplets (magenta), coated (i.e. not mixed) with liquid from the jet (green).

Design: T. Kamperman and C.W. Visser.

Chapter 8 (p. 144)

High-resolution scanning electron microscopic image of freeze-dried dextran-tyramine nanoparticles within a network of dextran-tyramine

Design: T. Kamperman and B. Zoetebier.

Acknowledgements

First of all, I want to thank Marcel Karperien for offering me the PhD position. I have learned a lot on both professional and personal fronts. Marcel, you were a great supervisor and I really appreciated your open door policy. Your advice on scientific as well as business matter was of great value to me. I'm convinced your lessons will be of continuous support during my future professional career.

I would also like to thank my daily supervisor Jeroen Leijten. Jeroen, your bright and creative mind is very inspiring and has been a true motivation throughout the PhD training. During our weekly meetings – the first three years via Skype, then as office neighbors – you taught me most of the written and unwritten lessons for pursuing a scientific career. This is truly invaluable. It is an honor to continue working on your projects as a postdoc for another year.

Many thanks to Sieger Henke. It was great fun to engineer the numerous microfluidic platforms together with you. I admire you for your great common sense, critical view on science, and helpful attitude towards everyone around you. I really enjoyed working with you and I am very pleased to have you as one of my paranymphs.

Claas Willem, I am grateful for our intensive collaboration. You are a very honest, hardworking, and inspiring scientist. Besides our collaborations in the lab, it has been a great pleasure to explore the business side of our invention 'in-air microfluidics' with you. Together with Menno Noorlander, we have now received a grant from the Dutch government to perform a feasibility study towards the commercial potential of our startup company IamFluidics. Menno, I thank you for all your help, enthusiasm, and trust. I would also like to thank Vasileios Trikalitis; my former master student who has recently joined us in setting up IamFluidics company. I am looking forward to continuing our fruitful collaboration in the future. Furthermore, I am thankful for the great support that we have received from Herman Blok, Wim van Hoeve, Cees van Rijn, Albert Poortinga, Benno Lansdorp, Frank Bakker, Richard Hogervorst, Christian Holtze, Ron Coenen, Gilles Meijer, Roy Kolkman, Peter Hoekstra, Albert van den Berg, Detlef Lohse, and Marcel Karperien.

Parts of this thesis are the result of the excellent bachelor and master students that I have supervised. Therefore I would like to thank Niels Ruiterkamp, Melvin Gurian, Cindy Kelder, Michelle Koerselman, Vasileios Trikalitis, and Vincent de Jong. You have all done a great job!

I also would like to acknowledge all members of my graduation committee. During my PhD training, I was constantly inspired by your scientific work. It is an honor to present this thesis to you.

Thanks to all of its members, it has been a great time in the department of Developmental BioEngineering: Piet Dijkstra for valuable input on many of my projects; Janneke Alers for giving me the opportunity to tutor and supervise so many students;

Janine Post for once motivating me to learn microfluidics; Jacqueline for every lab introduction, purchase order, and experimental advise; Ingrid van der Schoor for great administrative support; my former office mates Corina, Elahe, Giulia, Joost, Parthiban, Sakshi, Tim, Xiaobin, and all interns from Nothingham University for all discussions, laughs, and chocolates; and of course many thanks to Aart, Bram, Brenda, Elaheh, Jan, Jetse, João, Kannan, Leilei, Lisanne, Maurice, Milou, Mijke, Rong, Sanne, Sarah, and Yao, for the enjoyable discussions, lunches, and group outings.

I have learned the basics of microfluidics under supervision of Séverine le Gac during my master's in the BIOS lab on a chip group. Séverine also gave me the opportunity to perform research in the group of Michele Boiani at the Max-Planck Institute in Muenster. Thanks to all of you, it has been an amazing time that strongly motivated me to pursue an academic career.

Importantly, I would also like to thank my friends – in particular 'De Peppels' – and family. I am especially thankful for the endless support that my parents gave me. Robin, brother, your interest in biology once triggered me to choose this professional direction. I appreciate it that you now support me as a paranymph. Jolyn, your endless love and support are invaluable. I'm looking forward to our future together.

Thanks to all of you, this has been a wonderful experience.

- Tom Kamperman -

Biography

Tom Kamperman was born on the 13th of February 1988 in Winterswijk, The Netherlands. In 2006 he received his diploma for pre-university education (VWO) with a dual specialization (Nature & Technology and Nature & Health) from S.G. Marianum in Groenlo, The Netherlands. He studied Biomedical Engineering with a specialization in molecular, cellular, and tissue engineering at the University of Twente, The Netherlands. His bachelor's project focused on the determination of gene expression in human pluripotent stem cells using qPCR and was performed in the Molecular Cell Biology group within the MIRA Institute for Biomedical Technology and Technical Medicine under the supervision of Prof. Dr. Wiebe Kruijer and Dr. Marije Telgenkamp. He obtained his bachelor of engineering degree in 2009. His master's project focused on the development of a microfluidic platform to monitor the respiratory activity of embryos and was performed in the BIOS Lab-on-a-Chip group within the MESA+ Institute for Nanotechnology under the supervision of Prof. Dr. Albert van den Berg and Dr. Séverine Le Gac. During his master's he performed an internship within the Mouse Embryology Laboratory at the Max-Planck Institute for Molecular Biomedicine, Germany. Under the supervision of P.D. Dr. Michele Boiani and Dr. Martin Pfeiffer he focused on testing factors to increase reprogramming efficiency in induced pluripotent stem cell generation. During this period, he also obtained his didactic skills certificate and worked as a teaching assistant for the Biomedical Engineering master's program at the University of Twente. He obtained his master of engineering degree in 2012. Until 2013 he continued working as a researcher within the BIOS Lab-on-a-Chip group. In 2013, he started his PhD training at the department of Developmental BioEngineering within the MIRA Institute for Biomedical Technology and Technical Medicine at the University of Twente under the supervision of Prof. Dr. Marcel Karperien and Dr. Jeroen Leijten. The subject of his research was developing microgel technology to advance modular tissue engineering. For part of the work described in this thesis, he received a travel grant and poster award, as well as several stimulation grants to promote the continuance of this project. His work also resulted in a patent application, based on which he co-founded the company IamFluidics in 2017. From 2017 he continued his research within the department of Developmental BioEngineering at the University of Twente where he currently focuses on engineering microfluidic platforms and optimizing biomaterials for the 3D culture of individual stem cells within microgels.

Scientific Output

Peer-reviewed Papers

1. Visser CW*, **Kamperman T***, Karbaat LP, Lohse D, and Karperien M. In-air Microfluidics Enables Rapid Fabrication of Particles, Fibers, and Modular 3D (bio)materials. *Accepted for publication in Science Advances, 2018. Manuscript available on request.*

2. **Kamperman T***, Henke S*, Zoetebier B, Ruiterkamp N, Wang R, Pouran B, Weinans H, Karperien M., and Leijten, J. Nanoemulsion-induced Enzymatic Crosslinking of Tyramine-functionalized Polymer Droplets. *Published as back cover article in Journal of Materials Chemistry B, 2017, DOI: 10.1039/C7TB00686A, Impact Factor 4.9, Altmetric 1.*

3. **Kamperman T**, Henke S, Visser CW, Karperien M, and Leijten J. Centering Single Cells in Microgels via Delayed Crosslinking Supports Long-term 3D Culture by Preventing Cell Escape. *Published as front cover article in Small, 2017, DOI: 10.1002/smll.201603711, Impact Factor 8.3, Altmetric 76.*

4. **Kamperman T**, Henke S, Van den Berg A, Shin SR, Tamayol A, Khademhosseini A, Karperien M and Leijten J. Modular Bioinks Based on Single Cell Microgels for Uncoupled Cellular Micro- and Macroenvironments. *Published as front cover article in Advanced Healthcare Materials, 2016, DOI: 10.1002/adhm.201600913, Impact Factor 5.8, Altmetric 53. Top-downloaded of the month.*

5. **Kamperman T***, Visser CW*, Leijten J, Lohse D, and Karperien M. In-air Microfluidics for Chip-free Generation of Microdroplets-, Particles, -Fibers, and 3D Hierarchical Prints. *Published in Proceedings of MicroTAS, 2016, ISBN: 9781510834163.*

--- In progress ---

6. **Kamperman T**, Le Gac S, Leijten J. Single Cell Microgels: Engineered 3D Cellular Microniches. *In preparation as an Invited Review for Trends in Biotechnology.*

7. **Kamperman T**, Crispim JF, Henke S, Lee W, Offerhaus H, Neubauer M, Fery A, Karperien M, and Leijten J. Hydrogel Microniches with in Situ Tunable Stiffness Steer Long-term Single Stem Cell Fate. *In preparation.*

8. **Kamperman T**, Kelder C, Koerselman M, Crispim JF, Hendriks J, Henke S, De Peuter X, Wang R, Dijkstra PJ, Leijten J, and Karperien M. Building Blocks for Modular Tissue Engineering. *In preparation.*

9. **Kamperman T***, Visser CW*, Trikalitis V, Leijten J, Lohse D, Karperien M. In-air Microfluidics for Jet-based Production of Janus Microparticles. *In preparation.*

10. **Kamperman T***, Visser CW*, De Jong V, Leijten J, Lohse D, Karperien M. In-air Microfluidics for Jet-based Production of Core-shell Microparticles. *In preparation.*
11. Salehi S, **Kamperman T**, Henke S, Karperien M, and Leijten J. In Situ Self-assembly of Cellular Microaggregates using an Injectable and Modular Bio-ink. *In preparation.*
12. Karbaat L, **Kamperman T**, Both S, Karperien M, Leijten J. Extreme High-throughput Generation of Single Cell Microgels using In-air Microfluidics and Direct On-cell Crosslinking. *In preparation.*

Abstracts Selected for Oral Presentation (presenter; non-exhaustive list)

1. **Kamperman T***, Visser CW*, Leijten J, Lohse D, and Karperien M. In-air Microfluidics for Chip-free Production of Emulsions, Suspensions, and 3D Modular Biomaterials. FLOW17, 2017, Paris, FR.
2. **Kamperman T***, Visser CW*, Leijten J, Lohse D, and Karperien M. In-air Microfluidics. MIRA day, 2016, Enschede, NL. Invited speaker.
3. **Kamperman T***, Visser CW*, Leijten J, Lohse D, and Karperien M. In-air Microfluidics for Chip-free Generation of Microdroplets, -particles, -fibers, and 3D Hierarchical Prints. MicroTAS, 2016, Dublin, IE. *Published in Proceedings of MicroTAS, 2016, ISBN: 9781510834163.*
4. Visser CW*, **Kamperman T***, Lohse D, and Karperien M. In-air microfluidics: Drop and Jet Coalescence Enables Rapid Multi-phase 3D Printing. APS Division of Fluid Dynamics, 2016, Portland, USA.
5. **Kamperman T**, Henke S, Neubauer M, Fery A, Karperien M, and Leijten J. Single Cell Microgels as Modular Building Blocks for 3D Multiscale Tissue Engineering. NBTE, 2015, Lunteren, NL.
6. **Kamperman T**, Henke S, Neubauer M, Fery A, Karperien M, and Leijten J. High-Throughput Engineering Of Single Cell Microniches with Tunable Size And Elasticity. Biofabrication, 2015, Utrecht, NL
7. **Kamperman T**, Henke S, Van den Berg A, Karperien M, and Leijten J. High-Throughput Production of Single Cell Microgels as Pericellular Matrix Templates. BSTE, 2015, Leuven, BE. *Recipient of ESP Travel Grant*.
8. **Kamperman T**, Henke S, Van den Berg A, Karperien M, and Leijten J. Single Cell Microgels: High-Throughput Engineering of Customizable Microniches. NBTE, 2014, Lunteren, NL.

Abstracts Selected for Poster Presentation (presenter; non-exhaustive list)

1. **Kamperman T***, Visser CW*, Karbaat LP, Lohse D, and Karperien M. In-air Microfluidics for Chip-free Production of Emulsions, Suspensions, and 3D Modular Biomaterials. International MicroNanoConference, 2017, Amsterdam, NL.
2. **Kamperman T**, Henke S, Neubauer M, Fery A, Leijten J, and Karperien M. Engineering 3D Single Stem Cell Microniches with Dynamically Tunable Stiffness. TERMIS EU, 2016, Uppsala, SE.
3. **Kamperman T**, Henke S, Neubauer M, Fery A, Karperien M, and Leijten J. Engineering 3D Single Stem Cell Microniches with Dynamically Tunable Stiffness. Mechanobiology, 2016, Amsterdam, NL.
4. **Kamperman T**, Henke S, Leijten J, and Karperien M. Microfluidics for Complex Tissue Engineering. HDMT, 2016, Enschede, NL.
5. **Kamperman T**, Leijten J, Henke S, Van den Berg A, and Karperien M. High-yield single-cell microniche production using droplet microfluidics. New Frontiers, 2014, Nijmegen, NL.
6. **Kamperman T**, Leijten J, Henke S, Van den Berg A, and Karperien M. Microfluidic Encapsulation of Single Cells to Provide an Immunoprotective Microenvironment. FLOW14, 2014, Enschede, NL. *Recipient of runner-up poster award.*
7. **Kamperman T**, Leijten J, Henke S, and Karperien M. Producing Artificial Chondrons for Improved Cartilage Repair. OARSI, 2014, Paris, FR. *Abstract published in Osteoarthritis and Cartilage, 2014, DOI: 10.1016/j.joca.2014.02.921.*

Book Chapters

1. Henke S, **Kamperman T**, Wang R, Dijkstra PJ, Leijten J, and Karperien M. The Stiffness and Composition of Micro Hydrogels Independently Control Mesenchymal Stromal Cell Differentiation in the Osteogenic Lineage. *Published in PhD thesis S. Henke: Microgel Technology for Improved Beta Cell Transplantation, 2016, DOI: 10.3990/1.9789036542043.*
2. Henke S, Leijten J, **Kamperman T**, Groot Nibbelink M, Wang R, Plass J, Tons A, Hanegraaf M, Carlotti F, De Koning E, Dijkstra PJ, Van Apeldoorn A, and Karperien M. Proliferation Restrictive Micro-environments for Beta Cell Encapsulation. *Published in PhD thesis S. Henke: Microgel Technology for Improved Beta Cell Transplantation, 2016, DOI: 10.3990/1.9789036542043.*
3. Henke S*, **Kamperman T***, Plass J, Wang R, Dijkstra PJ, Leijten J, and Karperien M. Biofabrication of Core-shell Hydrogels as Microbioreactors for Controlled Cell Aggregation. *Published in PhD thesis S. Henke: Microgel Technology for Improved Beta Cell Transplantation, 2016, DOI: 10.3990/1.9789036542043.*

4. **Kamperman T***, Henke S*, Ruiterkamp N, Dijkstra PJ, Karperien M, and Leijten J. Centering Single Cells in Spherical Microgels by Uncoupling on-chip Emulsification and Enzymatic Crosslinking using Hydrogen Peroxide Diffusion. *Published in PhD thesis S. Henke: Microgel Technology for Improved Beta Cell Transplantation, 2016, DOI: 10.3990/1.9789036542043.*

Patents

1. Visser CW, **Kamperman T**, Karperien HBJ, Lohse D. Method and apparatus for in-air production of single droplets, compound droplets, and shape-controlled (compound) particles or fibers. *EU patent pending, EP16163060, priority date 30/03/2016.*

Invited Presentations

1. 9th Microfluidics Consortium, 2017, Beurs van Berlage, Amsterdam, The Netherlands
2. Lewis Lab, 2017, Harvard University, Boston, USA

Journal Covers

1. Back cover of Journal of Materials Chemistry B. *DOI: 10.1039/C7TB90093G*
2. Front cover of Small. *DOI: 10.1002/smll.201770120*
3. Front cover of Advanced Healthcare Materials. *DOI: 10.1002/adhm.201770012*

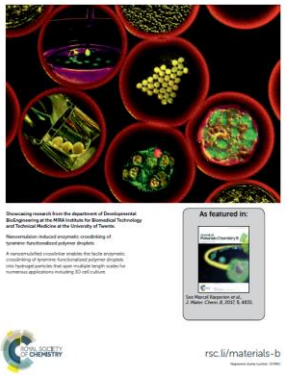

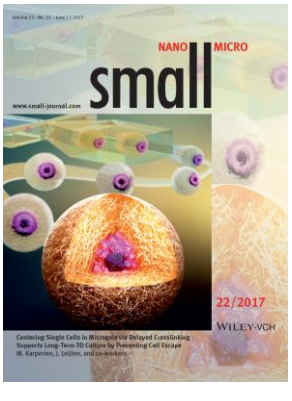

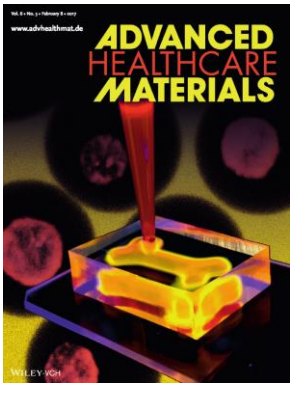

* **Co-first authorship**

Grants and Awards

1. "Commercializing In-air Microfluidics" (2017). TTW Take-off phase 2 soft loan to the company IamFluidics B.V. to commercialize in-air microfluidics. *Grant size: €250,000. Role: lead author.*
2. "In-air microfluidics" (2017). RVO (Dutch government) grant to study feasibility of feasibility of in-air microfluidics' commercialization. *Grant size: €25,000. Role: lead author.*
3. "In-air Microfluidics" (2016). STW Take-off phase 1 grant to study feasibility of in-air microfluidics' commercialization. *Grant size: €40,000. Role: lead author.*
4. "Unravelling Mechanotransduction in Stem Cell-laden Microgels" (2016). Strategic impulse for MIRA research. *Grant size: €33,000. Role: lead author.*
5. "Ultrafast copper-free click reactions for (cell laden) microgels" (2016). Strategic impulse for MIRA research. *Grant size: €7,500. Role: co-author.*
6. Demcon Nymus 3D voucher (2016) for high-quality illustrations of single cell encapsulation. *Grant size: €4,000. Role: co-author.*
7. BioNanoLab voucher (2015) to use facilities at MESA+ Institute. *Grant size: €4,000. Role: lead author.*
8. Travel Grant (2015) for BSTE, BE.
9. Runner-up poster award (2014) at FLOW14, NL.
10. Erasmus scholarship (2011) for internship at Max-Planck Institute for Molecular Biomedicine, DE.

Teaching and Supervision

Courses

2016 – 2018 Evaluator 'new technology business development'

2012 – 2017 Tutor and practical instructor 'creating biological tissues'

2010 – 2012 Teaching assistant 'cell biology', 'DNA technology', and 'tissue engineering'

Students

1. Vincent de Jong (M.Sc., Maastricht University, expected graduation January 2018).
2. Vasileios Trikalitis (M.Sc., University of Twente, August 2016) "3-jet In-air Microfluidics for Facile Ultra-High-Throughput Manufacturing of Janus and Core-shell Structures".

3. Michelle Koerselman (M.Sc., University of Twente, June 2016) "In Situ Modification of Injectable Tissue Engineered Constructs using Multi-functional Microgels".
4. Cindy Kelder (M.Sc., University of Twente, February 2016) "Biofunctionalization of Dextran-Tyramine Microgels".
5. Melvin Gurian (B.Sc., University of Twente, July 2015) "Engineering Hydrogel Microfibers: Development and Characterization of a 3D Microfluidic Device to Produce Hydrogel Microfibers for Tissue Engineering".
6. Niels Ruiterkamp (B.Sc., University of Twente, August 2014) "Production of Dextran-Tyramine Microgels for Cell Encapsulation using Droplet Microfluidics".

Public Outreach

News articles

2017 "Microfluidics Upside-down and in the Air". *Published on utoday.nl.*

2017 "Tiny Bricks of Single Cells for 3D Synthetic Tissue". *Published on advancedsciencenews.com. In top 5 'most read' articles of the month.*

2017 "Chip Captures Individual Cells in Minuscule Gels". *Published amongst others on sciencedaily.com, breitbart.com, phys.org, and utwente.nl.*

Microgel Technology to Advance Modular Tissue Engineering

Tom Kamperman

Native tissues are characterized by a complex multiscale hierarchical design. Recapitulating such complexity using a modular tissue engineering approach requires the integration of micromanufacturing techniques. In this thesis, we develop various droplet microfluidic platforms for the production of single- and multi-cell-laden hydrogel microparticles (i.e. microgels) that act as modular tissue engineering building blocks. We endow these building blocks with *in situ* tunable biomechanical and biochemical properties to enable spatiotemporal tailoring of the cellular microenvironment. Furthermore, we present two technological innovations that enable the facile biofabrication of modular tissue constructs based on cell-laden microgels. To aid clinical translation, we establish a novel platform technology called 'in-air microfluidics', which enables the chip-free production of monodisperse emulsions, suspensions, and 3D modular tissue constructs at production rates compatible with clinical and industrial applications.

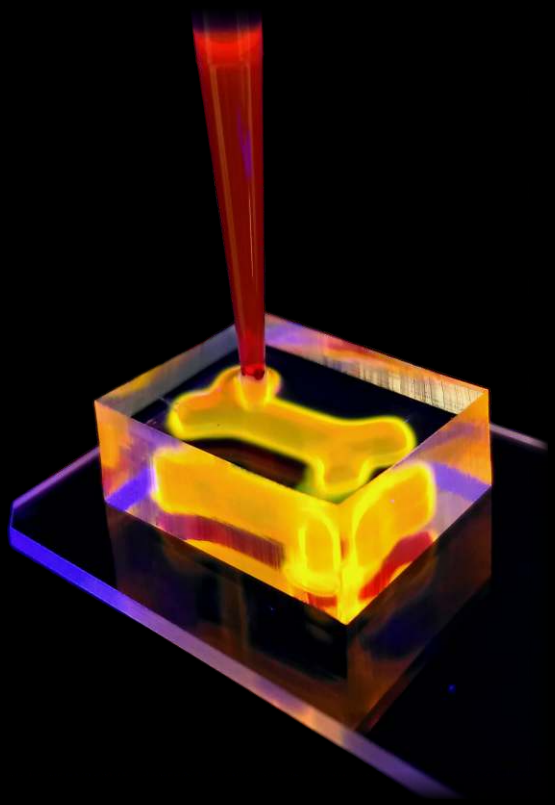

9 78903 544610 >

UNIVERSITY OF TWENTE.